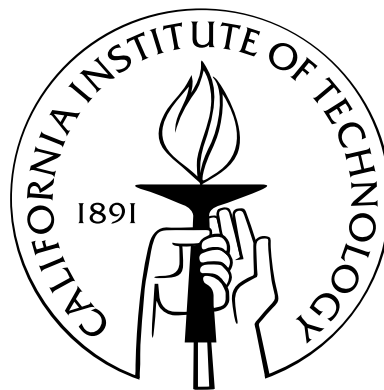


# Ladder studies of gapless quantum spin liquids: Spin-Bose metal and $SU(2)$ -invariant Majorana spin liquids

Thesis by

Hsin-Hua Lai

In Partial Fulfillment of the Requirements  
for the Degree of  
Doctor of Philosophy



California Institute of Technology  
Pasadena, California

2012

(Defended May 9 2012)

© 2012  
Hsin-Hua Lai  
All Rights Reserved

To my family and fiancée, for unconditional support, and to all my friends.

# Acknowledgements

First of all, I would like to express my gratitude to the committee members: Lesik Motrunich, Gil Refael, Michael Cross, and Nai-Chang Yeh for being willing to take the time to be my thesis defense committee, read the thesis, and give comments. Especially I want to thank my thesis advisor, Lesik Motrunich, who has always been very encouraging, patient, and willing to spend lots of time discussing with me. This dissertation would not have been possible without his guidance. I also would like to thank Gil Refael for sharing his insights and views now and then, which always brings different perspectives to thinking about physics.

I also would like to thank my officemates Tony Lee and Tiamhock Tay for sharing new ideas and chatting about things related to the real world. To my Caltech friends—Chang-Yu Hou, Eyal Kenig, Shankar Iyer, Shu-Ping Lee, Kun Woo Kim, Liyan Qiao, Jason Alicea, and many others in ACT—I want to thank you for enriching my life here at Caltech.

Finally, I am most grateful to my family for their support; to my fiancée U Shan Chen for love, patience, and always encouraging me to keep going forward.

# Abstract

The recent experimental realizations of spin-1/2 *gapless* quantum spin liquids in two-dimensional triangular lattice organic compounds  $\text{EtMe}_3\text{Sb}[\text{Pd}(\text{dmit})_2]_2$  and  $\kappa\text{-(ET)}_2\text{Cu}_2(\text{CN})_3$  have stimulated the investigation of the gapless spin liquid theories. The models in dimensions greater than one ( $D > 1$ ) usually involve multispin interactions, such as ring exchange interactions, that are difficult to study, while effective gauge theory descriptions are not well-controlled to give reliable physics information. Driven by the need for a systematic and controlled analysis of such phase, such models on ladders are seriously studied. This thesis first focuses on such ladder models. We propose that the gapless spin liquid phase can be accessed from a two-band interacting electron model by metal-Mott insulator phase transition. We use Bosonization analysis and weak-coupling Renormalization Group to further study the gapless spin liquid state in the presence of Zeeman magnetic fields or orbital magnetic fields. Several new exotic gapless spin liquids with dominant spin nematic correlations are predicted. In such a ladder spin liquid, we also consider the impurity effects. We conclude that the local energy textures and oscillating spin susceptibilities around the impurities are nontrivial and can be observed in the experiments. We then shift our focus to another theoretical candidate, an  $\text{SU}(2)$ -invariant spin liquid with Majorana excitations, which can also qualitatively explain the experimental phenomenology. We construct an exactly solvable Kitaev-type model realizing the long-wavelength Majorana spin liquid state and study its properties. We find that the state has equal power-law spin and spin-nematic correlations and behaves nontrivially in the presence of Zeeman magnetic fields. Finally, we realize such Majorana spin liquid states on a two-leg ladder and further explore their stability. We conclude the states can be stable against short-range interactions and gauge field fluctuations.

# Contents

<b>Acknowledgements</b>	<b>iv</b>
<b>Abstract</b>	<b>v</b>
<b>1 Introduction</b>	<b>1</b>
1.1 Gapless spin liquid material: $\kappa$ -(ET) <sub>2</sub> Cu <sub>2</sub> (CN) <sub>3</sub> . . . . .	4
1.1.1 Crystal and electronic structures of $\kappa$ -(ET) <sub>2</sub> Cu <sub>2</sub> (CN) <sub>3</sub> . . . . .	4
1.1.2 Spin liquid in $\kappa$ -(ET) <sub>2</sub> Cu <sub>2</sub> (CN) <sub>3</sub> . . . . .	5
1.2 Gapless spin liquid material: EtMe <sub>3</sub> Sb[Pd(dmit) <sub>2</sub> ] <sub>2</sub> . . . . .	8
1.2.1 Crystal and electronic structures of EtMe <sub>3</sub> Sb[Pd(dmit) <sub>2</sub> ] <sub>2</sub> . . . . .	8
1.2.2 Spin liquid in EtMe <sub>3</sub> Sb[Pd(dmit) <sub>2</sub> ] <sub>2</sub> . . . . .	9
1.3 Overview of thesis . . . . .	13
<b>2 Preliminaries</b>	<b>15</b>
2.1 Bosonization primer . . . . .	15
2.2 Weak-coupling renormalization group (RG) and current algebra . . . . .	21
2.3 Spin Bose-metal theory on the zigzag strip . . . . .	26
2.3.1 SBM via Bosonization of gauge theory . . . . .	28
2.3.2 SBM by Bosonizing interacting electrons . . . . .	30
2.3.3 Fixed-point theory of the SBM phase . . . . .	32
2.4 Original Kitaev model on the honeycomb lattice . . . . .	33
<b>3 Two-band electronic metal and neighboring spin liquid (spin Bose-metal) on a zigzag strip with longer-ranged repulsion</b>	<b>38</b>

3.1	Weak coupling analysis of $t_1 - t_2$ model with extended repulsion: Stabilizing C2S2 metal . . . . .	40
3.1.1	Setup for two-band electron system . . . . .	40
3.1.2	Weak coupling renormalization group . . . . .	43
3.1.3	Fixed point for stable C2S2 phase . . . . .	43
3.1.4	Numerical studies of the flows . . . . .	44
3.1.5	Examples of phase diagrams with C2S2 metal stabilized by extended interactions . . . . .	45
3.1.5.1	Weak coupling phase diagram for potential Eq. (3.31) . . . . .	46
3.1.5.2	Weak coupling phase diagram for potential Eq. (3.31) truncated at the 4th neighbor . . . . .	48
3.2	Weak-to-intermediate coupling: Phases out of C2S2 upon increasing interaction . . . . .	49
3.2.1	Harmonic description of the C2S2 phase . . . . .	49
3.2.2	Mott insulator driven by Umklapp interaction. Intermediate coupling procedure out of the C2S2 . . . . .	52
3.2.2.1	Instability out of C1[ $\rho^-$ ]S2 driven by spin-charge coupling $W$ . . . . .	53
3.2.2.2	Instability out of C1[ $\rho^+$ ]S0 driven by Umklapp $H_8$ . . . . .	54
3.2.3	Numerical results . . . . .	54
3.2.3.1	Intermediate coupling phase diagram for model with potential Eq. (3.31) . . . . .	54
3.2.3.2	Intermediate coupling phase diagram for model with potential Eq. (3.31) truncated at the 4th neighbor . . . . .	59
3.3	Summary and discussion . . . . .	59
3.A	Derivation of $\Delta[\cos(4\theta_{\rho^+})]$ and $\Delta[\cos(2\varphi_{\rho^-})]$ in C2S2 phase . . . . .	62
<b>4</b>	<b>Effects of Zeeman field on a spin Bose-metal phase</b>	<b>65</b>
4.1	Electrons on a two-leg zigzag strip in a Zeeman field: Weak coupling approach . . . . .	67

4.2	Transition to Mott insulator: SBM phase . . . . .	74
4.3	Observables in the SBM in Zeeman field . . . . .	77
4.4	Nearby phases out of the SBM in the field . . . . .	81
4.4.1	Phases when $w_{12}^\uparrow$ is relevant . . . . .	81
4.4.2	Phases when both $w_{12}^\uparrow$ and $w_{12}^\downarrow$ are relevant . . . . .	83
4.4.2.1	$w_{12}^\uparrow > 0, w_{12}^\downarrow > 0$ . . . . .	84
4.4.2.2	$w_{12}^\uparrow < 0, w_{12}^\downarrow < 0$ . . . . .	85
4.4.2.3	$w_{12}^\uparrow > 0, w_{12}^\downarrow < 0$ . . . . .	85
4.4.2.4	$w_{12}^\uparrow < 0, w_{12}^\downarrow > 0$ . . . . .	86
4.5	Discussion . . . . .	87
<b>5</b>	<b>Insulating phases of electrons on a zigzag strip in the orbital magnetic field</b>	<b>90</b>
5.1	Weak coupling approach to electrons on a zigzag strip with orbital field . . . . .	91
5.2	Observables in the Mott-insulating phase in orbital field . . . . .	98
5.3	Spin-gapped phases in orbital field . . . . .	103
5.3.1	$\lambda_{11}^\sigma < 0, \lambda_{22}^\sigma > 0, \lambda_{12}^\sigma > 0$ . . . . .	104
5.3.2	$\lambda_{11}^\sigma > 0, \lambda_{22}^\sigma < 0, \lambda_{12}^\sigma > 0$ . . . . .	104
5.3.3	$\lambda_{11}^\sigma, \lambda_{22}^\sigma > 0, \lambda_{12}^\sigma < 0$ . . . . .	104
5.3.4	$\lambda_{11}^\sigma, \lambda_{22}^\sigma < 0, \lambda_{12}^\sigma > 0$ . . . . .	105
5.3.5	$\lambda_{12}^\sigma < 0$ and either $\lambda_{11}^\sigma < 0$ or $\lambda_{22}^\sigma < 0$ . . . . .	106
5.4	Discussion . . . . .	106
<b>6</b>	<b>Effects of impurities in spin Bose-metal phase on a two-leg triangular strip</b>	<b>108</b>
6.1	Nonmagnetic impurities in the spin Bose-metal on the ladder . . . . .	109
6.1.1	Nonmagnetic defects treated as perturbations . . . . .	111
6.1.2	Physical calculations of oscillating susceptibility and bond textures in the fixed-point theory of semi-infinite chains . . . . .	114
6.1.3	Other situations with impurities . . . . .	116
6.1.3.1	Weakly coupled semi-infinite systems . . . . .	116
6.1.3.2	Spin- $\frac{1}{2}$ impurity coupled to a semi-infinite system . . . . .	117

6.1.3.3	Two semi-infinite systems coupled symmetrically to a spin- $\frac{1}{2}$ impurity . . . . .	117
6.2	Conclusions . . . . .	118
6.A	One-mode theory on a semi-infinite chain . . . . .	119
6.B	Calculations in a fixed-point theory of a semi-infinite system with pinned $\theta_{\sigma+}(0)$ , $\varphi_{\sigma-}(0)$ , and $\varphi_{\rho-}(0)$ . . . . .	120
<b>7</b>	<b>SU(2)-invariant Majorana spin liquid with stable parton Fermi surfaces in an exactly solvable model</b>	<b>123</b>
7.1	SU(2)-invariant Majorana spin liquid with stable Fermi surfaces . . . . .	125
7.2	Correlation functions . . . . .	129
7.2.1	Long wavelength analysis . . . . .	131
7.2.2	Exact numerical calculation . . . . .	134
7.3	Majorana spin liquid in the Zeeman field . . . . .	136
7.4	Discussion . . . . .	140
<b>8</b>	<b>Majorana spin liquids on a two-leg ladder</b>	<b>142</b>
8.1	Gapless Majorana orbital liquid (MOL) on a two-leg ladder . . . . .	144
8.1.1	Fixed-point theory of Majorana orbital liquid and observables . . . . .	148
8.1.2	Stability of Majorana orbital liquid . . . . .	152
8.2	Gapless SU(2)-invariant Majorana spin liquid (MSL) on the two-leg ladder . . . . .	155
8.3	Discussion . . . . .	159
8.A	Stability of gapless U(1) matter against $Z_2$ gauge field fluctuations in (1+1)D . . . . .	161
8.B	Fixed-point theory and observables in the SU(2) Majorana spin liquid . . . . .	166
8.C	Zeeman magnetic field effects on the SU(2) Majorana spin liquid . . . . .	173
8.D	SU(2) Majorana spin liquid with time reversal breaking (TRB) . . . . .	175
	<b>Bibliography</b>	<b>177</b>

# Chapter 1

## Introduction

At an early stage of introduction to interacting spin systems, students are taught that at low temperature the spin states mostly tend to “align” or “anti-align” with each other to form ordered states: the ferromagnet or the anti-ferromagnet. The phase transition to such states involves breaking of symmetries and can be described by phenomenological Ginzburg-Landau theory. However, quantum fluctuations can break the above naive classical picture and the spin states can even remain disordered down to zero temperature. One such example is that of the one-dimensional (1D) anti-ferromagnetic spin-1/2 Heisenberg chain, which has no long range order and its ground state possesses power law correlations [1]. Another famous example is the 1D spin-1 antiferromagnetic chain proposed by Haldane [2] to have a disordered ground state with a gap to excitations.

Another way to suppress magnetic long range order is “frustration” due to the geometry of lattice. Take a simple anti-ferromagnetic Ising model on a square and on a triangle for instance, Fig. 1.1. Due to the geometry of these two plaquettes, the ground state on the square is the Neel anti-ferromagnet. However, in the ground state of the triangle the spins cannot be arranged to simultaneously minimize all the interactions, which suppresses the magnetic order. The situation in the second case is what we call the frustration. Besides, low lattice dimension typically increases the frustration and also the quantum fluctuations. Hence, there is a possibility of quantum spin liquids(QSL) [3, 4, 5] in a low-dimensional highly frustrated lattice.

Focusing on the lattice dimension greater than one, we now know theoretically there are many different kinds of spin liquids. Gapped topological spin liquids [6, 7, 8, 9, 10,

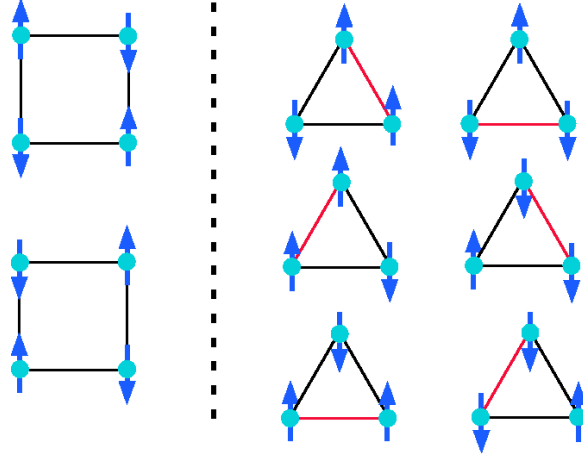


Figure 1.1: Schematic pictures of antiferromagnetic Ising spin model on a square and a triangle. For the spins on a square, each spin is antiparallel with its neighbor to end up with two exact ground states. However, all three spins on a triangle cannot be antiparallel and instead of the two ground states mandated by the Ising symmetry (up and down), there are six ground states. This is the simplest example of frustration. The red lines denote the axis on which the spins are parallel

[11, 12, 13, 14] are quite well-understood and have been theoretically shown to exist in model systems. However, none of these theoretically well-understood gapped spin liquids are realized in the experiment. On the other hand, even though “gapless” spin liquids [3, 13, 11] are less understood theoretically, there have been series of experimental reports of promising gapless spin liquid states in two-dimensional(2D) organic compounds  $\text{EtMe}_3\text{Sb}[\text{Pd}(\text{dmit})_2]_2$  and  $\kappa\text{-(ET)}_2\text{Cu}_2(\text{CN})_3$  [15, 16, 17, 18, 19, 20, 21, 22, 23, 24, 25, 26]. The details of these two spin liquid materials will be discussed in Chapters 1.1 and 1.2. The striking features of such compounds are the absence of long range magnetic order in the zero temperature limit, but the presence of finite spin susceptibilities, “metal-like” linear temperature dependent specific heat and thermal conductivity even though they are in Mott insulating phase.

One theoretical proposal suggests the state with Gutzwiller-projected spinon Fermi sea wave function [27, 28] in a 2D quantum spin-1/2 Heisenberg model with four-site ring exchange terms. This proposal leads to a theory of spinons coupled to  $U(1)$  gauge fields. However, there is no well-controlled theoretical access to such phase in 2D. From a theoretical point of view, it is difficult to analyze a model involving multi-spin interactions

(four-site ring exchange) and challenging to analyze gauge theory. From the perspective of numerics, most of the numerical tools cannot be used or do not give reliable unbiased information in such highly frustrated lattices. For example, the exact diagonalization (ED) studies are restricted to very small sizes, variational Monte Carlo (VMC) results are biased by the input wavefunctions, quantum Monte Carlo (QMC) fails due to the sign problem in such highly frustrated lattices, and density matrix renormalization group (DMRG) is able to give reliable unbiased information but suffers from the growth of entanglement in 2D and can not be applied in a large 2D lattice.

Driven by the needs for further understandings of the interesting phase, the ladder versions of such theoretical model have been studied [29, 30, 31, 32, 33, 34] and the ladder descendant of the gapless spin liquid state has been found and dubbed spin Bose-metal (SBM). Focusing on the SBM phase, in Chapters 3–5 we explore several experimentally motivated questions in the two-leg ladder. Since experiments suggest that the gapless spin liquid phase sit in the insulating side near the metal-Mott insulator phase transition line, in Chapter 3 we propose to access the SBM phase from a two-band Hubbard-type model. In Chapters 4–5 we consider separately the effects of Zeeman magnetic field and the effects of orbital magnetic field on the SBM. In Chapter 6 we consider the effects of impurities on the SBM.

For a smoking gun experiment for the proposal of spinon Fermi sea state, Katsura et al. [35] suggest that in the presence of orbital magnetic field, the flux of the spinon U(1) gauge field couples to the orbital field and leads to the observation of a finite thermal Hall conductance if the deconfined Fermionic spinons indeed exist and is responsible for the observed thermal current. However, the experiment reports no observation of the thermal Hall effect due to the deconfined spinons [23]. One theoretical possible explanation is the U(1) gauge fluctuations are suppressed due to some partial pairing of spinons [36, 37, 32], but it is not clear yet.

Searching for other theoretical proposals, Biswas et al. suggested a SU(2)-invariant gapless spin liquid with spinful Majorana excitations. The striking feature of the spin liquid state is that the external magnetic field has no orbital coupling to the SU(2) spin rotation-invariant Fermion bilinears that can give rise to a transverse thermal conductivity. Hence,

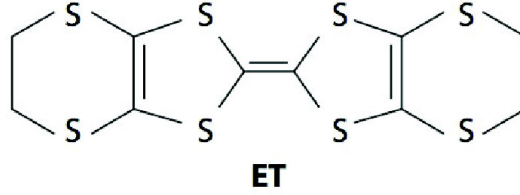


Figure 1.2: Adopted from [26]. The molecule BEDT-TTF(ET) is an electron donor and gives salt  $(\text{ET})_2\text{X}$  with monovalent anion  $\text{X}^{-1}$ .

there is no thermal Hall effect due to the deconfined parton excitations in this phase. To further explore the properties of such a new class of gapless spin liquids, we realize a long-wavelength  $\text{SU}(2)$ -invariant Majorana spin liquids in exactly solvable Kitaev-type models [14] in 2D and on a two-leg ladder which are detailed in Chapters 7–8.

In the remainder of this chapter, we summarize the experimental evidence of the spin liquids state in  $\kappa\text{-(ET)}_2\text{Cu}_2(\text{CN})_3$  in Chapter 1.1 and  $\text{EtMe}_3\text{Sb}[\text{Pd}(\text{dmit})_2]_2$  in Chapter 1.2. Finally, in Chapter 1.3 we provide an overview of the work reported in this thesis.

## 1.1 Gapless spin liquid material: $\kappa\text{-(ET)}_2\text{Cu}_2(\text{CN})_3$

In this section we briefly summarize the properties and the experimental evidence of the realization of the gapless spin liquids in  $\kappa\text{-(ET)}_2\text{Cu}_2(\text{CN})_3$  and point out some present controversial and open issues [26].

### 1.1.1 Crystal and electronic structures of $\kappa\text{-(ET)}_2\text{Cu}_2(\text{CN})_3$

The ET molecule shown in Fig. 1.2 provides many 2:1 compounds,  $(\text{ET})_2\text{X}$ , with various kinds of anion, X. Here we focus on  $\kappa\text{-(ET)}_2\text{X}$ . They are layered materials composed of conducting ET layers with 1/2 hole per ET and insulating X layers shown in Fig. 1.3(a). In the conducting layer, the ET molecules form dimers and are arranged in a checkerboard-like pattern shown in Fig. 1.3(b). From the band structure point of view, two ET and highest occupied molecular orbitals (HOMOs) in a dimer are energetically split into bonding and antibonding orbitals, each of which forms a conduction band due to the interdimer transfer

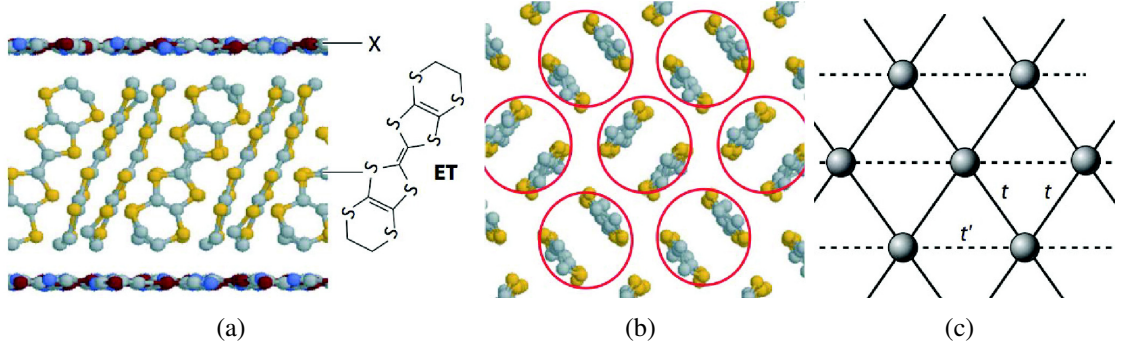


Figure 1.3: Adopted from [26]. (a) Side view of the layer structure of  $\kappa$ -(ET) $_2$ Cu $_2$ (CN) $_3$ . We can see the conducting ET layers are separated by the nonmagnetic cation layers, X. (b) Top view of the conducting ET layer. The ET molecules form dimers and are arranged in a checkerboard-like pattern. (c) The intradimer couplings are much stronger than the interdimer couplings and each dimer can be treated as a single unit. Hence, the ET dimers in (b) can be simplified to the triangular lattice model with each site occupied by exactly one electron.

integrals. The two bands are well separated so that the relevant band to the hole filling is the antibonding band, which is half-filled with one hole accommodated by one antibonding orbital. The dimer arrangement is modeled to an isosceles-triangular lattice characterized by two interdimer transfer integrals,  $t$  and  $t'$ , Fig. 1.3(c), of the order of 50 meV, whose anisotropy,  $t'/t$ , is 1.06 or 0.80 to 0.83 according to the tight-binding calculation of molecular orbital or first-principles calculation. [38, 39] The thermal transport experiment [40] indicates that the Mott-insulating compound  $\kappa$ -(ET) $_2$ Cu $_2$ (CN) $_3$  sits very close to the metal-Mott insulator transition line with a very small Mott charge gap, about 200 K. Because of the very small gap, we call  $\kappa$ -(ET) $_2$ Cu $_2$ (CN) $_3$  a *weak* Mott insulator. We remark that due to the small charge gap, the theoretical quantum spin model should include the high-order spin interactions (i.e., 3-site or 4-site ring exchange terms) besides the usual Heisenberg interactions.

### 1.1.2 Spin liquid in $\kappa$ -(ET) $_2$ Cu $_2$ (CN) $_3$

Figure 1.4(a) shows the temperature dependence of the magnetic susceptibility with the core diamagnetism subtracted [15].  $\kappa$ -(ET) $_2$ Cu $_2$ (CN) $_3$  has no anomaly down to the lowest temperature measured, 2 K, but does have a broad peak, which is well fitted to the

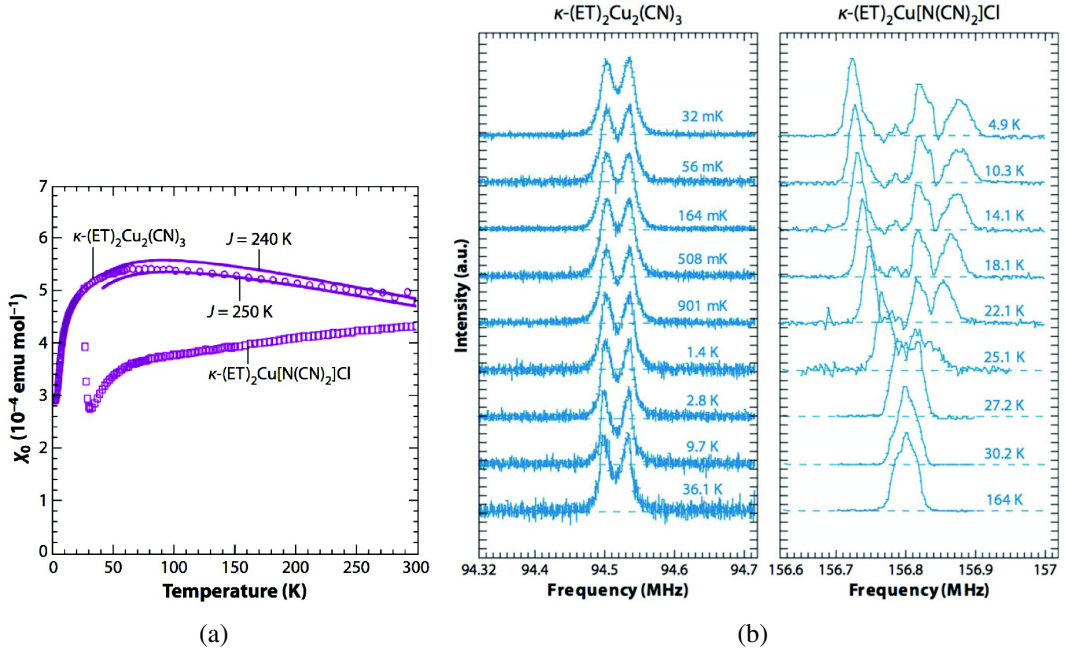


Figure 1.4: Adopted from [26]. (a) Temperature dependences of spin susceptibilities of  $\kappa$ -(ET) $_2$ Cu $_2$ (CN) $_3$  and  $\kappa$ -(ET) $_2$ Cu(N(CN) $_2$ )Cl. The solid lines represent the results of the series expansion of the triangular-lattice Heisenberg model. (b)  $^1$ H NMR spectra of single crystals of  $\kappa$ -(ET) $_2$ Cu $_2$ (CN) $_3$  (left) and  $\kappa$ -(ET) $_2$ Cu(N(CN) $_2$ )Cl (right) under magnetic fields applied perpendicular to the conducting layer

triangular-lattice Heisenberg model with an exchange interaction of  $J \sim 250$  K [15]. The magnetism is further probed by  $^1$ H nuclear magnetic resonance (NMR) measurements. Figure 1.4(b) shows the single-crystal  $^1$ H NMR spectra for  $\kappa$ -(ET) $_2$ Cu(N(CN) $_2$ )Cl and  $\kappa$ -(ET) $_2$ Cu $_2$ (CN) $_3$  under the magnetic field applied perpendicular to the conduction layer. The line shape at high temperatures comes from the fact that the nuclear dipole interaction is sensitive to the field direction relative to the molecular orientation, which is different between the two systems. The material  $\kappa$ -(ET) $_2$ Cu(N(CN) $_2$ )Cl shows a clear line splitting below 27 K, indicating a commensurate antiferromagnetic ordering, whose moment is estimated at  $0.45 \mu_B$  per an ET dimer by separate  $^{13}$ C NMR studies [41, 42, 43]. On the other hand, the spectra of  $\kappa$ -(ET) $_2$ Cu $_2$ (CN) $_3$  show neither distinct broadening nor splitting, which indicates the absence of long-range magnetic ordering at least down to 32 mK which is 4 orders of magnitude lower than the exchange coupling  $J$ . The result points to the first realization of a quantum spin liquid in  $\kappa$ -(ET) $_2$ Cu $_2$ (CN) $_3$  due to the strong spin frustration on the nearly equilateral triangular lattice.

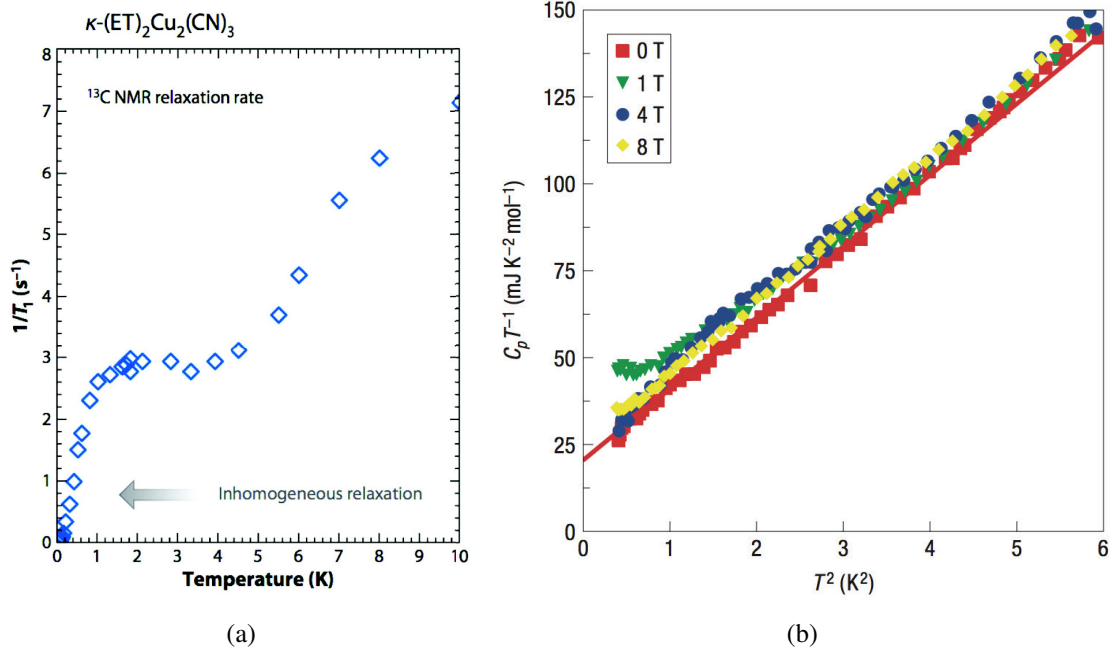


Figure 1.5: (a) is adopted from [26] and (b) is adopted from [17]. (a)  $^{13}\text{C}$  NMR relaxation rate of  $\kappa\text{-(ET)}_2\text{Cu}_2(\text{CN})_3$ . The nuclear relaxation becomes inhomogeneous at lower temperatures depicted by the graded arrow. (b) Specific heat divided by temperature,  $C_p T^{-1}$ , as a function of  $T^2$  for  $\kappa\text{-(ET)}_2\text{Cu}_2(\text{CN})_3$  under magnetic fields of 0 T (red square), 1 T (green down triangle), 4 T (blue circle), and 8 T (yellow diamond). At low temperature, the extrapolation indicates a finite constant at  $T=0$ , which suggests a linear temperature-dependent specific heat in  $\kappa\text{-(ET)}_2\text{Cu}_2(\text{CN})_3$ .

The properties of spin liquid in  $\kappa\text{-(ET)}_2\text{Cu}_2(\text{CN})_3$  was further studied by  $^{13}\text{C}$  NMR [44], specific heat [17], thermal conductivity [18], and expansivity [45] measurements. Figures 1.5(a) and 1.5(b) show  $^{13}\text{C}$  NMR relaxation rate and specific heat at low temperatures, respectively. Below 8 K,  $1/T_1$ , decreases more steeply and  $C/T$  starts to increase, followed by a kink and a peak around 5 to 6 K. This means that the anomaly is the thermodynamic and involves the spin degrees of freedom at least partially. This anomaly is accompanied by NMR spectral broadening, whose field dependence indicates that the broadening is not due to a spontaneous spin ordering but rather to a field-induced inhomogeneous staggered moment. This can be caused by impurities or a Dzyaloshinsky-Moriya interaction. The more interesting point is that although a steep decrease in  $1/T_1$  is observed well below 1 K, there appears no appreciable anomaly in specific heat and thermal conductivity around the corresponding temperatures.

Final key issue on the nature of this spin liquid material is whether the spin liquid is gapped. The experimental observations are still controversial. The specific heat points to the presence of a finite  $\gamma$  value (indication of linear temperature dependent  $C_p$ ) comparable to that in the metallic phase down to at least 0.3–0.4 K, below which the nuclear Schottky contribution becomes overwhelming [17]. The thermal conductivity measurements indicate that the thermal excitation is gapped below 0.46 K [18]. The  $^{13}\text{C}$  NMR relaxation rate shows a power-law temperature dependence with an exponent of 3/2; although, the nuclear relaxation is inhomogeneous at low temperature [44]. They are all inconsistent with each other. More systematic experimental studies are needed to provide more significant information of such spin liquid phase in  $\kappa\text{-(ET)}_2\text{Cu}_2(\text{CN})_3$ .

## 1.2 Gapless spin liquid material: $\text{EtMe}_3\text{Sb}[\text{Pd}(\text{dmit})_2]_2$

In this section we summarize the properties and the experimental evidence of the gapless spin liquid state in  $\text{EtMe}_3\text{Sb}[\text{Pd}(\text{dmit})_2]_2$  and discuss some present controversial and open issues. [26]

### 1.2.1 Crystal and electronic structures of $\text{EtMe}_3\text{Sb}[\text{Pd}(\text{dmit})_2]_2$

The  $\text{Pd}(\text{dmit})_2$  salts, (Cation)  $[\text{Pd}(\text{dmit})_2]_2$ , exhibit 2D layer structures and have the following features:

1.  $\text{Pd}(\text{dmit})_2$  units are strongly dimerized with an eclipsed overlapping mode to form  $[\text{Pd}(\text{dmit})_2]_2^-$  with one negative charge. The degree of dimerization is stronger than that in the  $\kappa$ -type ET salts.
2. In contrast to the  $\kappa$ -type ET salts, the dimer units show face-to-face stacking, Fig. 1.6(a).
3. Within the 2D conduction layer, the dimer units form a quasi-triangular lattice, Fig. 1.6(b).

Figure 1.6(a) shows the side view of the 3D crystal structure of  $\text{EtMe}_3\text{Sb}[\text{Pd}(\text{dmit})_2]_2$ . The unit cell contains two crystallographically equivalent conduction layers interrelated by a glide plane. They are separated from each other by the insulating cation layer.

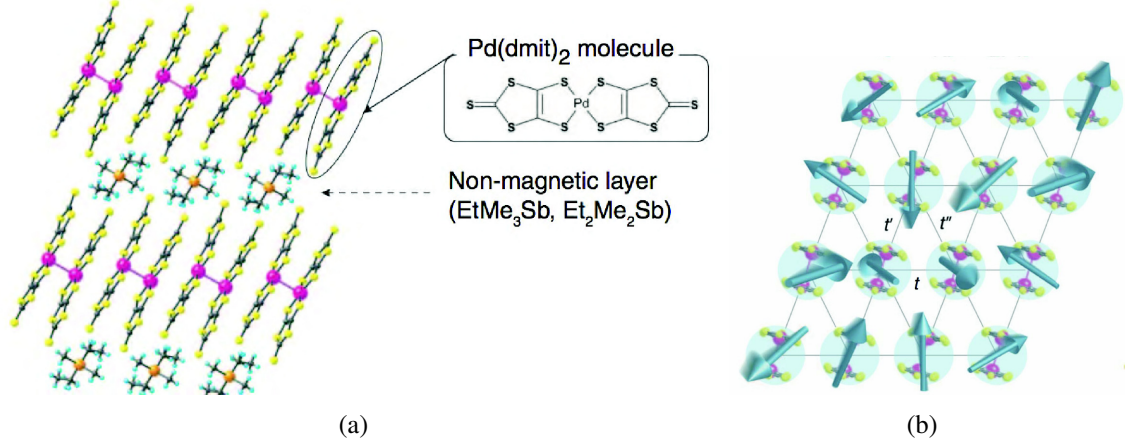


Figure 1.6: Adopted from [26]. (a) Side view of the layer structure of  $\text{EtMe}_3\text{Sb}[\text{Pd}(\text{dmit})_2]_2$ . We can see the conducting  $\text{Pd}(\text{dmit})_2$  molecule layers are separated by the nonmagnetic cation layers. (b) Top view of the  $\text{Pd}(\text{dmit})_2$  layer and the  $\text{Pd}(\text{dmit})_2$  molecules are strongly dimerized and are arranged in a checkerboard-like pattern. The intradimer couplings are much stronger than the interdimer couplings and thus each dimer can be treated as a single unit and in the end can be simplified to the triangular lattice model with three unequal transfer integrals,  $t$ ,  $t'$ , and  $t''$ . Since it is very close to an isosceles-triangular lattice, we treat  $t' \simeq t''$ .

The electronic structure around the Fermi level can be described by the dimer-based tight-binding approximation. The dimers,  $[\text{Pd}(\text{dmit})_2]_2^-$  form a scalene-triangular lattice where they are connected by three unequal transfer integrals,  $t$ ,  $t'$ , and  $t''$  in Fig. 1.6(b). However, they are very close to an isosceles-triangular lattice and thus we treat  $t' \simeq t''$ . From quantum chemistry calculation,  $t'/t \simeq 0.92$  for  $\text{EtMe}_3\text{Sb}[\text{Pd}(\text{dmit})_2]_2$  and is so frustrated that a spin liquid phase can be realized.

## 1.2.2 Spin liquid in $\text{EtMe}_3\text{Sb}[\text{Pd}(\text{dmit})_2]_2$

Figure 1.7(a) shows the temperature dependence of the magnetic susceptibility with the core diamagnetism subtracted.  $\text{EtMe}_3\text{Sb}[\text{Pd}(\text{dmit})_2]_2$  has no anomaly down to the lowest temperature measured, 5 K, but have a broad peak, which is well fitted to the triangular-lattice-Heisenberg model with an exchange interaction of  $J \sim 250$  K [21]. The magnetism is further probed by  $^{13}\text{C}$  NMR measurements. Figure 1.7(b) shows the single-crystal  $^{13}\text{C}$  NMR spectra for  $\text{EtMe}_3\text{Sb}[\text{Pd}(\text{dmit})_2]_2$ , which do not show significant broadening down to 19.4 mK [22]. Although very slight gradual broadening is observed, the width is much

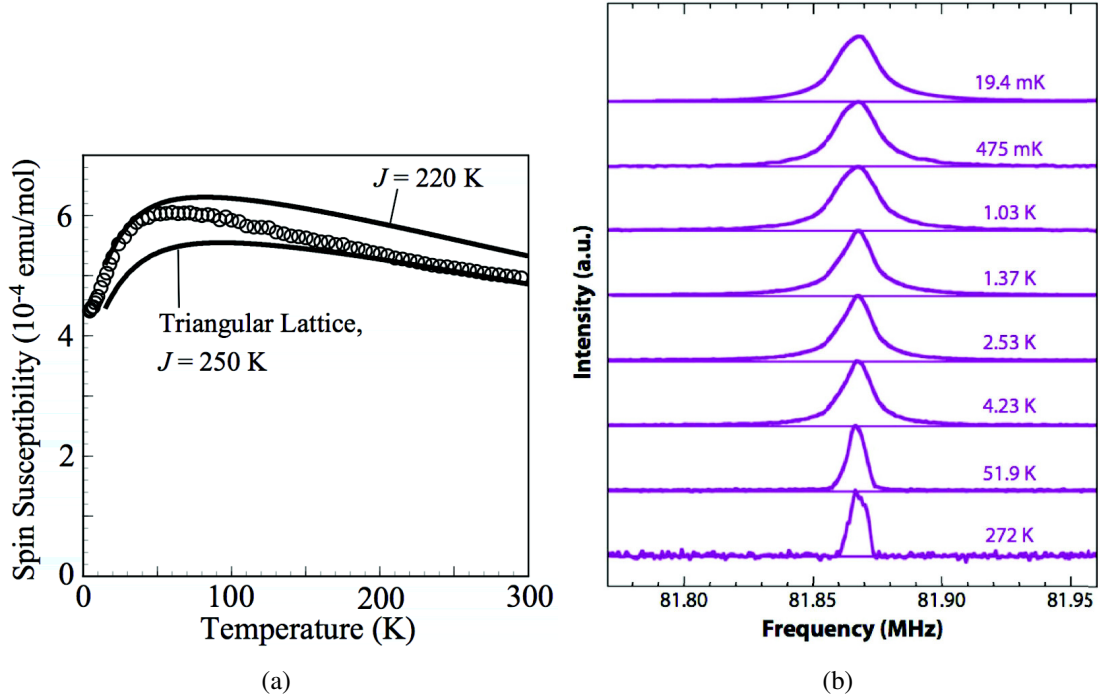


Figure 1.7: Adopted from [26]. (a) Temperature dependence of the spin susceptibility of randomly oriented samples of  $\text{EtMe}_3\text{Sb}[\text{Pd}(\text{dmit})_2]_2$ . Solid curves show the result of the [7/7] Padé approximants for the high-temperature expansion of the regular-triangular antiferromagnetic spin-1/2 system with  $J=220$  and  $250$  K. (b)  $^{13}\text{C}$  NMR spectra from  $272$  K to  $19.4$  mK for randomly oriented samples of  $\text{EtMe}_3\text{Sb}[\text{Pd}(\text{dmit})_2]_2$ . It is clear there is no further splitting of the peak, which indicates no formation of long-range magnetic order.

smaller than the scale of the hyperfine coupling constant of the  $^{13}\text{C}$  sites. This clearly indicates that there is no spin ordering or freezing down to the lowest temperature. Because this temperature is smaller than  $0.01\%$  of  $J$ , thermal fluctuations are negligible, and the absence of spin ordering or freezing should be attributed to quantum fluctuations.

As for the issue of whether the spin liquid state in  $\text{EtMe}_3\text{Sb}[\text{Pd}(\text{dmit})_2]_2$  is gapless, the experimental observations are still controversial but it seems the gapless spin liquid is more favored. Figure 1.8(a) shows the previous studies of the spin-lattice relaxation rate  $1/T_1$  curve fitted by the stretched exponential function. The stretching exponents  $\beta$  indicates homogeneity of the system. The  $\beta$  value being smaller than unity means that the system is inhomogeneous. The temperature dependence of  $\beta$  indicated that inhomogeneity is enhanced from approximately  $20$  K and reaches maximum around  $1$  K. A sharp drop of  $1/T_1$  below  $1$  K suggest a continuous phase transition that involves symmetry breaking

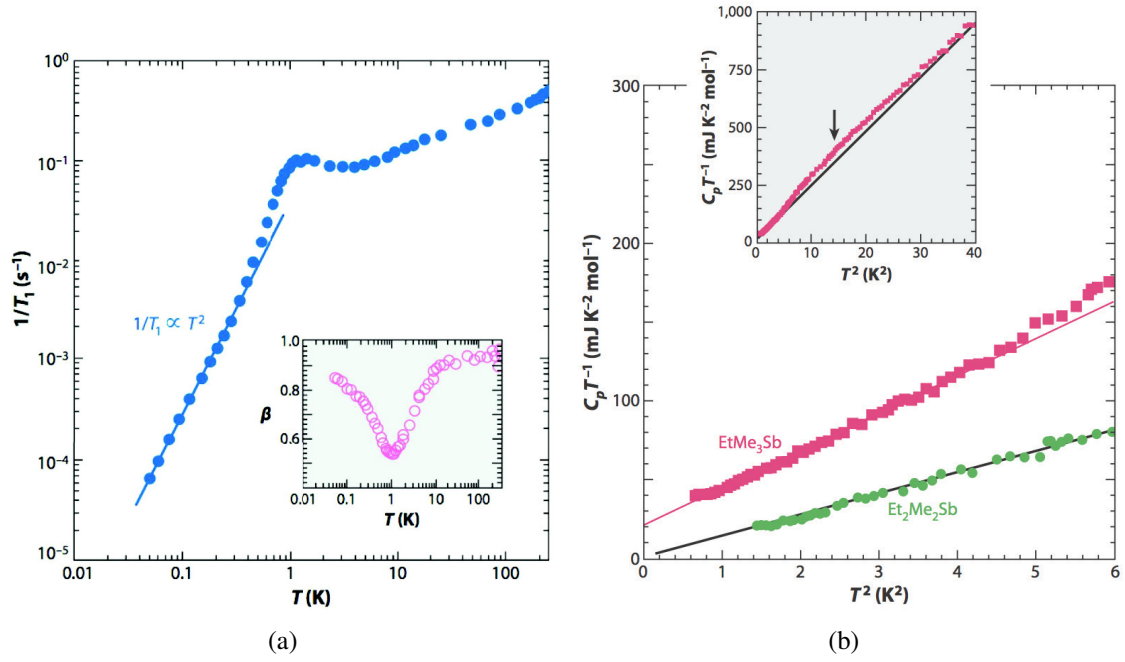


Figure 1.8: Adopted from [26]. (a) Temperature dependence of  $^{13}\text{C}$  nuclear spin-lattice relaxation rate ( $1/T_1$ ). The relaxation of the nuclear magnetization  $M(t)$  was analyzed using the stretched exponential function  $1 - M(t)/M(\infty) = \exp[-(t/T_1)^\beta]$ . The inset shows temperature dependence of the stretching exponent ( $\beta$ ). (b) Low-temperature heat capacity ( $C_p$ ) for  $\text{EtMe}_3\text{Sb}[\text{Pd}(\text{dmit})_2]_2$  and  $\text{Et}_2\text{Me}_2\text{Sb}$  salt. The main graph shows  $C_p T^{-1}$  versus  $T^2$  plots of the heat capacity. The inset shows a  $C_p T^{-1}$  versus  $T^2$  plot around a broad hump structure for the  $\text{EtMe}_3\text{Sb}[\text{Pd}(\text{dmit})_2]_2$ .

and/or topological ordering. However, a very recent report suggests that the transition is not intrinsic but field-induced [46]. Below 1 K, the relaxation curves recover the homogenous single-exponential nature, which is contradictory to the case of  $\kappa\text{-(ET)}_2\text{Cu}_2(\text{CN})_3$ . In this region,  $1/T_1$  is proportional to the square of the temperature, which suggests a spin gap formation in the low temperature phase. Because the temperature dependence of  $1/T_1$  does not obey an exponential law but a power law, the spin gap may be nodal, similar to that of anisotropic superconductivity. Such field-induced phase out of completely gapless spin liquid state can possibly be explained by our studies of Zeeman magnetic fields on the SBM phase in Chapter 4.

On the other hand, however, heat capacity shows a different aspect [25]. Compared with the  $\text{Et}_2\text{Me}_2\text{Sb}$  salt, which shows a nonmagnetic charge-ordered state with an excitation gap,  $\text{EtMe}_3\text{Sb}[\text{Pd}(\text{dmit})_2]_2$  gives large absolute values of heat capacity, Fig. 1.8(b). The

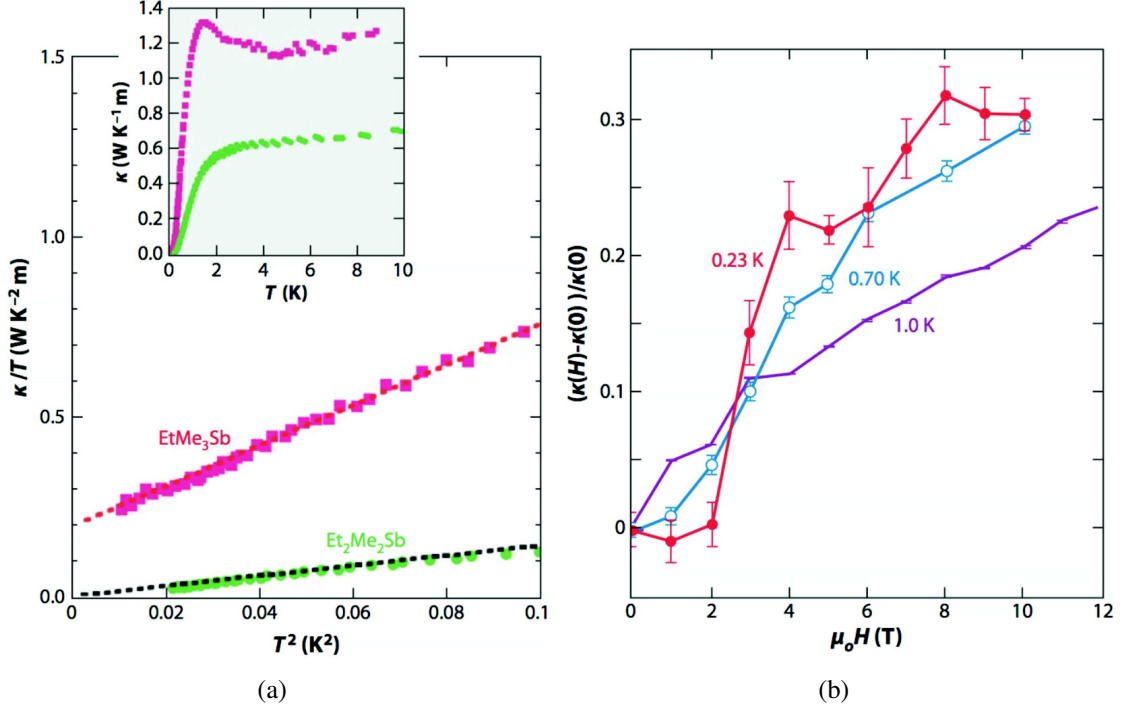


Figure 1.9: Adopted from [26]. Low-temperature thermal conductivity ( $\kappa$ ) for  $\text{EtMe}_3\text{Sb}[\text{Pd}(\text{dmit})_2]_2$  and  $\text{Et}_2\text{Me}_2\text{Sb}$  salt. (a) The main graph shows  $\kappa/T$  versus  $T^2$  plots of the thermal conductivity. The inset shows temperature dependence of  $\kappa$  below 10 K in zero field. (b) Field dependence of thermal conductivity normalized by the zero-field value. The heat current was applied within the 2D plane, and the magnetic field ( $H$ ) was perpendicular to the plane.

most important point is that the  $\text{EtMe}_3\text{Sb}[\text{Pd}(\text{dmit})_2]_2$  shows a linear temperature term at zero-temperature limit, which indicates that the excitation from the ground state is gapless. Another important point is that the broad hump structure is observed around 3 K. This corresponds to the kink of  $1/T_1$  in  $^{13}\text{C}$  NMR in the same temperature region, Fig. 1.8(a), and indicates a possibility of crossover phenomena.

More intriguingly, Fig. 1.9(a) shows temperature dependence of thermal conductivity [23]. Compared with the  $\text{Et}_2\text{Me}_2\text{Sb}$  salt,  $\text{EtMe}_3\text{Sb}[\text{Pd}(\text{dmit})_2]_2$  shows enhanced thermal conductivity, which indicates that spin-mediated contribution is added to the phonon contribution. Temperature dependence of the thermal conductivity has a peak structure around 1 K, inset in Fig. 1.9(a). Thermal conductivity of  $\text{EtMe}_3\text{Sb}[\text{Pd}(\text{dmit})_2]_2$  also shows a linear temperature term, indicating gapless excitation from the ground state. This is different from the case of  $\kappa\text{-(ET)}_2\text{Cu}_2(\text{CN})_3$ .

Field dependence of thermal conductivity of  $\text{EtMe}_3\text{Sb}[\text{Pd}(\text{dmit})_2]_2$ , however, suggest another kind of excitation, Fig 1.9(b). A steep increase above approximate 2 T is observed below 1 K, which implies that some spin-gap-like excitations are present at low temperatures, along with the gapless excitation indicated by the T-linear term. As mentioned earlier, there is a field-induced phase transition in low temperature in this spin liquid material [46]. Such field dependence of thermal conductivity of  $\text{EtMe}_3\text{Sb}[\text{Pd}(\text{dmit})_2]_2$  is likely to provide the excitation information of the field-induced phase but not the intrinsic properties of the completely gapless spin liquid state. Possible explanation is that there exists an exotic spin liquid state induced by the Zeeman magnetic field with part of the Fermi surface is gapped out due to pairing, which is detailed in Chapter 4. The theoretical scenarios are still debating and more experiments are required to uncover the mysterious physics in this material.

### 1.3 Overview of thesis

In Chapter 2 we introduce the techniques we mainly use in this thesis such as Bosonization and weak-coupling Renormalization Group (RG). The effective theory of SBM is also briefly summarized, which is the foundation for the studies of SBM in Chapters 3–6. We also provide a concise introduction to the original Kitaev model on the honeycomb lattice and focus on the relevant properties of the model. The same idea can be directly applied to construct other Kitaev-type models that we study in Chapters 7–8

In Chapter 3 we start from a two-band Hubbard-type model with longer-ranged repulsions on a two-leg triangular ladder and access to the SBM phase by metal-Mott insulator phase transition. We propose a schematic phase diagram in this model in which the SBM phase can be realized in the intermediate coupling regime.

In Chapter 4 we consider the Zeeman magnetic field effect on the SBM phase. We conjecture there should be a new exotic quantum spin liquid phase out of SBM. In this phase, only one species of spinons are paired up while the other species of spinons still have an intact Fermi surface. In Chapter 5 we study the orbital magnetic field effect on the SBM phase. We start from a two-band Hubbard-type model on the two-leg triangular ladder and

we conclude that the combination of the orbital magnetic field and interactions provides a mechanism to drive metal-insulator transition already at weak coupling. According to RG analysis, the SBM phase is fragile to the orbital magnetic field in this model.

For further understanding of other effects on the SBM phase, in Chapter 6 we study the impurity effects on the SBM and find the formation of bond-energy textures around impurities and nontrivial *increasing* oscillating spin susceptibility around impurities, which can be detected in Knight shift measurements in NMR.

In Chapter 7 we realize the long-wavelength SU(2) Majorana spin liquids (MSL) in a Kitaev-type model with broken time-reversal symmetry and lattice inversion symmetry to avoid discussing possible instability. Unlike usual SU(2)-invariant spin liquids, there are three species of Fermions that carry  $S^z = \pm 1$  and 0. We find that SU(2) MSL possess *equal* power-law spin and spin-nematic correlation functions. In the presence of Zeeman magnetic fields, we conjecture a nontrivial half-magnetization plateau phase in which spin excitations are gapful while there remains spinless gapless excitations that still produce metal-like thermal properties.

Finally, in Chapter 8 we realize the Majorana liquids [including Majorana orbital liquid (MOL) using only orbital degrees of freedom and SU(2) MSL using both spin and orbital degrees of freedom] on a two-leg ladder in a Kitaev-type model to systematically study its stability in a well-controlled RG analysis. We conclude such Majorana liquids are stable against weak local perturbations and  $Z_2$  gauge fields fluctuations.

# Chapter 2

## Preliminaries

In this chapter we introduce the techniques that we use in this thesis. In Chapter 2.1 we introduce the bosonization, a powerful tool of reformulating fermions in terms of Bosons, in a 1D spinless free electron system [47, 48]. In Chapter 2.2 we first introduce the concepts of weak-coupling RG and use current algebra [49] to derive the RG equations *algebraically* in 1D electron systems with weak interactions. We summarize the SBM theory [29] in Chapter 2.3 which is the foundation for the ladder studies of SBM in Chapters 3–6. In Chapter 2.4 we introduce the original Kitaev model on the honeycomb lattice [14] concisely whose spirits can be directly applied to construct other exactly solvable Kitaev-type models that we study in Chapters 7–8.

### 2.1 Bosonization primer

In this review, we follow closely [47] to introduce the Bosonization technique. Let us consider the Hamiltonian for non-interacting spinless electrons hopping on a 1D lattice, Fig. 2.1(a)

$$H = -t \sum_x [c^\dagger(x)c(x+1) + \text{H.c.}], \quad (2.1)$$

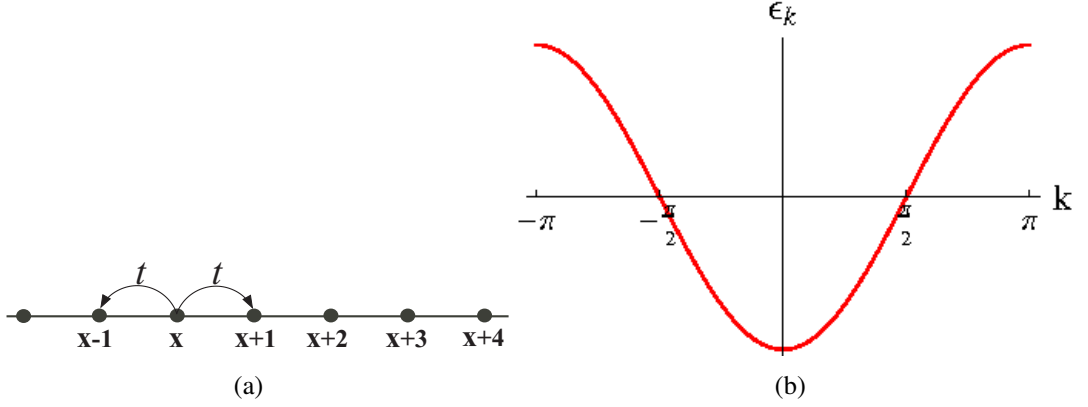


Figure 2.1: (a) Noninteracting electrons hop on the 1D chain with nearest-neighbor hopping amplitude  $t$ . (b) Band dispersion for the noninteracting 1D electron gas. The negative energy states are occupied with  $|k| < k_F$ . The dispersion can be linearized around  $\pm k_F$  leading to a continuum 1D Dirac fermionic theory.

with real hopping strength  $t$ . One can diagonalize the Hamiltonian by Fourier transforming to momentum space giving

$$H = \sum_k \epsilon_k c_k^\dagger c_k, \quad (2.2)$$

with energy dispersion  $\epsilon_k = -2t \cos(k)$  for momentum  $|k| < \pi$ , as shown in Figure 2.1(b). In the ground state, all the negative energy states with momentum  $|k| \leq k_F$  are occupied. At half-filling, the Fermi wavevector  $k_F = \pi/2$ . For the low-energy effective description of the excitations, one can focus on momentum close to Fermi wave vectors  $\pm k_F$  and define the continuum Fermion fields:

$$\psi_R(q) = c_{k_F+q}; \quad \psi_L(q) = c_{-k_F+q}. \quad (2.3)$$

The subscripts  $R/L$  refer to the right/left Fermi points, and  $q$  is assumed to be much smaller than a momentum cutoff,  $|q| < \Lambda$  with  $\Lambda \ll k_F$ . Linearizing the dispersion about the Fermi points, one can write  $\epsilon_{\pm k_F+q} = \pm v_F q$  with  $v_F$  the Fermi velocity. Transforming back to

real space, one can define fields

$$\psi_P(x) = \frac{1}{\sqrt{L}} \sum_{|q| < \Lambda} e^{iqx} \psi_P(q), \quad (2.4)$$

which vary slowly on the scale of the lattice spacing with  $P = R/L$ . The above equation is equivalent to expanding the usual lattice electron fields in terms of continuum fields,

$$c(x) \sim \psi_R(x)e^{ik_F x} + \psi_L(x)e^{-ik_F x}. \quad (2.5)$$

In terms of the continuum fields, the effective low-energy Hamiltonian takes the form,  $H = \int dx \mathcal{H}$ , with Hamiltonian density,

$$\mathcal{H} = v_F \left[ \psi_R^\dagger (-i\partial_x) \psi_R - \psi_L^\dagger (-i\partial_x) \psi_L \right], \quad (2.6)$$

which describes a 1D relativistic Dirac particle.

Consider a particle/hole excitation about the right Fermi point, where an electron is removed from an occupied state with  $k < k_F$  and placed into an unoccupied state with  $k + q > k_F$ . For small momentum change  $q$ , the energy of this excitation is  $\omega_q = v_F q$ . Together with the negative momentum excitations about the left Fermi point, this linear dispersion relation is identical to that for phonons in 1D. The method of bosonization exploits this similarity by introducing a phonon displacement field  $\theta$ , to describe this linearly dispersing density wave. Let us consider a Jordan-Wigner transformation which replace the electron operator,  $c(x)$ , by a boson operator with so-called Jordan-Wigner ‘‘string’’ attached to the boson operator,

$$c(x) = \mathcal{O}(x)b(x) \equiv e^{i\pi \sum_{x' < x} n(x')} b(x), \quad (2.7)$$

with  $n(x) = c^\dagger(x)c(x)$ , the number operator. This transformation of exchanging Fermions for bosons is a special feature of 1D. The boson operators can be (approximately) decom-

posed in terms of an amplitude and a phase,

$$b(x) \rightarrow \sqrt{\rho} e^{i\varphi}. \quad (2.8)$$

We now imagine going to the continuum limit, focusing on scales long compared to the lattice spacing. In this limit, we decompose the total density as,  $\rho(x) = \rho_0 + \tilde{\rho}$ , where the mean density,  $\rho_0 = k_F/\pi$ , and  $\tilde{\rho}$  is an operator measuring the fluctuations in the density. The density and phase are canonically conjugate quantum variables satisfying

$$[\varphi(x), \tilde{\rho}(x')] = i\delta(x - x'). \quad (2.9)$$

Now we introduce a phonon-like displacement field,  $\theta(x)$ , via  $\tilde{\rho}(x) = \partial_x \theta(x)/\pi$ . Then the full density takes the form,  $\pi\rho(x) = k_F + \partial_x \theta$  and the above commutation relations are satisfied if one takes

$$[\varphi(x), \theta(x')] = i\pi\Theta(x - x'). \quad (2.10)$$

Here  $\Theta(x)$  denotes the heavyside step function. Note that  $\partial_x \varphi/\pi$  is the momentum conjugate to  $\theta$ .

As described above, the goal of the bosonization is to replace the original low-energy continuum Fermions by the phonon-like bosons in 1D. To this end, we can start from the effective bosonized Hamiltonian density which describes the 1D density wave (phonon-like) takes the form:

$$\mathcal{H} = \frac{v}{2\pi} [g(\partial_x \varphi)^2 + g^{-1}(\partial_x \theta)^2]. \quad (2.11)$$

This Hamiltonian describes a wave propagating at velocity  $v$ . The equations of motions can be obtained using the commutation relation above,  $\partial_t^2 \theta = (gv)^2 \partial_x^2 \theta$ , and similarly for  $\varphi$ . In the “noninteracting” case, one can clearly equate  $v$  with the Fermi velocity  $v_F$ . The additional dimensionless parameter  $g$  can be determined as follows. Let us consider a 1D phonon-like system. A small variation in density  $\tilde{\rho}$  will lead to a change in the energy,

$E = \tilde{\rho}^2/2\kappa$ , where  $\kappa = \partial\rho/\partial\mu = \partial\rho/\partial E_F$ . Since  $\partial_x\theta = \pi\tilde{\rho}$ , one can obtain  $\kappa = g/\pi v$ . For a non-interacting electron system,  $\partial\rho/\partial\mu = \kappa = n(E_F) = 1/\pi v$ , so that  $g = 1$ . However, in the presence of short-ranged interactions between the electrons, the Hamiltonian density expression remains valid but the values of both  $g$  and  $v$  should be renormalized away from the non-interacting free electron gas. Therefore, this Hamiltonian would then describe a (spinless) Luttinger liquid.

To identify the relation between the usual electron operator  $c(x)$  and the Boson fields, one can consider first the Bose operator,  $b \sim e^{i\varphi}$ , which removes unit charge at  $x$ . Note that

$$e^{i\varphi(x)} = e^{i\pi \int_{-\infty}^x dx' P(x')}, \quad (2.12)$$

where  $P = \partial_x\varphi/\pi$  is the momentum conjugate to  $\theta$ . Since the momentum operator is the generator of translations in  $\theta$ , this creates a kink in  $\theta$  of height  $\pi$  centered at position  $x$ -which corresponds to a localized unit of charge since the density is  $\tilde{\rho} = \partial_x\theta/\pi$ . Besides, the attached Jordan-Wigner string in the bosonic language can be viewed as

$$\mathcal{O}(x) = e^{i\pi \sum_{x' < x} n(x')} \simeq e^{i\pi \int^x \rho(x')} = e^{i(k_F x + \theta)}, \quad (2.13)$$

where in the second equality we used the fact that  $\rho = \rho_0 + \tilde{\rho}$ . Hence, we can see the string operator carries momentum  $k_F$  and the resulting fermionic operator  $\mathcal{O}e^{i\varphi}$  should be identified as the ‘‘right-moving’’ continuum Fermi field,  $\psi_R$ . Similarly, we can introduce Boson field replacing the left-moving continuum Fermi field,  $\psi_L$ . The correct bosonized form for the continuum electron operators are

$$\psi_P(x) = e^{i\phi_P(x)}; \quad \phi_P = \varphi + P\theta, \quad (2.14)$$

with  $P = R/L = \pm$ . According to Eqs. (2.9)–(2.10), the chiral boson field  $\phi_P$  satisfy the so-called Kac-Moody commutation relations:

$$[\phi_P(x), \phi_P(x')] = iP\pi \text{sign}(x - x'), \quad (2.15)$$

$$[\phi_R(x), \phi_L(x')] = i\pi. \quad (2.16)$$

These commutation relations can be used to show that  $\psi_R$  and  $\psi_L$  anti-commute.

Let us now express the bosonized Hamiltonian density in terms of the chiral boson field. First, let us consider the “noninteracting” system. We define the right- and left-moving boson densities as

$$n_P = \frac{P}{2\pi} \partial_x \phi_P, \quad (2.17)$$

which gives the total density  $n_R + n_L = \partial_x \theta / \pi = \tilde{\rho}$ . The bosonized Hamiltonian density becomes

$$\mathcal{H} = \pi v_F [n_R^2 + n_L^2]. \quad (2.18)$$

These chiral boson density can be expressed in term of the chiral (continuum) electron operators as,

$$n_P =: \psi_P^\dagger \psi_P : \equiv \psi_P^\dagger \psi_P - \langle \psi_P^\dagger \psi_P \rangle. \quad (2.19)$$

In the noninteracting limit, the bosonized Hamiltonian decouples into right and left moving sectors as the case in usual continuum Fermi fields.

The advantage of bosonization is that we can easily take short-ranged electron interactions into account. For example, the density-density interaction,  $V(x) = U n(x) n(x+1)$ , can be added to the original Hamiltonian. Expansion in terms of continuum fermions using Eq. (2.5) gives three terms which conserve the momentum: Two chiral terms of the form  $(\psi_P^\dagger \psi_P)^2$ , and a term mixing right/left-moving fermions of the form  $\psi_R^\dagger \psi_R \psi_L^\dagger \psi_L$ . Under bosonization, the two chiral terms become of the “quadratic” form proportional to  $(\partial_x \phi_P)^2$ , and can be treated to renormalize the Fermi velocity in Eq. (2.18). The other term mixing left/right sectors also becomes a “quadratic” term proportional to  $(\partial_x \phi_R)(\partial_x \phi_L) \sim (\partial_x \theta)^2 - (\partial_x \varphi)^2$ , and renormalize the Luttinger parameter  $g$  away from one. For repulsive interaction, one finds  $g < 1$  while  $g > 1$  for attractive interaction. Therefore, we can see the power of the bosonization technique is that the “quartic” fermion interactions under bosonization can still give “quadratic” terms which can be treated analytically.

## 2.2 Weak-coupling renormalization group (RG) and current algebra

The starting point for the weak-coupling RG analysis is writing down the effective low-energy Hamiltonian of relativistic Dirac fermions after linearizing the spectrum around the Fermi points similar to the discussions in Chapter 2.1. The kinetic energy takes the form,  $H_0 = \int dx \mathcal{H}_0$ , with Hamiltonian density,

$$\mathcal{H}_0 = \sum_{i,\alpha} v_i^\alpha \left[ \psi_{Ri\alpha}^\dagger (-i\partial_x) \psi_{Ri\alpha} - \psi_{Li\alpha}^\dagger (-i\partial_x) \psi_{Li\alpha} \right], \quad (2.20)$$

with  $i$  labeling the different bands and  $\alpha$  labeling different species of fermions (usually labeling spin index, but can be more general). The Euclidean action, written as a space-time integral of the Lagrangian density, is

$$\mathcal{S} = \int d\tau dx \mathcal{L}_0, \quad (2.21)$$

$$\mathcal{L}_0 = \sum_{Pi\alpha} i\partial_\tau \psi_{Pi\alpha} + \mathcal{H}_0, \quad (2.22)$$

with  $P = R/L$ , and  $\tau$  denoting imaginary time. The partition function can be expressed as a coherent state Grassmann path integral,

$$\mathcal{Z} = \int [D\bar{\psi}][D\psi] e^{-S(\bar{\psi},\psi)}. \quad (2.23)$$

We can follow standard RG steps as described by Shankar [50]. First integrating out field  $\psi(k, \omega)$  with momentum  $k$  lying in the interval  $\Lambda/b < |k| < \Lambda$ , with rescaling parameter  $b > 1$ . We then perform the rescaling procedure which returns the cutoff to its original value:

$$x \rightarrow bx; \quad \tau \rightarrow b\tau; \quad \psi \rightarrow b^{-1/2}\psi. \quad (2.24)$$

The action remains invariant after the scaling, and the non-interacting theory above is at a RG “fixed point”.

Away from the noninteracting limit, the interactions can scatter right-moving Fermions into left-moving Fermions and vice-versa. For example, if we consider the usual on-site density–density repulsion, a.k.a Hubbard repulsion, after expansion in terms of continuum fermion fields, it contains terms of the quartic form as  $\psi_{P1}^\dagger \psi_{P2} \psi_{P3}^\dagger \psi_{P4}$ , with  $P1, P2, P3, P4 = R/L$ . In Euclidean space-time (1+1)D, such quartic terms are again “invariant” under rescaling procedure in RG and are marginal.

In order to know if such quartic terms are marginally relevant, strictly marginal, or marginally irrelevant, we need to consider the one-loop contribution in RG analysis. Reference [50] already detailed the standard procedure for analyzing RG at tree level and at one-loop corrections, which we will skip here. Instead, we will introduce the so-called “current-algebra” to “algebraically” calculate the one-loop RG correction. Most of the procedures are listed clearly in the Appendix in [49]. Below we will use a 1D Hubbard model at half-filling to illustrate how the current algebra works.

Let us consider a 1D spinful electron hopping system at half-filling with the Hamiltonian similar to Eq. (2.1) but now there is a spin index called  $\alpha$ . The band spectrum is the same to Fig. 2.1(b) but now there are two degenerate bands. After linearizing around the Fermi points, the effective low-energy, noninteracting Hamiltonian density is

$$\mathcal{H}_0 = v \sum_{\alpha} \left[ \psi_{R\alpha}^\dagger (-i\partial_x) \psi_{R\alpha} - \psi_{L\alpha}^\dagger (-i\partial_x) \psi_{L\alpha} \right]. \quad (2.25)$$

We can easily take interactions into account as perturbations. After expansion in terms of continuum fermions, the allowed four-fermion interactions are highly constrained by the symmetries of the system. In this model, these terms should be invariant under spin SU(2) rotation, parity transformation, time-reversal, and spatial translation. A convenient way to write down the interactions is by introducing the current operators as

$$J_P = \psi_{P\alpha}^\dagger \psi_{P\alpha}; \quad \vec{J}_P = \frac{1}{2} \psi_{P\alpha}^\dagger (\vec{\sigma})_{\alpha\beta} \psi_{P\beta}, \quad (2.26)$$

$$I_P = \psi_{P\alpha} \epsilon_{\alpha\beta} \psi_{P\beta}; \quad \vec{I}_P = \frac{1}{2} \psi_{P\alpha} (\epsilon \vec{\sigma})_{\alpha\beta} \psi_{P\beta}, \quad (2.27)$$

with  $P = R/L$  and repeated indices mean summation.  $J_P$  and  $I_P$  transform as scalars and  $\vec{J}_P$  and  $\vec{I}_P$  transform as vectors under  $SU(2)$  rotation. Note that since there is only one band in this model,  $\vec{I}_P$  are actually zero. However, the expressions above are more general and are readily generalized to other models with multibands.

With the current operators above, the allowed four-fermion interactions can be written in a concise form as

$$-\mathcal{H}_{int} = w_\rho J_R J_L + w_\sigma \vec{J}_R \cdot \vec{J}_L + u_\rho \left[ I_R^\dagger I_L + \text{H.c.} \right]. \quad (2.28)$$

We can now algebraically calculate the one-loop RG. The fermions in Euclidean space obey the operator product expansion (OPE) [51, 52]

$$\psi_{R\alpha}(x, \tau) \psi_{R\beta}^\dagger(0, 0) \sim \frac{\delta_{\alpha\beta}}{2\pi z} + O(1), \quad (2.29)$$

$$\psi_{L\alpha}(x, \tau) \psi_{L\beta}^\dagger(0, 0) \sim \frac{\delta_{\alpha\beta}}{2\pi z^*} + O(1), \quad (2.30)$$

where  $z = v\tau - ix$ , with  $v$  the Fermi velocity. The OPE are valid when two points  $(x, \tau)$  and  $(0, 0)$  are brought close together, as replacement within correlation functions. In principle, if we consider any product of the current operators, the operators products can be qualitatively considered as some generalized Wick contractions. As an example, we consider the product  $J_R^j J_R^k$ . Performing all possible contraction gives

$$\begin{aligned} J_R^j(z) J_R^k(0) &\sim : \psi_{R\alpha}^\dagger(z) \psi_{R\beta}(z) :: \psi_{R\gamma}^\dagger(0) \psi_{R\epsilon}(0) : \frac{1}{4} \sigma_{\alpha\beta}^j \sigma_{\gamma\epsilon}^k \\ &\sim \left[ - \left( \frac{-1}{2\pi z} \right) \left( \frac{1}{2\pi z} \right) \delta_{\alpha\epsilon} \delta_{\beta\gamma} + \frac{\delta_{\beta\gamma}}{2\pi z} : \psi_{R\alpha}^\dagger \psi_{R\epsilon} : \right. \\ &\quad \left. + \frac{\delta_{\alpha\epsilon}}{2\pi z} : \psi_{R\beta} \psi_{R\gamma}^\dagger : + : \psi_{R\alpha}^\dagger \psi_{R\beta} \psi_{R\gamma}^\dagger \psi_{R\epsilon} : \right] \frac{1}{4} \sigma_{\alpha\beta}^j \sigma_{\gamma\epsilon}^k \\ &\sim \frac{1}{2(2\pi z)^2} \delta^{jk} + \frac{1}{2\pi z} i\epsilon^{jkl} J_R^l + O(1) \\ &\sim \frac{1}{2\pi z} i\epsilon^{jkl} J_R^l, \end{aligned} \quad (2.31)$$

where above we used  $\sigma^j \sigma^k = \delta^{jk} + i\epsilon^{jkl} \sigma^l$ , and in the last line we dropped all the irrelevant terms. Skipping the derivations for other OPE, we list all the relevant results at half-filling

case

$$\begin{aligned}
J_R(z)I_R(0) &\sim \frac{-1}{\pi z}I_R; & J_L(z)I_L(0) &\sim \frac{-1}{\pi z^*}I_L, \\
J_R(z)I_R^\dagger(0) &\sim \frac{1}{\pi z}I_R^\dagger; & J_L(z)I_L^\dagger(0) &\sim \frac{1}{\pi z^*}I_L^\dagger, \\
I_RI_R^\dagger(0) &\sim -\frac{2}{\pi z}J_R; & I_L(z)I_L^\dagger(0) &\sim \frac{-2}{2\pi z^*}J_L, \\
J_L^j(z)J_L^k(0) &\sim \frac{1}{2\pi z^*}i\epsilon^{jkl}J_L^l.
\end{aligned} \tag{2.32}$$

The RG equations can be obtained from the equations above. In the Euclidean space, the action is  $S_E = \int dx d\tau \mathcal{H}$ , with  $\mathcal{H} = \mathcal{H}_0 + \mathcal{H}_{int}$ , and the partition function is

$$\mathcal{Z} = \int [d\bar{\psi}][d\psi] e^{-S_E}. \tag{2.33}$$

To perform the RG, the exponential is expanded to quadratic order in  $\mathcal{H}_{int}$ . For example, let us examine a term which takes the form

$$\begin{aligned}
&\frac{u_\rho^2}{2} \int_{z,w} \left\langle (I_R^\dagger(z)I_L(z) + \text{H.c.})(I_L^\dagger(w)I_R(w) + \text{H.c.}) \right\rangle \\
&\simeq u_\rho^2 \int_{z,w} \frac{4}{2\pi(z-w)} \frac{-4}{2\pi(z^* - w^*)} J_R J_L.
\end{aligned} \tag{2.34}$$

Following the steps in [49], we choose a short-distance (high-momentum) cutoff  $a$  in space, but none in imaginary time. For a rescaling factor  $b$ , we must then perform the integral

$$I = \int_{a < |x| < ba} dx \int_{-\infty}^{\infty} d\tau \frac{1}{(2\pi)^2 (v^2 \tau^2 + x^2)} = \frac{\ln b}{2\pi v} \tag{2.35}$$

over the relative coordinates  $(x, \tau)$ . Eq. (2.34) becomes

$$-\frac{4u_\rho^2}{\pi v} \ln b \int_z J_R J_L, \tag{2.36}$$

which when re-exponentiated, for  $b = e^{dl}$ , gives the RG equation for  $w_\rho$  as

$$\dot{w}_\rho = -\frac{8u_\rho^2}{\pi v}, \tag{2.37}$$

with  $\dot{O} \equiv \partial O / \partial l$ , and  $l$  is logarithm of the length scale.

We can follow similar steps to derive the complete RG equations for this 1D electron

model at half-filling,

$$\dot{w}_\rho = -\frac{8}{\pi v} u_\rho^2, \quad (2.38)$$

$$\dot{w}_\sigma = -\frac{1}{2\pi v} w_\sigma^2, \quad (2.39)$$

$$\dot{u}_\rho = -\frac{2}{\pi v} w_\rho u_\rho. \quad (2.40)$$

As an example, we consider the on-site Hubbard model with

$$H_U = U \sum_x n_\uparrow(x) n_\downarrow(x). \quad (2.41)$$

After expanding the interaction in terms of the continuum field, we find the bare values of the couplings,

$$w_\rho(l=0) = -\frac{U}{2}; \quad w_\sigma(l=0) = 2U; \quad u_\rho(l=0) = -\frac{U}{4}. \quad (2.42)$$

Once we have the RG equations, Eqs. (2.38)–(2.40), and the initial conditions (bare couplings), Eq. (2.42), we can qualitatively analyze the phase diagram at weak coupling. First, let us consider repulsive interaction,  $U > 0$ . After plugging the initial conditions, Eq. (2.42) into Eqs. (2.38)–(2.40), qualitatively  $w_\sigma$  keeps decreasing to become marginally irrelevant while  $u_\rho$  becomes divergent ( $u_\rho \rightarrow -\infty$ ) and relevant to drive  $w_\rho$  to diverge eventually ( $w_\rho \rightarrow -\infty$ ). The coupling  $u_\rho$  corresponds to coupling strength of the ( $I_R^\dagger I_L + \text{H.c.}$ ), which in Fermion language is the Umklapp interaction coming from commensurability. Hence, for  $U > 0$ , the phase with relevant  $u_\rho$  corresponds to a ‘‘Mott insulator’’.

On the other hand, if we consider attractive interaction,  $U < 0$ , qualitatively the Umklapp couplings  $u_\rho$  and  $w_\rho$  quickly become very small under RG and are marginally irrelevant, while  $w_\sigma$  becomes divergent ( $w_\sigma \rightarrow -\infty$ ) and relevant. The  $w_\sigma$  corresponds to the interactions which involve the currents,  $\vec{J}_P$ , defined in Eq. (2.26). From symmetry considerations, since  $\vec{J}_P$  transform as SU(2) vectors just as spins, such interactions are expected to affect mainly the spin degrees of freedom (spin sectors). Indeed, the marginally relevant coupling  $w_\sigma$  opens a gap in spin sector and the corresponding phase is the Emery-Luther

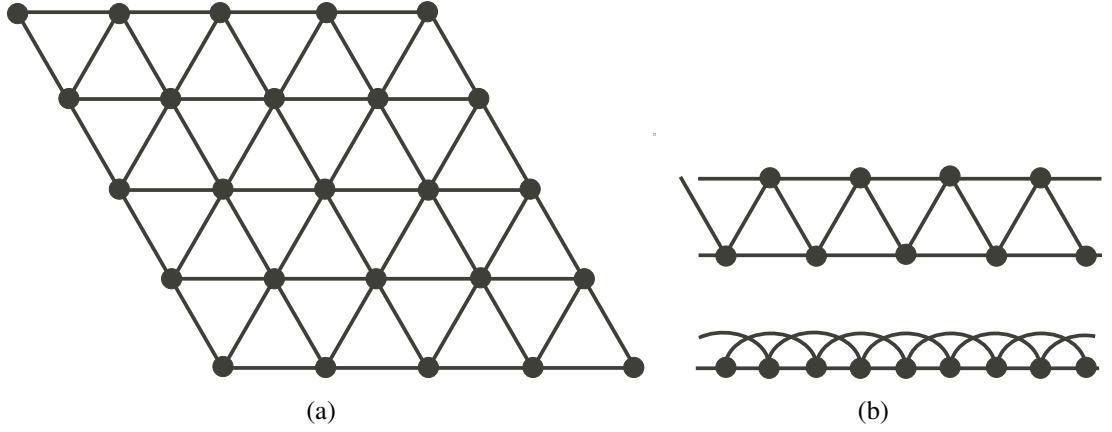


Figure 2.2: (a) 2D triangular lattice. (b) The top figure shows the two-leg triangular strip, which can be represented as 1D chain with nearest-neighbor and second-neighbor couplings shown in the bottom figure.

liquid. [53]

## 2.3 Spin Bose-metal theory on the zigzag strip

In this section we follow [29] to provide *effective* low energy theory for the SBM on the zigzag chain. In the 2D triangular lattice, Fig. 2.2(a), one approach to spin liquids is to decompose the spin operators in terms of an SU(2) spinor—the fermionic spinons:

$$\vec{S} = \frac{1}{2} f_{\alpha}^{\dagger} \vec{\sigma}_{\alpha\beta} f_{\beta}; \quad f_{\alpha}^{\dagger} f_{\alpha} = 1. \quad (2.43)$$

In the mean field one assumes that the spinons do not interact with one another and are hopping freely on the 2D lattice. For the present model in this thesis the mean field Hamiltonian would have the spinons hopping in zero magnetic field, and the ground state would correspond to filling up a spinon Fermi sea. In doing this one has artificially enlarged the Hilbert space, since the spinon hopping Hamiltonian allows for unoccupied and doubly occupied sites, which have no meaning in terms of the spin model of interest. It is thus necessary to project back down into the physical Hilbert space for the spin model, restricting the spinons to single occupancy. This can be readily achieved by the Gutzwiller projection, where one simply drops all terms in the wavefunction with unoccupied or doubly occupied

sites.

The alternate approach to implement the single occupancy constraint is by introducing a gauge field, a  $U(1)$  gauge field in this instance, that is minimally coupled to the spinons in the hopping Hamiltonian. This then becomes an intrinsically strongly-coupled lattice gauge field theory. To proceed, it is necessary to resort to an approximation by assuming that the gauge field fluctuations are weak. In 2D one then analyzes the problem of a Fermi sea of spinons coupled to a weakly fluctuating gauge field. This problem has a long history [54, 55, 56, 57, 58, 59, 60, 61, 3], but all the authors have chosen to sum the same class of diagrams. Within this approximation one can then compute physical spin correlation functions, which are gauge invariant. It is unclear, however, whether this is theoretically legitimate, and even less clear whether or not the spin liquid phase thereby constructed captures correctly the universal properties of a physical spin liquid that can occur for some spin Hamiltonian.

Fortunately, on the zigzag chain, Fig. 2.2(b), it is possible to employ bosonization to analyze the quasi-1D gauge theory, as we will detail below. While this still does not give an exact solution for the ground state of any spin Hamiltonian, with regard to capturing universal low-energy properties it is controlled. As we will see, the low-energy effective theory for the SBM phase is a Gaussian field theory, and perturbations about this can be analyzed in a systematic way to check for stability of the SBM and possible instabilities into other phases.

As detailed in Chapter 3, the-low energy effective theory for the SBM can also be obtained by starting with a model of interacting *electrons* hopping on the zigzag chain, i.e., a Hubbard-type Hamiltonian. If one starts with interacting electrons, it is possible to construct the gapped electron excitations in the SBM Mott insulator. Within the gauge theory approach, the analogous gapped spinon excitations are unphysical, being confined together with a linear potential. Moreover, within the electron formulation one can access the metallic phase, and also the Mott transition to the SBM insulator.

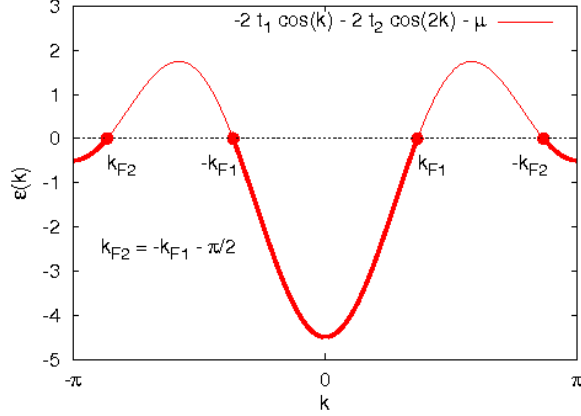


Figure 2.3: Spinon dispersion for  $t_2 > 0.5t_1$  showing two occupied Fermi sea segments

### 2.3.1 SBM via Bosonization of gauge theory

We first start by using bosonization, Chapter 2.1, to analyze the gauge theory. We assume a mean field state in which the spinons are hopping in zero flux. Here the spinons are hopping on the zigzag strip with nearest-neighbor and second-neighbor hopping strengths denoted  $t_1$  and  $t_2$ , Fig. 2.2(b). This is equivalent to a strictly 1D chain with first- and second-neighbor hopping. The dispersion is

$$\epsilon(k) = -2t_1 \cos(k) - 2t_2 \cos(2k) - \mu. \quad (2.44)$$

For  $t_2 > 0.5t_1$ , there are two sets of Fermi crossings at wavevectors  $\pm k_{F1}$  and  $\pm k_{F2}$ , as shown in Fig. 2.3. The fermions near  $k_{F1}$  and  $k_{F2}$  are moving to the right and the corresponding group velocities are  $v_1, v_2 > 0$ . The spinons are at half-filling, which implies  $k_{F1} + k_{F2} = -\pi/2 \text{ mod } 2\pi$ .

The spinon operators are expanded in terms of continuum fields,

$$f_\alpha(x) = \sum_{a,P} e^{iPk_{Fa}x} f_{Pa\alpha}, \quad (2.45)$$

with  $a = 1, 2$  denoting the two Fermi seas,  $\alpha = \uparrow, \downarrow$  denoting the spin, and  $P = R/L = \pm$  denoting the right- and left-moving fermions. We use bosonization to re-express the low

energy spinon operators with bosonic fields,

$$f_{Pa\alpha} = \eta_{a\alpha} e^{i(\varphi_{a\alpha} + P\theta_{a\alpha})}, \quad (2.46)$$

with canonically conjugate boson fields:

$$[\varphi_{a\alpha}(x), \varphi_{b\beta}(x')] = [\theta_{a\alpha}(x), \theta_{b\beta}(x')] = 0, \quad (2.47)$$

$$[\varphi_{a\alpha}(x), \theta_{b\beta}(x')] = i\pi\delta_{ab}\delta_{\alpha\beta}\Theta(x - x'), \quad (2.48)$$

where  $\Theta(x)$  is the heaviside step function and we have introduced Klein factors, the Majorana fermions  $\{\eta_{a\alpha}, \eta_{b\beta}\} = 2\delta_{ab}\delta_{\alpha\beta}$ , which assure that the spinon fields with different flavors anticommute with one another.

In this (1+1)D continuum theory, we work in the gauge eliminating spatial components of the gauge field. The imaginary-time bosonized Lagrangian density is:

$$\mathcal{L} = \frac{1}{2\pi} \sum_{a\alpha} \left[ \frac{1}{v_a} (\partial_\tau \theta_{a\alpha})^2 + v_a (\partial_x \theta_{a\alpha})^2 \right] + \mathcal{L}_A. \quad (2.49)$$

Here  $\mathcal{L}_A$  encodes the coupling to the slowly varying 1D (scalar) potential field  $A(x)$ ,

$$\mathcal{L}_A = \frac{1}{m} (\partial_x A / \pi)^2 + i\rho_A A, \quad (2.50)$$

where  $\rho_A$  denotes the total ‘‘gauge charge’’ density,

$$\rho_A = \sum_{a\alpha} \partial_x \theta_{a\alpha} / \pi. \quad (2.51)$$

It is useful to define ‘‘charge’’ and ‘‘spin’’ boson fields,

$$\theta_{a\rho/\sigma} = \frac{1}{\sqrt{2}} (\theta_{a\uparrow} \pm \theta_{a\downarrow}), \quad (2.52)$$

and “even” and “odd” flavor combinations,

$$\theta_{\mu\pm} = \frac{1}{\sqrt{2}}(\theta_{1\mu} \pm \theta_{2\mu}), \quad (2.53)$$

with  $\mu = \rho, \sigma$ . Similar definitions hold for the  $\varphi$  fields. The commutation relations for the new  $\theta, \varphi$  fields are unchanged.

Integration over the gauge potential generates a mass term,

$$\mathcal{L}_A = m(\theta_{\rho+} - \theta_{\rho+}^{(0)})^2, \quad (2.54)$$

for the field  $\theta_{\rho+} = \sum_{a\alpha} \theta_{a\alpha}/2$ . In the gauge theory analysis, we cannot determine the mean value  $\theta_{\rho+}^{(0)}$ , which is important for detailed properties of the SBM. However, if we start with an interacting electron model, one can readily argue that the correct value in the SBM phase satisfies

$$4\theta_{\rho+}^{(0)} = \pi \pmod{2\pi}. \quad (2.55)$$

### 2.3.2 SBM by Bosonizing interacting electrons

The SBM phase can be also accessed via a model of *electrons* hopping on the zigzag strip. The details are presented in Chapter 3. In this subsection we briefly summarize the approach. We assume that the electron hopping Hamiltonian is identical to the spinon mean field Hamiltonian, with first- and second-neighbor hopping strengths,  $t_1, t_2$ ;

$$H = - \sum_x [t_1 c_\alpha^\dagger(x) c_\alpha(x+1) + t_2 c_\alpha^\dagger(x) c_\alpha(x+2) + \text{H.c.}] + H_{int}. \quad (2.56)$$

The electrons are taken to be at half-filling. The interaction between the electrons could be taken as a usual on-site Hubbard repulsion or a longer-ranged repulsive interaction as in Chapter 3, but we do not need to specify the precise form for what follows.

For  $t_2 < 0.5t_1$ , the electron Fermi sea has only one segment spanning  $[-\pi/2, \pi/2]$ , and at low energy the model is essentially the same as the 1D Hubbard model. This case is the

same as the case we discussed in Chapter 2.2. We know that in this case even an arbitrary weak repulsive interaction will induce an allowed four-fermion Umklapp term that will be marginally relevant driving the system into a 1D Mott insulator. The residual spin sector will be described in terms of the Heisenberg chain, and is expected to be in the gapless Bethe-chain phase.

On the other hand, for  $t_2 > 0.5t_1$ , the electron band has two Fermi seas as shown in Fig. 2.3. As in the one-band case, Umklapp terms are required to drive the system into a Mott insulator. But in this two-band case there are no allowed four-fermion Umklapp terms. We focus on the allowed eight-fermion Umklapp term which takes the form,

$$H_8 = v_8(c_{R1\uparrow}^\dagger c_{R1\downarrow}^\dagger c_{R2\uparrow}^\dagger c_{R2\downarrow}^\dagger c_{L1\uparrow} c_{L1\downarrow} c_{L2\uparrow} c_{L2\downarrow} + \text{H.c.}) , \quad (2.57)$$

where we have introduced slowly varying electron fields for the two bands, at the right and left Fermi points. For repulsive electron interactions we have  $v_8 > 0$ . This Umklapp term is strongly irrelevant at weak coupling since its scaling dimension is  $\Delta_8 = 4$  (each electron field has scaling dimension  $1/2$ ), much larger than the space-time dimension  $D = 2$ .

We can bosonize the electrons,  $c_{Pa\alpha} \sim e^{i(\varphi_{a\alpha} + P\theta_{a\alpha})}$ . The eight-fermion Umklapp term becomes,

$$H_8 = 2v_8 \cos(4\theta_{\rho+}) , \quad (2.58)$$

where as before  $\theta_{\rho+} = \sum_{a\alpha} \theta_{a\alpha}/2$  and  $\rho_e(x) = 2\partial_x \theta_{\rho+}/\pi$  is now the *physical* slowly varying *electron* density. The bosonized form of the noninteracting electron Hamiltonian is precisely the first part of Eq. (2.49), and one can readily confirm that  $\Delta_8 = 4$ . But now imagine adding a *strong* density–density repulsion between the electrons. The slowly varying contributions, on scales larger than the lattice spacing, will take the simple form,  $H_\rho \sim V_\rho \rho_e^2(x) \sim V_\rho (\partial_x \theta_{\rho+})^2$ . These forward scattering interactions will “stiffen” the  $\theta_{\rho+}$  field and will reduce the scaling dimension  $\Delta_8$ . If  $\Delta_8$  drops below 2 then the Umklapp term becomes relevant and will grow at long scales. This destabilizes the two-band metallic state, driving a Mott metal-insulator transition. The  $\theta_{\rho+}$  field gets pinned in the minima of the  $H_8$  potential. Expanding to quadratic order about the minimum gives a mass term of the form Eq. (2.54). For the low-energy spin physics of primary interest this shows the

equivalence between the direct bosonization of the electron model and the spinon gauge theory approach.

### 2.3.3 Fixed-point theory of the SBM phase

The low-energy spin physics in either formulation can be obtained by integrating out the massive  $\theta_{\rho+}$  field, as we now demonstrate. Performing this Gaussian integration leads to the effective fixed-point (quadratic) Lagrangian for the SBM spin liquid:

$$\mathcal{L}_0^{\text{SBM}} = \mathcal{L}_0^\rho + \mathcal{L}_0^\sigma, \quad (2.59)$$

with the “charge” sector contribution,

$$\mathcal{L}_0^\rho = \frac{1}{2\pi g_0} \left[ \frac{1}{v_0} (\partial_\tau \theta_{\rho-})^2 + v_0 (\partial_x \theta_{\rho-})^2 \right], \quad (2.60)$$

and the spin sector contribution,

$$\mathcal{L}_0^\sigma = \frac{1}{2\pi} \sum_a \left[ \frac{1}{v_a} (\partial_\tau \theta_{a\sigma})^2 + v_a (\partial_x \theta_{a\sigma})^2 \right]. \quad (2.61)$$

The velocity  $v_0$  in the “charge” sector depends on the product of the flavor velocities,  $v_0 = \sqrt{v_1 v_2}$ , while the dimensionless “conductance” depends on their ratio:

$$g_0 = \frac{2}{\sqrt{v_1/v_2} + \sqrt{v_2/v_1}}. \quad (2.62)$$

Finally, we note that in the above effective theory only the interactions related to the charge sectors are considered. Of course, other interactions related to spin sectors should also be considered for discussing the stability of the SBM phase. We here skip the discussion of the SBM stability and remark that the SBM can be indeed a stable fixed point against all symmetry-allowed residual short-range interactions. [29]

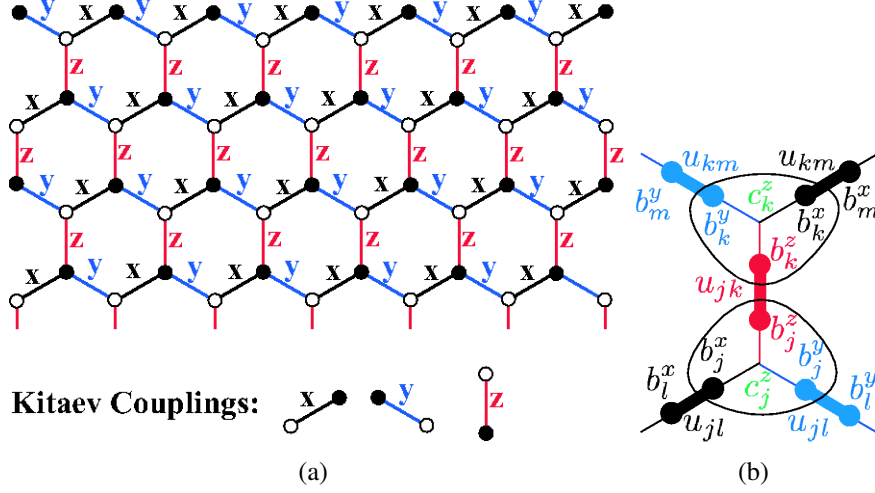


Figure 2.4: (a) Kitaev model on the honeycomb lattice. Note that there are three types of links (x, y, and z links in different colors) on the honeycomb lattice. (b) Graphical visualization of Majorana representation on the honeycomb lattice. Here we show the figure of a unit cell (two sublattices,  $j$ ,  $k$ ). Each site contains 4 Majoranas  $b^x$ ,  $b^y$ ,  $b^z$ , and  $c$ . The same species of  $b^\alpha$  Majoranas are connected to form static  $\mathbb{Z}_2$  gauge fields and can be treated as backgrounds, leaving only one species of free gapless Majorana,  $c$ -s.

## 2.4 Original Kitaev model on the honeycomb lattice

In this section we introduce concisely the original Kitaev model on the honeycomb lattice [14]. The same idea can be directly applied to construct other Kitaev-type models that we study in Chapters 7–8. The original Kitaev model is realized by locating spin-1/2 spins at the vertices of a honeycomb lattice. The honeycomb lattice is formed by three types of links called “ $x$ -links”, “ $y$ -links”, and “ $z$ -links”. The Hamiltonian is:

$$H = -J_x \sum_{x\text{-links}} \sigma_j^x \sigma_k^x - J_y \sum_{y\text{-links}} \sigma_j^y \sigma_k^y - J_z \sum_{z\text{-links}} \sigma_j^z \sigma_k^z, \quad (2.63)$$

where  $J_x$ ,  $J_y$ , and  $J_z$  are coupling strengths in different links. The nontrivial property of such highly anisotropic quantum spin model is that it can be “exactly” solved by mapping the quantum spin model to noninteracting Majorana fermion-hopping Hamiltonian. We introduce the Majorana representation of spin-1/2 operators at site  $j$

$$\sigma_j^\alpha = ib_j^\alpha c_j, \quad (2.64)$$

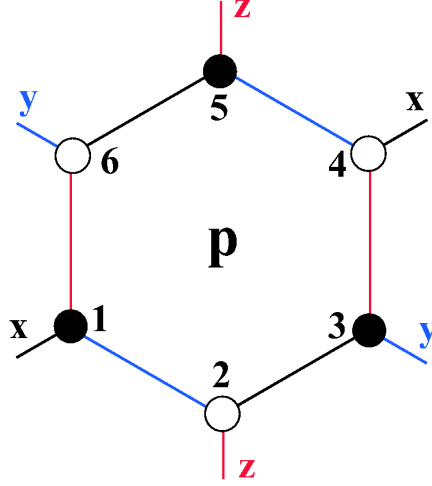


Figure 2.5: The  $W_p$  is defined around the lattice plaquette (i.e., hexagons) and  $p$  is a label of the plaquette.

with  $\alpha = x, y, z$ , and  $b^\alpha$  and  $c$  are Majorana fermions. The Majorana representation “enlarges” the Hilbert space per site by a factor of 2. It is necessary to include a constraint to project the enlarged Hilbert space back to the physical Hilbert space. The constraint is  $D_j = b_j^x b_j^y b_j^z c_j = 1$  (namely, for any physical state  $|\Phi\rangle_{\text{phys}}$ , we require  $D_j |\Phi\rangle_{\text{phys}} = |\Phi\rangle_{\text{phys}}$ ). The Hamiltonian can be rephrased in terms of Majorana fermions as

$$H = i \sum_{\langle jk \rangle} \hat{u}_{jk} J_{jk} c_j c_k, \quad (2.65)$$

where  $\hat{u}_{jk} \equiv -ib_j^\lambda b_k^\lambda$  for  $\lambda$ -link  $\langle jk \rangle$ . More intuitively, Fig. 2.4(b) shows the graphical representation of the Majorana representation of spin-1/2 spins.

The reason that this model is exactly solvable is because there are *infinite* number of conserved operators. The  $Z_2$  gauge fields  $u_{jk}$ -s defined in Eq. (2.65) commute with themselves and with the Hamiltonian,  $[u_{jk}, u_{j'k'}] = [u_{jk}, H] = 0$ . We can treat  $u_{jk}$ -s as static  $Z_2$  backgrounds, and replace  $u_{jk}$ -s with their eigenvalues  $\pm 1$ .

Besides the conserved operators  $u_{jk}$ -s, there are other conserved operators defined around the plaquettes (i.e., hexagons). We can define a plaquette operator called  $W_p$ ,

$$W_p = \sigma_1^x \sigma_2^z \sigma_3^y \sigma_4^x \sigma_5^z \sigma_6^y = - \prod_{\langle jk \rangle \in p} \hat{u}_{jk}, \quad (2.66)$$

around a lattice plaquette  $p$ , Fig. 2.5. Since  $\hat{u}_{jk}$ -s commute with themselves and with the Hamiltonian, so are the  $W_p$  plaquette terms. Each  $W_p$  term also has eigenvalues  $\pm 1$ .

Around each plaquette  $p$ , one can define the “fluxes”  $\phi_p$  via  $e^{-i\phi_p} \equiv \prod_{\langle jk \rangle \in p} iu_{jk}$ . The most interesting choice of  $\hat{u}_{jk}$  is the one that minimizes the ground state energy. The answer is provided by Lieb [62] saying that the ground state is the “uniform-flux” state. Therefore, we can simply assume that  $\hat{u}_{jk} = 1$  for all link  $\langle jk \rangle$ , where  $j$  belongs to even sublattice, and  $k$  belongs to the odd sublattice.

In order to diagonalize the Majorana Hamiltonian, first we note that because a Majorana Fermion is its own antiparticle, there is always the “particle-hole” symmetry in any general Majorana Hamiltonian. Due to such symmetry, only half of the degrees of freedom in the Majorana Hamiltonian are physical. For instance, for an eigenvector-eigenenergy pair,  $\{\vec{v}_{\mathbf{k}}, \epsilon_{\mathbf{k}}\}$ , there is a corresponding pair,  $\{\vec{v}_{\mathbf{k}'}, \epsilon_{\mathbf{k}'}\} = \{\vec{v}_{-\mathbf{k}'}, -\epsilon_{-\mathbf{k}}\}$  that is related by the particle-hole symmetry. More mathematically, we can introduce the expansion of the original Majoranas in terms of usual complex fermions as

$$c(\mathbf{r}, a) = \sqrt{\frac{2}{N_{uc}}} \sum_{\epsilon_{\mathbf{k}} > 0, \mathbf{k} \in \mathbf{B.Z.}} [e^{i\mathbf{k} \cdot \mathbf{r}} v_{\mathbf{k}}(a) f(\mathbf{k}) + \text{H.c.}], \quad (2.67)$$

where for clarity, we introduce  $j = (\mathbf{r}, a)$  with  $\mathbf{r}$  running over the Bravais lattice of unit cells,  $a = 1, 2$  the sublattice labeling in a unit cell.  $N_{uc}$  is the number of unit cells, and the complex Fermion  $f$  satisfies the usual anticommutation relation. The canonical form of the Hamiltonian is

$$H = \sum_{\epsilon_{\mathbf{k}} > 0, \mathbf{k} \in \mathbf{B.Z.}} 2\epsilon_{\mathbf{k}} \left[ f^\dagger(\mathbf{k}) f(\mathbf{k}) - \frac{1}{2} \right]. \quad (2.68)$$

In the present model on the honeycomb lattice,  $\epsilon_{\mathbf{k}} = |J_x e^{i\mathbf{k} \cdot \mathbf{n}_1} + J_y e^{i\mathbf{k} \cdot \mathbf{n}_2} + J_z|$ , with  $\mathbf{n}_{1/2} = (\pm 1/2, \sqrt{3}/2)$  in the standard  $xy$ -coordinates. An important property of the spectrum is whether it is gapless, i.e., whether  $\epsilon_{\mathbf{k}}$  is zero for some  $\mathbf{k}$ . The equation  $J_x e^{i\mathbf{k} \cdot \mathbf{n}_1} + J_y e^{i\mathbf{k} \cdot \mathbf{n}_2} + J_z = 0$  has a solution if and only if  $J_x$ ,  $J_y$ , and  $J_z$  (we assume

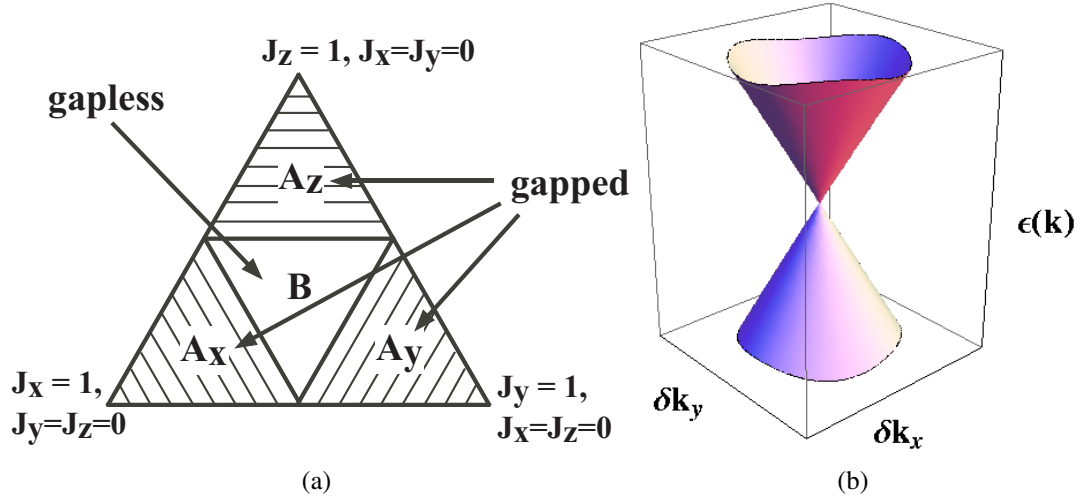


Figure 2.6: (a) Phase diagram of the model. The triangle is the section of the positive octant ( $J_x, J_y, J_z \geq 0$ ) by the plane  $J_x + J_y + J_z = 1$ . (b) Spectrum around a gapless point in gapless phase B. Here we show the spectrum close to a gapless point  $(k_x, k_y) = (4\pi/3 + \delta k_x, \delta k_y)$ . It clearly shows the spectrum of a Dirac cone. We remark that only the states for  $\epsilon(k) > 0$  (half of the Dirac cone) are physical.

$J$ -s are positive without loss of generality) satisfy the triangle inequalities

$$J_x \leq J_y + J_z; \quad J_y \leq J_x + J_z; \quad J_z \leq J_x + J_y. \quad (2.69)$$

The phase diagram is shown in Fig. 2.6(a). The gapless phase region defined by Eq. (2.69) is marked by B. The gapped phases  $A_x$ ,  $A_y$ , and  $A_z$ , are algebraically distinct, though related to each other by rotational symmetry. We note that we will focus on the gapless phase and skip all the discussions about the topological properties of the gapped phases since it is not really related to the studies in this thesis.

The spectrum of the gapless phase in the Brillouin zone contains two Dirac cones (more precisely, two half-Dirac cones since only half of the degrees of freedom are physical). For illustration, we take  $J_x = J_y = J_z = 1$  and focus on the gapless Dirac points which occur at the vertices of the hexagonal Brillouin zone. If we focus on a single gapless Dirac point and perform Taylor expansion around it, the spectrum is indeed conic shown in Fig. 2.6(b).

One remark we would like to make on the gapless phase is how to characterize such gapless spin liquid phase. It is interesting that even in the gapless spin liquid phase the spin correlations are ultra-short-ranged due to the lack of SU(2) spin rotation symmetry in

this model. In order to give a gauge-invariant characterization of such Kitaev-type gapless spin liquids, we suggest that the gaplessness can be detected by the local bond-energy correlations. The approach is detailed in our paper [63], which we do not include in this thesis because we will focus on  $SU(2)$ -invariant spin liquids in the remaining chapters.

Finally, the Kitaev model on the honeycomb lattice has many impacts on several fields including not only the new ways to study spin liquids, but also shedding light on the topological quantum computations. It is impossible to cover all the topics about the Kitaev model. For readers that are interested in all the details, please consult [14].

## Chapter 3

# Two-band electronic metal and neighboring spin liquid (spin Bose-metal) on a zigzag strip with longer-ranged repulsion

We mentioned in Chapter 2.3.1 that SBM phase can be accessed by bosonizing interacting electrons system. In this chapter, we focus on realizing such scenario for the SBM in explicit and realistic electronic models. Specifically, we start in the metallic phase with two gapless charge modes and two gapless spin modes—so-called “C2S2” metal. We can imagine gapping out just the overall charge mode to obtain a “C1S2” Mott insulator with one gapless “charge” mode and two gapless spin modes, where the former represents local current loop fluctuations and does not transport charge along the chain. This is precisely the SBM phase. If one thinks of a spin-only description of this Mott insulator, the gapless “charge” mode can be interpreted as spin singlet chirality mode.

Recently, Hubbard model on the zigzag chain ( $t_1 - t_2 - U$  chain) has received much attention [64, 65, 66, 67, 68, 69]. For free electrons, the two-band metal appears for  $t_2/t_1 > 0.5$ . However, in the case of Hubbard interaction, weak coupling approach [65, 66] finds that this phase is stable only over a narrow range  $t_2/t_1 \in [0.5, 0.57]$ , while a spin gap opens up for larger  $t_2/t_1$ . The Umklapp that can drive a transition to a Mott insulator requires eight fermions and is strongly irrelevant at weak coupling. Prior work [49, 64, 65] focused on the spin-gapped metal and eventual spin-gapped insulator for strong interaction, while the C1S2 spin liquid phase was not anticipated.

There have also been numerical DMRG studies of the Hubbard model [67, 68, 69, 66]. The focus has been on the prominent spin-gapped phases and, in particular, on the insulator that is continuously connected to the dimerized phase in the  $J_1 - J_2$  Heisenberg model, which is appropriate in the strong interaction limit  $U \gg t_1, t_2$ . The C2S2 metallic phase and possibility of nearby spin liquid on the Mott insulator side in the Hubbard model have not been explored. We hope our work will motivate more studies of this interesting possibility in the Hubbard model with intermediate  $U$  close to the C2S2 metal.

Since the C2S2 metallic phase is quite narrow in the Hubbard model, we would like to first widen the C2S2 region. To this end, we explore an electronic model with extended repulsive interactions. [70] Such interactions tend to suppress instabilities in the electronic system, similar to how long-ranged Coulomb repulsion suppresses pairing in metals. They are also more realistic than the on-site Hubbard, particularly for materials undergoing a metal-insulator transition where there is no conduction band screening on the insulator side. Thus, recent ab initio model construction for the  $\kappa$ -(ET)<sub>2</sub>Cu<sub>2</sub>(CN)<sub>3</sub> material found significant extended interactions in the corresponding electronic model on the half-filled triangular lattice [39, 38].

Applying weak coupling renormalization group (RG) approach to the zigzag ladder system [49, 64, 71, 65], we indeed find that extended interactions open a much wider window of the C2S2 metal phase. Building on this, we then use bosonization approach to explore a transition to a Mott insulator upon increasing the overall repulsion strength. We find that such longer-ranged interactions can drive the system into the C1S2 spin liquid Mott insulator rather than a spin-gapped insulator. This bodes well for finding spin liquid phases in more realistic electronic models for materials near the metal-insulator transition.

This chapter is organized as follows. In Chapter 3.1, we set up the weak coupling RG [49, 71, 65] and open a much wider window of the metallic C2S2 phase by introducing realistically motivated longer-ranged repulsion. In Chapter 3.2, we use bosonization to extend the analysis to intermediate coupling. We gradually increase the overall repulsion strength and determine thresholds for a Mott transition driven by the eight-fermion Umklapp term and also for spin gap instabilities, thus mapping out phases neighboring the C2S2 metal. In Chapter 3.3, we summarize our results and conclude with some discussion.

## 3.1 Weak coupling analysis of $t_1 - t_2$ model with extended repulsion: Stabilizing C2S2 metal

### 3.1.1 Setup for two-band electron system

We consider half-filled electronic  $t_1 - t_2$  model with extended interaction described by the Hamiltonian  $H = H_0 + H_V$ , with

$$\begin{aligned} H_0 &= - \sum_{x,\alpha} [t_1 c_\alpha^\dagger(x) c_\alpha(x+1) + t_2 c_\alpha^\dagger(x) c_\alpha(x+2) + \text{H.c.}] , \\ H_V &= \frac{1}{2} \sum_{x,x'} V(x-x') n(x) n(x') . \end{aligned} \quad (3.1)$$

Here  $c(c^\dagger)$  is fermion annihilation (creation) operator,  $x$  is a site label on the one-dimensional (1D) chain, and  $\alpha = \uparrow, \downarrow$  is a spin index;  $n(x) \equiv \sum_\alpha c_\alpha^\dagger(x) c_\alpha(x)$  is electron number on the site.

In weak coupling, the kinetic energy Eq. (3.1) gives free particle dispersion

$$\epsilon(k) = -2t_1 \cos(k) - 2t_2 \cos(2k) . \quad (3.2)$$

For  $t_2/t_1 > 0.5$ , there are two sets of Fermi points at wavevectors  $\pm k_{F1}$  and  $\pm k_{F2}$  as shown in Fig. 3.1. We adopt the same conventions as in [29]. Fermions near  $k_{F1}$  and  $k_{F2}$  are moving to the right, and the corresponding group velocities are  $v_1, v_2 > 0$ . Electrons are at half-filling, which implies  $k_{F1} + k_{F2} = -\pi/2 \pmod{2\pi}$  for the choices, as in Fig. 3.1.

The electron operators are expanded in terms of continuum fields,

$$c_\alpha(x) = \sum_{P,a} e^{iP k_{Fa} x} c_{Pa\alpha} , \quad (3.3)$$

with  $P = R/L = +/-$  denoting the right and left movers and  $a = 1, 2$  denoting the two Fermi seas.

Four-fermion interactions can be conveniently expressed in terms of chiral currents

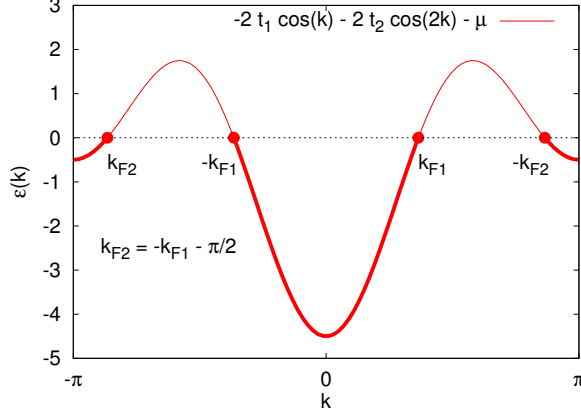


Figure 3.1: The electron band for  $t_2 > 0.5t_1$  has two occupied Fermi sea segments. This is free fermion C2S2 metal.

[49, 71, 29],

$$J_{Pab} = \sum_{\alpha} c_{Pa\alpha}^{\dagger} c_{Pb\alpha}, \quad (3.4)$$

$$\vec{J}_{Pab} = \sum_{\alpha,\beta} c_{Pa\alpha}^{\dagger} \frac{\vec{\sigma}_{\alpha\beta}}{2} c_{Pb\beta}. \quad (3.5)$$

Most general four-fermion interactions can be written as

$$\mathcal{H}_{RL}^{\rho} = \sum_{a,b} (w_{ab}^{\rho} J_{Rab} J_{Lab} + \lambda_{ab}^{\rho} J_{Raa} J_{Lbb}), \quad (3.6)$$

$$\mathcal{H}_{RL}^{\sigma} = - \sum_{a,b} (w_{ab}^{\sigma} \vec{J}_{Rab} \cdot \vec{J}_{Lab} + \lambda_{ab}^{\sigma} \vec{J}_{Raa} \cdot \vec{J}_{Lbb}), \quad (3.7)$$

$$\begin{aligned} \mathcal{H}_{\text{chiral}}^{\rho} = & \frac{1}{2} \sum_a C_{aa}^{\rho} (J_{Raa} J_{Raa} + J_{Laa} J_{Laa}) \\ & + C_{12}^{\rho} (J_{R11} J_{R22} + J_{L11} J_{L22}), \end{aligned} \quad (3.8)$$

$$\begin{aligned} \mathcal{H}_{\text{chiral}}^{\sigma} = & -\frac{1}{2} \sum_a C_{aa}^{\sigma} (\vec{J}_{Raa} \cdot \vec{J}_{Raa} + \vec{J}_{Laa} \cdot \vec{J}_{Laa}) \\ & - C_{12}^{\sigma} (\vec{J}_{R11} \cdot \vec{J}_{R22} + \vec{J}_{L11} \cdot \vec{J}_{L22}). \end{aligned} \quad (3.9)$$

Here  $\mathcal{H}_{RL}$  are terms that connect right and left movers, while  $\mathcal{H}_{\text{chiral}}$  are chiral terms with all fermions moving in the same direction.

Consider the couplings in  $\mathcal{H}_{RL}$ . We have  $w_{11} = w_{22} = 0$  (convention),  $w_{12} = w_{21}$  (from hermiticity), and  $\lambda_{12} = \lambda_{21}$  (from  $R \leftrightarrow L$  symmetry). Thus there are 8 independent

couplings:  $w_{12}^{\rho/\sigma}$ ,  $\lambda_{11}^{\rho/\sigma}$ ,  $\lambda_{22}^{\rho/\sigma}$ , and  $\lambda_{12}^{\rho/\sigma}$ . Note that there are no four-fermion Umklapp terms in our two-band system.

In the specific lattice model, we expand the interactions Eq. (3.1) in terms of the continuum fields and find “bare” values of the couplings:

$$\lambda_{11}^{\rho} = V_{Q=0} - \frac{V_{2k_{F1}}}{2}, \quad (3.10)$$

$$\lambda_{22}^{\rho} = V_{Q=0} - \frac{V_{2k_{F2}}}{2}, \quad (3.11)$$

$$\lambda_{12}^{\rho} = V_{Q=0} - \frac{V_{\pi/2}}{2}, \quad (3.12)$$

$$\lambda_{11}^{\sigma} = 2V_{2k_{F1}}, \quad (3.13)$$

$$\lambda_{22}^{\sigma} = 2V_{2k_{F2}}, \quad (3.14)$$

$$\lambda_{12}^{\sigma} = 2V_{\pi/2}, \quad (3.15)$$

$$w_{12}^{\rho} = V_{k_{F1}-k_{F2}} - \frac{V_{\pi/2}}{2}, \quad (3.16)$$

$$w_{12}^{\sigma} = 2V_{\pi/2}, \quad (3.17)$$

$$C_{11}^{\rho} = C_{22}^{\rho} = V_{Q=0} - \frac{U}{2}, \quad (3.18)$$

$$C_{12}^{\rho} = V_{Q=0} - \frac{V_{k_{F1}-k_{F2}}}{2}, \quad (3.19)$$

$$C_{11}^{\sigma} = C_{22}^{\sigma} = 2U, \quad (3.20)$$

$$C_{12}^{\sigma} = 2V_{k_{F1}-k_{F2}}. \quad (3.21)$$

Here  $V_Q \equiv \sum_{x'=-\infty}^{\infty} V(x-x')e^{iQ(x-x')} = V_{-Q}$ , since  $V(x-x') = V(x'-x)$ . We have also used explicitly  $k_{F1} + k_{F2} = -\pi/2$ .

The terms  $\mathcal{H}_{\text{chiral}}$  renormalize “velocities” of various modes. In the weak-coupling RG analysis, they only generate higher-order contributions and are therefore not important. The RG equations below contain only couplings from  $\mathcal{H}_{RL}$ . On the other hand, the chiral interactions are important in the intermediate coupling analysis to be done in Chapter 3.2, which is why we have listed their values as well. The on-site coupling  $U \equiv V(x-x'=0)$  appears explicitly in  $C_{11}^{\rho/\sigma}$  and  $C_{22}^{\rho/\sigma}$  because of our more careful treatment of the on-site interaction, which we first write as  $U n_{\uparrow}(x)n_{\downarrow}(x)$  and then insert the continuum fields (and bosonize in Chapter 3.2).

### 3.1.2 Weak coupling renormalization group

The RG equations in the two-band system are [49, 71, 65]:

$$\dot{\lambda}_{11}^{\rho} = -\frac{1}{2\pi v_2} \left[ (w_{12}^{\rho})^2 + \frac{3}{16} (w_{12}^{\sigma})^2 \right], \quad (3.22)$$

$$\dot{\lambda}_{22}^{\rho} = -\frac{1}{2\pi v_1} \left[ (w_{12}^{\rho})^2 + \frac{3}{16} (w_{12}^{\sigma})^2 \right], \quad (3.23)$$

$$\dot{\lambda}_{12}^{\rho} = \frac{1}{\pi(v_1 + v_2)} \left[ (w_{12}^{\rho})^2 + \frac{3}{16} (w_{12}^{\sigma})^2 \right], \quad (3.24)$$

$$\dot{\lambda}_{11}^{\sigma} = -\frac{1}{2\pi v_1} (\lambda_{11}^{\sigma})^2 - \frac{1}{4\pi v_2} [(w_{12}^{\sigma})^2 + 4w_{12}^{\rho} w_{12}^{\sigma}], \quad (3.25)$$

$$\dot{\lambda}_{22}^{\sigma} = -\frac{1}{2\pi v_2} (\lambda_{22}^{\sigma})^2 - \frac{1}{4\pi v_1} [(w_{12}^{\sigma})^2 + 4w_{12}^{\rho} w_{12}^{\sigma}], \quad (3.26)$$

$$\dot{\lambda}_{12}^{\sigma} = -\frac{1}{\pi(v_1 + v_2)} \left\{ (\lambda_{12}^{\sigma})^2 + \frac{(w_{12}^{\sigma})^2 - 4w_{12}^{\rho} w_{12}^{\sigma}}{2} \right\}, \quad (3.27)$$

$$\dot{w}_{12}^{\rho} = -\Lambda^{\rho} w_{12}^{\rho} - \frac{3}{16} \Lambda^{\sigma} w_{12}^{\sigma}, \quad (3.28)$$

$$\dot{w}_{12}^{\sigma} = -\Lambda^{\sigma} w_{12}^{\sigma} - \left( \Lambda^{\rho} + \frac{\Lambda^{\sigma}}{2} + \frac{2\lambda_{12}^{\sigma}}{\pi(v_1 + v_2)} \right) w_{12}^{\sigma}. \quad (3.29)$$

Here  $\dot{O} \equiv \partial O / \partial \ell$ , where  $\ell$  is logarithm of the length scale. We have also defined

$$\Lambda^{\rho/\sigma} = \frac{\lambda_{11}^{\rho/\sigma}}{2\pi v_1} + \frac{\lambda_{22}^{\rho/\sigma}}{2\pi v_2} - \frac{2\lambda_{12}^{\rho/\sigma}}{\pi(v_1 + v_2)}. \quad (3.30)$$

Details of our system enter through the band velocities  $v_1, v_2$ , and the initial conditions Eqs. (3.10)–(3.17).

### 3.1.3 Fixed point for stable C2S2 phase

We are primarily interested in the stability of the two-band metallic phase with two gapless charge and two gapless spin modes —“C2S2” in the notation of [49]. In the RG, this phase is characterized as having no divergent couplings. Before proceeding with detailed numerical studies of the flow Eqs. (3.22)–(3.29), we can describe such stable C2S2 fixed point qualitatively: The charge sector couplings reach some fixed values,  $\lambda_{11}^{\rho*}, \lambda_{22}^{\rho*}, \lambda_{12}^{\rho*}$ , and are strictly marginal; they also need to satisfy  $\Lambda^{\rho*} > 0$  (see below). The spin sector couplings

approach zero from positive values,  $\lambda_{11}^{\sigma*} = \lambda_{22}^{\sigma*} = \lambda_{12}^{\sigma*} = 0^+$ , and are marginally irrelevant. Finally, the “charge-spin” couplings  $w_{12}$  go to zero,  $w_{12}^{\rho*} = w_{12}^{\sigma*} = 0$ , and are irrelevant, which is insured by the condition  $\Lambda^{\rho*} > 0$ . Indeed, consider small deviations of comparable magnitudes for all couplings and allowing only positive  $\lambda_{ab}^{\sigma}$ . Since we have finite  $\Lambda^{\rho*} > 0$ , first the  $w_{12}^{\rho/\sigma}$  will renormalize quickly to zero, without significantly affecting the other couplings. Then the  $\lambda_{ab}^{\sigma}$  will renormalize to zero via slow marginal flows.

### 3.1.4 Numerical studies of the flows

We can solve the RG equations numerically for given initial conditions and check whether the couplings flow into the domain of attraction of the C2S2 fixed point or not. We use Mathematica to solve the flows up to long “time”  $\ell$  when the ultimate trends become apparent.

If the couplings always remain of the same order as their initial values or approach zero, we say the couplings are marginal or irrelevant and identify this as the C2S2 phase. The eventual trends here were discussed in Chapter 3.1.3.

On the other hand, if the magnitudes of some couplings grow significantly compared to the initial values, we say that the couplings are relevant and the C2S2 phase is destroyed. Thus, if either  $\lambda_{11}^{\sigma}$  or  $\lambda_{22}^{\sigma}$  coupling becomes negative while  $w_{12}^{\sigma}$  and  $w_{12}^{\rho}$  remain of the same sign, this  $\lambda^{\sigma}$  then runs away to large negative values and also induces the other couplings to diverge. Bosonizing the four-fermion interactions [49, 71, 29] (see Chapter 3.2), we can see that two spin modes and one charge mode become gapped and we obtain so-called “C1S0” phase. The overall charge propagation mode remains gapless and the system is conducting. Note that we do not distinguish which coupling diverges faster in the formal flow Eqs. (3.22)–(3.29). As discussed in [49], in the  $U \rightarrow 0+$  limit one can separate a so-called “C2S1” case where one of the spin couplings diverges qualitatively faster (but all couplings still diverge at the same  $\ell$ ). We do not make such subtle distinction and call any runaway flow situation as C1S0—all we want to know is that the two-band metal C2S2 became unstable.

The RG flows are qualitatively similar for different points in the same phase, so we only

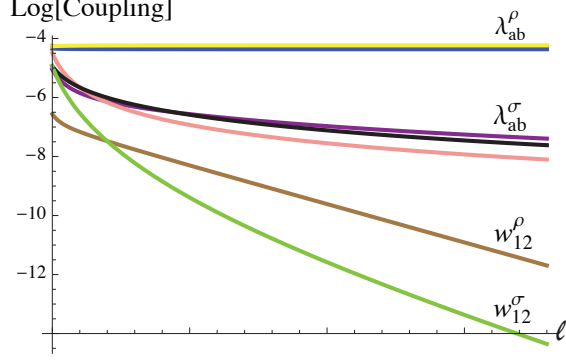


Figure 3.2: (Color online) Example of RG flows in the C2S2 phase. The model potential is Eq. (3.31) with  $\kappa = 1/2$ ,  $\gamma = 2/5$ ; the band parameter is  $t_2/t_1 = 0.9$ . We choose logarithm of the couplings to be the  $y$ -axis and RG “time”  $\ell$  to be the  $x$ -axis. We see that  $w_{12}^{\rho/\sigma}$  flows toward 0 rapidly (irrelevant couplings);  $\lambda_{ab}^{\rho}$  saturates very fast (strictly marginal couplings); while  $\lambda_{ab}^{\sigma}$  flows to 0 slowly (marginally irrelevant). More generally, if we fix these  $\kappa$  and  $\gamma$  values, for  $t_2/t_1 < 0.99$  the flows are similar to those shown here, and the phase is C2S2.

show one representative picture for each case. Fig. 3.2 shows the flows in the C2S2 phase. The scale parameter  $\ell$  is the  $x$ -axis, while logarithm of the couplings is the  $y$ -axis. In this way, we clearly see that the couplings separate into three groups, which is well explained by the C2S2 fixed point in Chapter 3.1.3: the  $w_{12}^{\rho/\sigma}$  flow to 0 exponentially rapidly, the  $\lambda_{ab}^{\sigma}$  flow to 0 marginally slowly, while the  $\lambda_{ab}^{\rho}$  saturate.

Fig. 3.3 illustrates the flows in the C1S0 phase. Here we use real values of the coupling as the  $y$ -axis and only show selected couplings,  $\lambda_{11}^{\sigma}$ ,  $\lambda_{22}^{\sigma}$ ,  $w_{12}^{\rho}$ , and  $w_{12}^{\sigma}$ . We clearly see that these couplings diverge (and so do the other couplings not shown in the figure).

### 3.1.5 Examples of phase diagrams with C2S2 metal stabilized by extended interactions

For illustration in our chapter, we consider the following interaction potential,

$$V(x - x') = \begin{cases} U & , \quad |x - x'| = 0 \\ \kappa U e^{-\gamma|x-x'|} & , \quad |x - x'| \geq 1 \end{cases} . \quad (3.31)$$

Here  $U$  is the overall energy scale and also the on-site repulsion. The relative magnitude of the extended repulsion is set by some factor  $\kappa < 1$ . Beyond one lattice spacing, the

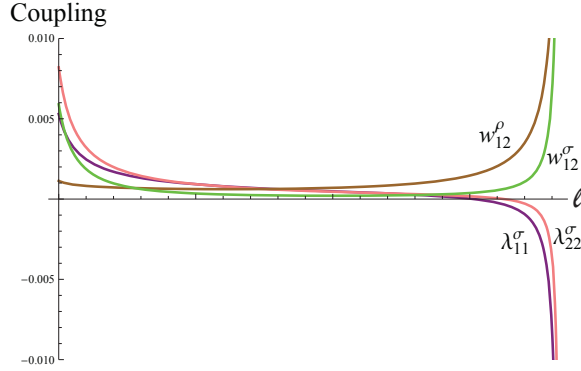


Figure 3.3: (Color) Example of RG flows of selected couplings in the C1S0 phase. The model is the same as in Fig. 3.2, but with  $t_2/t_1 = 1.05$ . We see that the selected couplings diverge after some time. For example, once the  $\lambda_{11}^\sigma$  and  $\lambda_{22}^\sigma$  become negative while  $w_{12}^\rho$  and  $w_{12}^\sigma$  remain positive, the RG equations (3.22)–(3.29) drive the  $\lambda_{11}^\sigma$  and  $\lambda_{22}^\sigma$  to  $-\infty$  and in turn  $w_{12}^\rho$  and  $w_{12}^\sigma$  to  $+\infty$ , and then all couplings diverge. More generally, if we fix  $\gamma = 2/5$ , for  $t_2/t_1 > 0.99$  the flows are similar to those shown here and we call this the C1S0 phase. Varying  $\gamma$ , we obtain the phase diagram Fig. 3.4.

potential decreases exponentially with decay rate  $\gamma$ . For  $\gamma \rightarrow \infty$  we obtain the Hubbard model with on-site interaction only, while for small  $\gamma$  the interaction extends over many lattice sites.

We also consider the above potential but truncated at the 4th neighbor. This tests robustness of our conclusions to modifications where the interactions have finite but still somewhat extended range, as may be preferable in numerical studies of such electronic models.

### 3.1.5.1 Weak coupling phase diagram for potential Eq. (3.31)

The extended repulsion, Eq. (3.31), is in Fourier space

$$V_Q = U \left[ 1 - \kappa + \frac{\kappa \sinh(\gamma)}{\cosh(\gamma) - \cos(Q)} \right]. \quad (3.32)$$

For given model parameters, we use Eqs. (3.10)–(3.17) to set initial conditions. We follow the RG flows and identify the phases as described above, thus mapping out the “weak coupling phase diagram”. Here and in the rest of the chapter, we take  $\kappa = 0.5$ . This is loosely motivated by the recent ab initio calculation [39] for the  $\kappa$ -(ET)<sub>2</sub>Cu<sub>2</sub>(CN)<sub>3</sub>, which

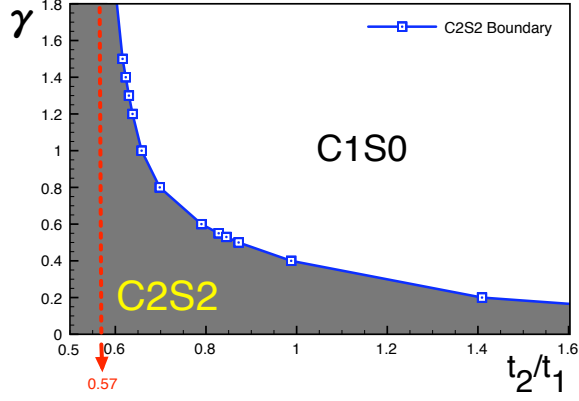


Figure 3.4: Stabilization of the C2S2 metal by extended interactions. The model potential is Eq. (3.31) with  $\kappa = 0.5$ . The noninteracting problem has one band for  $t_2/t_1 < 0.5$  and two bands for  $t_2/t_1 > 0.5$ , see Fig. 3.1, and we focus on the latter region. The limit  $\gamma \rightarrow \infty$  corresponds to the Hubbard model with on-site repulsion only, and the C2S2 phase is stable only over a narrow window  $t_2/t_1 \in [0.5 \dots 0.57]$  [65, 49]. The C2S2 region becomes progressively wider as we increase the interaction range  $1/\gamma$ .

gives the ratio of the nearest-neighbor repulsion  $V_1 \equiv V(|x - x'| = 1)$  to the on-site Hubbard  $U$  as  $V_1/U \simeq 0.43$ , while in our model  $V_1/U = \kappa e^{-\gamma}$ . The corresponding phase diagram showing stable C2S2 region is in Fig. 3.4.

We see that the C2S2 region becomes wider upon increasing the interaction range  $1/\gamma$ . We can understand this qualitatively as follows. For fixed band parameters, when  $\gamma \rightarrow 0$  the values of  $V_Q$  for all nonzero  $Q$  approach  $U(1 - \kappa)$ , while  $V_{Q=0} \simeq 2\kappa U/\gamma$  continues to increase. The corresponding contribution to  $\Lambda^\rho$  is

$$\delta\Lambda^\rho = \frac{V_{Q=0}}{2\pi} \left[ \frac{1}{v_1} + \frac{1}{v_2} - \frac{4}{v_1 + v_2} \right] = \frac{V_{Q=0}}{2\pi} \left[ \frac{(v_1 - v_2)^2}{v_1 v_2 (v_1 + v_2)} \right], \quad (3.33)$$

which is positive for any  $v_1 \neq v_2$  and grows with increasing  $V_{Q=0}$ . Note also from Eqs. (3.10)–(3.17) that the  $V_{Q=0}$  enters only in the  $\lambda_{ab}^\rho$  couplings. Large bare value of  $\Lambda^\rho$  makes the  $w_{12}^{\rho/\sigma}$  flows strongly irrelevant. Their effect on the  $\lambda_{ab}^\sigma$  flows is rapidly decreasing and expires. The  $\lambda_{ab}^\sigma$  couplings start repulsive and stay so and eventually flow to zero via marginal flows. This argument is strictly true in the small  $\gamma$  limit, while for finite  $\gamma$  the interplay of different flows is more complex and requires numerical study, as done in Fig. 3.4.

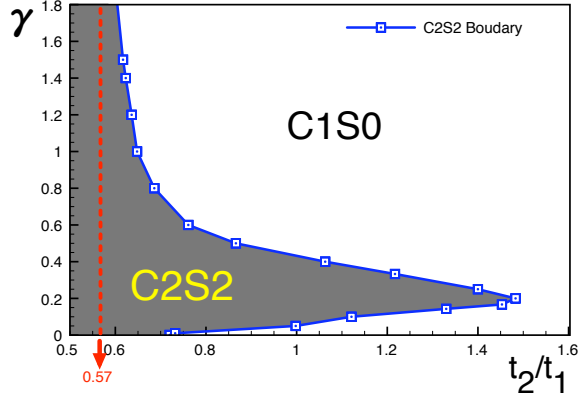


Figure 3.5: Same as Fig. 3.4 but for the potential Eq. (3.31) truncated at the 4th neighbor

### 3.1.5.2 Weak coupling phase diagram for potential Eq. (3.31) truncated at the 4th neighbor

Here, we truncate the interaction at the 4th neighbor, so the Fourier transform is,

$$V_Q = U \left[ 1 + 2\kappa \sum_{n=1}^4 e^{-n\gamma} \cos(nQ) \right].$$

The phase diagram in the weak coupling RG approach is shown in Fig. 3.5. We see that unlike the case without the truncation, the C1S0 phase opens again as  $\gamma \rightarrow 0$ . Since we only include up to the 4th neighbor interaction,  $V_{Q=0}$  does not dominate over  $V_{Q \neq 0}$  even in the  $\gamma \rightarrow 0$  limit. For  $\kappa = 0.5$  and  $\gamma = 0$ , there is significant structure in  $V_Q$  including sign changes as a function of  $Q$ , which can make bare spin couplings  $\lambda_{aa}^\sigma \sim V_{2k_{Fa}}$  be marginally relevant. Nevertheless, for intermediate  $\gamma$  there is still a wide window of the C2S2 phase.

## 3.2 Weak-to-intermediate coupling: Phases out of C2S2 upon increasing interaction

### 3.2.1 Harmonic description of the C2S2 phase

Let us begin with a harmonic description of the C2S2 metal. Technical steps and many details of the bosonization essentially follow [29] and references therein. We write

$$c_{Pa\alpha} = \eta_{a\alpha} e^{i(\varphi_{a\alpha} + P\theta_{a\alpha})}, \quad (3.34)$$

where  $\varphi$  and  $\theta$  are canonically conjugate boson fields and  $\eta$  are Klein factors.

We define “charge” and “spin” boson fields,

$$\theta_{a\rho/\sigma} = \frac{1}{\sqrt{2}}(\theta_{a\uparrow} \pm \theta_{a\downarrow}), \quad (3.35)$$

and “even” and “odd” flavor combinations,

$$\theta_{\mu\pm} = \frac{1}{\sqrt{2}}(\theta_{1\mu} \pm \theta_{2\mu}), \quad (3.36)$$

with  $\mu = \rho, \sigma$ . Similar definitions hold for the  $\varphi$  fields.

We can now bosonize all four-fermion interactions Eqs. (3.6)–(3.9). First consider the spin sector. The  $C_{ab}^\sigma$  terms give velocity renormalizations, while the  $\lambda_{ab}^\sigma$  terms are written out in Sec. IVA of [29] and are not repeated here. We assume that the  $\lambda_{ab}^\sigma$  are marginally irrelevant in the C2S2 phase. The fixed-point Lagrangian has effectively decoupled boson fields  $\theta_{1\sigma}$  and  $\theta_{2\sigma}$  with Luttinger parameters  $g_{1\sigma} = g_{2\sigma} = 1$ , dictated by SU(2) spin rotation invariance.

The Lagrangian in the charge sector is

$$\begin{aligned} \mathcal{L}^\rho = & \frac{1}{2\pi} [\partial_x \Theta^T \cdot \mathbf{A} \cdot \partial_x \Theta + \partial_x \Phi^T \cdot \mathbf{B} \cdot \partial_x \Phi] \\ & + \frac{i}{\pi} \partial_x \Theta^T \cdot \partial_\tau \Phi, \end{aligned} \quad (3.37)$$

where we defined  $\Theta^T = (\theta_{\rho+}, \theta_{\rho-})$  and  $\Phi^T = (\varphi_{\rho+}, \varphi_{\rho-})$ . Matrix elements of **A** and **B** are:

$$\begin{aligned} A_{11} &= \bar{v} + \frac{\lambda_{11}^\rho + \lambda_{22}^\rho + 2\lambda_{12}^\rho}{2\pi} + \frac{C_{11}^\rho + C_{22}^\rho + 2C_{12}^\rho}{2\pi} \\ &= \bar{v} + \frac{4V_{Q=0}}{\pi} - \frac{V_{2k_{F1}}}{4\pi} - \frac{V_{2k_{F2}}}{4\pi} - \frac{V_{\pi/2}}{2\pi} - \frac{V_{k_{F1}-k_{F2}}}{2\pi} - \frac{U}{2\pi}, \end{aligned} \quad (3.38)$$

$$\begin{aligned} A_{22} &= \bar{v} + \frac{\lambda_{11}^\rho + \lambda_{22}^\rho - 2\lambda_{12}^\rho}{2\pi} + \frac{C_{11}^\rho + C_{22}^\rho - 2C_{12}^\rho}{2\pi} \\ &= \bar{v} - \frac{V_{2k_{F1}}}{4\pi} - \frac{V_{2k_{F2}}}{4\pi} + \frac{V_{\pi/2}}{2\pi} + \frac{V_{k_{F1}-k_{F2}}}{2\pi} - \frac{U}{2\pi}, \end{aligned} \quad (3.39)$$

$$A_{12} = A_{21} = v_r + \frac{\lambda_{11}^\rho - \lambda_{22}^\rho}{2\pi} + \frac{C_{11}^\rho - C_{22}^\rho}{2\pi} = v_r - \frac{V_{2k_{F1}}}{4\pi} + \frac{V_{2k_{F2}}}{4\pi}, \quad (3.40)$$

$$\begin{aligned} B_{11} &= \bar{v} - \frac{\lambda_{11}^\rho + \lambda_{22}^\rho + 2\lambda_{12}^\rho}{2\pi} + \frac{C_{11}^\rho + C_{22}^\rho + 2C_{12}^\rho}{2\pi} \\ &= \bar{v} + \frac{V_{2k_{F1}}}{4\pi} + \frac{V_{2k_{F2}}}{4\pi} + \frac{V_{\pi/2}}{2\pi} - \frac{V_{k_{F1}-k_{F2}}}{2\pi} - \frac{U}{2\pi}, \end{aligned} \quad (3.41)$$

$$\begin{aligned} B_{22} &= \bar{v} - \frac{\lambda_{11}^\rho + \lambda_{22}^\rho - 2\lambda_{12}^\rho}{2\pi} + \frac{C_{11}^\rho + C_{22}^\rho - 2C_{12}^\rho}{2\pi} \\ &= \bar{v} + \frac{V_{2k_{F1}}}{4\pi} + \frac{V_{2k_{F2}}}{4\pi} - \frac{V_{\pi/2}}{2\pi} + \frac{V_{k_{F1}-k_{F2}}}{2\pi} - \frac{U}{2\pi}, \end{aligned} \quad (3.42)$$

$$B_{12} = B_{21} = v_r - \frac{\lambda_{11}^\rho - \lambda_{22}^\rho}{2\pi} + \frac{C_{11}^\rho - C_{22}^\rho}{2\pi} = v_r + \frac{V_{2k_{F1}}}{4\pi} - \frac{V_{2k_{F2}}}{4\pi}, \quad (3.43)$$

where

$$\bar{v} \equiv \frac{v_1 + v_2}{2}, \quad v_r \equiv \frac{v_1 - v_2}{2}. \quad (3.44)$$

The couplings  $\lambda_{ab}^\rho$  of the right–left mixing interactions  $\mathcal{H}_{RL}^\rho$  enter with opposite signs in **A** and **B** and directly affect Luttinger parameters, while the couplings  $C_{ab}^\rho$  of  $\mathcal{H}_{\text{chiral}}^\rho$  enter with the same sign and give velocity renormalizations.

From the final expressions in terms of  $V_Q$ , we see that the  $Q = 0$  component enters only in  $A_{11}$ . This can be understood by considering the  $Q = 0$  part of the interaction, [70]

$$\sum_{x,x'} V(x-x') n(x) n(x') \rightarrow V_{Q=0} \int_x [\rho(x)]^2 \quad (3.45)$$

where  $\rho(x) = 2\partial_x \theta_{\rho+}/\pi$  is the coarse-grained electron density.

Note also that the  $-U/(2\pi)$  in the diagonal matrix elements is due to our more careful treatment of the on-site repulsion, which we first write as  $Un_{\uparrow}(x)n_{\downarrow}(x)$  and then bosonize.

We obtain harmonic description of the C2S2 phase by combining the spin and charge sectors. The latter two-mode system  $\mathcal{L}^{\rho}$  has nontrivial Luttinger parameters, which can be determined from the matrices **A** and **B** (see Appendix 3.A). The fixed-point matrix elements will differ somewhat from the bare values above, but we ignore this in our crude analysis of the intermediate coupling regime.

To complete the bosonization of the four-fermion interactions, Eqs. (3.6)–(3.9), the  $w_{12}^{\rho/\sigma}$  terms give [71, 29]

$$W \equiv \left( w_{12}^{\rho} J_{R12} J_{L12} - w_{12}^{\sigma} \vec{J}_{R12} \cdot \vec{J}_{L12} \right) + \text{H.c.} \quad (3.46)$$

$$= \cos(2\varphi_{\rho-}) \left\{ 4w_{12}^{\rho} \left[ \cos(2\varphi_{\sigma-}) - \hat{\Gamma} \cos(2\theta_{\sigma-}) \right] - w_{12}^{\sigma} \left[ \cos(2\varphi_{\sigma-}) + \hat{\Gamma} \cos(2\theta_{\sigma-}) + 2\hat{\Gamma} \cos(2\theta_{\sigma+}) \right] \right\}, \quad (3.47)$$

where  $\hat{\Gamma} = \eta_{1\uparrow}\eta_{1\downarrow}\eta_{2\uparrow}\eta_{2\downarrow}$ . We see that  $W$  couples the charge and spin sectors. In the C2S2 theory described above, its scaling dimension is,

$$\Delta[W] = \Delta[\cos(2\varphi_{\rho-})] + 1, \quad (3.48)$$

where  $\Delta[\cos(2\varphi_{\rho-})]$  is evaluated in the Lagrangian  $\mathcal{L}^{\rho}$ , while the contribution 1 comes from the spin sector. For the C2S2 theory to be consistent, the  $W$  term must be irrelevant,  $\Delta[W] > 2$ . Once the  $W$  renormalizes to zero, the charge and spin sectors decouple. We thus have precise parallel with the weak coupling analysis of the C2S2 fixed point in Chapter 3.1.

On the other hand, if  $\Delta[W] < 2$ , the  $W$  term becomes relevant and the C2S2 state is unstable. In this case,  $\varphi_{\rho-}$  will get pinned and also the spin sector will become gapped. Only the “ $\rho+$ ” mode remains gapless and the system is some C1S0 conducting phase.

### 3.2.2 Mott insulator driven by Umklapp interaction. Intermediate coupling procedure out of the C2S2

The weak coupling analysis in Chapter 3.1 misses the possibility of gapping out the overall charge mode  $\theta_{\rho+}$  since there are no four-fermion Umklapp terms allowed in the two-band system. However, the half-filled electronic system does become a Mott insulator for sufficiently strong repulsion. In the theoretical description, this is achieved by an eight-fermion Umklapp term [29]

$$\begin{aligned} H_8 &= v_8 (c_{R1\uparrow}^\dagger c_{R1\downarrow}^\dagger c_{R2\uparrow}^\dagger c_{R2\downarrow}^\dagger c_{L1\uparrow} c_{L1\downarrow} c_{L2\uparrow} c_{L2\downarrow} + \text{H.c.}) \\ &= 2v_8 \cos(4\theta_{\rho+}) . \end{aligned} \quad (3.49)$$

At weak coupling, this term has scaling dimension  $\Delta[H_8] = 4$  and is strongly irrelevant. However, from Eq. (3.45) we see that overall repulsive interaction stiffens the  $\theta_{\rho+}$  mode and lowers the scaling dimension of  $H_8$ . For sufficiently strong repulsion,  $\Delta[H_8]$  drops below 2 and the Umklapp becomes relevant;  $\theta_{\rho+}$  gets pinned and we obtain a Mott insulator.

Our intermediate coupling procedure is as follows. Using the harmonic theory of the C2S2 phase, we calculate the scaling dimensions  $\Delta[W]$ , Eq. (3.48), and  $\Delta[H_8] = \Delta[\cos(4\theta_{\rho+})]$  from the Lagrangian  $\mathcal{L}^\rho$ , Eq. (3.37). Details are described in Appendix 3.A and calculations are done numerically in the end.

If both  $\Delta[W]$  and  $\Delta[H_8]$  are larger than 2, the C2S2 metal is stable. As interactions increase, eventually either  $W$  or  $H_8$  becomes relevant. In general, there are two cases:

1) If  $H_8$  becomes relevant first, we pin  $\theta_{\rho+}$  and enter ‘‘C1S2’’ Mott insulator. To be more precise, we can further qualify the label as ‘‘C1[ $\rho-$ ]S2’’; the remaining ‘‘charge’’ mode ‘‘ $\rho-$ ’’ represents local current loop fluctuations and does not conduct. This is the spin liquid phase called spin Bose-metal in [29] and described in detail there. Exploring conditions for finding such phase in electronic models is our main goal here.

2) On the other hand, if the  $W$  term becomes relevant first, we enter C1S0 conducting state with a spin gap (more precisely, ‘‘C1[ $\rho+$ ]S0’’).

Some reservations are in order. First, we use bare values of the couplings in the A

and  $\mathbf{B}$  matrices, which is not accurate since the couplings experience initial flows, see Chapter 3.1.2. Second, we consider only instabilities driven by changes in the harmonic  $\mathcal{L}^\rho$  theory as they translate to scaling dimensions of the  $H_8$  and  $W$  terms, i.e., we effectively treat the latter as small. We also assume that the spin sector is near the fixed point with all  $\lambda_{ab}^\sigma$  marginally irrelevant and small. We will address these reservations after presenting results of the above procedure. Keeping these remarks in mind, we now describe how we analyze phases out of the C1[ $\rho-$ ]S2 and C1[ $\rho+$ ]S0 in the same procedure.

### 3.2.2.1 Instability out of C1[ $\rho-$ ]S2 driven by spin-charge coupling $W$

In the present analysis focusing on the “ $\rho+$ ” and “ $\rho-$ ” fields, we can also crudely estimate the extent of the C1S2 or C1S0 phases once either happens out of the C2S2.

Suppose the Umklapp  $H_8$  is relevant first and we are in the C1S2 phase. We still need to remember the  $W$  term since it can become relevant if we continue increasing the interaction strength. To estimate the scaling dimension of the  $W$  term, we assume now that the  $\theta_{\rho+}$  field is massive and integrate out  $\theta_{\rho+}$  and  $\varphi_{\rho+}$ . Mathematically this amounts to sending  $A_{11} \rightarrow \infty$ , and we obtain

$$\Delta [W; \theta_{\rho+} \text{ is pinned}] = \left[ \frac{A_{22}B_{11}}{B_{11}B_{22} - B_{12}^2} \right]^{\frac{1}{2}} + 1. \quad (3.50)$$

This assumption is approximate but reasonable, since once the parameters are such that the system is in the C1S2 phase, the relevant  $H_8$  will grow and quickly stiffen the  $A_{11}$  in positive feedback loop.

The C1S2 phase is stable if  $\Delta[W] > 2$ , and this analysis is similar to the stability analysis of the SBM in [29]. If  $\Delta[W]$  drops below 2, the  $W$  term becomes relevant and the  $\varphi_{\rho-}$  field will be pinned, together with gapping out the spin sector, see Eq. (3.47). The final result is some “C0S0” phase, whose precise character depends on the details of the couplings  $w_{12}^{\rho/\sigma}$ . This is studied in Sec. IVB of [29]. For the present repulsive electron model, we have  $w_{12}^\rho, w_{12}^\sigma > 0$ , so the resulting C0S0 is likely a period-2 valence bond solid (VBS). [29] This connects to dimerized phase in the  $J_1 - J_2$  spin chain appropriate in the strong interaction limit of the electron system.

### 3.2.2.2 Instability out of C1[ $\rho+$ ]S0 driven by Umklapp $H_8$

Suppose now the  $W$  interaction becomes relevant first. From Eq. (3.47), it is natural that  $\varphi_{\rho-}$  is pinned, the spin sector gets gapped, and we are in C1S0 phase. Here we postulate mass for  $\varphi_{\rho-}$  (essentially sending  $B_{22} \rightarrow \infty$ ) and calculate the effective scaling dimension of the Umklapp term,

$$\Delta [H_8; \varphi_{\rho-} \text{ is pinned}] = 4 \left[ \frac{B_{11}A_{22}}{A_{11}A_{22} - A_{12}^2} \right]^{\frac{1}{2}}. \quad (3.51)$$

If  $\Delta[H_8] > 2$ , the C1S0 is stable. Once  $\Delta[H_8]$  drops below 2, the overall charge mode  $\theta_{\rho+}$  is pinned and we obtain fully gapped Mott insulator C0S0, which is likely the same period-2 VBS discussed earlier.

### 3.2.3 Numerical results

We consider the same models with extended density-density interactions as in the weak coupling analysis in Chapter 3.1.5, parking ourselves initially in the C2S2 phase in Fig. 3.4 and Fig. 3.5. From the preceding discussion, we can obtain two phases out of the C2S2 upon increasing interaction strength—either C1[ $\rho+$ ]S0 or C1[ $\rho-$ ]S2. To visualize the results, we imagine adding the overall interaction strength  $V$  as the  $z$ -axis to Fig. 3.4 and Fig. 3.5. We then project down which phase happens first for each such vertical line out of C2S2. Calculations are done numerically and the results are shown in Fig. 3.6 and Fig. 3.9. In Fig. 3.7 we take a cut through Fig. 3.6 at  $\gamma = 0.4$  and show details of the phase diagram in the  $t_2/t_1 - V$  plane.

#### 3.2.3.1 Intermediate coupling phase diagram for model with potential Eq. (3.31)

Fig. 3.6 shows results for the model potential Eq. (3.31). We can see that in two regimes  $\gamma \geq 1.2$  and  $\gamma \leq 0.4$  we exit from the C2S2 into the C1S2. The two limits can be understood analytically.

In the large  $\gamma$  case, we can replace all  $V_Q$  by simply  $U$ . The matrices **A** and **B** defined

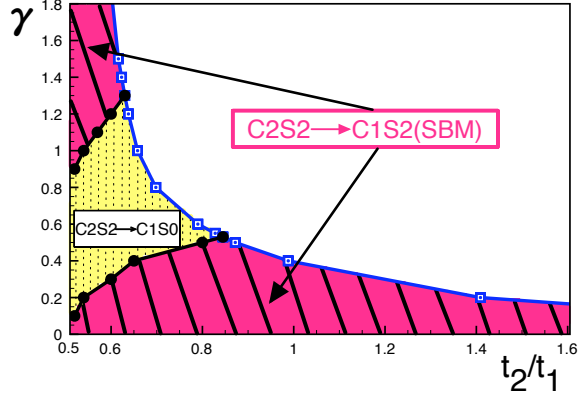


Figure 3.6: Projection of phases obtained out of the C2S2 of Fig. 3.4 as we increase overall repulsion strength  $V$ , which we imagine to be the  $z$ -axis perpendicular to the page (Fig. 3.7 gives one cut at  $\gamma = 0.4$  with such  $V$  axis shown explicitly). The results are obtained in the intermediate coupling procedure as explained in the text. White region is C1S0 at weak coupling, see Fig. 3.4, and is not considered here.

in Eq. (3.38)–(3.43) become

$$\mathbf{A} = \begin{pmatrix} \bar{v} + \frac{2U}{\pi} & v_r \\ v_r & \bar{v} \end{pmatrix}, \quad \mathbf{B} = \begin{pmatrix} \bar{v} & v_r \\ v_r & \bar{v} \end{pmatrix}. \quad (3.52)$$

We see that  $U$  only contributes to  $A_{11}$ . This monotonically “stiffens” the  $\theta_{\rho+}$  (lowering  $\Delta[H_8]$ ) but “softens” the  $\varphi_{\rho-}$  (increasing  $\Delta[W]$ ). Therefore we only expect the C1S2 phase out of the C2S2 as found in the numerical calculations.

On the other hand, for small  $\gamma$  we can see from Eq. (3.32) that  $V_{Q=0}$  will dominate over  $V_{Q \neq 0}$ . Keeping only  $V_{Q=0}$ , the matrices  $\mathbf{A}$  and  $\mathbf{B}$  become

$$\mathbf{A} \simeq \begin{pmatrix} \bar{v} + \frac{4V_{Q=0}}{\pi} & v_r \\ v_r & \bar{v} \end{pmatrix}, \quad \mathbf{B} \simeq \begin{pmatrix} \bar{v} & v_r \\ v_r & \bar{v} \end{pmatrix}. \quad (3.53)$$

Thus the small  $\gamma$  case has similar mathematical structure to the large  $\gamma$  case. The physical difference is that here the transition to the C1S2 is driven by the  $V_{Q=0}$  instead of the on-site Hubbard  $U$ . Note also that since  $V_{Q=0} \simeq 2\kappa U/\gamma$  for  $\gamma \ll 1$ , the transition requires only small values of  $U$ , which is why we can ignore all  $V_{Q \neq 0}$  compared to the band velocities.

Now we consider a cut at  $\gamma = 0.4$  to see more details in the  $t_2/t_1 - V$  plane. The

results are shown in Fig. 3.7. Compared with the two limits  $\gamma \gg 1$  and  $\gamma \ll 1$  above, all possibilities that we discussed out of the C2S2 are realized here. The C1S0 phase appears for  $t_2/t_1 < 0.65$  for some quantitative reasons. Various  $V_Q$  are all of the same order, unlike the  $\gamma \ll 1$  case. At the same time, they have some nontrivial  $Q$ -dependence, unlike the  $\gamma \gg 1$  case, which is somehow enough to make the  $W$  term become relevant and preempt the Umklapp term. Note that for small interactions the scaling dimension of the  $W$  term can be obtained from the weak coupling RG equations for the  $w_{12}^{\rho/\sigma}$  in Chapter 3.1.2 by setting all  $\lambda_{ab}^\sigma = 0$  (since we ignore the spin sector in the present procedure). Thus,  $\Delta[W] = 2 + \Lambda^\rho$ , where  $\Lambda^\rho$  is defined in Eq. (3.30). Since  $\Lambda^\rho$  can only decrease under the weak coupling RG and the shaded C2S2 region in Fig. 3.4 was found to be stable, we expect  $\Delta[W]$  here to increase with  $V$  for small  $V$ , in agreement with numerical calculations. However, we find that  $\Delta[W]$  eventually starts to decrease with increasing  $V$  and can become relevant before the Umklapp. This is a quantitative matter and comes from putting together all interactions  $\mathcal{H}_{RL}^\rho$  and  $\mathcal{H}_{\text{chiral}}^\rho$ , Eq. (3.6)–(3.8), in the intermediate coupling procedure. Such numerical calculations give us that the C2S2 can exit into the C1S0 phase. For larger  $t_2/t_1 > 0.65$  in Fig. 3.7, we obtain the sought for C1S2 spin liquid phase.

This concludes the presentation of formal results within the particular procedure for intermediate scale analysis. Let us now think how to combine the weak and intermediate coupling approaches more realistically and see where our results are more robust.

First of all, in the weak coupling analysis the C2S2 phase is unstable beyond the shaded regions in Figs. 3.4 and 3.5. However, this is lost in the specific intermediate coupling procedure, which, when applied for small coupling, would give C2S2 essentially everywhere. For example, in Fig. 3.7 we see monotonic growth of the C2S2 phase with  $t_2/t_1$  past the point where the weak coupling analysis predicts instability. The reason for this discrepancy is the complete neglect of the spin sector in the formal intermediate scale procedure. Indeed, in the weak coupling analysis, the instabilities manifest dramatically once one of the  $\lambda_{aa}^\sigma$  becomes negative, causing runaway flows. This can happen even when the bare  $\lambda_{aa}^\sigma$  are repulsive because they are renormalized downwards and can be driven negative by the  $w_{12}^{\rho/\sigma}$  contributions in Eqs. (3.25)–(3.26), where we assume  $w_{12}^\rho w_{12}^\sigma > 0$ . Also, the  $\lambda^\sigma$  couplings feed back into the flow of  $w_{12}^{\rho/\sigma}$ , so the RG flow behavior is even more complex. So far we

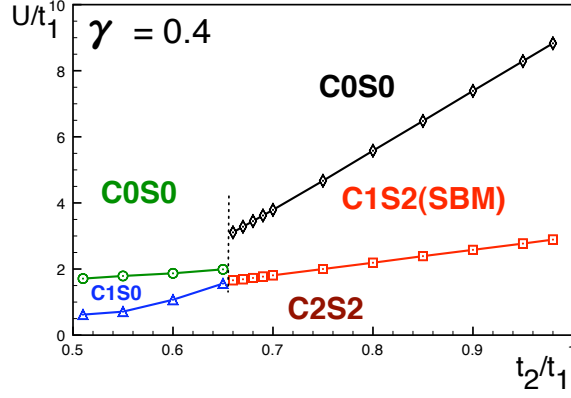


Figure 3.7: (Color) Intermediate coupling analysis of the model with potential Eq. (3.31) for  $\kappa = 0.5$  and  $\gamma = 0.4$ . Here the horizontal range is equal to the extent of the C2S2 phase in the weak coupling analysis from Fig. 3.4. We start in the C2S2 at small  $U$ . The boundary where the charge-spin coupling term  $W$  becomes relevant first is indicated with blue triangles and the system goes into the C1S0; the next stage where the C1S0 in turn becomes unstable and the system goes into the C0S0 is marked with green circles. The boundary where the Umklapp term  $H_8$  becomes relevant first is indicated with red squares and the system goes into the C1S2, which is the SBM phase of [29]; upon further increase of the interaction strength, the C1S2 eventually becomes unstable and goes to the C0S0 at locations marked with black diamonds. Note that the discontinuity shown with the dotted vertical line is not meaningful and is due to our crude analysis performed separately out of the C1S0 and C1S2; in either case, the final C0S0 is likely the same phase. Also note that the C1 mode content is distinct in the C1[ $\rho+$ ]S0 (conducting) and C1[ $\rho-$ ]S2 (insulating) cases and any transition between them is first order. The C2S2-to-C1S2 transition is Kosterlitz-Thouless-like.

have dealt with this inadequacy of the intermediate scale procedure by simply cutting it at the C2S2 boundaries determined from the weak coupling analysis. More realistically, we expect the extent of the C2S2 phase to peak somewhere in the middle of the range shown in Fig. 3.7 and decrease towards the right boundary. Similar considerations apply to the C1S2 phase, which is likely confined within the same  $t_2/t_1$  range as the C2S2. Therefore, the  $t_2/t_1 - U/t_1$  phase diagram should be more like Fig. 3.8.

We can also discuss our earlier reservation about using bare values of the couplings instead of some renormalized values. Thinking about some RG treatment, we expect that crude patterns of how various couplings affect each other are likely similar at intermediate and weak couplings. Now if we formally take the flow equations from Chapter 3.1.2, the outcome does not depend on the initial interaction scale, so we would conclude the

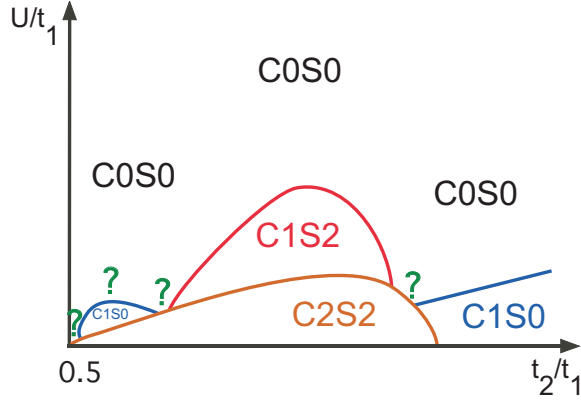


Figure 3.8: Schematic merging of the weak and intermediate coupling results in the model regimes, as in Fig. 3.7, in the whole range with  $t_2/t_1 > 0.5$ . In weak coupling, the C2S2 phase is unstable beyond the shaded region in Fig. 3.4. However, due to the crudeness of our intermediate coupling procedure, Fig. 3.7 shows monotonic growth of the C2S2 phase with  $t_2/t_1$  past this instability. This discrepancy arises because our intermediate coupling procedure completely ignores the spin sector. More realistically, we expect the C2S2 phase to peak somewhere in the middle of the range shown in Fig. 3.7 and be bounded by the C1S0 for larger  $t_2/t_1$ . Similar considerations apply to the C1S2 phase, which is bounded by the C0S0.

C2S2 phase throughout the shaded region in Fig. 3.4. The weak coupling flow equations miss velocity renormalizations due to chiral interactions, but these are not expected to flow strongly and are treated reasonably in the intermediate coupling analysis. The fact that the couplings are now finite and comparable with bare band energies is also treated reasonably at intermediate coupling due to the power of bosonization, so the outlined forging of weak and intermediate scales seems appropriate. Finally, the Umklapp term that is missing in the weak coupling approach will feed into stiffening of  $\theta_{\rho+}$  only, which is good for the first instability out of the C2S2 to be into the C1S2 spin liquid.

We think that our conclusions are more robust for small  $\gamma$  where the extent of the C2S2 phase is larger and also the longer-ranged potential is feeding precisely into stiffening the overall charge field  $\theta_{\rho+}$ , which is good for going to the C1S2 phase. On the other hand, results at medium to large  $\gamma$  are likely less reliable, with different scenarios depending on quantitative issues.

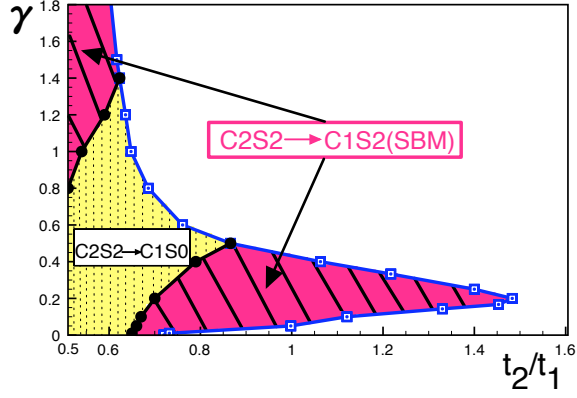


Figure 3.9: Same as Fig. 3.6 but for the model with interactions Eq. (3.31) truncated at the 4th neighbor and starting out of the C2S2 of Fig. 3.5

### 3.2.3.2 Intermediate coupling phase diagram for model with potential Eq. (3.31) truncated at the 4th neighbor

Figure 3.9 shows results of the intermediate coupling analysis for the model with interactions truncated at the 4th neighbor, see Chapter 3.1.5.2. We have a rather similar story to Fig. 3.6, except that the initial C2S2 region is bounded. Large part of the C2S2 phase exits into the C1S2 spin liquid upon increasing interactions, and our results are probably more robust near  $\gamma \sim 0.2-0.3$  where the C2S2 has the largest extent along the  $t_2/t_1$  axis.

## 3.3 Summary and discussion

To summarize, in this chapter we consider *electronic* models for realizing spin Bose-metal (spin liquid) phase on the two-leg triangular strip found in [29] in spin-1/2 model with ring exchanges. We identify the SBM with the C1S2 Mott insulator of electrons.

In Chapter 3.1, we start with a two-band electron system, which is C2S2. Instead of considering only the on-site Hubbard-type repulsion [65, 67, 68, 72, 69, 38, 73], we study generally longer ranged density-density repulsion. This is motivated in part by the expectation that real Coulomb interaction is not screened in Mott insulator materials, so further neighbor repulsion can be significant, as brought up by recent ab initio work [39] for the spin liquid material  $\kappa$ -(ET) $_2$ Cu $_2$ (CN) $_3$ . Using weak coupling RG analysis for the zigzag chain problem [49, 64, 71, 65], we find that such extended interactions open much

wider window of the C2S2 metal compared with the Hubbard model. The main results are shown in Fig. 3.4 and Fig. 3.5. In the first figure, we have essentially an independent control over the  $Q = 0$  part of the potential by allowing it to extend to far neighbors, and we identify the dominance of  $V_{Q=0}$  as the main stabilizing force for the metal. In the second figure, we truncate interactions at the 4th neighbor to check the robustness of our conclusions, in view that such models may be easier to explore using numerical DMRG. Our detailed quasi-1D considerations agree with the intuition that in real metals electronic pairing instabilities are suppressed by the long-ranged piece of the Coulomb interaction. Such widening of the C2S2 region by extending the model interaction range is warranted if we want to bring the electronic ladder system closer to realistic situations in the 2D candidate spin liquid materials.

In Chapter 3.2, we begin with stable C2S2 metal at weak coupling and use bosonization to extend the analysis to intermediate coupling by gradually increasing the overall repulsion strength. Within effective bosonic theory, we identify potential instabilities of the C2S2 phase to spin-charge interaction  $W$  (Eq. (3.47)) and Umklapp interaction  $H_8$  (Eq. (3.49)). The  $W$  can drive the system into C1[ $\rho+$ ]S0 phase with spin gap but still conducting along the chain, while the Umklapp  $H_8$  can produce C1[ $\rho-$ ]S2 Mott insulator with three gapless modes, which is the desired SBM phase. We calculate the scaling dimensions of the  $W$  and  $H_8$  terms in the harmonic theory of the C2S2 metal using bare couplings in the charge sector and assuming stability in the spin sector—this constitutes our naive intermediate coupling procedure. The calculation of scaling dimensions is described in Appendix 3.A and is done numerically in the end.

We consider two cases depending on which of the terms  $W$  or  $H_8$  becomes relevant first and apply similar intermediate coupling approach inside the resulting phase. Assuming strong field pinning by the already relevant term, we calculate the scaling dimension of the remaining term and estimate when it eventually drives the system into fully gapped COS0 paramagnet (which is likely connected to the dimerized phase of the  $J_1 - J_2$  Heisenberg model at strong coupling). With the help of such admittedly crude analysis, we can map out the phase diagram in weak to intermediate coupling regime as illustrated in schematic Fig. 3.8 (based on more naive Fig. 3.7). Figures 3.6 and 3.9 summarize our results and

show where the C2S2 metal goes to the C1S2 (SBM spin liquid) upon increasing overall repulsion strength. We conclude that the C1S2 phase is quite natural out of the wider C2S2 metallic region, in particular when driven by extended repulsive interactions. It would be very interesting to confront our theoretical predictions with numerical DMRG studies of such electronic models with extended repulsion.

So far, we have approached the intermediate coupling Mott insulator from the weak coupling metallic side. One could try to attack the same problem starting from the strong coupling limit deep in the Mott insulator where Heisenberg spin-1/2 model is appropriate. As one nears the metallic phase, it becomes important to include multiple spin exchanges in the effective spin Hamiltonian to better capture charge fluctuations in the underlying electron system [74, 27, 75, 76]. This is the motivation behind [29] studying  $J_1 - J_2$  chain with additional four-spin ring exchanges. The concept study [29] allowed arbitrary variation of the ring coupling compared with the Heisenberg couplings. However, coming from an electronic model these do not vary independently and more exchange terms are also generated. It would be interesting to pursue such approach systematically studying effective spin models with multi-spin exchanges for realistic electronic models to see if they harbor the SBM phase. We do not make such attempts here, but only give few simple observations on how the derivation of the spin model is modified in the presence of extended repulsion.

First of all, for the two-spin exchanges, the familiar Hubbard model expression  $J_{rr'} = 4t_{rr'}^2/U$  is modified to  $J_{rr'} = 4t_{rr'}^2/(V_0 - V_{r-r'})$ . The energy denominator is not simply the on-site  $U = V_0$  but also includes interaction potential between the two sites  $r$  and  $r'$ . For example, [39] estimates  $V_1/V_0 \approx 0.43$  for the  $\kappa$ -(ET)<sub>2</sub>Cu<sub>2</sub>(CN)<sub>3</sub> spin liquid material, and this would significantly affect values of the exchange constants. Energy denominators for all virtual processes are similarly affected and take a form of a charging energy for the deviations from the background. Multispin exchange amplitudes are given by a product of electron tunneling amplitudes for a given virtual path divided by a product of such charging energies in intermediate states along the path. Thus, the multi-spin exchanges may in fact be relatively more important in systems with extended interactions.

As an extreme example, imagine a very slow decrease of  $V(r - r')$  up to some distance  $R$  (and perhaps a faster drop thereafter). Then all exchange loops up to such radius  $R$

will have large amplitudes. The multispin exchanges encode the underlying kinetic energy of electrons, and our intuition is that this would like to retain some itinerancy in the spin degrees of freedom even when the charges are localized. From such strong to intermediate coupling perspective, it appears that extended interactions would tend to stabilize the SBM spin liquid near the insulator-metal transition, similar to our conclusion from the weak to intermediate coupling study in the quasi-1D models in this chapter. It would be interesting to pursue such considerations more carefully and in realistic electronic models. We hope that our work will further stimulate numerical studies of such models on ladders and in two dimensions.

### 3.A Derivation of $\Delta[\cos(4\theta_{\rho+})]$ and $\Delta[\cos(2\varphi_{\rho-})]$ in C2S2 phase

Equation (3.37) gives quadratic Lagrangian for the charge sector. First, we redefine the fields which still satisfy the same commutation relations,

$$\Theta = \mathbf{S} \cdot \Theta_1, \quad \Phi = \mathbf{S} \cdot \Phi_1. \quad (3.54)$$

Here  $\mathbf{S}$  is an orthogonal  $2 \times 2$  matrix diagonalizing the matrix  $\mathbf{A}$ ,

$$\mathbf{S}^T \cdot \mathbf{A} \cdot \mathbf{S} = \begin{pmatrix} A_1 & 0 \\ 0 & A_2 \end{pmatrix} \equiv \mathbf{A}_D. \quad (3.55)$$

The Lagrangian becomes,

$$\begin{aligned} \mathcal{L}^\rho = & \frac{1}{2\pi} [\partial_x \Theta_1^T \cdot \mathbf{A}_D \cdot \partial_x \Theta_1 + \partial_x \Phi_1^T \cdot \mathbf{S}^T \cdot \mathbf{B} \cdot \mathbf{S} \cdot \partial_x \Phi_1] \\ & + \frac{i}{\pi} \partial_x \Theta_1^T \cdot \partial_\tau \Phi_1. \end{aligned} \quad (3.56)$$

Define another set of conjugate fields,

$$\Theta_1 = \frac{1}{\sqrt{\mathbf{A}_D}} \cdot \Theta_2, \quad \Phi_1 = \sqrt{\mathbf{A}_D} \cdot \Phi_2. \quad (3.57)$$

We obtain,

$$\begin{aligned} \mathcal{L}^\rho = & \frac{1}{2\pi} [\partial_x \Theta_2^T \cdot \partial_x \Theta_2 + \partial_x \Phi_2^T \cdot \mathbf{B}' \cdot \partial_x \Phi_2] \\ & + \frac{i}{\pi} \partial_x \Theta_2^T \cdot \partial_\tau \Phi_2, \end{aligned} \quad (3.58)$$

where

$$\mathbf{B}' \equiv \sqrt{\mathbf{A}_D} \cdot \mathbf{S}^T \cdot \mathbf{B} \cdot \mathbf{S} \cdot \sqrt{\mathbf{A}_D}. \quad (3.59)$$

We use the same trick to diagonalize matrix  $\mathbf{B}'$ :

$$\Theta_2 = \mathbf{R} \cdot \Theta_3, \quad \Phi_2 = \mathbf{R} \cdot \Phi_3, \quad (3.60)$$

where  $\mathbf{R}$  is an orthogonal matrix which satisfies,

$$\mathbf{R}^T \cdot \mathbf{B}' \cdot \mathbf{R} = \begin{pmatrix} B'_1 & 0 \\ 0 & B'_2 \end{pmatrix} \equiv \mathbf{B}'_D. \quad (3.61)$$

The Lagrangian becomes,

$$\begin{aligned} \mathcal{L}^\rho = & \frac{1}{2\pi} [\partial_x \Theta_3^T \cdot \partial_x \Theta_3 + \partial_x \Phi_3^T \cdot \mathbf{B}'_D \cdot \partial_x \Phi_3] \\ & + \frac{i}{\pi} \partial_x \Theta_3^T \cdot \partial_\tau \Phi_3. \end{aligned} \quad (3.62)$$

Now we can calculate the scaling dimension of  $\cos(4\theta_{\rho+})$  and  $\cos(2\varphi_{\rho-})$  from Eq. (3.62) through relations,

$$\Theta = \mathbf{S} \cdot \frac{1}{\sqrt{\mathbf{A}_D}} \cdot \mathbf{R} \cdot \Theta_3, \quad (3.63)$$

$$\Phi = \mathbf{S} \cdot \sqrt{\mathbf{A}_D} \cdot \mathbf{R} \cdot \Phi_3, \quad (3.64)$$

and scaling dimensions of the final fields,

$$\Delta[e^{i\Theta_3}] = \frac{\sqrt{\mathbf{B}'_D}}{4}, \quad \Delta[e^{i\Phi_3}] = \frac{1}{4\sqrt{\mathbf{B}'_D}}, \quad (3.65)$$

where the right-hand sides mean corresponding diagonal matrix elements. Therefore, we find general form for the dimensions we are interested in,

$$\begin{aligned} \Delta[\cos(4\theta_{\rho+})] &= 4\sqrt{B'_1} \left( \frac{S_{11}R_{11}}{\sqrt{A_1}} + \frac{S_{12}R_{21}}{\sqrt{A_2}} \right)^2 \\ &+ 4\sqrt{B'_2} \left( \frac{S_{11}R_{12}}{\sqrt{A_1}} + \frac{S_{12}R_{22}}{\sqrt{A_2}} \right)^2, \end{aligned} \quad (3.66)$$

$$\begin{aligned} \Delta[\cos(2\varphi_{\rho-})] &= \frac{(\sqrt{A_1}S_{21}R_{11} + \sqrt{A_2}S_{22}R_{21})^2}{\sqrt{B'_1}} \\ &+ \frac{(\sqrt{A_1}S_{21}R_{12} + \sqrt{A_2}S_{22}R_{22})^2}{\sqrt{B'_2}}, \end{aligned} \quad (3.67)$$

where  $S_{ab}$  and  $R_{ab}$  are matrix elements of  $\mathbf{S}$  and  $\mathbf{R}$ .

# Chapter 4

## Effects of Zeeman field on a spin Bose-metal phase

This chapter continues efforts to gain insights about the 2D spin liquid from the solvable two-leg ladder example. Here we study the Zeeman magnetic field effects on the SBM phase, while in a separate chapter, Chapter 5, we will study orbital field effects. One motivation comes from experiments on the 2D spin liquid materials  $\kappa$ -(ET)<sub>2</sub>Cu<sub>2</sub>(CN)<sub>3</sub> and EtMe<sub>3</sub>Sb[Pd(dmit)<sub>2</sub>]<sub>2</sub> measuring thermodynamic, transport, and local magnetic properties under strong fields [15, 77, 44, 78, 17, 21]. An important question is whether the field can induce changes in the physical state of the system.

To this end, we explore possible instabilities of the two-leg SBM state in the Zeeman field. There have been many studies of 2D and 1D spin models under magnetic field showing rich behaviors. For example, the phase diagram of the  $J_1$ - $J_2$  antiferromagnetic chain with  $J_1, J_2 > 0$  in the field [79, 80, 81, 82, 83] contains one-component and two-component Luttinger liquids, a plateau, a phase with static chirality order, and a phase with spin-nematic correlations. In the spirit of such studies, we allow a large range of fields, which could be numerically explored in spin or electronic models realizing the SBM phase [29, 31]. We remark that experiments on the spin liquid materials achieve only relatively small fields—e.g., the maximum magnetization is  $\lesssim 0.01\mu_B$  per spin. Nevertheless, some of our two-leg ladder phases from the broader theoretical study motivate interesting 2D states that are worth exploring.

The SBM phase on the zigzag chain can be viewed as a Gutzwiller-projected spinon

state where both  $\uparrow$  and  $\downarrow$  spinon species populate two Fermi segments (see Fig. 4.1). The projection eliminates the overall charge mode leaving three gapless modes. We find that this phase can in principle remain stable under the Zeeman field. We also identify all possible instabilities out of the SBM.

Loosely speaking, the instabilities correspond to pairing of spinons separately within each species (a kind of triplet pairing). More precisely, the relevant interactions can be interpreted as moving a “Cooper pair” from one band to the other of the same species. Of course, there is no long-range pairing order in the quasi-1D and in fact the dominant correlations in our system need not be of “pair-type”—the bosonization provides the proper treatment, while this language is only for convenience.

It can happen that the pairing is relevant for one spinon species but not the other. In this case the system retains two gapless modes. Interestingly, spin-1 excitations become gapped (i.e., transverse spin correlations are short-ranged), while spin-2 excitations are gapless (i.e., nematic or two-magnon correlation functions show power law).

It can also happen that the pairing is relevant for each spinon species. In this case the system retains only one gapless mode. Again, spin-1 excitations are gapped while spin-2 remain gapless. It further turns out that the system breaks translational symmetry and has either period 2 valence bond solid (VBS) or period 2 static chirality order.

Such thinking about pairing within the same spinon species can be extended to 2D. Here, if we pair only one species and not the other, we have a gap to spin-1 excitations while at the same time we have critical spin-2 correlations and the system retains the gapless Fermi surface for the unpaired species. On the other hand, if we have pairing within both spinon species, the system acquires a long-range spin-nematic order. [84]

Spin-nematic phases were discovered and much discussed recently in other interesting frustrated systems. For instance, such phases were found in the antiferromagnetic zigzag ladder with easy-plane anisotropy [85] and in the ferro/antiferro zigzag ladder ( $J_1 < 0$ ,  $J_2 > 0$ ) in the Zeeman field [86, 87, 88, 89]. As for examples in 2D, spin-nematic order was found in the frustrated square lattice with ferromagnetic  $J_1 < 0$  and antiferromagnetic  $J_2 > 0$  and ring exchanges [90], and in the triangular lattice with ferromagnetic Heisenberg and antiferromagnetic ring exchanges [91]. Though, many details of the nematic phases

proximate to the SBM studied here are of course different.

The chapter is organized as follows. In Chapter 4.1, we consider an electronic Hubbard-type model with longer-ranged repulsion under Zeeman magnetic field and discuss the weak coupling phase diagram in the two-band regime. We then take a leap to the Mott insulator regime, which can be achieved from the electronic perspective by gapping out the overall charge mode using an eight-fermion Umklapp interaction. In Chapters 4.2–4.3, we discuss the theory and properties of the SBM under Zeeman field, and in Chapter 4.4 we consider possible instabilities and characterize the resulting phases. We conclude by discussing generalizations of these phases to 2D.

## 4.1 Electrons on a two-leg zigzag strip in a Zeeman field: Weak coupling approach

In this section, we consider half-filled electronic  $t_1 - t_2$  chain with extended repulsive interaction in the magnetic Zeeman field. The Hamiltonian is  $H = H_0 + H_Z + H_V$  with

$$H_0 = - \sum_{x,\alpha} [t_1 c_\alpha^\dagger(x) c_\alpha(x+1) + t_2 c_\alpha^\dagger(x) c_\alpha(x+2) + \text{H.c.}] , \quad (4.1)$$

$$H_Z = -h \sum_x S^z(x) , \quad (4.2)$$

$$H_V = \frac{1}{2} \sum_{x,x'} V(x-x') n(x) n(x') . \quad (4.3)$$

Here  $c_\alpha(x)$  is a fermion annihilation operator,  $x$  is a site label on the one-dimensional (1D) chain, and  $\alpha = \uparrow, \downarrow$  is a spin index;  $n(x) \equiv c_\uparrow^\dagger(x) c_\uparrow(x) + c_\downarrow^\dagger(x) c_\downarrow(x)$  is electron number on the site. Throughout, electrons are at half-filling. The Zeeman field couples to electron spin  $S^z(x) \equiv \frac{1}{2} [c_\uparrow^\dagger(x) c_\uparrow(x) - c_\downarrow^\dagger(x) c_\downarrow(x)]$ .

In the weak coupling approach, we assume  $H_V \ll H_0, H_Z$  and start with the non-interacting band structure given by  $H_0 + H_Z$  and illustrated in Fig. 4.1. In this chapter, we focus on the regime  $t_2/t_1 > 0.5$  and not too large Zeeman field so that there are two occu-

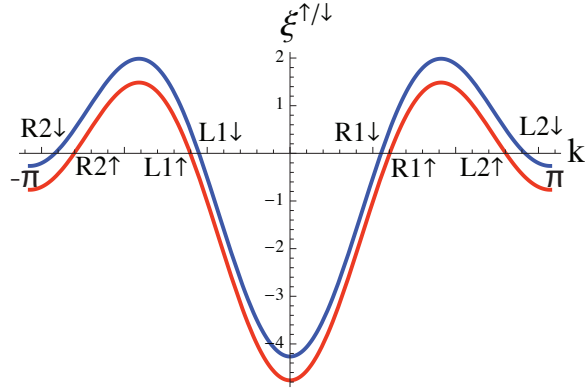


Figure 4.1: Single-particle spectrum in the presence of the Zeeman field,  $\xi^{\uparrow/\downarrow}(k) = -2t_1 \cos(k) - 2t_2 \cos(2k) \mp \frac{\hbar}{2} - \mu$ , shown for parameters  $t_2/t_1 = 1$  and  $\hbar/t_1 = 1/2$ . Our  $k_F$ -s denote right-moving momenta  $\in (-\pi, \pi)$ ; with this convention, the half-filling condition reads  $k_{F1\uparrow} + k_{F1\downarrow} + k_{F2\uparrow} + k_{F2\downarrow} = -\pi$ .

pied Fermi segments (“bands”) for each spin species. The corresponding phase boundary in the  $t_2/t_1 - \hbar/t_1$  plane is shown in Fig. 4.2. For fields exceeding some critical values, the second spin- $\downarrow$  Fermi segment gets completely depopulated; this regime leads to a different theory and is not considered here.

The spectrum is linearized near the Fermi points and the electron operators are expanded in terms of continuum fields,

$$c_\alpha(x) = \sum_{P,a} e^{iPk_{Fa\alpha}x} c_{Pa\alpha}, \quad (4.4)$$

with  $P = R/L = +/-$  denoting the right/left movers and  $a = 1, 2$  denoting the two Fermi seas for each spin species, see Fig. 4.1. There are four different Fermi velocities  $v_{a\alpha}$ .

Using symmetry arguments, we can write down the most general form of the four-

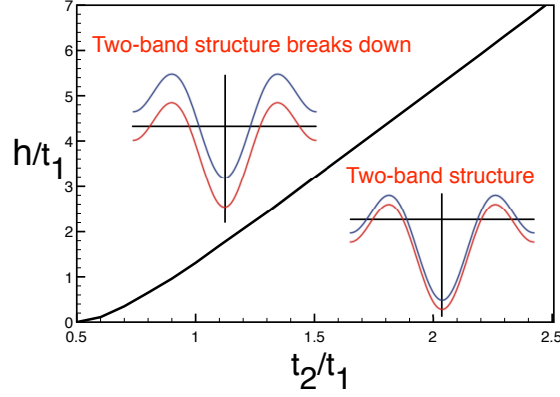


Figure 4.2: Free electron phase diagram in the  $t_2/t_1$ - $h/t_1$  plane. In this chapter, we focus solely on the lower region where both spin species have two Fermi seas (“bands”). For reference, we give the magnetization  $M^z \equiv (n_\uparrow - n_\downarrow)/(n_\uparrow + n_\downarrow)$  at the transition for several band parameters:  $M_{\text{crit}}^z = 0.32, 0.46, 0.54$  for  $t_2/t_1 = 1.0, 1.5, 2.0$ .

fermion interactions which mix the right- and left-moving fields:

$$H_{\text{int}} = H_\uparrow + H_\downarrow + H_{\uparrow\downarrow}, \quad (4.5)$$

$$H_\alpha = \lambda_{11}^\alpha \rho_{R1\alpha} \rho_{L1\alpha} + \lambda_{22}^\alpha \rho_{R2\alpha} \rho_{L2\alpha} \quad (4.6)$$

$$+ \lambda_{12}^\alpha (\rho_{R1\alpha} \rho_{L2\alpha} + \rho_{L1\alpha} \rho_{R2\alpha}) \quad (4.7)$$

$$+ w_{12}^\alpha (c_{R1\alpha}^\dagger c_{L1\alpha}^\dagger c_{L2\alpha} c_{R2\alpha} + \text{H.c.}), \quad (4.8)$$

$$H_{\uparrow\downarrow} = \sum_{a,b} \lambda_{ab}^{\uparrow\downarrow} (\rho_{Ra\uparrow} \rho_{Lb\downarrow} + \rho_{La\uparrow} \rho_{Rb\downarrow}). \quad (4.9)$$

(Interactions that do not mix right and left movers only shift velocities and do not affect the weak coupling treatment.)

The weak coupling renormalization group (RG) equations are [92, 93, 94, 76]

$$\dot{\lambda}_{11}^\alpha = -\frac{(w_{12}^\alpha)^2}{2\pi v_{2\alpha}}, \quad (4.10)$$

$$\dot{\lambda}_{22}^\alpha = -\frac{(w_{12}^\alpha)^2}{2\pi v_{1\alpha}}, \quad (4.11)$$

$$\dot{\lambda}_{12}^\alpha = \frac{(w_{12}^\alpha)^2}{\pi(v_{1\alpha} + v_{2\alpha})}, \quad (4.12)$$

$$\dot{w}_{12}^\alpha = -\left[ \frac{\lambda_{11}^\alpha}{v_{1\alpha}} + \frac{\lambda_{22}^\alpha}{v_{2\alpha}} - \frac{4\lambda_{12}^\alpha}{v_{1\alpha} + v_{2\alpha}} \right] \frac{w_{12}^\alpha}{2\pi}, \quad (4.13)$$

$$\dot{\lambda}_{ab}^{\uparrow\downarrow} = 0. \quad (4.14)$$

Here  $\dot{O} \equiv dO/d\ell$ , where  $\ell$  is logarithm of the length scale;  $\alpha = \uparrow, \downarrow$ ; and  $a, b \in \{1, 2\}$ . We see that the terms  $\lambda_{ab}^{\uparrow\downarrow}$  do not flow and the two spin species behave independently from each other in the weak coupling regime.

We therefore focus on one species at a time. Effectively, this is equivalent to a two-band model of spinless fermions in one dimensions [92, 93, 94, 76] in the absence of any Umklapps. The RG Eqs. (4.10)–(4.13) have the Kosterlitz-Thouless form and can be solved exactly. We define

$$y^\alpha \equiv \frac{\lambda_{11}^\alpha}{2\pi v_{1\alpha}} + \frac{\lambda_{22}^\alpha}{2\pi v_{2\alpha}} - \frac{2\lambda_{12}^\alpha}{\pi(v_{1\alpha} + v_{2\alpha})}. \quad (4.15)$$

Eqs. (4.10)–(4.13) simplify,

$$\dot{y}^\alpha = -\frac{(v_{1\alpha} + v_{2\alpha})^2 + 4v_{1\alpha}v_{2\alpha}}{2\pi^2 v_{1\alpha}v_{2\alpha}(v_{1\alpha} + v_{2\alpha})^2} (w_{12}^\alpha)^2, \quad (4.16)$$

$$\dot{w}_{12}^\alpha = -y^\alpha w_{12}^\alpha. \quad (4.17)$$

The  $w_{12}^\alpha$  renormalizes to zero if the bare couplings satisfy

$$y^\alpha(\ell = 0) \geq \sqrt{\frac{(v_{1\alpha} + v_{2\alpha})^2 + 4v_{1\alpha}v_{2\alpha}}{2\pi^2 v_{1\alpha}v_{2\alpha}(v_{1\alpha} + v_{2\alpha})^2}} |w_{12}^\alpha(\ell = 0)|. \quad (4.18)$$

In this case, the two-band state of species  $\alpha$  is stable and gives two gapless modes.

On the other hand, if the condition Eq. (4.18) is not satisfied, then  $w_{12}^\alpha$  runs to strong coupling. In this case, only one gapless mode remains. To analyze this, we bosonize

$$c_{Pa\alpha} \sim \eta_{a\alpha} e^{i(\varphi_{a\alpha} + P\theta_{a\alpha})}, \quad (4.19)$$

with canonically conjugate boson fields:

$$[\varphi_{a\alpha}(x), \varphi_{b\beta}(x')] = [\theta_{a\alpha}(x), \theta_{b\beta}(x')] = 0, \quad (4.20)$$

$$[\varphi_{a\alpha}(x), \theta_{b\beta}(x')] = i\pi\delta_{ab}\delta_{\alpha\beta}\Theta(x - x'), \quad (4.21)$$

where  $\Theta(x)$  is the heaviside step function. Here we use Majorana fermions ( $\{\eta_{a\alpha}, \eta_{b\beta}\} =$

$2\delta_{ab}\delta_{\alpha\beta}$ ) as Klein factors, which assure that the fermion fields with different flavors anti-commute with one another.

For convenience, we introduce

$$\theta_{\alpha}^{\pm} \equiv \frac{\theta_{1\alpha} \pm \theta_{2\alpha}}{\sqrt{2}}, \quad \alpha = \uparrow \text{ or } \downarrow, \quad (4.22)$$

$$\theta_{\rho+} \equiv \frac{\theta_{\uparrow}^+ + \theta_{\downarrow}^+}{\sqrt{2}} = \frac{\theta_{1\uparrow} + \theta_{2\uparrow} + \theta_{1\downarrow} + \theta_{2\downarrow}}{2}, \quad (4.23)$$

$$\theta_{\sigma+} \equiv \frac{\theta_{\uparrow}^+ - \theta_{\downarrow}^+}{\sqrt{2}} = \frac{\theta_{1\uparrow} + \theta_{2\uparrow} - \theta_{1\downarrow} - \theta_{2\downarrow}}{2}, \quad (4.24)$$

and similarly for  $\varphi$  variables. The  $w_{12}^{\alpha}$  term becomes

$$w_{12}^{\alpha}(c_{R1\alpha}^{\dagger}c_{L1\alpha}^{\dagger}c_{L2\alpha}c_{R2\alpha} + \text{H.c.}) \sim w_{12}^{\alpha} \cos(2\sqrt{2}\varphi_{\alpha}^{-}). \quad (4.25)$$

When  $w_{12}^{\alpha}$  is relevant and flows to large values, it pins the difference field  $\varphi_{\alpha}^{-}$ , while the overall field  $\varphi_{\alpha}^{+}$  remains gapless (as it should, since the  $\alpha$ -electrons have an incommensurate conserved density and there are no four-fermion Umklapps). In this phase, the  $\alpha$ -electron operator becomes gapped. Pair- $\alpha$ -electron operator is gapless, and also specific particle-hole composites are gapless, with details depending on the sign of  $w_{12}^{\alpha}$ . We are primarily interested in repulsively interacting electrons and expect the particle-hole observables to be more prominent, although not dramatically since for too strong repulsion the conducting state of the  $\uparrow$  and  $\downarrow$  electrons is destroyed towards Mott insulator as described below. We do not provide more detailed characterization of the conducting phases of electrons here, as we are eventually interested in the Mott insulating regime where the  $\uparrow$  and  $\downarrow$  species become strongly coupled. (The two-band spinless electron system was considered, e.g., in [92, 93, 94, 76], and our analysis in Chapter 4.3 can be readily tailored to the electronic phases here.)

In the model with longer-ranged density–density repulsion, Eq. (4.3), the bare couplings

are

$$\lambda_{11}^\alpha = V_{Q=0} - V_{2k_{F1\alpha}}, \quad (4.26)$$

$$\lambda_{22}^\alpha = V_{Q=0} - V_{2k_{F2\alpha}}, \quad (4.27)$$

$$\lambda_{12}^\alpha = V_{Q=0} - V_{k_{F1\alpha} + k_{F2\alpha}}, \quad (4.28)$$

$$w_{12}^\alpha = V_{k_{F1\alpha} - k_{F2\alpha}} - V_{k_{F1\alpha} + k_{F2\alpha}}, \quad (4.29)$$

$$\lambda_{ab}^{\uparrow\downarrow} = V_{Q=0}. \quad (4.30)$$

Here  $V_Q \equiv \sum_{x'=-\infty}^{\infty} V(x-x')e^{iQ(x-x')} = V_{-Q}$ .

As an example, we consider the following potential:

$$V(x-x') = \begin{cases} U & , \quad |x-x'| = 0 \\ \kappa U e^{-\gamma|x-x'|} & , \quad |x-x'| \geq 1 \end{cases}. \quad (4.31)$$

This was used in [31] to provide stable realizations of the C2S2 metal and the SBM Mott insulator of electrons in zero field. Here  $U$  is the overall energy scale and also the on-site repulsion; dimensionless parameter  $\kappa$  controls the relative strength of further-neighbor interactions; and  $\gamma$  defines the decay rate. Applying the stability condition, Eq. (4.18), we can now determine the phase diagram in the weak coupling approach in the regime where the kinetic energy gives four modes.

Figure 4.3 provides an illustration for  $\gamma = 0.3$  and  $\kappa = 0.5$ . The  $w_{12}^\uparrow$  interaction is relevant in the region with hash lines at roughly 45 degrees and the  $w_{12}^\downarrow$  is relevant in the region with hash lines at 135 degrees with respect to the horizontal axis. There are four distinct phases. First, when both  $w_{12}^\uparrow$  and  $w_{12}^\downarrow$  are irrelevant, we have a phase with four gapless modes, which is connected to the C2S2 phase at  $h = 0$ . (Note, however, that we assumed  $H_Z \gg H_V$ , so the formal  $h \rightarrow 0$  limit here is different from the weak coupling analysis at  $h = 0$  in [65, 31].)

Next, when  $w_{12}^\uparrow$  is relevant while  $w_{12}^\downarrow$  is irrelevant, we have a phase with three gapless modes: one associated with the  $\uparrow$ -electrons and two associated with the  $\downarrow$ -electrons. In this phase, inserting a single  $\uparrow$ -electron costs a finite gap while inserting a pair of  $\uparrow$ -electrons

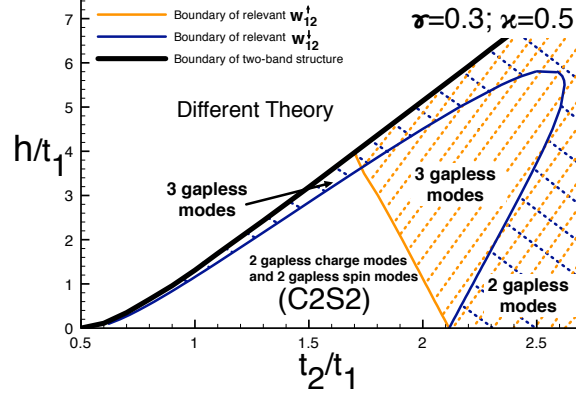


Figure 4.3: An example of the weak-coupling phase diagram in the electron system under the Zeeman field, using model interactions Eq. (4.31) with  $\kappa = 0.5$  and  $\gamma = 0.3$ . We focus on the region where the kinetic energy gives four modes (see Figs. 4.1, 4.2) and find four phases: metallic phase with four gapless modes evolving out of the C2S2 phase in zero field; phase with three gapless modes where only the  $w_{12}^{\uparrow}$ -term is relevant and flows to strong coupling; phase with three gapless modes where only the  $w_{12}^{\downarrow}$ -term is relevant; and phase with two gapless modes where both the  $w_{12}^{\uparrow}$  and  $w_{12}^{\downarrow}$  are relevant. The  $w_{12}^{\uparrow}$ -term is relevant in the region with hash lines at roughly 45 degrees and the  $w_{12}^{\downarrow}$ -term is relevant in the region with hash lines at 135 degrees with respect to the horizontal axis. Note that the  $w_{12}^{\downarrow}$ -term always becomes relevant upon approaching the boundary of the two-band structure [76].

or a particle-hole combination of  $\uparrow$ -electrons is gapless. The  $\downarrow$  electrons are completely gapless.

When  $w_{12}^{\downarrow}$  is relevant while  $w_{12}^{\uparrow}$  is irrelevant, we have another phase with three gapless modes, which is similar to the preceding paragraph but with  $\uparrow$  and  $\downarrow$  interchanged. As can be seen in Fig. 4.3,  $w_{12}^{\downarrow}$  is always relevant when  $h$  approaches the critical value, [76] and the instability arises because the  $v_{2\downarrow}$  approaches zero.

Finally, for large  $t_2/t_1$ , both  $w_{12}^{\uparrow}$  and  $w_{12}^{\downarrow}$  are relevant and we have a phase with only two gapless modes: one associated with spin- $\uparrow$  and the other with spin- $\downarrow$  species. In this case, inserting a single electron of either spin is gapped, while inserting a pair or a particle-hole combination of same-spin electrons is gapless.

## 4.2 Transition to Mott insulator: SBM phase

Note that all phases accessed from the weak coupling analysis are conducting along the zigzag chain. Mott insulating states do not appear since there is no four-fermion Umklapp. The half-filled system does become insulating for sufficiently strong repulsion. This can be achieved by including a valid eight-fermion Umklapp, which is irrelevant at weak coupling but can become relevant at intermediate to strong coupling [29, 31]:

$$\begin{aligned} H_8 &= v_8 (c_{R1\uparrow}^\dagger c_{R1\downarrow}^\dagger c_{R2\uparrow}^\dagger c_{R2\downarrow}^\dagger c_{L1\uparrow} c_{L1\downarrow} c_{L2\uparrow} c_{L2\downarrow} + \text{H.c.}) \\ &\sim 2v_8 \cos(4\theta_{\rho+}), \end{aligned} \quad (4.32)$$

where  $\theta_{\rho+}$  is defined in Eq. (4.23) and describes slowly varying electron density,  $\rho_e(x) = 2\partial_x\theta_{\rho+}/\pi$ . The density–density repulsion gives coarse-grained interaction  $H_{\text{int}} \sim V_{Q=0}(\partial_x\theta_{\rho+})^2$ . This will stiffen the  $\theta_{\rho+}$  field and will reduce the scaling dimension of the Umklapp term. For sufficiently strong repulsion the Umklapp becomes relevant and will grow at long scales, pinning the  $\theta_{\rho+}$  and driving a metal-insulator transition. As discussed in [29, 31], we expect that Mott insulator corresponding to a spin model with spins residing on sites is described by  $v_8 > 0$  and the pinning condition

$$4\theta_{\rho+}^{(0)} = \pi \pmod{2\pi}. \quad (4.33)$$

Such gapping out of the overall charge mode can occur out of any of the four conducting phases discussed in Fig. 4.3. When this happens out of the four-mode metal, we obtain spin liquid Mott insulator with three gapless modes—the spin Bose-metal. In principle, one could perform an intermediate coupling analysis similar to that in [31] to estimate the strength of the repulsion needed to drive the metal-insulator transition, but we will not try this here. Below we discuss qualitatively the stability and physical observables in the SBM phase under the Zeeman field. We will then consider instabilities of the SBM similar to the  $w_{12}^\alpha$ -driven transitions out of the four-mode metal above, but now with the  $\uparrow$  and  $\downarrow$  systems strongly coupled to form the Mott insulator.

Reference [29] also presented another route to describe the SBM in a spin-only model

by using bosonization to analyze slave particle gauge theory. The formalism is similar to the electron model analysis, but with electron operators  $c_\alpha(x)$  replaced with spinon operators  $f_\alpha(x)$  and the gauge theory constraint realized via an explicit mass term for  $\theta_{\rho+}$ ,

$$\mathcal{L}_{\text{gauge theory}} = m \left( \theta_{\rho+} - \theta_{\rho+}^{(0)} \right)^2. \quad (4.34)$$

Loosely speaking, spinons are electrons that shed their overall charge once the Umklapp term  $H_8$  became relevant [29]. Note, however, that in the spin-only model, there are no free spinons, unlike the situation in the electronic model where we have electron excitations above the charge gap.

From now on, we will use the spinon-gauge language. To get some quantitative example, we consider the case where spinons do not have any interactions other than Eq. (4.34), i.e., all residual interactions like Eq. (4.5) are set to zero. Once the  $\theta_{\rho+}$  field is pinned and after integrating out the  $\varphi_{\rho+}$ , we obtain an effective action for the remaining fields  $(\theta_{\sigma+}, \theta_{\uparrow}^-, \theta_{\downarrow}^-) \equiv \Theta^T$  and  $(\varphi_{\sigma+}, \varphi_{\uparrow}^-, \varphi_{\downarrow}^-) \equiv \Phi^T$  defined in Eqs. (4.22)–(4.24):

$$\mathcal{L}_{\text{eff}} = \frac{1}{2\pi} \left[ \partial_x \Theta^T \cdot \mathbf{A} \cdot \partial_x \Theta + \partial_x \Phi^T \cdot \mathbf{B} \cdot \partial_x \Phi \right] \quad (4.35)$$

$$+ \frac{i}{\pi} \partial_x \Theta^T \cdot \partial_\tau \Phi. \quad (4.36)$$

Matrix elements of  $\mathbf{A}$  and  $\mathbf{B}$  are,

$$\mathbf{A} = \begin{pmatrix} \bar{v} & \frac{v_{\uparrow}^-}{\sqrt{2}} & -\frac{v_{\downarrow}^-}{\sqrt{2}} \\ \frac{v_{\uparrow}^-}{\sqrt{2}} & v_{\uparrow}^+ & 0 \\ -\frac{v_{\downarrow}^-}{\sqrt{2}} & 0 & v_{\downarrow}^+ \end{pmatrix},$$

$$\mathbf{B} = \begin{pmatrix} \frac{v_{\uparrow}^+ v_{\downarrow}^+}{\bar{v}} & \frac{v_{\downarrow}^+ v_{\uparrow}^-}{\sqrt{2}\bar{v}} & -\frac{v_{\uparrow}^+ v_{\downarrow}^-}{\sqrt{2}\bar{v}} \\ \frac{v_{\downarrow}^+ v_{\uparrow}^-}{\sqrt{2}\bar{v}} & \frac{(v_{\uparrow}^+)^2 - (v_{\uparrow}^-)^2 + v_{\uparrow}^+ v_{\downarrow}^+}{2\bar{v}} & -\frac{v_{\uparrow}^- v_{\downarrow}^-}{2\bar{v}} \\ -\frac{v_{\uparrow}^+ v_{\downarrow}^-}{\sqrt{2}\bar{v}} & -\frac{v_{\uparrow}^- v_{\downarrow}^-}{2\bar{v}} & \frac{(v_{\downarrow}^+)^2 - (v_{\downarrow}^-)^2 + v_{\uparrow}^+ v_{\downarrow}^+}{2\bar{v}} \end{pmatrix},$$

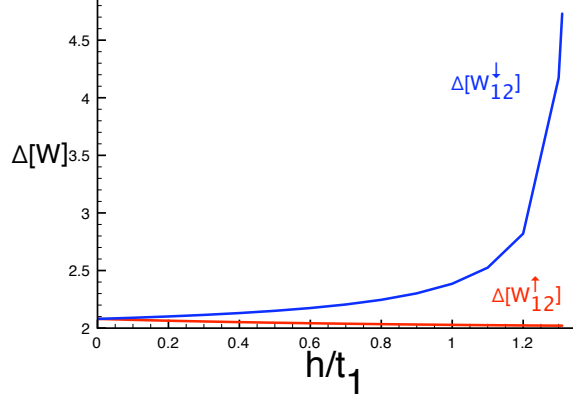


Figure 4.4: Scaling dimensions  $\Delta[w_{12}^\uparrow]$  and  $\Delta[w_{12}^\downarrow]$  as a function of  $h/t_1$  for fixed  $t_2/t_1 = 1$ , calculated in the absence of residual spinon interactions. In this case, the scaling dimensions stay greater than 2 and the SBM phase remains stable under the Zeeman field.

where

$$v_\alpha^\pm \equiv \frac{v_{1\alpha} \pm v_{2\alpha}}{2}, \quad \alpha = \uparrow, \downarrow; \quad (4.37)$$

$$\bar{v} \equiv \frac{v_\uparrow^+ + v_\downarrow^+}{2} = \frac{v_{1\uparrow} + v_{2\uparrow} + v_{1\downarrow} + v_{2\downarrow}}{4}. \quad (4.38)$$

Having all the matrix elements, we can numerically calculate the scaling dimensions of the  $w_{12}^\alpha$ -terms in Eq. (4.25).

As an illustration, Fig. 4.4 shows the results along a vertical cut at  $t_2/t_1 = 1$  from Fig. 4.3 (assumed driven into the Mott insulator as described above). We see that in the absence of the residual interactions the SBM remains stable under the Zeeman field. We also note that the scaling dimensions of the  $w_{12}^\uparrow$  and  $w_{12}^\downarrow$  have opposite trends, which implies that the overall stability is reduced. Since the scaling dimension of the  $w_{12}^\uparrow$  interaction decreases with increasing field, it is likely that this will be the first instability channel upon including the residual interactions. This finding is similar to the weak coupling analysis where the  $\uparrow$ -system tends to become unstable first. We want to emphasize, however, that neglecting the residual spinon interactions is likely a poor approximation for any realistic spin model, and any calculations in this scheme should be taken with caution. The only precise statement here is that the SBM can in principle remain stable under the Zeeman field.

In Chapter 4.4 we discuss phases proximate to the SBM. Motivated by the above observations, we will consider first the case where only the  $w_{12}^\dagger$  term becomes relevant; we will also consider the situation where both  $w_{12}^\dagger$  and  $w_{12}$  are relevant. Before this, we need to describe main physical observables in the SBM under the Zeeman field, which we will then use to analyze the instabilities and the properties of the resulting phases.

### 4.3 Observables in the SBM in Zeeman field

In the presence of the Zeeman field, the system has  $S_{\text{tot}}^z$  spin conservation symmetry and complex conjugation symmetry ( $\mathcal{C} : i \rightarrow -i$ ) in the  $S^z$  basis. The system also has lattice translation and inversion ( $I : x \rightarrow -x$ ) symmetries. The internal symmetries are sufficiently reduced compared with the  $SU(2)$ -invariant case of [29] that we need to revisit the physical observables in the SBM.

We first consider  $S^z$ -conserving bilinears, which we will also call “spin-0” objects,

$$\epsilon_{2k_{Fa\alpha}} \equiv f_{La\alpha}^\dagger f_{Ra\alpha} , \quad (4.39)$$

$$\epsilon_{k_{F1\alpha} + k_{F2\alpha}} \equiv \frac{1}{2} \left( f_{L1\alpha}^\dagger f_{R2\alpha} + f_{L2\alpha}^\dagger f_{R1\alpha} \right) , \quad (4.40)$$

$$\chi_{k_{F1\alpha} + k_{F2\alpha}} \equiv \frac{1}{2} \left( f_{L1\alpha}^\dagger f_{R2\alpha} - f_{L2\alpha}^\dagger f_{R1\alpha} \right) , \quad (4.41)$$

$$\epsilon_{k_{F1\alpha} - k_{F2\alpha}} \equiv \frac{1}{2} \left( f_{L1\alpha}^\dagger f_{L2\alpha} + f_{R2\alpha}^\dagger f_{R1\alpha} \right) , \quad (4.42)$$

$$\chi_{k_{F1\alpha} - k_{F2\alpha}} \equiv \frac{1}{2} \left( f_{L1\alpha}^\dagger f_{L2\alpha} - f_{R2\alpha}^\dagger f_{R1\alpha} \right) , \quad (4.43)$$

(no summation over  $a$  or  $\alpha$ ). We define  $\epsilon_{-Q} = \epsilon_Q^\dagger$  and  $\chi_{-Q} = \chi_Q^\dagger$  so that  $\epsilon(x)$  and  $\chi(x)$  are Hermitian operators.

The  $\epsilon$  bilinears appear, e.g., when expressing spinon hopping energies, while the  $\chi$  bilinears appear in currents. Specifically, consider a bond  $[x, x+n]$ ,

$$\mathcal{B}^{(n)}(x) \sim f_\alpha^\dagger(x) f_\alpha(x+n) + \text{H.c.} , \quad (4.44)$$

$$\mathcal{J}^{(n)}(x) \sim i [f_\alpha^\dagger(x) f_\alpha(x+n) - \text{H.c.}] , \quad (4.45)$$

where  $\alpha = \uparrow$  or  $\downarrow$  species can come with independent amplitudes. Expansion in terms of the continuum fields gives, up to real factors,

$$\mathcal{B}_Q^{(n)} \sim e^{inQ/2} \epsilon_Q, \quad (4.46)$$

$$\mathcal{J}_Q^{(n)} \sim e^{inQ/2} \chi_Q. \quad (4.47)$$

Note that we can view  $\epsilon(x)$  as a site-centered energy operator, e.g.,  $\epsilon(x) \sim \mathcal{B}^{(1)}(x-1) + \mathcal{B}^{(1)}(x) \sim \mathcal{B}^{(2)}(x-1)$ , in the sense of having the same symmetry properties. We can also view  $\epsilon(x) \sim S^z(x)$  in the same sense because of the presence of the Zeeman energy. [More generally, the symmetry properties of any operator are not changed upon multiplying by  $S^z(x)$ .] On the other hand, the bond operator  $\mathcal{B}^{(n)}(x)$  has the same symmetry properties as a bond energy such as  $\vec{S}(x) \cdot \vec{S}(x+n)$  and can be used to characterize VBS correlations in the spin system.

Similarly, we can view  $\chi(x)$  as a site-centered current,  $\chi(x) \sim \mathcal{J}^{(1)}(x-1) + \mathcal{J}^{(1)}(x) \sim \mathcal{J}^{(2)}(x-1)$ , and also as a scalar chirality,  $\chi(x) \sim \vec{S}(x-1) \cdot \vec{S}(x) \times \vec{S}(x+1)$ , while  $\mathcal{J}^{(n)}(x)$  has the same symmetry properties as a spin current,  $\mathcal{J}^{(n)}(x) \sim i[S^+(x)S^-(x+n) - \text{H.c.}]$ .

Symmetry analysis shows that  $\epsilon_Q$  transforms to  $\epsilon_{-Q}$  under either lattice inversion  $I$  or complex conjugation  $\mathcal{C}$ , while  $\chi_Q$  transforms to  $-\chi_{-Q}$  under either  $I$  or  $\mathcal{C}$ . We can then give an independent argument for the relations Eqs. (4.46) and (4.47) for  $Q \neq 0, \pi$ , and can show generally that, up to complex phase factors, such  $\epsilon_Q$  and  $\chi_Q$  cover all independent spin-0 observables for the system in the Zeeman field.

Special care is needed for  $Q = \pi$ . In this case, Eqs. (4.46) and (4.47) hold only for  $n = \text{even}$ . On the other hand,  $\mathcal{B}_\pi^{(n=\text{odd})}$  is odd under inversion  $I$  and even under complex conjugation  $\mathcal{C}$ , while  $\mathcal{J}_\pi^{(n=\text{odd})}$  is even under  $I$  and odd under  $\mathcal{C}$ . In particular, the nearest-neighbor bond  $\mathcal{B}_\pi^{(1)}$  and  $\mathcal{J}_\pi^{(1)}$  are independent observables from  $\epsilon_\pi \sim \mathcal{B}_\pi^{(2)}$  and  $\chi_\pi \sim \mathcal{J}_\pi^{(2)}$ . In the present SBM problem, such  $Q = \pi$  observables do not appear as bilinears but appear as four-fermion terms below.

The bosonized expressions for the spin-0 bilinears are:

$$\epsilon_{2k_{F a \alpha}} = i e^{i(\theta_{\rho+} + \alpha \theta_{\sigma+} + a \sqrt{2} \theta_{\alpha}^-)}, \quad (4.48)$$

$$\epsilon_{k_{F1\alpha} + k_{F2\alpha}} = -i \eta_{1\alpha} \eta_{2\alpha} e^{i(\theta_{\rho+} + \alpha \theta_{\sigma+})} \sin(\sqrt{2} \varphi_{\alpha}^-), \quad (4.49)$$

$$\chi_{k_{F1\alpha} + k_{F2\alpha}} = \eta_{1\alpha} \eta_{2\alpha} e^{i(\theta_{\rho+} + \alpha \theta_{\sigma+})} \cos(\sqrt{2} \varphi_{\alpha}^-), \quad (4.50)$$

$$\epsilon_{k_{F1\alpha} - k_{F2\alpha}} = -i \eta_{1\alpha} \eta_{2\alpha} e^{i\sqrt{2} \theta_{\alpha}^-} \sin(\sqrt{2} \varphi_{\alpha}^-), \quad (4.51)$$

$$\chi_{k_{F1\alpha} - k_{F2\alpha}} = \eta_{1\alpha} \eta_{2\alpha} e^{i\sqrt{2} \theta_{\alpha}^-} \cos(\sqrt{2} \varphi_{\alpha}^-), \quad (4.52)$$

where we used definitions Eqs. (4.22)–(4.24) and  $\alpha = +/−$  for spin  $\uparrow$  or  $\downarrow$  and  $a = +/−$  for band 1 or 2.

To bring out the wavevector  $Q = \pi$  that will play an important role in the analysis of phases near the SBM, we need to consider four-fermion terms. We find,

$$\mathcal{B}_{\pi}^{(1)} : i(\epsilon_{k_{F1\uparrow} + k_{F2\uparrow}} \epsilon_{k_{F1\downarrow} + k_{F2\downarrow}} - \text{H.c.}) \sim \quad (4.53)$$

$$\sim \hat{\Gamma} \sin(\sqrt{2} \varphi_{\uparrow}^-) \sin(\sqrt{2} \varphi_{\downarrow}^-) \sin(2\theta_{\rho+}); \quad (4.54)$$

$$i(\chi_{k_{F1\uparrow} + k_{F2\uparrow}} \chi_{k_{F1\downarrow} + k_{F2\downarrow}} - \text{H.c.}) \sim \quad (4.55)$$

$$\sim \hat{\Gamma} \cos(\sqrt{2} \varphi_{\uparrow}^-) \cos(\sqrt{2} \varphi_{\downarrow}^-) \sin(2\theta_{\rho+}); \quad (4.56)$$

and also

$$\chi_{\pi} : \epsilon_{k_{F1\uparrow} + k_{F2\uparrow}} \chi_{k_{F1\downarrow} + k_{F2\downarrow}} + \text{H.c.} \sim \quad (4.57)$$

$$\sim \hat{\Gamma} \sin(\sqrt{2} \varphi_{\uparrow}^-) \cos(\sqrt{2} \varphi_{\downarrow}^-) \sin(2\theta_{\rho+}); \quad (4.58)$$

$$\chi_{k_{F1\uparrow} + k_{F2\uparrow}} \epsilon_{k_{F1\downarrow} + k_{F2\downarrow}} + \text{H.c.} \sim \quad (4.59)$$

$$\sim \hat{\Gamma} \cos(\sqrt{2} \varphi_{\uparrow}^-) \sin(\sqrt{2} \varphi_{\downarrow}^-) \sin(2\theta_{\rho+}). \quad (4.60)$$

Here  $\hat{\Gamma} \equiv \eta_{1\uparrow} \eta_{1\downarrow} \eta_{2\uparrow} \eta_{2\downarrow}$ . Note that we have only listed observables containing  $\sin(2\theta_{\rho+})$ . The other independent spin-0 objects  $\epsilon_{\pi}$  and  $\mathcal{J}_{\pi}^{(1)}$  contain  $\cos(2\theta_{\rho+})$  and vanish because of the pinning condition Eq. (4.33).

Having discussed  $S^z$ -conserving observables, we can similarly consider  $S^z$ -raising ob-

servables. We will call objects corresponding to  $\delta S^z = 1$  or  $2$  as “spin-1” or “spin-2”, respectively. We have spin-1 bilinears,

$$S_{-Pk_{Fa\uparrow}+P'k_{Fb\downarrow}}^+ \equiv f_{Pa\uparrow}^\dagger f_{P'b\downarrow}. \quad (4.61)$$

Generically, these all carry different momenta. We can readily write bosonized expressions. For reference, we give the main ones that contain oppositely moving fields:

$$S_{k_{Fa\uparrow}+k_{Fb\downarrow}}^+ = \eta_{a\uparrow}\eta_{b\downarrow} e^{-i[\varphi_{\sigma+} + \frac{1}{\sqrt{2}}(a\varphi_{\uparrow}^- - b\varphi_{\downarrow}^-)]} \times e^{i[\theta_{\rho+} + \frac{1}{\sqrt{2}}(a\theta_{\uparrow}^- + b\theta_{\downarrow}^-)]}, \quad (4.62)$$

where we used convention  $a, b = +/-$  for band 1 or 2. We can generally argue that at  $Q \neq 0, \pi$ , objects  $S_Q^+$  that transform like Fourier modes of the  $S^+(x)$  operator cover, up to complex phases, all distinct spin-1 observables. In the present SBM system, we do not find any interesting spin-1 observables at  $Q = 0, \pi$ .

Since we will encounter phases where  $S^+$  is gapped, we also need to consider  $\delta S^z = 2$  observables, i.e., some kind of “magnon pair” creation operators. Because of the hard spin condition, we define them on bonds  $[x, x + n]$ ,

$$\mathcal{P}^{+, (n)}(x) \equiv S^+(x)S^+(x + n) \quad (4.63)$$

$$\sim f_{\uparrow}^\dagger(x)f_{\uparrow}^\dagger(x + n)f_{\downarrow}(x + n)f_{\downarrow}(x). \quad (4.64)$$

The last line can be expanded in terms of the continuum fields and organized as follows. For  $\alpha$ -species, a “pair” operator  $f_{\alpha}^\dagger(x)f_{\alpha}^\dagger(x + n)$  contains zero momentum contributions  $f_{Ra\alpha}^\dagger f_{La\alpha}^\dagger$ ,  $a = 1$  or  $2$ ;  $\pm(k_{F1\alpha} + k_{F2\alpha})$  momentum contributions  $f_{P1\alpha}^\dagger f_{P2\alpha}^\dagger$ ,  $P = L/R$ ; and  $\pm(k_{F1\alpha} - k_{F2\alpha})$  contributions  $f_{P1\alpha}^\dagger f_{-P2\alpha}^\dagger$ . Multiplying the pair creation operator for  $\uparrow$  species and pair destruction operator for  $\downarrow$  species, we obtain contributions to  $\mathcal{P}^+$  carrying combinations of the above momenta.

We can argue on general symmetry grounds that, up to complex phases, there is a single independent spin-2 object at  $Q \neq 0, \pi$ . On the other hand, at  $Q = \pi$  there are two

independent objects that transform differently under lattice inversion; they can be realized by  $\mathcal{P}_\pi^{+,(n=\text{even})}$  and  $\mathcal{P}_\pi^{+,(n=\text{odd})}$  respectively. At  $Q = 0$ , we consider only objects  $\mathcal{P}_{Q=0}^{+,(n)}$  which have the same symmetry properties for any  $n$ .

In the present SBM problem, the main spin-2 observables occur precisely at  $Q = 0, \pi$ , and we give bosonized expressions only for these. For  $Q = 0$ , there are four possible terms:

$$\mathcal{P}_{Q=0}^{+,(n)} : f_{Ra\uparrow}^\dagger f_{La\uparrow}^\dagger f_{Lb\downarrow} f_{Rb\downarrow} \sim e^{-i[2\varphi_{\sigma+} + \sqrt{2}(a\varphi_\uparrow^- - b\varphi_\downarrow^-)]} \quad (4.65)$$

with independent  $a, b = +/−$  corresponding to bands 1 or 2. For  $Q = \pi$  we find

$$\begin{aligned} \mathcal{P}_{Q=\pi}^{+,(n)} &\sim f_{R1\uparrow}^\dagger f_{R2\uparrow}^\dagger f_{L2\downarrow} f_{L1\downarrow} e^{i\frac{\pi n}{2}} + f_{L1\uparrow}^\dagger f_{L2\uparrow}^\dagger f_{R2\downarrow} f_{R1\downarrow} e^{-i\frac{\pi n}{2}} \\ &\sim \hat{\Gamma} e^{-i2\varphi_{\sigma+}} \sin \left[ 2\theta_{\rho+} + \frac{\pi}{2}(n-1) \right]. \end{aligned} \quad (4.66)$$

Because of the pinning condition on the  $\theta_{\rho+}$ , only the  $\mathcal{P}_{Q=\pi}^{+,(n=\text{odd})}$  are nonzero, and we can use the nearest-neighbor magnon-pair operator  $\mathcal{P}^{+,(1)}$  as the main representative.

## 4.4 Nearby phases out of the SBM in the field

We now consider what happens when either  $w_{12}^\uparrow$  or  $w_{12}^\downarrow$  from Eq. (4.25) or both become relevant.

### 4.4.1 Phases when $w_{12}^\uparrow$ is relevant

Let us start with the case when the  $w_{12}^\uparrow$  term is relevant while  $w_{12}^\downarrow$  is irrelevant. The field  $\varphi_\uparrow^-$  is pinned, while fields  $\varphi_\downarrow^-$  and  $\varphi_{\sigma+}$  remain gapless, so we have two gapless modes. There is no static order. We summarize characteristic power law observables in Table 4.1 and discuss them in turn.

First, all observables  $\epsilon_Q$  and  $\chi_Q$  in Eqs. (4.48)–(4.52) constructed out of the  $f_\downarrow$  fields show power law. On the other hand, such observables constructed out of the  $f_\uparrow$  fields that contain  $\theta_\uparrow^-$  become short-ranged once we pin the conjugate  $\varphi_\uparrow^-$ ; thus, only  $Q = k_{F1\uparrow} + k_{F2\uparrow}$

can remain power law. There are two cases depending on the sign of  $w_{12}^\uparrow$ :

$$w_{12}^\uparrow > 0 : \varphi_\uparrow^- = \frac{(2n+1)\pi}{2\sqrt{2}}, \quad n \in \mathbb{Z}, \quad (4.67)$$

$$\epsilon_{k_{F1\uparrow}+k_{F2\uparrow}} \sim e^{i\theta_{\sigma+}}, \quad \chi_{k_{F1\uparrow}+k_{F2\uparrow}} = 0; \quad (4.68)$$

$$w_{12}^\uparrow < 0 : \varphi_\uparrow^- = \frac{2n\pi}{2\sqrt{2}}, \quad n \in \mathbb{Z}, \quad (4.69)$$

$$\chi_{k_{F1\uparrow}+k_{F2\uparrow}} \sim e^{i\theta_{\sigma+}}, \quad \epsilon_{k_{F1\uparrow}+k_{F2\uparrow}} = 0. \quad (4.70)$$

Next, note that all spin-1 observables  $S_Q^+$  become short-ranged since they all contain the wildly fluctuating field  $\theta_\uparrow^-$ . Schematically, the individual  $f_\uparrow$  become gapped because of their ‘‘pairing’’. On the other hand, spin-2 observables contain pairs of  $f_\uparrow$  and can remain gapless. Explicitly, after pinning the  $\varphi_\uparrow^-$ , we have for the dominant correlations at  $Q = 0$  and  $\pi$

$$\mathcal{P}_{Q=0}^+ \sim e^{-i2\varphi_{\sigma+}} e^{\pm i\sqrt{2}\varphi_\downarrow^-}, \quad (4.71)$$

$$\mathcal{P}_{Q=\pi}^{+,(1)} \sim e^{-i2\varphi_{\sigma+}}. \quad (4.72)$$

The gaplessness of the  $\varphi_{\sigma+}$  is required since  $S_{\text{tot}}^z$  is conserved and incommensurate with the lattice. We can map the spin system to hard-core bosons, [88] and in the present case single boson excitations are gapped, while pair boson excitations are gapless and created by  $e^{i2\varphi_{\sigma+}} \dots$ . In the ‘‘particle-hole’’ sector, we have strong ‘‘density’’ or ‘‘current’’ correlations, Eq. (4.68) or (4.70), at wavelengths that can be related to typical separations between boson pairs, and such  $e^{i\theta_{\sigma+}}$  contribution is generally expected in a Luttinger liquid of pairs. Thus, the resulting state has spin-nematic power law correlations as well as density or current power law correlations. Which one is dominant depends on the scaling dimensions of  $e^{i2\varphi_{\sigma+}}$  versus  $e^{i\theta_{\sigma+}}$ . The scaling dimensions would need to be calculated numerically since the  $\varphi_{\sigma+}$  and  $\varphi_\downarrow^-$  mix in general; we do not attempt such quantitative estimates here.

Having discussed observables controlled by the gapless  $\sigma+$  part, let us finally mention that  $\mathcal{B}_\pi^{(1)}$  and  $\chi_\pi$  directly detect the gapless  $\varphi_\downarrow^-$  field, cf. Eqs. (4.53)–(4.60). In the phase discussed in this section they have the same power law decays.

We have considered the case when only  $w_{12}^\uparrow$  becomes relevant. The case when only  $w_{12}^\downarrow$

Pinned $\varphi_{\uparrow}^-$ : Common power-law order for either sign of $w_{12}^{\uparrow}$				
$\epsilon_{\pm 2k_{F\alpha\downarrow}}$	$\epsilon_{\pm(k_{F1\downarrow}+k_{F2\downarrow})};$ $\chi_{\pm(k_{F1\downarrow}+k_{F2\downarrow})}$	$\epsilon_{\pm(k_{F1\downarrow}-k_{F2\downarrow})};$ $\chi_{\pm(k_{F1\downarrow}-k_{F2\downarrow})}$	$\mathcal{B}_{\pi}^{(1)};$ $\chi_{\pi}$	$\mathcal{P}_{\{Q\}}^+$
Distinct power law correlations				
$w_{12}^{\uparrow} > 0$ : $\epsilon_{\pm(k_{F1\uparrow}+k_{F2\uparrow})}$				
$w_{12}^{\uparrow} < 0$ : $\chi_{\pm(k_{F1\uparrow}+k_{F2\uparrow})}$				

Table 4.1: Summary of the main observables when  $w_{12}^{\uparrow}$  term is relevant and pins  $\varphi_{\uparrow}^-$ . Critical wavevectors  $Q$  for the magnon-pair creation operator are obtained by combining any of  $q_{\uparrow} = \{0, \pm(k_{F1\uparrow} + k_{F2\uparrow})\}$  with any of  $q_{\downarrow} = \{0, \pm(k_{F1\downarrow} + k_{F2\downarrow}), \pm(k_{F1\downarrow} - k_{F2\downarrow})\}$ ,  $Q = q_{\uparrow} + q_{\downarrow}$ ; the most important ones are  $Q = 0$  and  $\pi$ .

becomes relevant can be treated similarly by interchanging  $\uparrow$  and  $\downarrow$ .

#### 4.4.2 Phases when both $w_{12}^{\uparrow}$ and $w_{12}^{\downarrow}$ are relevant

Let us now discuss the phases out of the SBM when both  $w_{12}^{\uparrow}$  and  $w_{12}^{\downarrow}$  terms get relevant. Once the couplings flow to large values, both variables  $\varphi_{\uparrow}^-$  and  $\varphi_{\downarrow}^-$  will be pinned so as to minimize the energy. There are four possible situations depending on the signs of the  $w_{12}^{\uparrow}$  and  $w_{12}^{\downarrow}$ .

In all cases, we find that the translational symmetry is broken by either a static order in  $\mathcal{B}_{\pi}$  (corresponding to period-2 valence bond solid) or  $\chi_{\pi}$  (corresponding to period-2 chirality order). Coexisting with this, we have one gapless mode, namely the overall spin mode “ $\sigma+$ ”, which must remain gapless as long as the magnetization density is incommensurate with the lattice. Similarly to the case with one relevant coupling, spin-1 observables are gapped. Spin-2 observables are gapless, with the dominant contributions

$$\mathcal{P}_{Q=0}^+ \sim \mathcal{P}_{Q=\pi}^+ \sim e^{-i2\varphi_{\sigma+}}. \quad (4.73)$$

(Note that the original wavevectors  $Q = 0$  and  $\pi$  are not distinguishable once we have the period-2 static orders.) Together with such spin-nematic observables, we also have spin-0 observables of the  $\epsilon$ - or  $\chi$ -type depending on the pinning details, with the wavevectors  $\pm(k_{F1\alpha} + k_{F2\alpha})$  which satisfy  $k_{F1\uparrow} + k_{F2\uparrow} = -(k_{F1\downarrow} + k_{F2\downarrow}) - \pi$ .

Below, we consider four different pinning situations in more details. The main features

$w_{12}^\uparrow$	$w_{12}^\downarrow$	Static Order	Power-Law Correlations	
+	+	$\mathcal{B}_\pi^{(1)}$	$\epsilon_{\pm(k_{F1\alpha}+k_{F2\alpha})}$	$\mathcal{P}_{\{Q\}}^+$
-	-	$\mathcal{B}_\pi^{(1)}$	$\chi_{\pm(k_{F1\alpha}+k_{F2\alpha})}$	$\mathcal{P}_{\{Q\}}^+$
+	-	$\chi_\pi$	$\epsilon_{\pm(k_{F1\uparrow}+k_{F2\uparrow})};$ $\chi_{\pm(k_{F1\downarrow}+k_{F2\downarrow})}$	$\mathcal{P}_{\{Q\}}^+$
-	+	$\chi_\pi$	$\epsilon_{\pm(k_{F1\downarrow}+k_{F2\downarrow})};$ $\chi_{\pm(k_{F1\uparrow}+k_{F2\uparrow})}$	$\mathcal{P}_{\{Q\}}^+$

Table 4.2: Summary of the cases when both  $w_{12}^\uparrow$  and  $w_{12}^\downarrow$  terms are relevant. For  $w_{12}^\uparrow w_{12}^\downarrow > 0$  we have period-2 VBS order, while for  $w_{12}^\uparrow w_{12}^\downarrow < 0$  we have period-2 chirality order. In all cases, coexisting with such static order, we have power law correlations in the spin-2 (magnon pair) observable  $\mathcal{P}^+$  and in the specific  $\epsilon/\chi$  observables.

in each case are summarized in Table 4.2.

#### 4.4.2.1 $w_{12}^\uparrow > 0, w_{12}^\downarrow > 0$

The pinning conditions for fields  $\varphi_\uparrow^-$  and  $\varphi_\downarrow^-$  are

$$\varphi_\uparrow^- = \frac{(2n+1)\pi}{2\sqrt{2}}, \quad \varphi_\downarrow^- = \frac{(2m+1)\pi}{2\sqrt{2}}, \quad n, m \in \mathbb{Z}. \quad (4.74)$$

In this case,  $\mathcal{B}_\pi^{(1)}$  obtains an expectation value while  $\chi_\pi = 0$ . Thus we expect to see period-2 VBS order as illustrated in Fig. 4.5. We also have power law correlations in

$$\epsilon_{k_{F1\uparrow}+k_{F2\uparrow}} \sim \epsilon_{-k_{F1\downarrow}-k_{F2\downarrow}} \sim e^{i\theta_{\sigma^+}}, \quad (4.75)$$

while  $\chi_{k_{F1\alpha}+k_{F2\alpha}} = 0$ . Note that because of the relation Eq. (4.53) [in the sense that  $i(\epsilon_{k_{F1\uparrow}+k_{F2\uparrow}}\epsilon_{k_{F1\downarrow}+k_{F2\downarrow}} - \text{H.c.})$  has the same symmetry properties as  $\mathcal{B}_\pi^{(1)}$ ], once the system develops static order in  $\mathcal{B}_\pi^{(1)}$ , the  $\epsilon_{k_{F1\uparrow}+k_{F2\uparrow}}$  and  $\epsilon_{-k_{F1\downarrow}-k_{F2\downarrow}} = \epsilon_{k_{F1\downarrow}+k_{F2\downarrow}}^\dagger$  are no longer independent. Appropriately, the wavevectors  $k_{F1\uparrow}+k_{F2\uparrow}$  and  $-k_{F1\downarrow}-k_{F2\downarrow}$  differ by  $\pi$  and also become connected.

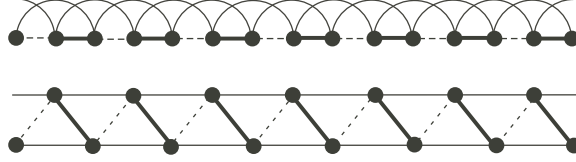


Figure 4.5: Picture of the valence bond solid order when  $\mathcal{B}_\pi^{(1)}$  gains an expectation value. Top: 1D chain view. Bottom: the same in two-leg ladder view. Coexisting with the static order, we also have spin-nematic power law correlations and power law in either  $\epsilon$  or  $\chi$  channels (these properties are not depicted in any way).

#### 4.4.2.2 $w_{12}^\uparrow < 0, w_{12}^\downarrow < 0$

Here, the pinning conditions are

$$\varphi_\uparrow^- = \frac{2n\pi}{2\sqrt{2}}, \quad \varphi_\downarrow^- = \frac{2m\pi}{2\sqrt{2}}, \quad n, m \in \mathbb{Z}. \quad (4.76)$$

Again,  $\mathcal{B}_\pi^{(1)}$  obtains an expectation value while  $\chi_\pi = 0$ . However, here we have power law correlations in

$$\chi_{k_{F1\uparrow}+k_{F2\uparrow}} \sim \chi_{-k_{F1\downarrow}-k_{F2\downarrow}} \sim e^{i\theta_{\sigma+}} \quad (4.77)$$

while  $\epsilon_{k_{F1\alpha}+k_{F2\alpha}} = 0$ . Similar to the discussion in the preceding case and using relation Eq. (4.55),  $\chi_{k_{F1\uparrow}+k_{F2\uparrow}}$  and  $\chi_{-k_{F1\downarrow}-k_{F2\downarrow}}$  are not independent observables in the presence of the static order in  $\mathcal{B}_\pi^{(1)}$ .

#### 4.4.2.3 $w_{12}^\uparrow > 0, w_{12}^\downarrow < 0$

In this case, the pinning conditions are

$$\varphi_\uparrow^- = \frac{(2n+1)\pi}{2\sqrt{2}}, \quad \varphi_\downarrow^- = \frac{2m\pi}{2\sqrt{2}}, \quad n, m \in \mathbb{Z}. \quad (4.78)$$

In this phase,  $\chi_\pi$  obtains an expectation value while  $\mathcal{B}_\pi^{(1)} = 0$ . Thus we expect to see period-2 chirality order as illustrated in Fig. 4.6. We also have power law correlations in

$$\epsilon_{k_{F1\uparrow}+k_{F2\uparrow}} \sim \chi_{-k_{F1\downarrow}-k_{F2\downarrow}} \sim e^{i\theta_{\sigma+}}, \quad (4.79)$$

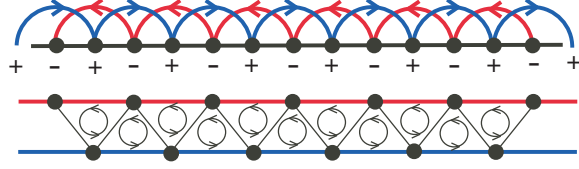


Figure 4.6: Picture of the static period-2 order in spin chirality when  $\chi_\pi$  gains an expectation value. Since  $\mathcal{J}_\pi^{(2)} \sim \chi_\pi$ , we have static staggered second-neighbor bond currents in the chain view (top figure). In the ladder view (bottom figure), we have oppositely oriented spin currents flowing on the two legs. Coexisting with the static order, we also have spin-nematic power law correlations and power laws in  $\epsilon/\chi$  channels (these properties are not depicted in any way).

while  $\chi_{k_{F1\uparrow}+k_{F2\uparrow}} = \epsilon_{-k_{F1\downarrow}-k_{F2\downarrow}} = 0$ . By using Eq. (4.57), we can understand the equivalence of the two observables  $\epsilon_{k_{F1\uparrow}+k_{F2\uparrow}}$  and  $\chi_{-k_{F1\downarrow}-k_{F2\downarrow}}$  once there is the static order in  $\chi_\pi$ .

#### 4.4.2.4 $w_{12}^\uparrow < 0, w_{12}^\downarrow > 0$

In this case, the pinning conditions are

$$\varphi_\uparrow^- = \frac{2n\pi}{2\sqrt{2}}, \quad \varphi_\downarrow^- = \frac{(2m+1)\pi}{2\sqrt{2}}, \quad n, m \in \mathbb{Z}. \quad (4.80)$$

$\chi_\pi$  obtains an expectation value while  $\mathcal{B}_\pi^{(1)} = 0$ . We also have power law correlations in

$$\chi_{k_{F1\uparrow}+k_{F2\uparrow}} \sim \epsilon_{-k_{F1\downarrow}-k_{F2\downarrow}} \sim e^{i\theta_{\sigma+}}, \quad (4.81)$$

while  $\epsilon_{k_{F1\uparrow}+k_{F2\uparrow}} = \chi_{-k_{F1\downarrow}-k_{F2\downarrow}} = 0$ . The two observables  $\chi_{k_{F1\uparrow}+k_{F2\uparrow}}$  and  $\epsilon_{-k_{F1\downarrow}-k_{F2\downarrow}}$  become related because of Eq. (4.59) and the static order in  $\chi_\pi$ .

This completes our discussion of the phases out of the SBM. We cannot tell which of the different cases are more likely in particular microscopic models. Also, the power law correlation exponents depend on the unknown Luttinger parameter  $g_{\sigma+}$  of the “ $\sigma+$ ” field, and we cannot tell whether spin-2 or spin-0 observables dominate (their scaling dimensions are  $1/g_{\sigma+}$  and  $g_{\sigma+}/4$ , respectively). However, we have developed a qualitative understanding of the phases and observables needed to identify them, which we hope will be useful in numerical studies of models realizing the SBM phase.

## 4.5 Discussion

In this chapter, we studied instabilities of the two-leg SBM under the Zeeman magnetic field. The instabilities are driven by the  $w_{12}^\alpha$  interactions, Eq. (4.8), and we analyzed possible outcomes using Bosonization. In all cases, we found a gap to spin-1 excitations, while spin-nematic (two-magnon) correlations are power law. Loosely speaking, this appears because of some pairing of spinons, while the precise characterization is obtained by analyzing all physical observables.

Here we want to discuss consequences if such spinon pairing were to occur in a 2D spin liquid under the Zeeman field. At present, we do not have any energetics justification under which circumstances this may happen and whether this applies to the candidate spin liquid materials. However, the resulting states are quite interesting on their own and perhaps such phases may occur in some other 2D systems (several papers [37, 95] considered mechanisms for spinon pairing in zero field).

First of all, the analog of the stable SBM phase in Chapter 4.2 has gapless Fermi surfaces for both  $\uparrow$  and  $\downarrow$  spinon species, with somewhat different  $k_{F\uparrow}$  and  $k_{F\downarrow}$ . In the organic  $\kappa$ -(ET)<sub>2</sub>Cu<sub>2</sub>(CN)<sub>3</sub> and EtMe<sub>3</sub>Sb[Pd(dmit)<sub>2</sub>]<sub>2</sub> materials, we estimate  $(n_\uparrow - n_\downarrow)/(n_\uparrow + n_\downarrow) < 0.02$  under laboratory fields, so the difference between the two Fermi surfaces is small. In mean field, the spin correlations are

$$\langle S^+(\mathbf{r})S^-(\mathbf{0}) \rangle_{\text{mf}} \sim -\frac{\cos[(\mathbf{k}_{F\uparrow} + \mathbf{k}_{F\downarrow}) \cdot \mathbf{r} + \frac{\pi}{2}]}{|\mathbf{r}|^3} \quad (4.82)$$

$$-\frac{\cos[(\mathbf{k}_{F\uparrow} - \mathbf{k}_{F\downarrow}) \cdot \mathbf{r}]}{|\mathbf{r}|^3}, \quad (4.83)$$

$$\langle \delta S^z(\mathbf{r})\delta S^z(\mathbf{0}) \rangle_{\text{mf}} \sim -\sum_{\alpha=\uparrow,\downarrow} \frac{1 + \cos[2\mathbf{k}_{F\alpha} \cdot \mathbf{r} + \frac{\pi}{2}]}{|\mathbf{r}|^3}, \quad (4.84)$$

while gauge fluctuations are expected to enhance the  $\mathbf{k}_{F\uparrow} + \mathbf{k}_{F\downarrow}$  and  $2\mathbf{k}_{F\alpha}$  parts [60], similarly to the ladder case [29].

Next, we want to discuss the analog of the situation in Chapter 4.4.1, where there is pairing in one spinon species (say,  $f_\uparrow$ ) and no pairing in the other species. Note that the pairing must be odd-wave since it is within one fermion type. We will not consider any

energetics selection of the pairing and just mention possibilities like  $p$ -wave ( $p_x + ip_y$ ) or  $f$ -wave that can be nicely placed on the triangular lattice.

The properties of the resulting phase are as follows. The  $f_\downarrow$  species are gapless with Fermi surface, so we expect metal-like specific heat  $C = \gamma T$ ; note that this is the full result since the gauge field is Higgsed out by the  $f_\uparrow$  pairing. We also expect constant spin susceptibility at  $T \rightarrow 0$  since both  $f_\uparrow$  and  $f_\downarrow$  systems are compressible, the former due to the pair-condensate and the latter by virtue of finite density of states at the Fermi level. Because of the  $f_\downarrow$  Fermi surface, we expect  $\langle S^z(\mathbf{r})S^z(\mathbf{0}) \rangle$  to show  $2k_{F\downarrow}$  oscillations with  $1/r^3$  power law. On the other hand,  $\langle S^+(\mathbf{r})S^-(\mathbf{0}) \rangle$  will show either a full gap if the  $f_\uparrow$  pairing is fully gapped as in the case of  $p_x + ip_y$  pairing, or a pseudogap if the  $f_\uparrow$  pairing has gapless parts as in the case of  $f$ -wave pairing. Note that this does not contradict the finite susceptibility since the  $f_\uparrow$ -pair condensate can readily accommodate  $\Delta N_\uparrow = \pm 2$  changes. Related to this, spin-nematic correlations are gapless and show  $1/r^3$  power law at zero wavevector (in the mean field calculation). Interestingly, the gap or pseudo-gap to spin-1 operators would have consequences for NMR experiments done with  $^1\text{H}$  or  $^{13}\text{C}$  that are both spin- $\frac{1}{2}$  nuclei and relax only by spin-1 excitations. From such measurements, this phase might appear gapped, but it actually has a gapless Fermi surface of one species. (In the context of 1D models exhibiting spin-nematic phases, consequences for the NMR relaxation rate were discussed in detail, e.g., in [89].)

Finally, let us consider the analog of the situation in Chapter 4.4.2, where both  $f_\uparrow$  and  $f_\downarrow$  become paired, with possibly different pairing  $\Delta_{\mathbf{r}\mathbf{r}'}^\uparrow, \Delta_{\mathbf{r}\mathbf{r}'}^\downarrow$ . In this case,  $S^z$  and  $S^+$  correlations are both gapped (or pseudo-gapped), while spin-nematic correlation shows long-range order. Specifically, in the mean field,

$$\langle S^+(\mathbf{r})S^+(\mathbf{r}') \rangle_{\text{mf}} = \Delta_{\mathbf{r}\mathbf{r}'}^{\uparrow*} \Delta_{\mathbf{r}\mathbf{r}'}^\downarrow. \quad (4.85)$$

Note that this nematic order resides on the bonds of the lattice and details depend on the  $\Delta^\uparrow$  and  $\Delta^\downarrow$ . For example, if we take  $\Delta^\uparrow$  and  $\Delta^\downarrow$  to have the same pattern, this will give ferro-nematic state. Curiously, if we take  $\Delta^\uparrow \sim p_x + ip_y$  and  $\Delta^\downarrow \sim p_x - ip_y$ , we get  $q = 0$  antiferromagnetic nematic order on the Kagome lattice formed by the bonds of the

triangular lattice. We emphasize that we have not discussed any energetics that may be selecting among such states. Whether something like this can appear in realistic models on the triangular lattice is an interesting open question.

# Chapter 5

## Insulating phases of electrons on a zigzag strip in the orbital magnetic field

This chapter complements our earlier discussing in chapter 4 on the effects of Zeeman field on a SBM phase [29]. Here we consider the orbital magnetic field on the electronic two-leg triangular ladder.

Previous studies of ladders with orbital field were done on a square two-leg case and mainly focused on generic density (see [96, 97, 98, 99] and citations therein), while the triangular two-leg case has not been considered so far. In the context of Mott insulators at half-filling, microscopic orbital fields were shown to give rise to interesting scalar chirality terms operating on triangles in the effective spin Hamiltonian [100, 101, 102, 35]. On the other hand, it was also argued [103, 104, 105] that if a Mott insulator develops a noncoplanar magnetic order with nontrivial chiralities, this can imply spontaneous orbital electronic currents.

In this chapter, we focus on the simplest ladder model with triangles, the zigzag strip, and discuss instabilities due to existence of orbital magnetic field and properties of the resulting phases. Our main findings are presented as follows. In Chapter 5.1, we determine the electron dispersion in the orbital field and perform weak coupling renormalization group (RG) analysis in a two-band regime [29, 31, 65, 64]. Unlike the case with no field, we find that there is a four-fermion Umklapp interaction which is always relevant for repulsively interacting electrons and provides a mechanism to drive the metal-insulator transition. This Umklapp gaps out all charge modes and produces a C0S2 state. In Chapter 5.2

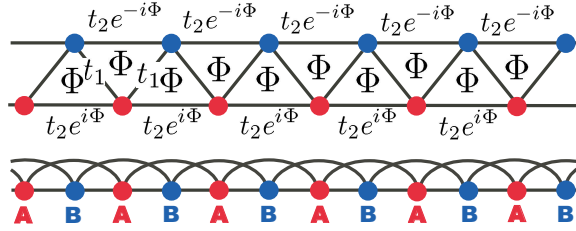


Figure 5.1: Top: Zigzag strip with uniform flux  $\Phi$  penetrating each triangular plaquette. Bottom: Convenient representation of the model as a 1D chain with first- and second-neighbor hoppings. We choose a gauge such that  $t_{x,x+1} = t_1$  and  $t_{x,x+2} = t_2 e^{i\Phi \cos(\pi x)}$ . The unit cell consists of two sites labelled **A** and **B**.

we describe physical observables in this phase, and in Chapter 5.3 we analyze possible further instabilities in the spin sector and properties of the resulting phases. We conclude with discussion of the orbital field effects in the context of the spin Bose-metal phase of [29] where the Mott insulator is first produced by an eight-fermion Umklapp and the new four-fermion Umklapp appears as a residual interaction.

## 5.1 Weak coupling approach to electrons on a zigzag strip with orbital field

Let us apply weak coupling renormalization group (RG) to study effects of electronic interactions in the presence of the orbital magnetic field. We start with free electrons hopping on the triangular strip with uniform flux  $\Phi$  passing through each triangle. Figure 5.1 illustrates our gauge choice,

$$t_{x,x+1} = t_1, \quad (5.1)$$

$$t_{x,x+2} = t_2 e^{i\Phi \cos(\pi x)}. \quad (5.2)$$

Here and throughout, we refer to sites by their 1D chain coordinate  $x$ . Since the second-neighbor hopping depends on whether  $x$  is even or odd, the unit cell has two sites which we label **A** and **B**. The Hamiltonian for such an interacting electron system is  $H = H_0 + H_V$ ,

with

$$H_0 = - \sum_{x;\alpha} [t_1 c_\alpha^\dagger(x) c_\alpha(x+1) + \text{H.c.}] \quad (5.3)$$

$$- \sum_{x \in \mathbf{A}; \alpha} [t_2 e^{-i\Phi} c_{\mathbf{A}\alpha}^\dagger(x) c_{\mathbf{A}\alpha}(x+2) + \text{H.c.}] \quad (5.4)$$

$$- \sum_{x \in \mathbf{B}; \alpha} [t_2 e^{i\Phi} c_{\mathbf{B}\alpha}^\dagger(x) c_{\mathbf{B}\alpha}(x+2) + \text{H.c.}] , \quad (5.5)$$

$$H_V = \frac{1}{2} \sum_{x,x'} V(x-x') n(x) n(x') . \quad (5.6)$$

In the first and last lines, we suppressed the sublattice labels, and  $n(x) \equiv \sum_\alpha c_\alpha^\dagger(x) c_\alpha(x)$ . We assume that  $H_V$  is small and treat it as a perturbation to  $H_0$ . The free electron dispersion is

$$\begin{aligned} \xi(k) = & \pm 2 \sqrt{[t_1 \cos(k)]^2 + [t_2 \sin(\Phi) \sin(2k)]^2} \\ & - 2t_2 \cos(\Phi) \cos(2k) - \mu . \end{aligned} \quad (5.7)$$

We are focusing on the regime with two partially filled bands as shown in Fig. 5.2. For small flux, this regime appears when  $t_2/t_1 > 0.5$ . We denote Fermi wavevectors for the right-moving electrons as  $k_{F1}$  and  $k_{F2}$  and the corresponding Fermi velocities as  $v_1$  and  $v_2$ . The half-filling condition reads  $k_{F1} + k_{F2} = \pi/2$ .

The electron operators are expanded in terms of continuum fields,

$$c_{\mathbf{M}\alpha}(x) = \sum_{P,a} e^{iPk_{Fa}x} U_{Pa}^{\mathbf{M}} c_{Pa\alpha} , \quad (5.8)$$

where  $P = R/L = +/-$  denotes the right and left movers,  $a = 1, 2$  denotes the two Fermi seas, and  $\mathbf{M} = \mathbf{A}$  or  $\mathbf{B}$  denotes the sublattices. In the specific gauge, the wavefunctions

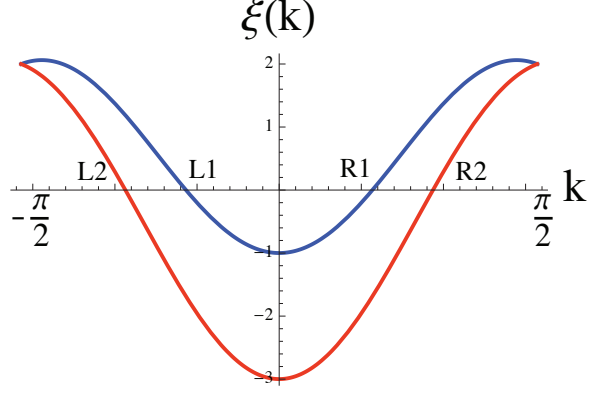


Figure 5.2: Free electron spectrum in the presence of the orbital field, see Fig. 5.1. Here  $\xi(k)$  is given by Eq. (5.7) with two branches and we focus on the regime when both bands are partially populated; we take  $t_1 = 1$ ,  $t_2 = 1$ , and  $\Phi = \pi/100$  for illustration. The half-filling condition requires  $k_{F1} + k_{F2} = \pi/2$ .

$U_{Pa}^M$  are

$$\begin{aligned}
U_{R1}^A &= \cos\left(\frac{\theta_{k_{F1}}}{2}\right), & U_{L1}^A &= \sin\left(\frac{\theta_{k_{F1}}}{2}\right), \\
U_{R2}^A &= -\sin\left(\frac{\theta_{k_{F2}}}{2}\right), & U_{L2}^A &= \cos\left(\frac{\theta_{k_{F2}}}{2}\right), \\
U_{R1}^B &= \sin\left(\frac{\theta_{k_{F1}}}{2}\right), & U_{L1}^B &= \cos\left(\frac{\theta_{k_{F1}}}{2}\right), \\
U_{R2}^B &= \cos\left(\frac{\theta_{k_{F2}}}{2}\right), & U_{L2}^B &= -\sin\left(\frac{\theta_{k_{F2}}}{2}\right),
\end{aligned} \tag{5.9}$$

with

$$\{\sin(\theta_k), \cos(\theta_k)\} \propto \{t_1 \cos(k), t_2 \sin(\Phi) \sin(2k)\}. \tag{5.10}$$

Note that  $k$  belongs to the reduced Brillouin zone  $[-\pi/2, \pi/2]$ .

Few words about physical symmetries. The present problem has  $SU(2)$  spin rotation symmetry ( $\mathcal{R}$ ) but lacks time reversal because of the orbital field. It also lacks inversion symmetry and translation by one lattice spacing. However, the system is invariant under combined transformations such as inversion plus complex conjugation ( $I^* : x \rightarrow -x, i \rightarrow -i$ ) and translation by one lattice spacing plus complex conjugation ( $T_1^* : x \rightarrow x + 1, i \rightarrow -i$ ). Table 5.1 lists transformation properties of the continuum fields under these two discrete transformations and under the  $SU(2)$  spin rotation. Since the symmetries are reduced compared to the case without the orbital field [31, 65, 64], we need to scrutinize interactions allowed in the continuum field theory.

Table 5.1: Transformation properties of the continuum fields under  $I^*$  (inversion plus complex conjugation),  $T_1^*$  (translation by one lattice spacing plus complex conjugation), and  $\mathcal{R}$  (SU(2) spin rotation about arbitrary axis  $\vec{n}$  by an angle  $\phi$ ). We also show transformation properties of bilinears  $E_{1,2}$  defined in Eqs. (5.41)–(5.42).

	$\mathcal{R}$	$I^*$	$T_1^*$
$c_{Pa\alpha} \rightarrow$	$\left( e^{-i\frac{\phi}{2}\vec{n}\cdot\vec{\sigma}} \right)_{\alpha\beta} c_{Pa\beta}$	$c_{Pa\alpha}$	$e^{iPk_F a} c_{-P,a\alpha}$
$E_j \rightarrow$	$E_j$	$E_j$	$-iE_j^\dagger$
$E_j^\dagger \rightarrow$	$E_j^\dagger$	$E_j^\dagger$	$iE_j$

Using symmetry considerations, we can write down the general form of the four-fermion interactions which mix the right- and left-moving fields:

$$\mathcal{H}^\rho = \sum_{a,b} (w_{ab}^\rho J_{Rab} J_{Lab} + \lambda_{ab}^\rho J_{Raa} J_{Lbb}) , \quad (5.11)$$

$$\mathcal{H}^\sigma = - \sum_{a,b} (w_{ab}^\sigma \vec{J}_{Rab} \cdot \vec{J}_{Lab} + \lambda_{ab}^\sigma \vec{J}_{Raa} \cdot \vec{J}_{Lbb}) , \quad (5.12)$$

$$\mathcal{H}^u = u_4 (c_{R2\uparrow}^\dagger c_{R2\downarrow}^\dagger c_{L1\uparrow} c_{L1\downarrow} - c_{L2\uparrow}^\dagger c_{L2\downarrow}^\dagger c_{R1\uparrow} c_{R1\downarrow} + \text{H.c.}) , \quad (5.13)$$

where we defined

$$J_{Pab} \equiv c_{Pa\alpha}^\dagger c_{Pb\alpha} , \quad (5.14)$$

$$\vec{J}_{Pab} \equiv \frac{1}{2} c_{Pa\alpha}^\dagger \vec{\sigma}_{\alpha\beta} c_{Pb\beta} . \quad (5.15)$$

Note that besides the familiar momentum-conserving four-fermion interactions  $\mathcal{H}^\rho$  and  $\mathcal{H}^\sigma$ , there is also an Umklapp-type interaction  $\mathcal{H}^u$ .

Using the symmetries of the problem, we can check that all couplings are real and satisfy  $w_{12} = w_{21}$  and  $\lambda_{12} = \lambda_{21}$ , and we also use convention  $w_{11} = w_{22} = 0$ . Thus there are 9 independent couplings:  $w_{12}^{\rho/\sigma}$ ,  $\lambda_{11}^{\rho/\sigma}$ ,  $\lambda_{22}^{\rho/\sigma}$ ,  $\lambda_{12}^{\rho/\sigma}$ , and  $u_4$ .

With all terms defined above, we can derive weak-coupling RG equations:

$$\dot{\lambda}_{11}^{\rho} = -\frac{1}{2\pi v_2} \left[ (w_{12}^{\rho})^2 + \frac{3}{16} (w_{12}^{\sigma})^2 \right], \quad (5.16)$$

$$\dot{\lambda}_{22}^{\rho} = -\frac{1}{2\pi v_1} \left[ (w_{12}^{\rho})^2 + \frac{3}{16} (w_{12}^{\sigma})^2 \right], \quad (5.17)$$

$$\dot{\lambda}_{12}^{\rho} = \frac{1}{\pi(v_1 + v_2)} \left[ (w_{12}^{\rho})^2 + \frac{3}{16} (w_{12}^{\sigma})^2 + (u_4)^2 \right], \quad (5.18)$$

$$\dot{\lambda}_{11}^{\sigma} = -\frac{1}{2\pi v_1} (\lambda_{11}^{\sigma})^2 - \frac{1}{4\pi v_2} [(w_{12}^{\sigma})^2 + 4w_{12}^{\rho} w_{12}^{\sigma}], \quad (5.19)$$

$$\dot{\lambda}_{22}^{\sigma} = -\frac{1}{2\pi v_2} (\lambda_{22}^{\sigma})^2 - \frac{1}{4\pi v_1} [(w_{12}^{\sigma})^2 + 4w_{12}^{\rho} w_{12}^{\sigma}], \quad (5.20)$$

$$\dot{\lambda}_{12}^{\sigma} = -\frac{1}{\pi(v_1 + v_2)} \left\{ (\lambda_{12}^{\sigma})^2 + \frac{(w_{12}^{\sigma})^2 - 4w_{12}^{\rho} w_{12}^{\sigma}}{2} \right\}, \quad (5.21)$$

$$\dot{w}_{12}^{\rho} = -\Lambda^{\rho} w_{12}^{\rho} - \frac{3}{16} \Lambda^{\sigma} w_{12}^{\sigma}, \quad (5.22)$$

$$\dot{w}_{12}^{\sigma} = -\Lambda^{\sigma} w_{12}^{\sigma} - \left( \Lambda^{\rho} + \frac{\Lambda^{\sigma}}{2} + \frac{2\lambda_{12}^{\sigma}}{\pi(v_1 + v_2)} \right) w_{12}^{\rho}, \quad (5.23)$$

$$\dot{u}_4 = \frac{4\lambda_{12}^{\rho} u_4}{\pi(v_1 + v_2)}. \quad (5.24)$$

Here  $\dot{O} \equiv \partial O / \partial \ell$ , where  $\ell$  is logarithm of the length scale. We have also defined

$$\Lambda^{\rho/\sigma} = \frac{\lambda_{11}^{\rho/\sigma}}{2\pi v_1} + \frac{\lambda_{22}^{\rho/\sigma}}{2\pi v_2} - \frac{2\lambda_{12}^{\rho/\sigma}}{\pi(v_1 + v_2)}. \quad (5.25)$$

We can obtain bare values of the couplings for any electronic interactions by expanding in terms of the continuum fields. In the case of small flux, the couplings  $\lambda^{\rho/\sigma}$  and  $w^{\rho/\sigma}$  in Eqs. (5.11) and (5.12) are only modified slightly and can be treated as the same as in [31] with extended repulsion. For the coupling  $u_4$  in Eq. (5.13), the bare value of  $u_4$  in the small flux limit is  $\sum_{x'} V(x - x') e^{i\frac{\pi}{2}(x-x')} \times \frac{t_2}{t_1} [\sin(k_{F1}) + \sin(k_{F2})] \Phi \propto \Phi$ , where  $x$  and  $x'$  belong to the same sublattice (A or B). Therefore, we can see that the parameter  $u_4$  which measures the strength of the umklapp process is linearly proportional to the flux and goes to zero if we gradually switch off the flux. For repulsive interactions, we generally expect positive  $\lambda^{\rho}$  (see, e.g., [31] with extended repulsion). Then according to the RG Eq. (5.24), positive initial  $\lambda_{12}^{\rho}$  will drive  $u_4$  to increase exponentially. Thus we conclude

that the starting two-band metallic phase is unstable due to the new Umklapp term.

To analyze the resulting phase(s), we use bosonization to rewrite fermionic fields in terms of bosonic fields,

$$c_{Pa\alpha} \sim \eta_{a\alpha} e^{i(\varphi_{a\alpha} + P\theta_{a\alpha})}, \quad (5.26)$$

with canonically conjugate boson fields:

$$[\varphi_{a\alpha}(x), \varphi_{b\beta}(x')] = [\theta_{a\alpha}(x), \theta_{b\beta}(x')] = 0, \quad (5.27)$$

$$[\varphi_{a\alpha}(x), \theta_{b\beta}(x')] = i\pi\delta_{ab}\delta_{\alpha\beta}\Theta(x - x'), \quad (5.28)$$

where  $\Theta(x)$  is the heaviside step function. Here we use Majorana fermions  $\{\eta_{a\alpha}, \eta_{b\beta}\} = 2\delta_{ab}\delta_{\alpha\beta}$  as Klein factors, which assure that the fermion fields with different flavors anti-commute.

It is convenient to introduce new variables

$$\theta_{\rho\pm} \equiv \frac{1}{2}[\theta_{1\uparrow} + \theta_{1\downarrow} \pm (\theta_{2\uparrow} + \theta_{2\downarrow})], \quad (5.29)$$

$$\theta_{a\sigma} \equiv \frac{1}{\sqrt{2}}(\theta_{a\uparrow} - \theta_{a\downarrow}), \quad a = 1 \text{ or } 2, \quad (5.30)$$

$$\theta_{\sigma\pm} \equiv \frac{1}{\sqrt{2}}(\theta_{1\sigma} \pm \theta_{2\sigma}), \quad (5.31)$$

and similarly for  $\varphi$  variables. We can then write compactly all nonlinear potentials obtained

upon bosonization of the four-fermion interactions:

$$\mathcal{H}^u = 4u_4 \hat{\Gamma} \sin(2\varphi_{\rho-}) \sin(2\theta_{\rho+}) , \quad (5.32)$$

$$W \equiv (w_{12}^\rho J_{R12} J_{L12} - w_{12}^\sigma \vec{J}_{R12} \cdot \vec{J}_{L12}) + \text{H.c.} = \quad (5.33)$$

$$= \cos(2\varphi_{\rho-}) \left\{ 4w_{12}^\rho \left[ \cos(2\varphi_{\sigma-}) - \hat{\Gamma} \cos(2\theta_{\sigma-}) \right] \right. \\ \left. - w_{12}^\sigma \left[ \cos(2\varphi_{\sigma-}) + \hat{\Gamma} \cos(2\theta_{\sigma-}) + 2\hat{\Gamma} \cos(2\theta_{\sigma+}) \right] \right\} , \quad (5.34)$$

$$V_\perp \equiv - \sum_a \frac{\lambda_{aa}^\sigma}{2} (J_{Raa}^+ J_{Laa}^- + J_{Raa}^- J_{Laa}^+) \quad (5.35)$$

$$- \frac{\lambda_{12}^\sigma}{2} [J_{R11}^+ J_{L22}^- + J_{R11}^- J_{L22}^+ + (R \leftrightarrow L)] \quad (5.36)$$

$$= \sum_a \lambda_{aa}^\sigma \cos(2\sqrt{2}\theta_{a\sigma}) \quad (5.37)$$

$$+ 2\lambda_{12}^\sigma \hat{\Gamma} \cos(2\theta_{\sigma+}) \cos(2\varphi_{\sigma-}) , \quad (5.38)$$

where

$$\hat{\Gamma} \equiv \eta_{1\uparrow} \eta_{1\downarrow} \eta_{2\uparrow} \eta_{2\downarrow} . \quad (5.39)$$

We will not analyze the RG flows in all cases. Our main interest is in exploring the orbital magnetic field effects on the C2S2 metallic phase and nearby C1[ $\rho-$ ]S2 spin liquid. Therefore we consider the situation where in the absence of the  $u_4$  term we have the stable C2S2 phase described by RG flows such that  $\lambda_{ab}^\rho$  reach some fixed point values,  $w_{12}^{\rho/\sigma}$  are irrelevant, and  $\lambda_{ab}^\sigma$  are marginally irrelevant—this is realized, for example, in [31] for sufficiently long-ranged repulsion.

As we have already discussed, for repulsive interactions we expect  $\lambda_{12}^\rho > 0$  and hence any nonzero  $u_4$  will increase quickly. In this setting it is then natural to focus on the effects of the  $\mathcal{H}^u$  first. From the bosonized form Eq. (5.32), we see that it pins

$$\sin(2\theta_{\rho+}) = -\text{sign}(u_4) \sin(2\varphi_{\rho-}) = \pm 1 . \quad (5.40)$$

Thus, both “ $\rho-$ ” and “ $\rho+$ ” modes become gapped and the system is an insulator. This insulator arises because of the combined localizing effects of the orbital field and repulsive

interactions.

Having concluded that  $u_4$  becomes large, if we were to continue using the weak coupling RG Eqs. (5.16)–(5.24), we would find that  $u_4$  drives  $\lambda_{12}^\rho$  to large positive value, which in turn drives  $\Lambda^\rho$  to negative values and destabilizes couplings  $w_{12}^{\rho/\sigma}$ , and all couplings eventually diverge. If we do not make finer distinctions as to which couplings diverge faster, we would conclude that the ultimate outcome is a fully gapped COS0. We will analyze different COS0 phases arising from the combined effects of  $u_4$  and  $\lambda^\sigma$  later. Here we only note that the bosonized theory suggests that a COS2 phase can in principle be stable. Indeed, once we pin  $\varphi_{\rho-}$  to satisfy Eq. (5.40), the  $W$  interaction vanishes leaving only the effective  $\lambda^\sigma$  couplings in the spin sector. The stability in the spin sector is then determined by the signs of the  $\lambda^\sigma$  couplings. If  $\lambda_{ab}^\sigma > 0$ , the spin sector is stable and we have the COS2 phase. In what follows, we will identify all interesting physical observables in this phase and will use it as a starting point for analysis of possible further instabilities and features of the resulting phases.

## 5.2 Observables in the Mott-insulating phase in orbital field

To characterize the induced insulating phase(s), we consider observables constructed out of the fermion fields. The only important bilinear operators are

$$E_1 = \frac{1}{2}c_{R1\alpha}^\dagger c_{L2\alpha} + \frac{1}{2}c_{R2\alpha}^\dagger c_{L1\alpha}, \quad (5.41)$$

$$E_2 = \frac{1}{2}c_{L2\alpha}^\dagger c_{R1\alpha} - \frac{1}{2}c_{L1\alpha}^\dagger c_{R2\alpha}, \quad (5.42)$$

$$\vec{V}_1 = \frac{1}{2}c_{R1\alpha}^\dagger \vec{\sigma}_{\alpha\beta} c_{L2\beta} + \frac{1}{2}c_{R2\alpha}^\dagger \vec{\sigma}_{\alpha\beta} c_{L1\beta}, \quad (5.43)$$

$$\vec{V}_2 = \frac{1}{2}c_{L2\alpha}^\dagger \vec{\sigma}_{\alpha\beta} c_{R1\beta} - \frac{1}{2}c_{L1\alpha}^\dagger \vec{\sigma}_{\alpha\beta} c_{R2\beta}, \quad (5.44)$$

and their Hermitian conjugates. All other bilinears contain field  $\theta_{\rho-}$  and hence have exponentially decaying correlations once  $\varphi_{\rho-}$  is pinned. Here and below, repeated spin indices imply summation. Operators  $E_1, E_2$  are scalars and  $\vec{V}_1, \vec{V}_2$  are vectors under spin SU(2).

One can check that  $E_1$  and  $E_2$  have identical transformation properties under all symmetries and therefore are not independent observables, and the same holds for  $\vec{V}_1$  and  $\vec{V}_2$ .

The scalar bilinears  $E_1$  and  $E_2$  appear, e.g., when expressing fermion-hopping energies and currents. Specifically, consider a bond  $[x, x' = x + n]$  (we will focus on  $n = 1$  or  $2$ ),

$$\mathcal{B}^{(n)}(x) \sim t_{x,x+n} c_\alpha^\dagger(x) c_\alpha(x+n) + \text{H.c.}, \quad (5.45)$$

$$\mathcal{J}^{(n)}(x) \sim i[t_{x,x+n} c_\alpha^\dagger(x) c_\alpha(x+n) - \text{H.c.}], \quad (5.46)$$

where we have suppressed “sublattice” site labels  $\mathbf{A}$  or  $\mathbf{B}$  and  $t_{x,x+n}$  is defined in Eqs. (5.1)–(5.2). In general, we need to consider separately cases  $[x \in \mathbf{A}, x' \in \mathbf{A}]$ ,  $[x \in \mathbf{B}, x' \in \mathbf{B}]$ ,  $[x \in \mathbf{A}, x' \in \mathbf{B}]$ ,  $[x \in \mathbf{B}, x' \in \mathbf{A}]$ . After expansion in terms of the continuum fields in each case, we find that all cases can be summarized by a single form that requires only the physical coordinate  $x$  but not the sublattice labels:

$$\mathcal{B}^{(n)}(x) : e^{i\frac{\pi}{2}x} e^{i\frac{n}{2}\cdot\frac{\pi}{2}} \left( A_1^{(n)} E_1^\dagger + A_2^{(n)} E_2^\dagger \right) + \text{H.c.}, \quad (5.47)$$

$$\mathcal{J}^{(n)}(x) : e^{i\frac{\pi}{2}x} e^{i\frac{n}{2}\cdot\frac{\pi}{2}} \left( A_3^{(n)} E_1 + A_4^{(n)} E_2 \right) + \text{H.c.}, \quad (5.48)$$

where  $A_{1,2,3,4}^{(n)}$  are some real numbers. The above concise form is possible because of the  $T_1^*$  symmetry involving translation by one lattice spacing.

In our analysis below, we will also use a scalar spin chirality defined as

$$\chi(x) = \vec{S}(x) \cdot [\vec{S}(x-1) \times \vec{S}(x+1)]. \quad (5.49)$$

From the perspective of symmetry transformation properties, the scalar spin chirality and the so-called “site-centered” currents

$$\chi(x), \quad \mathcal{J}^{(2)}(x-1), \quad \mathcal{J}^{(1)}(x-1) + \mathcal{J}^{(1)}(x) \quad (5.50)$$

have the same transformation properties. (Note that the above currents are named site-centered because they get inverted under inversion about site  $x$ . Similarly, we can also call  $\mathcal{J}^{(1)}(x)$  to be “bond-centered” since it is inverted under inversion about  $x + 1/2$ , the center

of the bond between  $x$  and  $x + 1$ .)

Thus, up to some real factors, we can deduce that the scalar spin chirality in Eq. (5.49) contains the following contributions (focusing on terms that have power law correlations):

$$\chi(x) : e^{i\frac{\pi}{2}x} (A'_3 E_1 + A'_4 E_2) + \text{H.c.} \quad (5.51)$$

The vector bilinears  $\vec{V}_1$  and  $\vec{V}_2$  appear when expressing spin operator,

$$\vec{S}(x) = \frac{1}{2} c_\alpha^\dagger(x) \vec{\sigma}_{\alpha\beta} c_\beta(x) . \quad (5.52)$$

We consider separately two cases  $x \in \mathbf{A}$  and  $x \in \mathbf{B}$ . After expanding in terms of the continuum fields, we find that both cases can be summarized by a single form that requires only the physical coordinate  $x$ ,

$$\vec{S}(x) \sim e^{i\frac{\pi}{2}x} \left( A'_1 \vec{V}_1^\dagger + A'_2 \vec{V}_2^\dagger \right) + \text{H.c.} , \quad (5.53)$$

where  $A'_{1,2}$  are some real factors.

The bosonized expressions for  $E_{1,2}$  are:

$$E_1 = e^{-i\theta_{\rho+}} \left[ -i\eta_{1\uparrow}\eta_{2\uparrow} e^{-i\theta_{\sigma+}} \sin(\varphi_{\rho-} + \varphi_{\sigma-}) - i\eta_{1\downarrow}\eta_{2\downarrow} e^{i\theta_{\sigma+}} \sin(\varphi_{\rho-} - \varphi_{\sigma-}) \right] , \quad (5.54)$$

$$E_2 = e^{i\theta_{\rho+}} \left[ \eta_{1\uparrow}\eta_{2\uparrow} e^{i\theta_{\sigma+}} \cos(\varphi_{\rho-} + \varphi_{\sigma-}) + \eta_{1\downarrow}\eta_{2\downarrow} e^{-i\theta_{\sigma+}} \cos(\varphi_{\rho-} - \varphi_{\sigma-}) \right] . \quad (5.55)$$

The bosonized expressions for  $\vec{V}_1$  and  $\vec{V}_2$  are similarly straightforward. Since we have

SU(2) spin invariance, for simplicity, we only write out  $V^z$ :

$$V_1^z = e^{-i\theta_{\rho+}} \left[ -i\eta_{1\uparrow}\eta_{2\uparrow}e^{-i\theta_{\sigma+}} \sin(\varphi_{\rho-} + \varphi_{\sigma-}) + i\eta_{1\downarrow}\eta_{2\downarrow}e^{i\theta_{\sigma+}} \sin(\varphi_{\rho-} - \varphi_{\sigma-}) \right], \quad (5.56)$$

$$V_2^z = e^{i\theta_{\rho+}} \left[ \eta_{1\uparrow}\eta_{2\uparrow}e^{i\theta_{\sigma+}} \cos(\varphi_{\rho-} + \varphi_{\sigma-}) - \eta_{1\downarrow}\eta_{2\downarrow}e^{-i\theta_{\sigma+}} \cos(\varphi_{\rho-} - \varphi_{\sigma-}) \right]. \quad (5.57)$$

Besides the bilinears considered above, we have also identified important four-fermion operators,

$$\begin{aligned} \mathcal{B}_{\text{stagg,I}}^{(1)} &= i(c_{R1}^\dagger \sigma^0 c_{L1})(c_{R2}^\dagger \sigma^0 c_{L2}) + \text{H.c.} \\ &\sim \left[ \cos(2\theta_{\sigma+}) + \cos(2\theta_{\sigma-}) \right] \sin(2\theta_{\rho+}), \end{aligned} \quad (5.58)$$

$$\begin{aligned} \mathcal{B}_{\text{stagg,II}}^{(1)} &= i(c_{R1}^\dagger \vec{\sigma} c_{L1}) \cdot (c_{R2}^\dagger \vec{\sigma} c_{L2}) + \text{H.c.} \\ &\sim \left[ \cos(2\theta_{\sigma+}) - \cos(2\theta_{\sigma-}) + 2\hat{\Gamma} \cos(2\varphi_{\sigma-}) \right] \times \\ &\quad \times \sin(2\theta_{\rho+}); \end{aligned} \quad (5.59)$$

$$\begin{aligned} S_{\text{stagg,I}}^z &= (c_{R1}^\dagger \sigma^z c_{L1})(c_{R2}^\dagger \sigma^0 c_{L2}) + \text{H.c.} \\ &\sim \left[ \sin(2\theta_{\sigma+}) + \sin(2\theta_{\sigma-}) \right] \sin(2\theta_{\rho+}), \end{aligned} \quad (5.60)$$

$$\begin{aligned} S_{\text{stagg,II}}^z &= (c_{R1}^\dagger \sigma^0 c_{L1})(c_{R2}^\dagger \sigma^z c_{L2}) + \text{H.c.} \\ &\sim \left[ \sin(2\theta_{\sigma+}) - \sin(2\theta_{\sigma-}) \right] \sin(2\theta_{\rho+}). \end{aligned} \quad (5.61)$$

$\sigma^0$  above is the  $2 \times 2$  identity matrix and  $\vec{\sigma}$  are the usual Pauli matrices. The label ‘‘staggered’’ informs how they contribute to the spin and bond energy observables,

$$\mathcal{B}^{(1)}(x) : e^{i\pi x} (A_I \mathcal{B}_{\text{stagg,I}}^{(1)} + A_{II} \mathcal{B}_{\text{stagg,II}}^{(1)}), \quad (5.62)$$

$$S^z(x) : e^{i\pi x} (A'_I S_{\text{stagg,I}}^z + A'_{II} S_{\text{stagg,II}}^z). \quad (5.63)$$

As an example, the above contributions to the bond energy arise from expanding nearest-neighbor energies  $n(x)n(x+1)$  and  $\vec{S}(x) \cdot \vec{S}(x+1)$  in terms of the continuum fields. Again, we need to consider separately cases  $x \in \mathbf{A}$  or  $x \in \mathbf{B}$ , but we find that both can be

summarized by the form that requires only the physical coordinate  $x$ .

Note that we have only listed observables containing  $\sin(2\theta_{\rho+})$ . Expressions that contain  $\cos(2\theta_{\rho+})$  vanish because of the pinning condition Eq. (5.40); in particular, there is no  $\mathcal{B}_{\text{stagg}}^{(n=\text{even})}$ . Also, for brevity we have only listed the bosonized form of the  $z$ -component of the spin observable.

There are several other non-vanishing four-fermion terms. Thus, there is a term which can be interpreted as a staggered scalar spin chirality; however, it is identical to  $\mathcal{H}^u$ , Eq. (5.13), and is always present as a static background in our system. In addition, there is a spin-1 observable which can be interpreted as a spin current, and a spin-2 (i.e., spin-nematic) observable. In the COS2 phase, these will have the same power laws as  $\mathcal{B}_{\text{stagg}}^{(1)}$  and  $\vec{S}_{\text{stagg}}$ . However, in our model, they become short-ranged if any spin mode gets gapped, and we do not list them explicitly as the main observables.

Let us briefly describe treatment of the Klein factors (see, e.g., [106] for more details). We need this in the next section when determining “order parameters” of various phases obtained as instabilities of the COS2 phase. The operator  $\hat{\Gamma} = \eta_{1\uparrow}\eta_{1\downarrow}\eta_{2\uparrow}\eta_{2\downarrow}$  has eigenvalues  $\pm 1$ . For concreteness, we work with the eigenstate corresponding to  $+1$ :  $\hat{\Gamma}|+\rangle = |+\rangle$ . We then find the following relation

$$\langle +|\eta_{1\uparrow}\eta_{2\uparrow}|+\rangle = \langle +|\eta_{1\downarrow}\eta_{2\downarrow}|+\rangle = \text{pure imaginary}, \quad (5.64)$$

and the scalar bilinears are expressed as

$$E_1 = -e^{-i\theta_{\rho+}} \langle +|\eta_{1\uparrow}\eta_{2\uparrow}|+\rangle \left[ \cos(\varphi_{\rho-}) \sin(\theta_{\sigma+}) \sin(\varphi_{\sigma-}) + i \sin(\varphi_{\rho-}) \cos(\theta_{\sigma+}) \cos(\varphi_{\sigma-}) \right], \quad (5.65)$$

$$E_2 = e^{i\theta_{\rho+}} \langle +|\eta_{1\uparrow}\eta_{2\uparrow}|+\rangle \left[ \cos(\varphi_{\rho-}) \cos(\theta_{\sigma+}) \cos(\varphi_{\sigma-}) - i \sin(\varphi_{\rho-}) \sin(\theta_{\sigma+}) \sin(\varphi_{\sigma-}) \right]. \quad (5.66)$$

For repulsively interacting electrons, the Umklapp term  $\mathcal{H}^u$  appearing in the presence of the orbital field is always relevant and pins  $\theta_{\rho+}$  and  $\varphi_{\rho-}$  as in Eq. (5.40). As already discussed, for such pinning the  $W$ -term Eq. (5.33) vanishes. Therefore, as far as further

$\lambda_{11}^\sigma$	$\lambda_{22}^\sigma$	$\lambda_{12}^\sigma$	Static Order	Power-Law Correlations
+	+	+	None	$E_1, E_2;$ $\vec{V}_1, \vec{V}_2;$ $\vec{S}_{stagg}, \mathcal{B}_{stagg}^{(1)}$
-	+	+	None	$\vec{S}_{stagg}, \mathcal{B}_{stagg}^{(1)}$
+	-	+	None	$\vec{S}_{stagg}, \mathcal{B}_{stagg}^{(1)}$
+	+	-	$E_1, E_2;$ $\mathcal{B}_{stagg}^{(1)}$	None
-	-	+	$\mathcal{B}_{stagg}^{(1)}$	None
$\pm$	$\mp$	-	?	?
-	-	-	?	?

Table 5.2: Summary of the properties of the phases from different instabilities in the spin sector

instabilities of this COS2 Mott insulator are concerned, we need to discuss the  $V_\perp$ -terms Eq. (5.38) that can gap out fields in the spin sector.

The instabilities depend on the signs of the couplings  $\lambda_{11}^\sigma$ ,  $\lambda_{22}^\sigma$ , and  $\lambda_{12}^\sigma$ , so there are eight cases. The simplest case is when all three  $\lambda_{ab}^\sigma > 0$  and are all marginally irrelevant. In this case, the phase is COS2[1 $\sigma$ , 2 $\sigma$ ] with two gapless modes in the spin sector. SU(2) spin invariance fixes the Luttinger parameters in the spin sector,  $g_{1\sigma} = g_{2\sigma} = 1$ . After pinning the  $\theta_{\rho+}$  and  $\varphi_{\rho-}$ , the scaling dimensions for the observables are

$$\Delta[E_{1,2}] = \Delta[\vec{V}_{1,2}] = 1/2, \quad (5.67)$$

$$\Delta[\mathcal{B}_{stagg}^{(1)}] = \Delta[\vec{S}_{stagg}] = 1. \quad (5.68)$$

Thus we have spin and bond energy correlations oscillating with period 4 and decaying with power law  $1/x$ .

### 5.3 Spin-gapped phases in orbital field

Besides the spin-gapless phase, COS2, there are other cases in which the spin sector is partially or fully gapped. Below we discuss each case in detail and summarize the main properties in Table 5.2.

### 5.3.1 $\lambda_{11}^\sigma < 0, \lambda_{22}^\sigma > 0, \lambda_{12}^\sigma > 0$

In this case, only  $\lambda_{11}^\sigma$  is relevant and flows to strong coupling. We pin  $\theta_{1\sigma}$  such that  $\cos(2\sqrt{2}\theta_{1\sigma}) = 1$  and the phase is COS1[2 $\sigma$ ]. We have  $S_{\text{stagg}}^z \sim \sin(\sqrt{2}\theta_{2\sigma})$  and  $B_{\text{stagg}}^{(1)} \sim \cos(\sqrt{2}\theta_{2\sigma})$ , so both show  $1/x$  power law correlations.

### 5.3.2 $\lambda_{11}^\sigma > 0, \lambda_{22}^\sigma < 0, \lambda_{12}^\sigma > 0$

In this case, we pin  $\theta_{2\sigma}$  such that  $\cos(2\sqrt{2}\theta_{2\sigma}) = 1$ . The phase is COS1[1 $\sigma$ ] and is qualitatively similar to the previous case.

### 5.3.3 $\lambda_{11}^\sigma, \lambda_{22}^\sigma > 0, \lambda_{12}^\sigma < 0$

In this case,  $\lambda_{11}^\sigma$  and  $\lambda_{22}^\sigma$  are marginally irrelevant while  $\lambda_{12}^\sigma$  is marginally relevant and flows to strong coupling. To minimize the energy associated with  $\lambda_{12}^\sigma$ , see Eq. (5.38), we pin  $\theta_{\sigma+}$  and  $\varphi_{\sigma-}$  to satisfy,

$$\cos(2\theta_{\sigma+}) \cos(2\varphi_{\sigma-}) = 1. \quad (5.69)$$

To characterize the resulting COS0 fully gapped phase, we note that  $E_j$  and  $\mathcal{B}_{\text{stagg}}^{(1)}$  gain expectation values. We calculate the first- and second-neighbor bond energies,

$$\begin{aligned} \delta\mathcal{B}^{(1)}(x) &\sim e^{i\frac{\pi}{2}x} e^{i\frac{\pi}{4}} \left( A_1^{(1)} E_1^\dagger + A_2^{(1)} E_2^\dagger \right) + \text{H.c.} \\ &\quad + e^{i\pi x} \mathcal{B}_{\text{stagg}}^{(1)} \\ &\simeq \tilde{A} \cos\left(\frac{\pi}{2}x + \frac{\pi}{4} + \alpha\right) + \tilde{C} \cos(\pi x), \end{aligned} \quad (5.70)$$

$$\begin{aligned} \delta\mathcal{B}^{(2)}(x) &\sim e^{i\frac{\pi}{2}x} e^{i\frac{\pi}{2}} \left( A_1^{(2)} E_1^\dagger + A_2^{(2)} E_2^\dagger \right) + \text{H.c.} \\ &\simeq \tilde{A}' \cos\left(\frac{\pi}{2}x + \frac{\pi}{2} + \alpha\right), \end{aligned} \quad (5.71)$$

where  $\tilde{A}$ ,  $\tilde{C}$ , and  $\tilde{A}'$  are some non-universal real numbers, while  $\alpha$  is fixed to one of the values  $\{\pm\frac{\pi}{4}, \pm\frac{3\pi}{4}\}$ . We see that this phase has translation symmetry breaking with period 4 as illustrated in Fig. 5.3. The four independent values of  $\alpha$  correspond to four translations of the bond pattern along  $x$ .

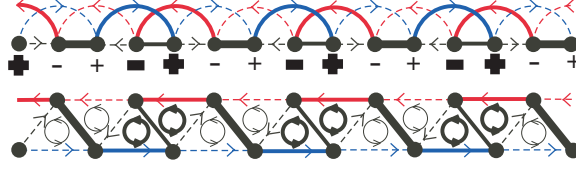


Figure 5.3: Top: Period-4 translational symmetry breaking when  $\lambda_{11}^\sigma, \lambda_{22}^\sigma > 0, \lambda_{12}^\sigma < 0$ , drawn in the 1D chain picture. The bond energy pattern is given by Eqs. (5.70)–(5.71) and the chirality pattern by Eq. (5.72). Thicker lines represent stronger bond; “+” and “-” symbols of varying boldness schematize the scalar chirality associated with sites (or equivalently with site-centered loops); and arrows on the links show the bond currents. Bottom: The same pattern in the two-leg triangular ladder drawing

To further characterize the state, we also calculate the scalar chirality,

$$\chi(x) \sim \tilde{A}'' \cos\left(\frac{\pi}{2}x - \frac{\pi}{2} + \alpha\right) + \tilde{C}'' \cos(\pi x), \quad (5.72)$$

where  $\tilde{A}''$  and  $\tilde{C}''$  are some non-universal real amplitudes, while  $\alpha$  is the same as in Eqs. (5.70)–(5.71). The period-4 pattern induced in the chirality is also shown in Fig. 5.3 and is consistent with the spontaneous period-4 bond order on top of the staggered chirality background present from the outset.

### 5.3.4 $\lambda_{11}^\sigma, \lambda_{22}^\sigma < 0, \lambda_{12}^\sigma > 0$

In this case,  $\lambda_{11}^\sigma$  and  $\lambda_{22}^\sigma$  are marginally relevant and flow to strong coupling while  $\lambda_{12}^\sigma$  is marginally irrelevant. To minimize the relevant interactions, we pin

$$\cos(2\sqrt{2}\theta_{1\sigma}) = \cos(2\sqrt{2}\theta_{2\sigma}) = 1. \quad (5.73)$$

This is a different COS0 fully gapped phase where only  $B_{\text{stagg}}^{(n=\text{odd})}$  gain expectation values. The nearest-neighbor bond energy is

$$\delta\mathcal{B}^{(1)}(x) \simeq e^{i\pi x} \mathcal{B}_{\text{stagg}}^{(1)} = \tilde{C} \cos(\pi x). \quad (5.74)$$

The physical picture of this phase is shown in Fig. 5.4.

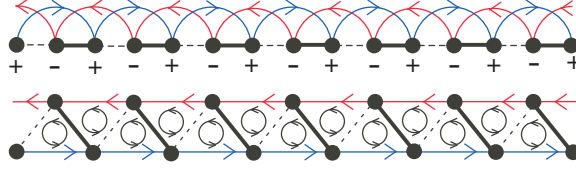


Figure 5.4: Top: Static period-2 VBS when  $\lambda_{11}^\sigma, \lambda_{22}^\sigma < 0, \lambda_{12}^\sigma > 0$ , drawn in the 1D chain picture. Note that the background staggered chirality is present from the outset due to the orbital field. Bottom: The same pattern in the two-leg triangular ladder drawing

### 5.3.5 $\lambda_{12}^\sigma < 0$ and either $\lambda_{11}^\sigma < 0$ or $\lambda_{22}^\sigma < 0$

Here, we do not know how to minimize the relevant interactions due to the competition of the pinning conditions in  $V_\perp$ , Eq. (5.38). However, we expect that, depending which terms grow faster under the RG and win, the final outcome reduces to one of the phases discussed above.

## 5.4 Discussion

In this chapter, we considered the effects of orbital field on the half-filled electronic two-leg triangular ladder. In weak coupling, the Umklapp  $\mathcal{H}^u$  (Eqs. (5.13) and (5.32)) always makes the system Mott-insulating, and we described in detail possible phases.

We would like to conclude by indicating a connection with the spin Bose-metal (SBM) theory in [29] and discussing effects of the orbital field on the SBM. It turns out that our present electronic results translate readily to this case. The SBM can be viewed as an intermediate coupling C1[ $\rho-$ ]S2 phase and is obtained in the absence of the field by gapping out the overall charge mode using an *eight-fermion* Umklapp term, whose bosonized form is [29]

$$H_8 = 2v_8 \cos(4\theta_{\rho+}). \quad (5.75)$$

Reference [29] argued that  $v_8 > 0$  is appropriate for the electronic case that corresponds to a spin-1/2 system with ring exchanges on the zigzag ladder. This gives pinning condition for the overall charge mode,

$$4\theta_{\rho+} = \pi \pmod{2\pi}. \quad (5.76)$$

Note that this pinning condition is compatible with the pinning Eq. (5.40) due to the new four-fermion Umklapp  $\mathcal{H}^u$  arising in the presence of the orbital field, so the two Umklapps lead to similar Mott insulators.

We can consider situations where the main driving force to produce Mott insulator is the eight-fermion Umklapp while the orbital field is a small perturbation onto the SBM phase. Formulated entirely in the spin language, the underlying electronic orbital fields give rise to new terms in the Hamiltonian of a form  $\vec{S}_1 \cdot [\vec{S}_2 \times \vec{S}_3]$  on each triangle circled in the same direction. [100, 101, 102] In the 1D chain language, this becomes a staggered spin chirality term  $(-1)^x \vec{S}(x-1) \cdot [\vec{S}(x) \times \vec{S}(x+1)]$ . Starting from the SBM theory in the absence of the field, this gives a new residual interaction of the same form as  $\mathcal{H}^u$  (similar to  $\chi_\pi$  in [29]). In principle, this  $\mathcal{H}^u$  can be irrelevant in the SBM phase if the one Luttinger parameter  $g_{\rho-}$  in the SBM theory [29] is less than 1/2, and in this case the orbital effects will renormalize down on long length scales. On the other hand, if this terms is relevant and pins  $\varphi_{\rho-}$ , then the resulting phases are precisely as already considered in the electronic language. In this simple-minded approach, all the phases we discussed in the chapter are proximate to the SBM phase. It would be interesting to explore spin models realizing the SBM in the presence of such additional chirality terms [29, 107].

The presented physics appears to be rather special to the two-leg ladder case, but is quite interesting in the context of such models. Perhaps the most intriguing finding is the COS2 phase with two gapless spin modes. Note that the relevant chirality interaction involves both chains and the system is far from the regime of decoupled chains. Our characterization of this state comes from the formal bosonization treatment, but it would be interesting to develop a simpler intuitive picture.

## Chapter 6

# Effects of impurities in spin Bose-metal phase on a two-leg triangular strip

To further explore other effects on the SBM phase and motivated by  $^{13}\text{C}$  NMR experiments [77, 44, 78, 21] in the organic spin liquid material that observed strong inhomogeneous line broadening at low temperatures. Theoretical [108] studied effects of nonmagnetic impurities in the candidate spin liquid with spinon Fermi surface and calculated the local spin susceptibility using mean field approach. The susceptibility has an oscillating  $2k_F$  component decaying with a  $1/x$  power law envelope. A more complete gauge theory treatment is expected to modify this power law [109, 110, 108], but one cannot calculate the exponent quantitatively.

For comparison, the 1D Heisenberg chain can be loosely viewed as a 1D version of the spinon Fermi sea state [111], and in this case the staggered component of the local susceptibility *grows* away from an impurity as  $x^{1/2}$  in the limit of zero temperature and zero field. This was discovered by Eggert and Affleck [112, 113] and is responsible for strong inhomogeneous line broadening observed in several 1D spin-1/2 chain materials [114, 115].

In this chapter we calculate effects of nonmagnetic impurities in SBM phase, in the hope of obtaining some interpolation between the 1D chain and 2D spin liquid. In short summary, we find strong enhancement of the  $2k_F$  components of the local susceptibility compared with the mean field. The susceptibility increases away from an impurity as  $\sim x^{1/2-g/4} \geq x^{1/4}$ , where  $g$  is one Luttinger parameter describing the phase, see Chapter 2.3,

and can take values  $g < 1$ . This is a slower increase than in the 1D chain, but is still a dramatic effect. We also calculate bond textures around the defect.

## 6.1 Nonmagnetic impurities in the spin Bose-metal on the ladder

The spin system resides on the two-leg triangular ladder shown in Fig. 6.1, which we can also view as a zigzag chain. Throughout we assume that the model is in the described descendant phase, which we will refer to as “spin Bose-metal” (SBM) following [29]. Examples of nonmagnetic defects are shown in Fig. 6.1 and are discussed in detail later. Generally speaking, even though there are different types of defects, we find that they eventually (at low energies) cut the system into finite sections with essentially open boundary conditions [116, 112, 113]. We can then perform analytical calculations in a semi-infinite system studying physical properties as a function of the distance from the boundary. In the following, we focus on induced textures in two measurable quantities—the bond energy and local spin susceptibility. The physics is that an impurity perturbation has components on all wavevectors and can directly “nucleate” the dominant bond energy correlations. The impurity also allows the uniform external magnetic field to couple to the dominant spin correlations, producing textures in the local susceptibility.

Following the description in Chapter 2.3, there are three gapless modes with the fixed-point Lagrangian density

$$\begin{aligned} \mathcal{L}_{\text{SBM}} = & \frac{1}{2\pi g} \left[ \frac{1}{v} (\partial_\tau \theta_{\rho-})^2 + v (\partial_x \theta_{\rho-})^2 \right] \\ & + \sum_{a=1,2} \frac{1}{2\pi} \left[ \frac{1}{v_a} (\partial_\tau \theta_{a\sigma})^2 + v_a (\partial_x \theta_{a\sigma})^2 \right]. \end{aligned} \quad (6.1)$$

Schematically, one route to this theory is via a bosonization treatment of electrons at half-filling on the ladder, where we start with two bands,  $a = 1, 2$ , and assume that the umklapp gaps out only the overall charge mode  $\theta_{\rho+}$  while the other three modes  $\theta_{\rho-}$ ,  $\theta_{1\sigma}$ , and  $\theta_{2\sigma}$  remain gapless. In addition,  $g_{1\sigma}$  and  $g_{2\sigma}$  are equal to 1 because of SU(2) spin invariance.

Reference [29] describes various observables in the SBM. For the magnetic susceptibility calculations, we will need the spin operator. The  $S^z$  component under bosonization is

$$S^z(x) \simeq \frac{\partial_x(\theta_{1\sigma} + \theta_{2\sigma})}{\sqrt{2\pi}} + \sum_Q S_Q^z(x) e^{iQx}. \quad (6.2)$$

The most important wavevectors are  $Q = \pm 2k_{F1}, \pm 2k_{F2}, \mp(k_{F1} + k_{F2}) = \pm\pi/2$ , and  $\pi$ . Each term can be expressed as in [29]:

$$S_{2k_{Fa}}^z = -e^{i\theta_{\rho+}} e^{\pm i\theta_{\rho-}} \sin(\sqrt{2}\theta_{a\sigma}), \quad (6.3)$$

$$S_{\pi/2}^z = e^{-i\theta_{\rho+}} \left[ -i\eta_{1\uparrow}\eta_{2\uparrow} e^{-i\theta_{\sigma+}} \sin(\varphi_{\rho-} + \varphi_{\sigma-}) + i\eta_{1\downarrow}\eta_{2\downarrow} e^{i\theta_{\sigma+}} \sin(\varphi_{\rho-} - \varphi_{\sigma-}) \right], \quad (6.4)$$

$$S_{\pi}^z = [\alpha \sin(2\theta_{\sigma+}) + \alpha' \sin(2\theta_{\sigma-})] \sin(2\theta_{\rho+}). \quad (6.5)$$

Throughout, we keep  $\theta_{\rho+}$  general, but it is understood to be pinned; details about the pinning value as well as the Klein factors  $\eta_{a\sigma}$  can be found in [29]. In the first line, the upper or lower sign corresponds to  $a = 1$  or  $2$ . We also introduce combinations  $\theta_{\sigma\pm} = (\theta_{1\sigma} \pm \theta_{2\sigma})/\sqrt{2}$  and similarly for the conjugate fields  $\varphi_{\sigma\pm}$ . In the last line,  $\alpha$  and  $\alpha'$  are independent numerical constants.

When discussing nonmagnetic defects and also in the bond energy texture calculations, we need an  $n$ th neighbor bond energy operator like

$$B^{(n)}(x) \equiv \vec{S}_x \cdot \vec{S}_{x+n}. \quad (6.6)$$

The bosonized form can be obtained from [29]:

$$B^{(n)} \simeq \sum_{a=1,2} B_{2k_{Fa}}^{(n)} + B_{4k_{F1}}^{(n)} + B_{\pi/2}^{(n)}, \quad (6.7)$$

where we keep only the most important wavevectors and

$$B_{2k_{F_a}}^{(n)}(x) \sim \cos(\sqrt{2}\theta_{a\sigma}) \quad (6.8)$$

$$\times \cos(2k_{F_a}x + \gamma_{2k_{F_a}}^{(n)} + \frac{\pi}{2} + \theta_{\rho+} \pm \theta_{\rho-}),$$

$$B_{4k_{F_1}}^{(n)}(x) \sim \cos(4k_{F_1}x + \gamma_{4k_{F_1}}^{(n)} + 2\theta_{\rho+} + 2\theta_{\rho-}), \quad (6.9)$$

$$B_{\pi/2}^{(n)}(x) \sim \quad (6.10)$$

$$-i\eta_{1\uparrow}\eta_{2\uparrow} \cos\left(\frac{\pi}{2}x + \gamma_{\frac{\pi}{2}}^{(n)} - \theta_{\rho+} - \theta_{\sigma+}\right) \sin(\varphi_{\rho-} + \varphi_{\sigma-})$$

$$-i\eta_{1\downarrow}\eta_{2\downarrow} \cos\left(\frac{\pi}{2}x + \gamma_{\frac{\pi}{2}}^{(n)} - \theta_{\rho+} + \theta_{\sigma+}\right) \sin(\varphi_{\rho-} - \varphi_{\sigma-}).$$

We do not show real factors in front of all terms. Here  $\gamma_Q^{(n)}$  are phases that depend on  $Q$  and the bond type:

$$\gamma_Q^{(n)} = nQ/2, \quad (6.11)$$

valid for  $Q \neq \pi$ . Note also that since  $4k_{F_2} = -4k_{F_1} \pmod{2\pi}$ , there is only one independent term  $B_{4k_{F_1}}$ .

### 6.1.1 Nonmagnetic defects treated as perturbations

When a nonmagnetic defect is introduced at  $x_0$ , we can treat it as a local perturbation in the Hamiltonian [112, 116]. Figure 6.1 shows some possible defects; the corresponding perturbations are

$$\delta H^{(1)} \sim \vec{S}(x_0) \cdot \vec{S}(x_0 + 1) \sim B^{(1)}(x_0), \quad (6.12)$$

$$\delta H^{(2)} \sim \vec{S}(x_0 - 1) \cdot \vec{S}(x_0 + 1) \sim B^{(2)}(x_0 - 1), \quad (6.13)$$

$$\delta H^{(3)} \sim \vec{S}(x_0) \cdot [\vec{S}(x_0 - 1) + \vec{S}(x_0 + 1)] \quad (6.14)$$

$$\sim B^{(1)}(x_0 - 1) + B^{(1)}(x_0), \quad (6.15)$$

$$\delta H^{(4)} \sim \vec{S}(x_0) \cdot [\vec{S}(x_0 - 2) + \vec{S}(x_0 + 2)] \quad (6.16)$$

$$\sim B^{(2)}(x_0 - 2) + B^{(2)}(x_0). \quad (6.17)$$

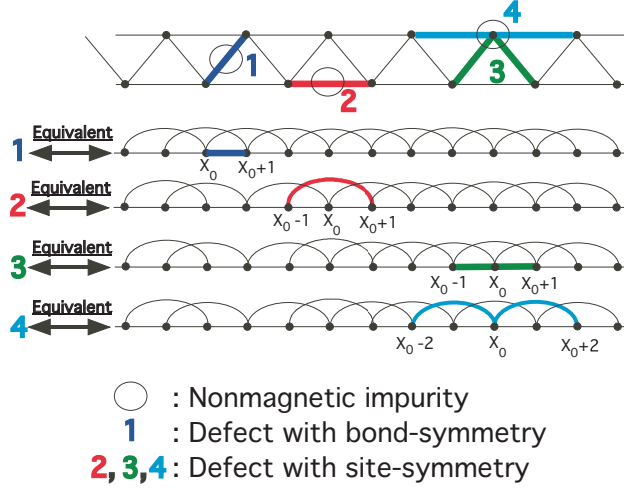


Figure 6.1: The top figure represents the original 2-leg triangular ladder model with ring exchanges, and the thick lines represent the defects due to the impurities. The bottom figures represent the corresponding defects in the equivalent 1D model [29]. 1 represents the defect symmetric with respect to a bond center, while 2, 3, and 4 represent defects symmetric about a site of the 1D chain. In general, different impurities will lead to different fixed points. Impurity 1 will likely lead to a fixed point with decoupled semi-infinite systems and a nonmagnetic cluster containing an even number of sites, while impurities 2, 3, and 4 will likely lead to a fixed point with decoupled semi-infinite systems and an effective spin formed by a cluster with an odd number of sites.

Here  $B^{(1)}$  and  $B^{(2)}$  are given by Eq. (6.7). We can characterize the defects by symmetry. In the 1D chain picture,  $\delta H^{(1)}$  represents defects symmetric under inversion in a bond center, while  $\delta H^{(2,3,4)}$  are defects symmetric under inversion in a site. One can readily check that  $\delta H^{(2,3,4)}$  give equivalent expressions up to constant factors and, importantly, contain all  $Q$  modes in general. We see that although the defects can be characterized as two distinct symmetry types  $\delta H^{(1)}$  and  $\delta H^{(2)}$ , the perturbations to the Hamiltonian have the same dynamical field content and differ only by constant phases. This is unlike the Bethe phase of the 1D Heisenberg chain where a bond-symmetric perturbation contains a relevant contribution from a  $Q = \pi$  bond operator while a site-symmetric perturbation does not [112].

The scaling dimensions of the different contributions are

$$\Delta[B_{2k_{Fa}}] = \frac{1}{2} + \frac{g}{4}, \quad (6.18)$$

$$\Delta[B_{4k_{F1}}] = g, \quad (6.19)$$

$$\Delta[B_{\pi/2}] = \frac{1}{2} + \frac{1}{4g}. \quad (6.20)$$

In the spin Bose-metal phase we have  $g \leq 1$ , so the  $2k_{Fa}$  and  $4k_{F1}$  terms are always relevant 0+1D perturbations, while the  $\pi/2$  term is relevant if  $g > 1/2$ . The relevant perturbations grow and one scenario is that they eventually pin the fields at the origin. Physically this leads to breaking the chain into two decoupled semi-infinite systems, which we can then study separately. The pinning conditions on the fields at the defect can be guessed by considering the most relevant perturbation and minimizing the corresponding energy. We expect the  $B_{2k_{Fa}}$  and  $B_{4k_{F1}}$  terms to be the dominant, which would

$$\text{Pin } \theta_{1\sigma}(x_0), \theta_{2\sigma}(x_0), \theta_{\rho-}(x_0). \quad (6.21)$$

This is the case that we focus on. In Appendix 6.B we will consider pinning conditions preferred by the  $B_{\pi/2}$  term, which may be of interest in the borderline case  $g = 1$ .

A comment is in order. On physical grounds, the symmetry of the defect perturbation is important. For the case with no site inversion symmetry like the impurity 1 in Fig. 6.1, we can envision a possible outcome of the RG growth of the perturbation by considering a situation where the defect bond is strong. The two spins will form a singlet, and if we integrate it out, we get two semi-infinite chains weakly coupled to each other, which under further RG will eventually flow to decoupled semi-infinite systems with pinned values of the fields at the boundary. We can envision more general situations where an even number of spins will form a strongly coupled cluster with a singlet ground state, and upon integrating this out we again have two weakly coupled semi-infinite systems. Below, we will consider a fixed point of a semi-infinite system and give physical calculations of the bond textures and the oscillating susceptibility near the boundary (impurity). Turning to the case with impurities with site inversion symmetry like 2, 3, 4 in Fig. 6.1, such reasoning would give us a

half-integer spin (formed by some effective strongly coupled cluster with an odd number of sites) weakly coupled to two semi-infinite systems. This would need to be analyzed further, which we briefly discuss in Chapter 6.1.3.

### 6.1.2 Physical calculations of oscillating susceptibility and bond textures in the fixed-point theory of semi-infinite chains

From now on, we set the location of the defect to be the origin. We work with a semi-infinite system with specified boundary conditions at the origin and calculate the bond energy texture

$$\langle B(x) \rangle = \sum_{a=1,2} \langle B_{2k_{F_a}}(x) \rangle + \langle B_{4k_{F_1}}(x) \rangle + \langle B_{\frac{\pi}{2}}(x) \rangle. \quad (6.22)$$

We also calculate the local spin susceptibility, which can be measured in Knight shift experiments. We will see that there are contributions that oscillate as a function of distance from the boundary:  $\chi(x) = \chi^{uni}(x) + \chi^{osc}(x)$ ; in fact,  $\chi^{osc}(x)$  dominates over  $\chi^{uni}(x)$  and can produce strong inhomogeneous broadening of the NMR lineshapes. The local spin susceptibility  $\chi(i)$  at a lattice site  $i$  measured in a small uniform magnetic field  $h$  is

$$\chi(i) \equiv \left. \frac{\partial \langle S_i^z \rangle}{\partial h} \right|_{h=0} = \beta \langle S_i^z S_{tot}^z \rangle, \quad (6.23)$$

where  $S_{tot}^z \equiv \sum_j S_j^z$  is the total spin and  $\beta$  is the inverse temperature. Rewriting the spin operators in terms of bosonic fields introduced above,

$$\chi^{osc}(x) = \beta \left\langle S_{osc}^z(x) \int_0^\infty dy S_{uni}^z(y) \right\rangle, \quad (6.24)$$

where  $S_{osc}^z = \sum_Q e^{iQx} S_Q^z$  and we are interested in  $Q = 2k_{F_1}, 2k_{F_2}, \pi/2$ , and  $\pi$ ; while  $S_{uni}^z(y) = \sum_{a=1,2} \frac{\partial_y \theta_{a\sigma}(y)}{\sqrt{2\pi}}$ . Hence we define

$$\chi_Q^{osc} \equiv \beta \langle e^{iQx} S_Q^z(x) \int_0^\infty dy S_{uni}^z(y) + \text{c.c.} \rangle. \quad (6.25)$$

We consider the pinning Eq. (6.21) driven by the relevant local terms  $B_{2k_{F_a}}$ ,  $B_{4k_{F_1}}$ ; in order to minimize these energies, the natural pinning values of  $\theta_{1\sigma}(0)$  and  $\theta_{2\sigma}(0)$  are

$$\cos[\sqrt{2}\theta_{a\sigma}(0)] = \pm 1 \Rightarrow \sqrt{2}\theta_{a\sigma}(0) = \text{integer} \times \pi. \quad (6.26)$$

The pinning value of the field  $\theta_{\rho-}$  depends on the details such as the amplitudes and phases  $\gamma$  in Eqs. (6.8)–(6.10). As discussed in Appendix 6.A, the pinning of a  $\theta$  at the origin implies stronger fluctuation of the dual field  $\varphi$  and consequently  $\langle e^{i\varphi(x)} \rangle = 0$ .

*Bond energy texture* is given by Eq. (6.22). The  $\langle B_{\pi/2}(x) \rangle$  term vanishes and the other contributions can be easily derived by applying the formulas in Appendix 6.A:

$$\langle B_{2k_{F_a}}(x) \rangle \simeq \frac{A_{2k_{F_a}} \cos(2k_{F_a}x + \delta_{2k_{F_a}})}{\left[ \frac{v_a\beta}{\pi} \sinh\left(\frac{2\pi x}{v_a\beta}\right) \right]^{\frac{1}{2}} \left[ \frac{v\beta}{\pi} \sinh\left(\frac{2\pi x}{v\beta}\right) \right]^{\frac{g}{4}}}, \quad (6.27)$$

$$\langle B_{4k_{F_1}}(x) \rangle \simeq \frac{A_{4k_{F_1}} \cos(4k_{F_1}x + \delta_{4k_{F_1}})}{\left[ \frac{v\beta}{\pi} \sinh\left(\frac{2\pi x}{v\beta}\right) \right]^g}, \quad (6.28)$$

where  $a = 1, 2$ ;  $A_Q$  are some amplitudes; and  $\delta_Q$  are phases that depend on the pinned  $\theta$  values at the origin and are ultimately determined by the details of the defect. At low temperature  $T \rightarrow 0$ , we have the following behavior as a function of the distance  $x$  from the open boundary (defect):

$$\langle B_{2k_{F_a}}(x) \rangle \sim \frac{\cos(2k_{F_a}x + \delta_{2k_{F_a}})}{x^{\frac{1}{2} + \frac{g}{4}}}, \quad (6.29)$$

$$\langle B_{4k_{F_1}}(x) \rangle \sim \frac{\cos(4k_{F_1}x + \delta_{4k_{F_1}})}{x^g}. \quad (6.30)$$

Thus, at low temperature the bond energy texture around the impurity reveals the correlations present in the system, and the physics can be viewed as a “nucleation” of the dominant “bond orders” near the defect. If we can tune the Luttinger parameter  $g$ , we see that there are two regimes: for  $2/3 < g < 1$  the  $2k_{F_a}$  terms dominate, while for  $g < 2/3$  the  $4k_{F_1}$  dominates.

Turning to the *oscillating susceptibility*, the  $\chi_{\pi/2}^{osc}$  term vanishes and only the  $\chi_{2k_{F_a}}^{osc}$  and

$\chi_\pi^{osc}$  contribute to the final result. Applying the formulas from Appendix 6.A gives

$$\chi_{2k_{Fa}}^{osc} \simeq \frac{C_{2k_{Fa}} \cdot x \cdot \cos(2k_{Fa}x + \delta'_{2k_{Fa}})}{\left[\frac{v_a\beta}{\pi} \sinh\left(\frac{2\pi x}{v_a\beta}\right)\right]^{\frac{1}{2}} \left[\frac{v\beta}{\pi} \sinh\left(\frac{2\pi x}{v\beta}\right)\right]^{\frac{g}{4}}}, \quad (6.31)$$

$$\chi_\pi^{osc} \simeq \frac{C_\pi \cdot x \cdot (-1)^x}{\left[\frac{v_1\beta}{\pi} \sinh\left(\frac{2\pi x}{v_1\beta}\right)\right]^{\frac{1}{2}} \left[\frac{v_2\beta}{\pi} \sinh\left(\frac{2\pi x}{v_2\beta}\right)\right]^{\frac{1}{2}}}, \quad (6.32)$$

where  $a = 1, 2$ ;  $C_Q$  are some constant amplitudes; and  $\delta'_Q$  some phases absorbing all pinned field values and eventually determined by the details of the defect. At low temperatures  $T \rightarrow 0$ , the oscillating susceptibilities at  $2k_{Fa}$  and  $\pi$  become

$$\chi_{2k_{Fa}}^{osc}(x) \sim x^{\frac{1}{2} - \frac{g}{4}} \cos(2k_{Fa}x + \delta'_{2k_{Fa}}), \quad (6.33)$$

$$\chi_\pi^{osc}(x) \sim x^0 (-1)^x. \quad (6.34)$$

The envelope function in the first line satisfies  $x^{\frac{1}{2} - \frac{g}{4}} \geq x^{\frac{1}{4}}$ , which comes from the condition  $g < 1$ . Therefore, at low temperatures the oscillating susceptibility at  $2k_{Fa}$  actually *increases* with the distance from the open end. On the other hand, the oscillating susceptibility at  $\pi$  reaches a constant amplitude.

To conclude the discussion of the semi-infinite system with the boundary conditions Eq. (6.21), we note that this fixed point is stable [e.g., the scaling dimension of  $B_{\pi/2}(0)$  becomes  $1/2 + 1/(2g) > 1$ , so it is irrelevant]. The boundary spin operator has scaling dimension 1: e.g.,  $S_{\text{bound}}^z \sim \partial_x(\theta_{1\sigma} + \theta_{2\sigma})$  at the boundary. Knowing the fixed-point theory of the semi-infinite chain, we can briefly discuss other situations with impurities [112, 117, 118, 119]. (For a recent review of impurity problems, see [120].)

## 6.1.3 Other situations with impurities

### 6.1.3.1 Weakly coupled semi-infinite systems

In this case, we imagine two semi-infinite chains coupled to each other at the origin. Since in each semi-infinite system the scaling dimension of the boundary spin operator is 1, the spin-spin coupling between the two systems is irrelevant and they will decouple at low

energies. This is the reason why a nonmagnetic impurity like 1 in Fig. 6.1 breaks the system into two halves at low energies and the physical calculations in Chapter 6.1.2 apply generically.

### 6.1.3.2 Spin- $\frac{1}{2}$ impurity coupled to a semi-infinite system

In this case, the spin-1/2 impurity is coupled to the boundary spin operator which contains contributions from both “ $1\sigma$ ” and “ $2\sigma$ ” channels,  $\delta H = \lambda \vec{S}_{\text{imp}} \cdot (\vec{S}_{\text{bound},1} + \vec{S}_{\text{bound},2}) \rightarrow \lambda_1 \vec{S}_{\text{imp}} \cdot \vec{S}_{\text{bound},1} + \lambda_2 \vec{S}_{\text{imp}} \cdot \vec{S}_{\text{bound},2}$ . (The “ $\rho-$ ” sector does not enter in the important terms.) The couplings  $\lambda_1$  and  $\lambda_2$  are both marginal. If they are marginally irrelevant, the impurity spin will decouple. If one of the couplings is marginally relevant while the other is marginally irrelevant, the relevant coupling will grow and the impurity spin will be absorbed into the corresponding channel. Finally, if both of the couplings are relevant, since the two channels are not equivalent, one coupling will grow faster; a likely scenario is that the impurity spin will be absorbed into the dominating channel and eventually the two channels will decouple.

### 6.1.3.3 Two semi-infinite systems coupled symmetrically to a spin- $\frac{1}{2}$ impurity

Now let us take two semi-infinite chains and couple them together through a spin-1/2 impurity symmetrically. This case is also relevant for the site-symmetric nonmagnetic impurities like impurity 2, 3, and 4 in Fig. 6.1: The reason is that, because of the site inversion symmetry, the non-magnetic impurity affects an even number of bonds which couple an odd number of spins; then we can imagine a strongly-coupled cluster with the odd number of spins, which will effectively behave as a half-integer spin weakly coupled to the left and right semi-infinite systems.

The situation is more complex than in the previous subsection because we now have symmetry between the two semi-infinite systems, reminiscent of the 2-channel Kondo problem. We can imagine the following possibilities. When all couplings are marginally irrelevant, the impurity spin and the two semi-infinite systems will decouple at low energies (and the physical calculations of textures in Chapter 6.1.2 are valid in this case). Suppose

now we have marginally relevant couplings and the dominant growth is for the channels  $1\sigma$  in the two semi-infinite systems. One is tempted to speculate about the possibility of “healing” the channels  $1\sigma$  across the impurity, while the channels  $2\sigma$  remain open. However, it is likely that this is not a stable fixed point in the presence of the allowed terms in the Hamiltonian coming from the microscopic ladder system. While the eventual outcome is not clear and depends on details, on physical grounds we again expect arriving at some stage at a fixed point with some odd number of spins forming a half-integer spin that is decoupled from two semi-infinite systems.

## 6.2 Conclusions

To summarize, following the theoretical description of the spin Bose-metal phase in the triangular strip spin-1/2 model with ring exchanges, we discussed the effects due to different types of impurities. The defects can have additional bond or site symmetry in the 1D zigzag chain language. We first treated the defects as local perturbations in the Hamiltonian and saw that all types produce relevant perturbations, eventually breaking the system into two halves and a separate decoupled cluster of spins. In the bond-symmetric case (or more general cases with no symmetries) the decoupled cluster is likely to be non-magnetic, while in the site-symmetric case it has half-integer spin, and the details of such fixed points depend on the microscopic details [112, 118, 119]. This analysis also motivated appropriate boundary conditions for pinning the fields in the fixed point theory for the semi-infinite systems.

For such a semi-infinite chain, we calculated the bond energy texture near the boundary and found power law decays Eqs. (6.27, 6.28) of the oscillating components at wavevectors  $2k_{Fa}$ ,  $4k_{F1}$ . The dominant power law switches from the  $2k_{Fa}$  to the  $4k_{F1}$  when the Luttinger parameter  $g$  drops below  $2/3$ . We suggest that characterizing such bond textures in numerical studies, e.g., DMRG [29], could be useful for determining the Luttinger parameter  $g$  of the SBM theory.

We also calculated the oscillating susceptibilities at  $2k_{Fa}$  and  $\pi$ , Eqs. (6.31, 6.32), which behave differently at low temperatures. The susceptibilities at  $2k_{Fa}$  actually *increase* with

the distance from the boundary in the limit of zero temperature (and zero field), while the susceptibility at  $\pi$  becomes distance independent. Transfer-matrix density-matrix renormalization group (TMRG) [117, 118, 121, 122, 123] technique can measure local susceptibility at finite temperature and can be useful for exploring the susceptibility near defects in numerical studies. The rate of increase at  $2k_{Fa}$  is slower than in the 1D chain [113], but would still produce strong NMR line broadening at low temperatures. Of course, this is the result for the long-distance behavior along the 1D direction. If we are thinking about the 2D spin liquid, we would likely expect a power-law decay away from an impurity [109, 110, 108]. Nevertheless, the persistence of the oscillating susceptibilities on the quasi-1D ladders suggests that in the 2D case the decay may be slow and also produce significant inhomogeneous line broadening. Finally, in this chapter, we focused on non-magnetic impurities and the simplest “fixed-point” model with open boundary. We have not touched interesting and experimentally relevant crossovers present for a magnetic impurity weakly coupled to the system [117, 118]. Here again theoretical and numerical studies similar to [117, 118] could be very helpful, for example, in estimating the size of the Kondo screening cloud, which is an additional and potentially large effect near the magnetic impurity.

## 6.A One-mode theory on a semi-infinite chain

For the simplest case [112, 113, 118, 124] consider a one-mode theory on a semi-infinite chain with pinned value at the origin,  $\theta(0, \tau) = \text{pinned} = \theta_0$ . The action is

$$S = \int_0^\infty dx \int_0^\beta d\tau \frac{1}{2\pi g} \left[ v(\partial_x \theta)^2 + \frac{1}{v}(\partial_\tau \theta)^2 \right]. \quad (6.35)$$

The correlation functions needed in this chapter are

$$\langle e^{iu\theta(x,\tau)} \rangle \simeq \frac{Ae^{iu\theta_0}}{\left[\frac{v\beta}{\pi} \sinh\left(\frac{2\pi x}{v\beta}\right)\right]^{\frac{u^2g}{4}}}, \quad (6.36)$$

$$\left\langle e^{iu\theta(x,\tau)} \int_0^\infty dy \frac{\partial_y \theta(y, \tau')}{\pi} \right\rangle = \frac{iugx}{\beta v} \times \langle e^{iu\theta(x,\tau)} \rangle \quad (6.37)$$

$$\simeq \frac{iugx}{\beta v} \frac{Ae^{iu\theta_0}}{\left[\frac{v\beta}{\pi} \sinh\left(\frac{2\pi x}{v\beta}\right)\right]^{\frac{u^2g}{4}}}, \quad (6.38)$$

$$\langle e^{iu\varphi(x,\tau)} \rangle = 0. \quad (6.39)$$

Here  $u$  is a parameter depending on which quantity is being measured and  $A$  is some real constant. The  $\langle e^{iu\theta} \rangle$  is non-zero because of the pinning at  $x = 0$  and decays as a power-law away from the origin at  $T = 0$ . On the other hand, the conjugate field  $\varphi$  fluctuates more strongly than in the bulk and  $\langle e^{iu\varphi} \rangle = 0$  everywhere.

We can similarly consider a one mode theory with the dual field pinned at the origin,  $\varphi(0, \tau) = \text{pinned} = \varphi_0$ . It is convenient to work with the action

$$S = \int_0^\infty dx \int_0^\beta d\tau \frac{g}{2\pi} \left[ v(\partial_x \varphi)^2 + \frac{1}{v}(\partial_\tau \varphi)^2 \right]. \quad (6.40)$$

The correlation function needed is

$$\langle e^{iu\varphi(x,\tau)} \rangle \simeq \frac{\tilde{A}e^{iu\varphi_0}}{\left[\frac{v\beta}{\pi} \sinh\left(\frac{2\pi x}{v\beta}\right)\right]^{\frac{u^2}{4g}}}, \quad (6.41)$$

where  $\tilde{A}$  is some constant.

## 6.B Calculations in a fixed-point theory of a semi-infinite system with pinned $\theta_{\sigma+}(0)$ , $\varphi_{\sigma-}(0)$ , and $\varphi_{\rho-}(0)$

Here we consider the theory Eq. (6.1) on a semi-infinite chain with boundary conditions

$$\text{Pin } \theta_{\sigma+}(0), \varphi_{\sigma-}(0), \varphi_{\rho-}(0). \quad (6.42)$$

This can arise if we minimize the  $B_{\pi/2}(0)$  perturbation instead of the  $B_{2k_{F\alpha}}(0)$  and  $B_{4k_{F1}}(0)$ , see Eqs. (6.8)–(6.10). Coming from the microscopic ladder spin system in the SBM phase with  $g < 1$ , this fixed point is unstable to the allowed  $B_{2k_{F\alpha}}(0)$  terms. Nevertheless, it can be of interest in the special case with  $g = 1$ , which is realized, e.g., by the Gutzwiller wavefunctions or at phase transitions out of the SBM [29]. The calculations of the physical textures are simple and we summarize these below.

Because of the pinning Eq. (6.42), the dual fields  $\varphi_{\sigma+}$ ,  $\theta_{\sigma-}$ , and  $\theta_{\rho-}$  fluctuate more strongly. The only non-vanishing term in the *bond energy texture* is

$$\langle B(x) \rangle = \langle B_{\pi/2}(x) \rangle. \quad (6.43)$$

If  $v_1 = v_2$ , then “ $\sigma+$ ” and “ $\sigma-$ ” variables decouple and we can apply the formulas in Appendix 6.A. In the general case  $v_1 \neq v_2$ , the calculations are more demanding but the result is simple:

$$\langle B_{\pi/2}(x) \rangle \simeq \frac{A_{\pi/2} \cos\left(\frac{\pi}{2}x + \delta_{\pi/2}\right)}{\left[\frac{v_r\beta}{\pi} \sinh\left(\frac{2\pi x}{v_r\beta}\right)\right]^{\frac{1}{2}} \left[\frac{v\beta}{\pi} \sinh\left(\frac{2\pi x}{v\beta}\right)\right]^{\frac{1}{4g}}}, \quad (6.44)$$

where  $\frac{1}{v_r} = \frac{1}{2} \left( \frac{1}{v_1} + \frac{1}{v_2} \right)$ ,  $A_{\pi/2}$  is some amplitude and  $\delta_{\pi/2}$  is a constant phase. The pinned values at the origin as well as the Klein numbers enter in the same way as they enter the assumed minimization of  $B_{\pi/2}(0)$ , Eq. (6.10), so the final result depends only on the physical details of this term at the origin. In the limit  $T \rightarrow 0$ ,

$$\langle B_{\pi/2}(x) \rangle \sim \frac{\cos\left(\frac{\pi}{2}x + \delta_{\pi/2}\right)}{x^{\frac{1}{2} + \frac{1}{4g}}}. \quad (6.45)$$

As for the *oscillating susceptibility*, similarly to the bond energy texture, only the  $Q = \pi/2$  term contributes to the final result. Again, for  $v_1 = v_2$  we can apply the formulas in Appendix 6.A, while in the general case we get

$$\chi_{\pi/2}^{osc} \simeq \frac{C \cdot x \cdot \cos\left(\frac{\pi}{2}x + \delta'_{\pi/2}\right)}{\left[\frac{v_r\beta}{\pi} \sinh\left(\frac{2\pi x}{v_r\beta}\right)\right]^{\frac{1}{2}} \left[\frac{v\beta}{\pi} \sinh\left(\frac{2\pi x}{v\beta}\right)\right]^{\frac{1}{4g}}}, \quad (6.46)$$

where  $C_{\pi/2}$  is some amplitude and  $\delta'_{\pi/2}$  is a constant phase absorbing all pinned values and eventually determined by the details of the defining energy  $B_{\pi/2}(0)$ . In the low temperature limit  $T \rightarrow 0$ ,

$$\chi_{\pi/2}^{osc} \sim x^{\frac{1}{2} - \frac{1}{4g}} \cos\left(\frac{\pi}{2}x + \delta'_{\pi/2}\right). \quad (6.47)$$

## Chapter 7

# **SU(2)-invariant Majorana spin liquid with stable parton Fermi surfaces in an exactly solvable model**

In this chapter we want to explore the properties of the new class of gapless spin liquids with Majorana excitations—SU(2)-invariant Majorana spin liquids (MSL). Much interest in this theoretical studies is motivated by recent experimental realizations in 2D organic compounds  $\text{EtMe}_3\text{Sb}[\text{Pd}(\text{dmit})_2]_2$  and  $\kappa\text{-(ET)}_2\text{Cu}_2(\text{CN})_3$  [15, 16, 17, 18, 19, 20, 21, 22, 23, 24, 25, 26]. One proposal with Gutzwiller-projected Fermi sea wave function [27, 125] is an appealing candidate but does not appear to be able to capture all experimental phenomenology. Searching for alternatives, many possible proposals have been presented [95, 126, 127, 128]. Very recently, Biswas et al. [128] proposed an SU(2)-invariant MSL, which we find fascinating and in need of more attention. Motivated by this proposal, here we realize such long-wavelength quantum spin liquids in an exactly solvable microscopic model. Following the route discovered by Kitaev [14] and generalized to produce many other exactly solvable models [129, 130, 131, 132, 133, 134, 135, 136, 137, 138, 139, 140, 141, 142, 143, 144, 145, 146, 147, 148], in particular with SU(2) spin invariance [145, 147] or with parton Fermi surfaces [140, 142, 146], we find a Kitaev-type model with both SU(2)-invariance and parton Fermi surfaces.

Our model is realized using both spin-1/2 and orbital degrees of freedom [149, 147] at each site of a decorated square lattice [140]. The system can be reduced to three species of free Majorana fermions coupled to background  $Z_2$  gauge fields such that it is exactly

solvable and parton Fermi surfaces are realized. We formulate long wavelength description in terms of an occupied Fermi pocket of three complex fermions ( $f^x$ ,  $f^y$ ,  $f^z$ ) that transform as a vector under spin rotation. For general illustration (and also for preventing possible pairing instabilities away from the exactly solvable limit), we consider a model that lacks time-reversal and lattice inversion symmetries. Because of the exact solvability, we can learn much reliable physics information about such MSL.

Specifically, we study spin correlations and spin-nematic correlations in our model. The main result is that these correlations have the *same* dominant power-law behaviors with  $1/|\mathbf{r}|^3$  envelope in real space and oscillations at incommensurate wavevectors which form what we call singular surfaces [3, 60, 150] in the momentum space. Because of the  $Z_2$  nature of the QSL and the absence of the time-reversal and inversion symmetries, there are additional non-trivial  $\pm(\mathbf{k}_{FR} + \mathbf{k}_{FL})$  and  $\pm 2\mathbf{k}_F$  critical surfaces besides the more familiar  $\mathbf{k}_{FR} - \mathbf{k}_{FL}$  surface in the correlations.

The model is still exactly solvable in the presence of Zeeman magnetic field. An interesting property is that the Zeeman field only couples to the  $f^x$  and  $f^y$  fermions while the  $f^z$  fermion remains unaltered and therefore the  $f^z$  Fermi surface remains and always gives gapless excitations. We calculate the magnetization as a function of magnetic field. Interestingly, there is a plateau phase in which the spins are half-polarized with short-ranged spin correlations while the Fermi surface of  $f^z$  still exists and gives gapless excitations, which can be detected using local energy operator like bond energy. [63]

The chapter is organized as follows. In Chapter 7.1, we define the model on the decorated square lattice and solve it and discuss qualitative properties of the spin liquid phase. In Chapter 7.2, we define the spin correlation functions and spin-nematic correlation functions. In Chapter 7.2.1 we provide a theoretical approach to describe the long-distance behavior of the correlations. In Chapter 7.2.2, we present exact numerical calculations of the spin correlations and spin-nematic correlations. In Chapter 7.3, we consider our model in the presence of the Zeeman magnetic field and specifically calculate the magnetization curve as a function of the field. We conclude with some discussion.

## 7.1 SU(2)-invariant Majorana spin liquid with stable Fermi surfaces

Motivated by the ideas from Baskaran et al. [140], Yao et al. [147], and Wang [145], we construct an exactly solvable Kitaev-type model including both orbital and spin degrees of freedom with spin-rotation invariance. The Hamiltonian is

$$\mathcal{H} = \mathcal{H}_0 + H_{TRB} + K_\diamond \sum_\diamond W_\diamond + K_\circ \sum_\circ W_\circ, \quad (7.1)$$

where,

$$\mathcal{H}_0 = \sum_{\lambda\text{-link } \langle jk \rangle} J_{jk}^\lambda (\tau_j^\lambda \tau_k^\lambda) (\vec{\sigma}_j \cdot \vec{\sigma}_k), \quad (7.2)$$

$$\begin{aligned} \mathcal{H}_{TRB} = \frac{\hbar}{2} \sum_\diamond \left[ (\tau_3^x \tau_4^z \tau_1^y - \tau_1^x \tau_2^z \tau_3^y) (\vec{\sigma}_3 \cdot \vec{\sigma}_1) \right. \\ \left. + (\tau_4^y \tau_1^z \tau_2^x - \tau_2^y \tau_3^z \tau_4^x) (\vec{\sigma}_4 \cdot \vec{\sigma}_2) \right], \end{aligned} \quad (7.3)$$

$$W_\diamond = \tau_1^z \tau_2^z \tau_3^z \tau_4^z, \quad (7.4)$$

$$W_\circ = \tau_3^x \tau_2^x \tau_5^y \tau_6^y \tau_7^x \tau_8^x \tau_9^y \tau_{10}^y. \quad (7.5)$$

The graphical representation of the model is shown in Fig. 7.1. At each site of the decorated square lattice, there are spin and orbital degrees of freedom.  $\mathcal{H}_0$  is a Kugel-Khomskii-like Hamiltonian with  $\vec{\sigma}$  being the spin-1/2 Pauli matrices and  $\vec{\tau}$  being the Pauli matrices acting on the orbital states [149, 147]. The site labels in Eqs. (7.3)–(7.5) are shown in Fig. 7.1.  $\mathcal{H}_{TRB}$  represents an additional time-reversal-breaking (TRB) interaction in the small diamonds [147] (in principle, all four terms in the square brackets can have independent couplings). The reason for introducing the TRB and allowing different  $J^\lambda$  couplings in  $\mathcal{H}_0$  that break the lattice point group symmetries is to avoid worrying about Cooper pair instabilities of the parton Fermi surface away from the exactly solvable limit.

In addition, there are two types of elementary plaquettes (square and octagon) in the decorated square lattice (Fig. 7.1), and two types of local conserved operators,  $W_\diamond$  for the

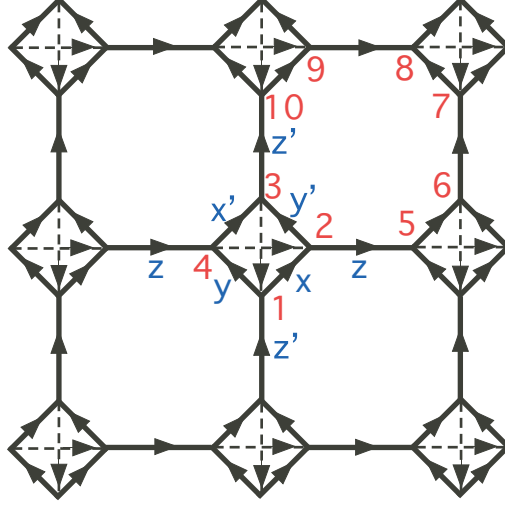


Figure 7.1: Graphical representation of the exactly solvable Kitaev-type model and its solution in the zero flux sector. The  $c^{x,y,z}$  Majoranas propagate with pure imaginary hopping amplitudes specified by the couplings  $J^x$ ,  $J^y$ ,  $J^z$ ,  $J^{x'}$ ,  $J^{y'}$ , and  $J^{z'}$ ; the signs in our chosen gauge are indicated by the arrows.

squares and  $W_{\square}$  for the octagons in Eq. (7.4) and Eq. (7.5). The plaquette operators  $W_p$  commute among themselves and with all other terms in the Hamiltonian and the  $K_p$  terms are added to stabilize particular flux sector (see Fig. 7.1).

Introducing Majorana representation of spin-1/2 [151, 152, 153], we write the spin and orbital operators as

$$\sigma_j^\alpha = -\frac{i}{2} \sum_{\beta,\gamma} \epsilon^{\alpha\beta\gamma} c_j^\beta c_j^\gamma, \quad (7.6)$$

$$\tau_j^\alpha = -\frac{i}{2} \sum_{\beta,\gamma} \epsilon^{\alpha\beta\gamma} d_j^\beta d_j^\gamma. \quad (7.7)$$

On each site  $j$  of the decorated square lattice, we realize the physical four-dimensional Hilbert space using six Majorana fermions  $c_j^x$ ,  $c_j^y$ ,  $c_j^z$ ,  $d_j^x$ ,  $d_j^y$ , and  $d_j^z$ , with the constraint  $D_j \equiv -ic_j^x c_j^y c_j^z d_j^x d_j^y d_j^z = 1$  (namely, for any physical state  $|\Phi\rangle_{\text{phys}}$ , we require  $D_j |\Phi\rangle_{\text{phys}} = |\Phi\rangle_{\text{phys}}$ ). Therefore,  $\sigma_j^\alpha \tau_j^\beta |\Phi\rangle_{\text{phys}} = ic_j^\alpha d_j^\beta |\Phi\rangle_{\text{phys}}$ .

In terms of the Majoranas, the Hamiltonian can be rephrased as

$$\mathcal{H}_0 = i \sum_{\langle jk \rangle} \hat{u}_{jk} J_{jk} \sum_{\alpha=x,y,z} c_j^\alpha c_k^\alpha, \quad (7.8)$$

$$\mathcal{H}_{TRB} = i \frac{\hbar}{2} \sum_{\diamond} \left[ (\hat{u}_{34} \hat{u}_{41} + \hat{u}_{12} \hat{u}_{23}) \sum_{\alpha=x,y,z} c_3^\alpha c_1^\alpha \right. \quad (7.9)$$

$$\left. - (\hat{u}_{41} \hat{u}_{12} + \hat{u}_{23} \hat{u}_{34}) \sum_{\alpha=x,y,z} c_4^\alpha c_2^\alpha \right], \quad (7.10)$$

$$W_{p=\{\diamond, \circ\}} = - \prod_{\langle jk \rangle \in p} \hat{u}_{jk}, \quad (7.11)$$

where  $\hat{u}_{jk} \equiv -i d_j^\lambda d_k^\lambda$  for  $\lambda$ -link  $\langle jk \rangle$ . Following familiar analysis in Kitaev-type models, we observe that in the enlarged Hilbert space,  $\hat{u}_{jk}$  commute among themselves and with the Hamiltonian, and we can proceed by replacing them by their eigenvalues  $\pm 1$  and interpreting as static  $Z_2$  gauge fields. The  $W_p$  terms, with  $K_p > 0$  and assumed to be sufficiently large, can be used to stabilize the sector with zero fluxes through all elementary plackets, and this can produce parton Fermi surfaces [140]. In our work, we fix the gauge by taking  $u_{jk} = 1$  for bonds  $j \rightarrow k$  as shown by the arrows in Fig. 7.1. There are four physical sites per unit cell, so for each species  $c^\alpha$ ,  $\alpha = x, y, z$ , there are four Majoranas per unit cell. From now on, we replace the site labeling  $j$  with  $j = \{\mathbf{r}, a\}$ , where  $\mathbf{r}$  runs over the Bravais lattice of unit cells of the decorated square network and  $a$  runs over the four sites in the unit cell. The Hamiltonian can be written in a concise form,

$$\begin{aligned} \mathcal{H} &= \sum_{\alpha} \sum_{\langle jk \rangle} c_j^\alpha \mathcal{A}_{jk} c_k^\alpha \\ &= \sum_{\alpha} \sum_{\langle (\mathbf{r}, a), (\mathbf{r}', a') \rangle} c_{\mathbf{r}, a}^\alpha \mathcal{A}_{\mathbf{r}, a; \mathbf{r}', a'} c_{\mathbf{r}', a'}^\alpha. \end{aligned} \quad (7.12)$$

There is translational symmetry between different unit cells, and  $\mathcal{A}_{\mathbf{r}, a; \mathbf{r}', a'} = \mathcal{A}_{a a'}(\mathbf{r} - \mathbf{r}')$ .

In order to give a concise long-wavelength description, it will be convenient to use familiar complex fermion fields. To this end, we can proceed as follows. For a general Majorana problem specified by an antisymmetric pure imaginary matrix  $\mathcal{A}_{jk}$ , we diagonalize  $\mathcal{A}_{jk}$  for spectra, but only half of the bands are needed, while the rest of the bands

can be obtained by a specific relation and are redundant. Explicitly, for a system with  $2m$  bands, we can divide them into two groups. The first group contains bands from 1 to  $m$  with eigenvector-eigenenergy pairs  $\{\vec{v}_{b,\mathbf{k}}, \epsilon_{b,\mathbf{k}}\}$ , where  $b = 1, 2, \dots, m$  are band indices, and the second group contains bands from  $m + 1$  to  $2m$  related to the first group,  $\{\vec{v}_{b'=m+b,\mathbf{k}}, \epsilon_{b'=m+b,\mathbf{k}}\} = \{\vec{v}_{b,-\mathbf{k}}^*, -\epsilon_{b,-\mathbf{k}}\}$ . Using only the bands with  $b = 1$  to  $m$ , we can write the original Majoranas in terms of usual complex fermions as

$$c^\alpha(\mathbf{r}, a) = \sqrt{\frac{2}{N_{uc}}} \sum_{b=1}^m \sum_{\mathbf{k} \in \text{B.Z.}} [e^{i\mathbf{k} \cdot \mathbf{r}} v_{b,\mathbf{k}}(a) f_b^\alpha(\mathbf{k}) + \text{H.c.}], \quad (7.13)$$

where  $N_{uc}$  is the number of unit cells, and the complex fermion field  $f$  satisfies the usual anticommutation relation,  $\{f_b^{\alpha\dagger}(\mathbf{k}), f_{b'}^{\alpha'}(\mathbf{k}')\} = \delta_{\alpha\alpha'} \delta_{bb'} \delta_{\mathbf{k}\mathbf{k}'}$ . Note that in this SU(2)-invariant model, the eigenvectors for each spin species are the same,  $v_{b,\mathbf{k}}^\alpha = v_{b,\mathbf{k}}$ . In terms of the complex fermion fields, the Hamiltonian becomes

$$\mathcal{H} = \sum_{b=1}^m \sum_{\mathbf{k} \in \text{B.Z.}} 2\epsilon_b(\mathbf{k}) \left[ f_b^{\alpha\dagger}(\mathbf{k}) f_b^\alpha(\mathbf{k}) - \frac{1}{2} \right]. \quad (7.14)$$

In the present case,  $2m = 4$  and therefore two bands are sufficient to give us the full solution of the Majorana problem. Depending on the parameters, the model can realize different gapped and gapless phases. The latter generally have Fermi surfaces, and here we are focusing on such gapless phases and their qualitative properties. For all illustrations below, we use parameters  $\{J_x, J_y, J_z, J'_x, J'_y, J'_z, h\} = \{1.7, 1.4, 0.4, 1.0, 1.3, 0.2, 0.95\}$  with  $x, y, z, x', y',$  and  $z'$  defined in Fig. 7.1. Gapless phases with Fermi surfaces appear in wide parameter regimes, and we remark that there is no fine tuning of parameters to find such phases. The reason we choose to present the specific parameters is that in this case, the Fermi surfaces are sufficiently small, so when we analyze the singularities in the structure factors in Chapter 7.2.2, it is easier to clearly see the locations of the singularities.

For an illustration of how these two bands of usual complex fermion fields vary with momentum  $\mathbf{k}$ , we show them in Fig. 7.2(a) along a cut with  $k_y = -3\pi/4$ . We label the bands from top to bottom as 1 to 2. We can see that only the band 2 crosses the zero energy, which is true also when we scan the whole  $k_y$  axis, and the populated Fermi pocket in the

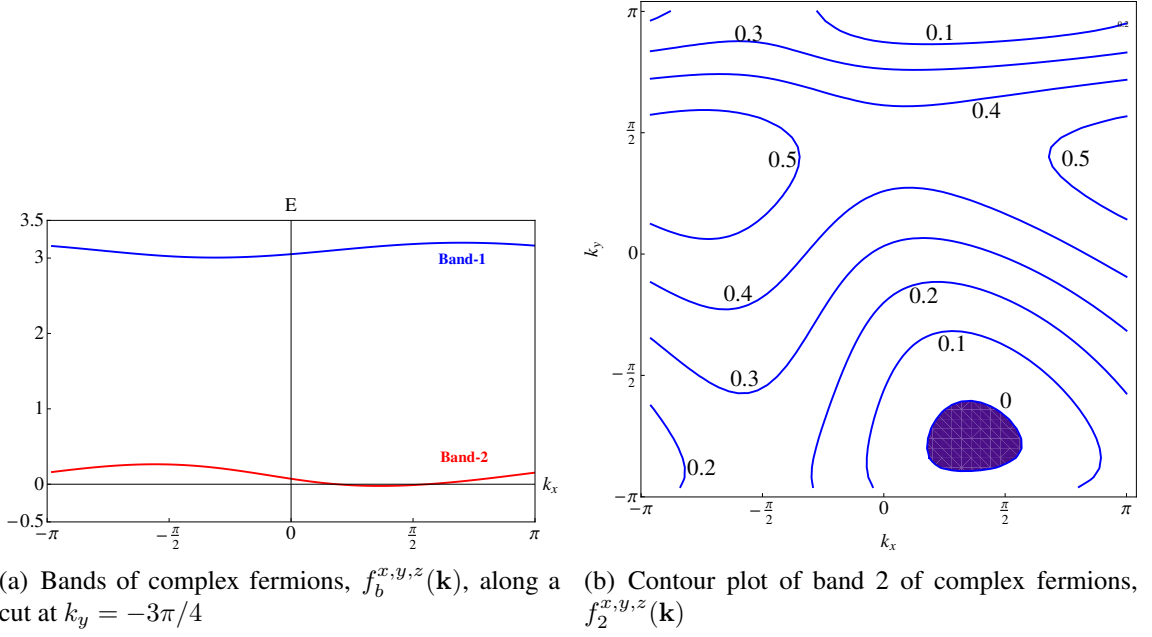


Figure 7.2: (a) Illustration of energy spectra of the two bands of the complex fermion fields along a cut with  $k_y = -3\pi/4$ . Here we take parameters  $\{J_x, J_y, J_z, J'_x, J'_y, J'_z, h\} = \{1.7, 1.4, 0.4, 1.0, 1.3, 0.2, 0.95\}$ . Diagonalizing the  $\mathcal{A}_{ij}$  matrix in Eq. (7.12) gives four bands, but only the two bands shown are needed for solving the Majorana problem (see text). Because only band 2 crosses zero energy, we simply focus on it for long wavelength analysis. (b) Contour plot of band 2, with the occupied Fermi pocket shaded

B.Z. is shown shaded in Fig. 7.2(b) [154].

It is interesting to discuss qualitatively the thermodynamic properties in this phase. Because of the presence of the gapless Fermi surface, such spin liquid is expected to show metal-like specific heat and spin susceptibility at low temperature, although the Wilson ratio is different from that of spin-1/2 fermions [128]. Furthermore, magnetic impurities coupled to this model would possibly show an unusual Kondo effect and Ruderman-Kittel-Kasuya-Yosida interaction [148].

## 7.2 Correlation functions

We mainly focus on the spin correlations and spin-nematic correlations, and since there are four sites per unit cell, there are many correlation functions one can define. However, since all the spin correlations show similar behaviors among themselves and so do spin-nematic

correlations, we consider specific examples defined as

$$\mathcal{F}_1(\mathbf{r}) \equiv \langle S^+(\mathbf{r}, 2) S^-(\mathbf{0}, 2) \rangle, \quad (7.15)$$

$$\mathcal{F}_2(\mathbf{r}) \equiv \langle P^+(\mathbf{r}) P^-(0) \rangle, \quad (7.16)$$

with

$$S^{+/-} \equiv S^x \pm iS^y = (\sigma^x \pm i\sigma^y)/2, \quad (7.17)$$

and magnon-pair creation operator

$$\begin{aligned} P^+(\mathbf{r}) &\equiv S^+(\mathbf{r}, 2) S^+(\mathbf{r} + \hat{x}, 4) \\ &= S^+(\mathbf{r}_c - \frac{\boldsymbol{\xi}}{2}, 2) S^+(\mathbf{r}_c + \frac{\boldsymbol{\xi}}{2}, 4), \end{aligned} \quad (7.18)$$

associated with the bond  $\langle \mathbf{r}, 2; \mathbf{r} + \hat{x}, 4 \rangle$ . In the last line,  $\mathbf{r}_c \equiv \mathbf{r} + \hat{x}/2$  is the center of mass coordinate, and  $\boldsymbol{\xi}$  is the vector joining the two sites of the nematic operator, which is simply  $\boldsymbol{\xi} = \hat{x}$  here. The magnon-pair operator,  $P_{jk}^+ \equiv S_j^+ S_k^+$  for a local pair of sites  $\{j, k\}$ , describes spin-nematic properties [86, 90, 84] and can be connected to the usual traceless rank two quadrupolar tensor defined as

$$\mathcal{Q}_{jk}^{\alpha\beta} = \frac{1}{2} \left( S_j^\alpha S_k^\beta + S_j^\beta S_k^\alpha \right) - \frac{1}{3} \delta^{\alpha\beta} \langle \mathbf{S}_j \cdot \mathbf{S}_k \rangle, \quad (7.19)$$

through  $P_{jk}^+ = \mathcal{Q}_{jk}^{xx} - \mathcal{Q}_{jk}^{yy} + 2i\mathcal{Q}_{jk}^{xy}$ .

Furthermore, power-law correlations in real space correspond to singularities in momentum space, which we can study by considering the corresponding structure factors

$$\mathcal{D}_{1/2}(\mathbf{q}) \equiv \sum_{\mathbf{r}} \mathcal{F}_{1/2}(\mathbf{r}) e^{-i\mathbf{q}\cdot\mathbf{r}}. \quad (7.20)$$

## 7.2.1 Long wavelength analysis

We focus on the long-distance behavior and therefore retain only the contribution from band-2. The spin operator can be compactly written as

$$S^\alpha(\mathbf{r}, a) \simeq \sum_{\mathbf{k}, \mathbf{k}' \in \text{B.Z.}} \sum_{\beta, \gamma} \left\{ N_{\mathbf{k}\mathbf{k}'}(a) \epsilon^{\alpha\beta\gamma} f_2^{\beta\dagger}(\mathbf{k}) f_2^\gamma(\mathbf{k}') e^{-i(\mathbf{k}-\mathbf{k}') \cdot \mathbf{r}} + \left[ \frac{M_{\mathbf{k}\mathbf{k}'}(a)}{2} \epsilon^{\alpha\beta\gamma} f_2^\beta(\mathbf{k}) f_2^\gamma(\mathbf{k}') e^{i(\mathbf{k}+\mathbf{k}') \cdot \mathbf{r}} + \text{H.c.} \right] \right\},$$

where  $M_{\mathbf{k}\mathbf{k}'} = -iv_{2,\mathbf{k}}(a)v_{2,\mathbf{k}'}(a)/N_{uc}$  and  $N_{\mathbf{k}\mathbf{k}'} = -iv_{2,\mathbf{k}}^*(a)v_{2,\mathbf{k}'}(a)/N_{uc} = -N_{\mathbf{k}'\mathbf{k}}^*$ .

In order to determine long-distance behavior at separation  $\mathbf{r}$ , we focus on patches near the Fermi surface of band 2 where the group velocity is parallel or antiparallel to the observation direction  $\hat{\mathbf{n}} = \mathbf{r}/|\mathbf{r}|$ , because at large separation  $|\mathbf{r}| \gg k_F^{-1}$ , the main contributions to the correlations come precisely from such patches. Specifically, we introduce right (R) and left (L) Fermi patch fields and the corresponding energies

$$f_P^{\alpha,(\hat{\mathbf{n}})}(\delta\mathbf{k}) = f_2^\alpha(\mathbf{k}_{FP}^{(\hat{\mathbf{n}})} + \delta\mathbf{k}), \quad (7.21)$$

$$\epsilon_P^{(\hat{\mathbf{n}})}(\delta\mathbf{k}) = |\mathbf{v}_{FP}^{(\hat{\mathbf{n}})}| \left( P\delta k_{\parallel} + \frac{\mathfrak{C}_P^{(\hat{\mathbf{n}})}}{2} \delta k_{\perp}^2 \right), \quad (7.22)$$

where the superscript  $(\hat{\mathbf{n}})$  refers to the observation direction and  $P = R/L = +/ -$ ;  $\mathbf{v}_{FP}^{(\hat{\mathbf{n}})}$  is the corresponding group velocity (parallel to  $\hat{\mathbf{n}}$  for the right patch and anti-parallel for the left patch);  $\mathfrak{C}_{P=R/L}$  is the curvature of the Fermi surface at the right/left patch;  $\delta k_{\parallel}$  and  $\delta k_{\perp}$  are respectively components of  $\delta\mathbf{k}$  parallel and perpendicular to  $\hat{\mathbf{n}}$ . It is convenient to define fields in real space

$$f_P^{\alpha,(\hat{\mathbf{n}})}(\mathbf{r}) \sim \sum_{\delta\mathbf{k} \in \text{Fermi Patch}} f_P^{\alpha,(\hat{\mathbf{n}})}(\delta\mathbf{k}) e^{i\delta\mathbf{k} \cdot \mathbf{r}}, \quad (7.23)$$

which vary slowly on the scale of the lattice spacing [and from now on we will drop the superscript  $(\hat{\mathbf{n}})$ ]. In this long-wavelength analysis, the relevant terms in the spin operator

are

$$S^\alpha(\mathbf{r}, a) \sim \sum_{P, P'} \sum_{\beta, \gamma} \left\{ N_{PP'}(a) \epsilon^{\alpha\beta\gamma} f_P^{\beta\dagger}(\mathbf{r}) f_{P'}^\gamma(\mathbf{r}) e^{-i(\mathbf{k}_{FP} - \mathbf{k}_{FP'}) \cdot \mathbf{r}} + \left[ \frac{M_{PP'}(a)}{2} \epsilon^{\alpha\beta\gamma} f_P^\beta(\mathbf{r}) f_{P'}^\gamma(\mathbf{r}) e^{i(\mathbf{k}_{FP} + \mathbf{k}_{FP'}) \cdot \mathbf{r}} + \text{H.c.} \right] \right\}, \quad (7.24)$$

The above long-wavelength expression for the  $S^\alpha$  operator implies that the corresponding correlation function defined in Eq. (7.15) contains contributions with  $\mathbf{q} = 0$ ,  $\mathbf{k}_{FR} - \mathbf{k}_{FL}$ ,  $\pm 2\mathbf{k}_F$ , and  $\pm(\mathbf{k}_{FR} + \mathbf{k}_{FL})$ . More explicitly, for a patch specified by  $\epsilon_P(\delta\mathbf{k})$  in Eqs. (7.21)–(7.22), we can derive the Green's function for the continuum complex fermion fields as

$$\langle f_{R/L}^{\alpha\dagger}(\mathbf{0}) f_{R/L}^\alpha(\mathbf{r}) \rangle = \frac{\exp[\mp i \frac{3\pi}{4}]}{2^{3/2} \pi^{3/2} \mathfrak{C}_{R/L}^{1/2} |\mathbf{r}|^{3/2}}. \quad (7.25)$$

Using this and Eq. (7.24), we can obtain the spin correlation

$$\mathcal{F}_1(\mathbf{r}) \sim -\frac{|N_{RR}|^2}{\mathfrak{C}_R |\mathbf{r}|^3} - \frac{|N_{LL}|^2}{\mathfrak{C}_L |\mathbf{r}|^3} \quad (7.26)$$

$$+ \frac{2|N_{RL}|^2 \sin[(\mathbf{k}_{FR} - \mathbf{k}_{FL}) \cdot \mathbf{r}]}{\mathfrak{C}_R^{1/2} \mathfrak{C}_L^{1/2} |\mathbf{r}|^3} \quad (7.27)$$

$$- \frac{|M_{RR}|^2 \sin(2\mathbf{k}_{FR} \cdot \mathbf{r})}{\mathfrak{C}_R |\mathbf{r}|^3} + \frac{|M_{LL}|^2 \sin(2\mathbf{k}_{FL} \cdot \mathbf{r})}{\mathfrak{C}_L |\mathbf{r}|^3} \quad (7.28)$$

$$+ \frac{2|M_{RL}|^2 \cos[(\mathbf{k}_{FR} + \mathbf{k}_{FL}) \cdot \mathbf{r}]}{\mathfrak{C}_R^{1/2} \mathfrak{C}_L^{1/2} |\mathbf{r}|^3}, \quad (7.29)$$

where we used  $N_{LR} = -N_{RL}^*$  and  $M_{LR} = M_{RL}$ .

For the long-wavelength description of the spin-nematic correlations, we can in principle plug the expression of spin operator, Eq. (7.24), into either Eq. (7.18) or Eq. (7.19). We remark that even though the microscopic spin-nematic operators contain four local Majorana fermions expressed in general as  $c_j^\alpha c_k^\beta c_j^\gamma c_k^\delta$ , when calculating the correlation functions, there are cases when pairs of Majorana fermions Wick-contract locally and produce a constant factor. Take  $Q^{xy}$  as an example,  $Q_{jk}^{xy} \sim -(c_j^x c_k^y + c_j^y c_k^x) c_j^z c_k^z$ , and observe that the last two Majoranas  $c_j^z c_k^z$  can Wick-contract when calculating the correlation functions. For this reason, the spin-nematic correlations show the same dominant power-law behavior as spin

correlations, and effectively we have fermion bilinear contributions to the spin-nematic.

From now on, we focus on the dominant contributions to the spin-nematic correlations. The diagonal and off-diagonal elements of the quadrupolar tensor can be written concisely using center of mass and relative coordinates, where we define  $(j, k) = (\{\mathbf{r}, a\}, \{\mathbf{r}', a'\}) = (\{\mathbf{r}_c - \boldsymbol{\xi}/2, a\}, \{\mathbf{r}_c + \boldsymbol{\xi}/2, a'\})$ ,

$$\mathcal{Q}^{\alpha\alpha} \sim \sum_{PP'} \sum_{\beta \neq \alpha} \left\{ \left[ A_{PP'}^{aa'} e^{i(\mathbf{k}_{FP} + \mathbf{k}_{FP'}) \cdot \mathbf{r}_c} f_P^\beta f_{P'}^\beta + B_{PP'}^{aa'} e^{-i(\mathbf{k}_{FP} - \mathbf{k}_{FP'}) \cdot \mathbf{r}_c} f_P^{\beta\dagger} f_{P'}^\beta \right] + \text{H.c.} \right\}, \quad (7.30)$$

$$\mathcal{Q}^{\alpha\beta} \sim \frac{1}{2} \sum_{PP'} \left\{ \left[ A_{PP'}^{aa'} e^{i(\mathbf{k}_{FP} + \mathbf{k}_{FP'}) \cdot \mathbf{r}_c} (f_P^\alpha f_{P'}^\beta + \alpha \leftrightarrow \beta) + B_{PP'}^{aa'} e^{-i(\mathbf{k}_{FP} - \mathbf{k}_{FP'}) \cdot \mathbf{r}_c} (f_P^{\alpha\dagger} f_{P'}^\beta + \alpha \leftrightarrow \beta) \right] + \text{H.c.} \right\}. \quad (7.31)$$

Above we define the matrices  $A_{PP'}^{aa'} \equiv -iv_{2,P}(a)v_{2,P'}(a')e^{-i(\mathbf{k}_{FP} - \mathbf{k}_{FP'}) \cdot \boldsymbol{\xi}/2}/N_{uc}$  and  $B_{PP'}^{aa'} \equiv -iv_{2,P}^*(a)v_{2,P'}(a')e^{i(\mathbf{k}_{FP} + \mathbf{k}_{FP'}) \cdot \boldsymbol{\xi}/2}/N_{uc}$ ; the slowly varying fermion fields are evaluated at  $\mathbf{r}_c$ . The above implies that the spin-nematic correlations contain dominant contributions at wavevectors  $\mathbf{q} = \mathbf{0}, \mathbf{k}_{FR} - \mathbf{k}_{FL}, \pm(\mathbf{k}_{FR} + \mathbf{k}_{FL})$ . Note that the contributions with  $\mathbf{q} = \pm 2\mathbf{k}_F$  vanish by Fermi statistics.

The long-wavelength expression for the dominant contributions to the spin-nematic correlations, Eq. (7.16), is

$$\mathcal{F}_2(\mathbf{r}) \sim - \left[ \frac{(B_{RR} + B_{RR}^*)^2}{2\mathfrak{C}_R |\mathbf{r}_c|^3} + R \rightarrow L \right] \quad (7.32)$$

$$+ \frac{|B_{RL} + B_{LR}^*|^2}{\mathfrak{C}_R^{1/2} \mathfrak{C}_L^{1/2} |\mathbf{r}_c|^3} \sin[(\mathbf{k}_{FR} - \mathbf{k}_{FL}) \cdot \mathbf{r}_c] \quad (7.33)$$

$$+ \frac{|A_{RL} - A_{LR}|^2}{\mathfrak{C}_R^{1/2} \mathfrak{C}_L^{1/2} |\mathbf{r}_c|^3} \cos[(\mathbf{k}_{FR} + \mathbf{k}_{FL}) \cdot \mathbf{r}_c], \quad (7.34)$$

where we abbreviate  $A_{PP'}^{a=2;a'=4} = A_{PP'}$  and  $B_{PP'}^{a=2;a'=4} = B_{PP'}$ . The above long-wavelength descriptions can be used to analyze the data obtained by exact numerical calculations. Here we also note that the model does not have time-reversal and inversion symmetries, so the location of the corresponding R-L patches which are parallel or antiparallel to the observa-

tion direction can not be determined easily and need to be found numerically.

Before leaving this subsection, we remark that we can similarly analyze local energy operators such as bond energy, [63]  $\mathcal{B}_{jk} \equiv iu_{jk} \sum_{\beta} c_j^{\beta} c_k^{\beta}$ ; the long wavelength description contains terms  $\sum_{\beta} f_P^{\beta} f_{P'}^{\beta}$  and  $\sum_{\beta} f_P^{\beta\dagger} f_{P'}^{\beta}$  that are spin-singlet variants of terms in Eq. (7.30). We can therefore see that the spin, spin-nematic, and local energy observables cover all fermionic bilinears. Below, we focus on the spin and spin-nematic operators.

## 7.2.2 Exact numerical calculation

We calculate the spin correlations, Eq. (7.15), and the spin-nematic correlations, Eq. (7.16), for any real-space separations  $\mathbf{r}$  and confirm that they have the same dominant power law envelope  $1/|\mathbf{r}|^3$ . For an illustration, we show the spin correlations and spin-nematic correlations for  $\mathbf{r}$  along a specific direction, e.g.,  $\hat{x}$ -axis, calculated on a  $300 \times 300$  lattice. In Fig. 7.3, the log-log plot of  $|\mathcal{F}_1(\mathbf{r})|$  and  $|\mathcal{F}_2(\mathbf{r})|$  clearly shows the same  $1/|\mathbf{r}|^3$  envelope. In addition, the irregular behavior of the data is due to oscillating components. The wavevectors of the real-space oscillations form some singular surfaces in the momentum space, which we analyze next.

Focusing on the structure factors  $\mathcal{D}_{1/2}(\mathbf{q})$  defined in Eq. (7.20), we calculate the spin correlation and spin-nematic correlation at each site within a  $100 \times 100$  lattice and numerically take Fourier transform. Figure 7.4(a) gives a three-dimensional (3D) view of the spin structure factor. We can clearly see cone-shaped singularity at  $\mathbf{q} = 0$ , which is expected from Eq. (7.26):

$$\mathcal{D}_1(\mathbf{q} \sim \mathbf{0}) \sim |\mathbf{q}|. \quad (7.35)$$

A closer look at the spin structure factor also reveals singular surfaces at  $\mathbf{k}_{FR} - \mathbf{k}_{FL}$ ,  $\pm 2\mathbf{k}_F$ , and  $\pm(\mathbf{k}_{FR} + \mathbf{k}_{FL})$ , as expected from Eqs. (7.27)–(7.29). In order to see the locations of the singular surfaces more clearly and compare with our long-wavelength analysis, we show top view of  $\mathcal{D}_1(\mathbf{q})$  in Fig. 7.4(b). We numerically calculate the wavevectors  $2\mathbf{k}_{FP}$  and  $\mathbf{Q}_{\pm} = \mathbf{k}_{FR} \pm \mathbf{k}_{FL}$  for all observation directions (by first finding corresponding Right and Left Fermi points with anti-parallel group velocities) and superpose the traced lines

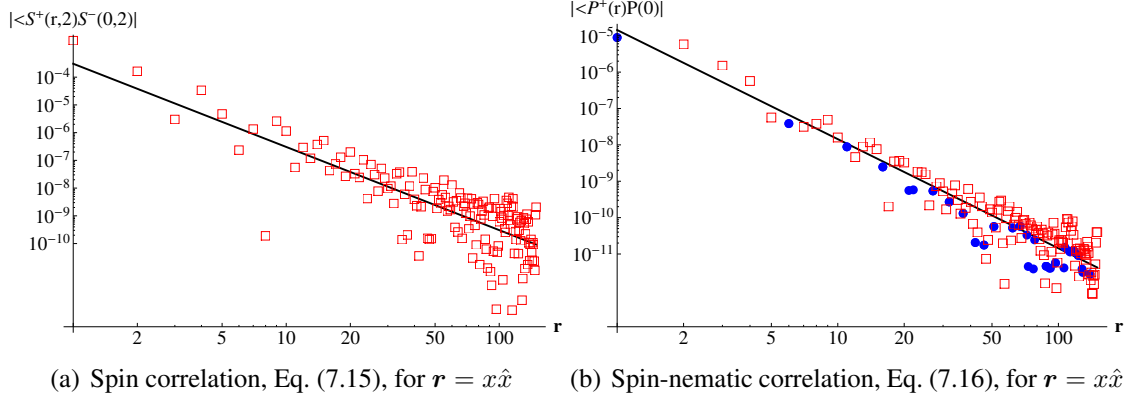


Figure 7.3: Figures (a) and (b) illustrate power-law behaviors of the spin correlations and spin-nematic correlations. We calculate  $\mathcal{F}_1(\mathbf{r})$  and  $\mathcal{F}_2(\mathbf{r})$  with  $\mathbf{r}$  taken along the  $\hat{x}$ -axis for a system containing  $300 \times 300$  unit cells. The log-log plots in (a) and (b) clearly show the *same* dominant  $1/x^3$  envelope (straight line in the figures). Here, we show the absolute values of  $|\mathcal{F}_1(\mathbf{r})|$  and  $|\mathcal{F}_2(\mathbf{r})|$ , and indicate the sign with open square boxes for negative correlations and filled circles for positive correlations. The irregular behaviors are due to oscillating parts. The reason that panel (a) has no positive data is likely because the nonoscillating part is quantitatively stronger, although we can still see oscillations about the  $1/x^3$  line.

on the figure. We see that the lines we get from the long-wavelength analysis match the singular features in the exact spin structure factor. Note that the singularities are expected to be one-sided,

$$\mathcal{D}_1(\mathbf{Q}_- + \delta\mathbf{q}) \sim |\delta q_{\parallel}|^{3/2} \Theta(-\delta q_{\parallel}), \quad (7.36)$$

$$\mathcal{D}_1(2\mathbf{k}_{FR} + \delta\mathbf{q}) \sim |\delta q_{\parallel}|^{3/2} \Theta(-\delta q_{\parallel}), \quad (7.37)$$

$$\mathcal{D}_1(\mathbf{Q}_+ + \delta\mathbf{q}) \sim |\delta q_{\parallel}|^{3/2} \Theta[-\delta q_{\parallel} \text{sign}(\mathbf{c}_R - \mathbf{c}_L)]. \quad (7.38)$$

The first and second equations are singular from the inner side of the central “ring” and the closed rings sitting roughly on one diagonal of the B.Z. in Fig. 7.4(b), and the last equation is singular from the inner side of the small “triangles”.

Similar analysis can be applied to the spin-nematic structure factor except that there are no  $\pm 2\mathbf{k}_F$  singularities. The 3D view of the spin-nematic structure factor is shown in Fig. 7.5(a) and we can clearly see the  $\mathbf{q} = 0$  singularity and  $\mathbf{q} = \mathbf{k}_{FR} - \mathbf{k}_{FL}$  singular line (central ring). The  $\mathbf{q} = \pm(\mathbf{k}_{FR} + \mathbf{k}_{FL})$  singular lines (small triangles) are quite weak but

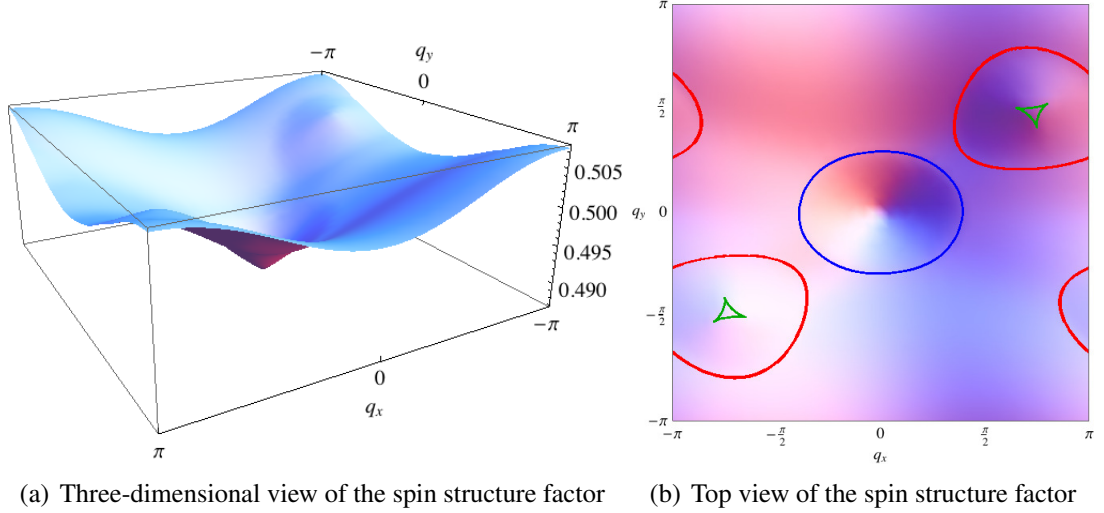


Figure 7.4: (a) 3D view of the spin structure factor,  $\mathcal{D}_1(\mathbf{q})$ , defined in Eq. (7.20). We can clearly see the singularity  $\mathcal{D}_1(\mathbf{q}) \sim |\mathbf{q}|$  at  $\mathbf{q} = 0$  and we also see weak singular lines: forming central closed ring, two closed rings sitting roughly on one diagonal of the B.Z.; and additional weak singular features near the centers of the latter rings. (b) These singular lines are brought out more clearly when the structure factor is viewed from top. We superposed the locations of the singularities calculated using the Fermi surface information: The inner blue ring specifies the line at  $\mathbf{k}_{FR} - \mathbf{k}_{FL}$ ; the red closed rings specify the lines at  $\pm 2\mathbf{k}_F$ ; the small green triangles specify the lines at  $\pm(\mathbf{k}_{FR} + \mathbf{k}_{FL})$ .

still visible, and their locations can be seen more clearly in the view from top shown in Fig. 7.5(b).

### 7.3 Majorana spin liquid in the Zeeman field

In the presence of the Zeeman magnetic field, we need to consider the additional term in the Hamiltonian

$$\mathcal{H}_Z = -B_z \sum_i \sigma_i^z = B_z \sum_{\mathbf{r}, a} i c^x(\mathbf{r}, a) c^y(\mathbf{r}, a), \quad (7.39)$$

where we used explicitly the rewriting of spin in terms of Majoranas, Eq. (7.6). We remark that the Zeeman magnetic field only couples to the spin degrees of freedom ( $c^\alpha$  Majoranas) and not to the orbital degrees of freedom ( $d^\alpha$  Majoranas that produce the  $Z_2$  gauge fields). Therefore, the model is exactly solvable even in the presence of the magnetic field.

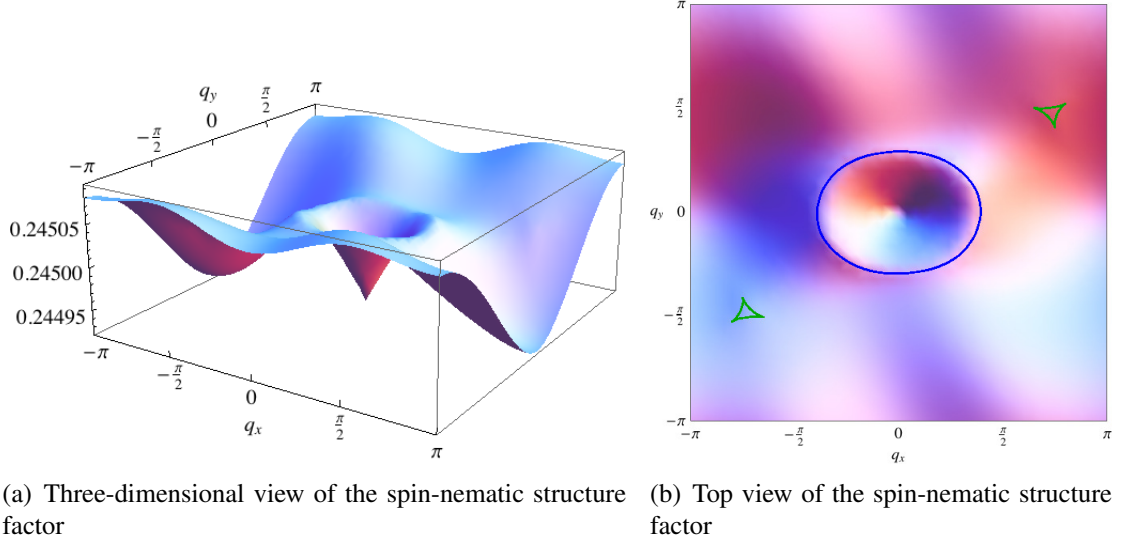


Figure 7.5: (a) 3D view of the spin-nematic structure factor,  $\mathcal{D}_2(\mathbf{q})$ , defined in Eq. (7.20). Like the spin structure factor, there is a clear singularity  $\mathcal{D}_2(\mathbf{q}) \sim |\mathbf{q}|$  at  $\mathbf{q} = 0$  and there are weak singular lines, one forming a central closed ring and the other forming small triangles sitting roughly on one diagonal of the B.Z. (b) The view from the top shows more clearly the location of the singular lines. We superposed the locations of the singularities calculated using the Fermi surface information: The inner blue ring specifies the line at  $\mathbf{k}_{FR} - \mathbf{k}_{FL}$ , and the small green triangles specify the lines at  $\pm(\mathbf{k}_{FR} + \mathbf{k}_{FL})$ . Note that, unlike the spin structure factor, there are no  $\pm 2\mathbf{k}_F$  singularities.

Throughout, we assume the  $K_p$  terms, Eq. (7.1), are large enough so that the ground state remains in the zero  $Z_2$  flux sector.

It is interesting to note that the Zeeman term only affects the  $c^x$  and  $c^y$  Majoranas while leaving the  $c^z$  Majorana unaltered [147, 128]. We can diagonalize the Hamiltonian by starting with the zero-field solution, Eqs. (7.13)–(7.14). We define two complex fermion fields,

$$f_{b,+/-}^\dagger(\mathbf{k}) \equiv [f_b^{x\dagger}(\mathbf{k}) \pm i f_b^{y\dagger}(\mathbf{k})]/\sqrt{2}. \quad (7.40)$$

The Hamiltonian in the Zeeman magnetic field becomes

$$\mathcal{H} = \sum_{b=1}^2 \sum_{\mathbf{k} \in \text{B.Z.}} (2\epsilon_b(\mathbf{k}) + 2B_z) \left[ f_{b,-}^\dagger(\mathbf{k}) f_{b,-}(\mathbf{k}) - \frac{1}{2} \right] \quad (7.41)$$

$$+ \sum_{b=1}^2 \sum_{\mathbf{k} \in \text{B.Z.}} (2\epsilon_b(\mathbf{k}) - 2B_z) \left[ f_{b,+}^\dagger(\mathbf{k}) f_{b,+}(\mathbf{k}) - \frac{1}{2} \right] \quad (7.42)$$

$$+ \sum_{b=1}^2 \sum_{\mathbf{k} \in \text{B.Z.}} 2\epsilon_b(\mathbf{k}) \left[ f_b^{z\dagger}(\mathbf{k}) f_b^z(\mathbf{k}) - \frac{1}{2} \right]. \quad (7.43)$$

This form implies that  $f_{b,+}^\dagger$  carries  $S^z$  quantum number  $+1$  and  $f_{b,-}^\dagger$  carries  $S^z = -1$ , while  $f^{z\dagger}$  carries  $S^z = 0$ .

An interesting property in this model is that the  $f^z$  Fermi surface (associated with the  $c^z$  Majorana) remains no matter how large the magnetic field is; [128] therefore, there are *always* gapless excitations in this system.

For an illustration of several different phases that can occur under the magnetic field, we take the same parameters as in Fig. 7.2 and examine the effective Zeeman shifting of the band-1 and band-2 for each complex fermion species. Figure 7.6 shows the magnetization as a function of magnetic field  $B_z$ . There are quite rich features in this model. When we turn on the magnetic field, the  $f_{b,+}$  bands move downwards while the  $f_{b,-}$  bands move upwards. First, the field increases up to a threshold value, roughly  $B_z = 0.024$ , where the Fermi surface of the  $f_{2,-}$  vanishes and there is a discontinuity in the slope of the magnetization curve shown in the inset in Fig. 7.6. The  $f_{2,+}$  band is pushed down and the  $f_{2,+}$  Fermi sea keeps growing until it completely covers the B.Z. at  $B_z \simeq 0.5$ . For the field between 0.5 and 2.8, the  $f_{1,+}$  band remains above the zero energy, and we have the half-polarized magnetization plateau phase. The  $f_{1,+}$  band reaches zero energy at  $B_z \simeq 2.8$ , we leave the first plateau phase and the magnetization starts to increase. When the magnetic field is large enough to completely push the  $f_{1,+}$  band below zero,  $B_z \simeq 3.3$ , the  $f_{1,+}$  Fermi surface also vanishes and we enter the fully-polarized phase, the second plateau phase. We also see some weak features in the regimes of increasing magnetization that are due to the van Hove singularities when the energy passes the saddle points of bands 1 or 2 ( see the contour plot of band 2 in Fig. 7.2(b)), but these van Hove singularities are rather weak in

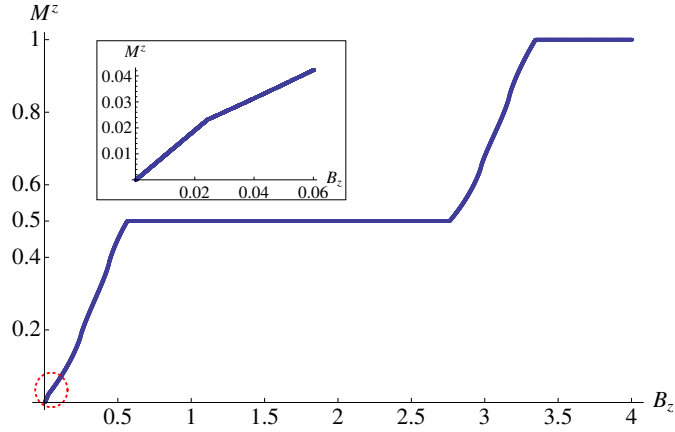


Figure 7.6: The magnetization per site,  $M^z \equiv \langle \sum_j \sigma_j^z \rangle / N_{\text{sites}}$ , can be calculated as  $(\rho_{1,+} + \rho_{2,+} - \rho_{1,-} - \rho_{2,-})/2$ , where  $\rho_{b,\pm}$  is the population of the  $f_{b,\pm}$  fermions per unit cell. The magnetization curve for our model in the Zeeman field shows rich features (see text) including half- and fully polarized plateaus. The inset shows a blow-up of the small  $B_z$  region where the Fermi surface  $f_{2,-}$  disappears and there is a slope discontinuity. We note that the magnetization inside the unit cell is not completely uniform (because of the reduced lattice symmetries) but is quantitatively similar at each site.

## 2D.

We remark that in all regimes, the Fermi surface of the  $f_2^z$  remains the same and gives gapless excitations. The fully polarized phase is actually the original Kitaev-type model proposed by Baskaran et al.. [140] This can be seen either directly by examining the physical Hamiltonian Eq. (7.1), or in the Majorana representation where  $\sigma_j^z = 1 = -ic_j^x c_j^y$ , so the constraint becomes  $D_j = -ic_j^x c_j^y c_j^z d_j^x d_j^y d_j^z = c_j^z d_j^x d_j^y d_j^z = 1$ , and the model in terms of the orbital degrees of freedom reduces to that in [140].

It is interesting that in the half-polarized plateau phase, even though the spin excitations are gapped, the spin degrees of freedom are entangled in the ground state. The spinless gapless excitations can be in principle detected by measuring bond-energy correlations or by entanglement entropy calculations. Finally, the regimes of increasing magnetization can be viewed as generic compressible Bose-metals [150] in the model with global U(1) symmetry.

## 7.4 Discussion

We proposed SU(2)-invariant Kitaev-type model on the decorated square lattice that realizes quantum spin liquids with parton Fermi surfaces. Having the benefit of the exact solutions, we can make robust general observations about such SU(2)-invariant MSL. One of the distinguishing characteristics of this state is that it has strong spin and spin-nematic fluctuations as manifested by the same power-law behavior in the correlations considered in our work. Because of the finite density of states at the Fermi surface, properties such as the specific heat, spin susceptibility, and NMR relaxation rates are essentially similar to a metal. Note that the volume/shape of the Fermi sea can be arbitrary, and we can easily tune the model to have larger or smaller Fermi pockets. In this way, the phase is quite distinct from the conventional spinon Fermi sea quantum spin liquids, [3] where half of the Brillouin zone is populated by spin-1/2 spinons before the Gutzwiller projection. Given the variability of the Fermi surface, the properties of the SU(2) MSL can be very sensitive to parameters, which we can also easily tune to produce gapped phases.

Let us briefly discuss stability of the exactly solvable model to general perturbations. First, we note that our complex fermions  $f_\alpha$  are not conserved microscopically. In principle, allowed four-fermion interactions would contain terms such as  $f_\alpha^\dagger f_\beta^\dagger f_\gamma^\dagger f_\delta^\dagger$  and  $f_\alpha^\dagger f_\beta^\dagger f_\gamma^\dagger f_\delta$ , in addition to the more familiar terms  $f_\alpha^\dagger f_\beta^\dagger f_\gamma f_\delta$ . The origin of the non-conservation of the complex fermions is because the microscopic fields are Majorana fermions, while we used the complex fermions as a convenient tool to reduce the problem to more familiar calculations. However, if the symmetries of the model are sufficiently low, there can be an “emergent” conservation of  $f$ -s. For example, if in our treatment we have a very small Fermi pocket of  $f$ -s centered at some momentum  $\mathbf{K} = (K_x, K_y)$ , then the four-fermion terms  $f^\dagger f^\dagger f^\dagger f^\dagger$  carry approximate momentum  $4\mathbf{K}$  while  $f^\dagger f^\dagger f^\dagger f$  carry  $\approx 2\mathbf{K}$ , so these terms are not allowed by momentum conservation if  $\mathbf{K}$  is some generic non-special wavevector. In this case, only the familiar terms  $f^\dagger f^\dagger f f$  conserving the fermion number are left and we have the emergent fermion number conservation law in the long-wavelength theory. The above is also true in this chapter in which the nonsymmetric small Fermi pockets are realized. Furthermore, only benign forward-scattering four-fermion terms survive in our model

since the Cooper-pair interactions carry nonzero momentum. We do not need to consider six- and eight-fermion terms as they are irrelevant in the renormalization group (RG) sense.

We have chosen a model that lacks time-reversal and lattice point group symmetries so as not to worry about possible residual pairing instabilities away from the exactly solvable limit. Such instabilities can be relatively weak also in more symmetric models and the discussed phenomenology can apply in these cases as well. In Chapter 8 we explore the stability and the nearby phases by studying such models on ladders [155] using weak-coupling RG technique and Bosonization analysis [49, 71, 156, 50].

In the presence of the Zeeman magnetic field, there are more interesting phases with distinct stable Fermi pockets of  $f_{b,+}$ ,  $f_{b,-}$ , and  $f_b^z$ . The Zeeman field breaks the global SU(2) down to U(1), and the compressible phases in the field are Bose-metal-like phases [150, 29].

We also found an interesting plateau phase at half-magnetization. Due to the gap for spin excitations, it is a spin insulator, but since the  $f^z$  remains gapless, we expect to still have metal-like specific heat and thermal conductivity.

This behavior in the plateau phase arises because some of the parton constituents of the spin operator acquire a gap (band gap in the present case). Some such physics perhaps can be relevant for the explanation of very recent NMR experiments [22] in  $\text{EtMe}_3\text{Sb}[\text{Pd}(\text{dmit})_2]_2$  showing a drastic reduction in the spin relaxation below temperature of the order 1K as if a spin gap opens up, while the thermal conductivity measurements and thermodynamic measurements [23, 25] are consistent with the presence of a Fermi surface of fermionic excitations down to the lowest temperatures. This phenomenology is also qualitatively similar to Chapter 4 [32] working in a setting closer to the  $\text{EtMe}_3\text{Sb}[\text{Pd}(\text{dmit})_2]_2$  experiments. We considered a scenario in which, upon writing the spin operator as  $S^+ = f_\uparrow^+ f_\downarrow$ , there could be a phase in which one spinon species becomes gapped due to pairing, while the other species retains the Fermi surface. It is fascinating to further explore such idea where some partons are gapped and some are gapless in more realistic settings.

## Chapter 8

# Majorana spin liquids on a two-leg ladder

In Chapter 7 we constructed an exactly solvable microscopic model in Kitaev’s spirit to study the properties of such  $SU(2)$ -invariant Majorana spin liquids (MSL) with Fermi surfaces of partons [157]. However, we allowed very low symmetries—lack of parity, inversion, and time reversal symmetry (TRS)—to sidestep discussing possible perturbations such as Cooper pairing instability, which can destabilize the gapless quantum spin liquids (QSL) phases away from the exactly solvable limit. In order to study the stability of such new class of gapless QSL and further explore their properties, we realize such states on a two-leg square ladder and show that they represent new quasi-1D phases.

We first consider a gapless Majorana orbital liquid (MOL) realized in a Kitaev-type model on the two-leg ladder using orbital degrees of freedom. The system can be reduced to one species of Majorana fermions coupled to background  $Z_2$  gauge fields such that it is exactly solvable and has gapless partons with incommensurate Fermi wave vectors. We formulate a long-wavelength description in terms of right-moving and left-moving complex fermions  $f_{R/L}$  and show that local energy observable has power law correlations at incommensurate “ $2k_F$ ” wavevectors. Going away from the exactly solvable point, we first consider allowed residual parton interactions and find that there is only one valid four-fermion term and it is strictly marginal; hence, the MOL is stable to such perturbations.

An important question is the stability of the MOL to allowing  $Z_2$  gauge field fluctuations, as these lead to confinement of partons in gapped phases in so-called even  $Z_2$  gauge

theories in (1+1)D [11, 158]. We argue that because of the nontrivial momenta carried by the gapless partons, there is a destructive interference for  $Z_2$  vortices (instantons) in space-time, and hence these are suppressed and do not affect the count of gapless modes. The local energy observables obtain new contributions beyond the mean field, and in this sense the partons become “less free”, but their bosonized fields still remain very convenient for characterizing the MOL phase.

We next realize an SU(2)-invariant MSL using both spin-1/2 and orbital degrees of freedom [149, 147] at each site of the two-leg ladder [130]. The system can be reduced to three species of Majorana fermions coupled to background  $Z_2$  gauge fields such that it is exactly solvable and has gapless partons with incommensurate wave vectors. We formulate long-wavelength description in terms of three right-moving and left-moving complex fermions ( $f_{R/L}^x, f_{R/L}^y, f_{R/L}^z$ ) that transform as a vector under spin rotation. Because there is no global U(1) symmetry, in addition to familiar four-fermion residual interactions expressed as  $f_R^{\alpha\dagger} f_L^{\beta\dagger} f_R^\gamma f_L^\delta$ , there are other allowed terms such as  $f_R^{\alpha\dagger} f_L^{\beta\dagger} f_R^\gamma f_L^{\delta\dagger}$ . Despite of having more allowed interactions, a weak coupling renormalization group (RG) analysis gives a large regime of a stable phase. Similarly to the MOL case, we argue that such MSL with gapless matter can be also stable against  $Z_2$  gauge field fluctuations even in (1+1)D [159, 160, 158].

The chapter is organized as follows. In Chapter 8.1, we realize the MOL with one fermion species in a Kitaev-type model [14] on the two-leg ladder and consider its long-wavelength properties and stability against perturbations. In Chapter 8.2, we realize the SU(2) MSL and use weak coupling RG analysis to study the stability of such phase against residual parton interactions and also discuss the stability against gauge field fluctuations. We conclude in Chapter 8.3 with some discussions. In Appendix 8.A, we consider more abstractly the stability of gapless U(1) matter against  $Z_2$  gauge field fluctuations in (1+1)D. In Appendix 8.B, we give long-wavelength description of the SU(2) MSL and discuss observable properties. In Appendix 8.C, we consider Zeeman magnetic fields on the SU(2) MSL. In Appendix 8.D, we realize the SU(2) MSL in a model with explicitly broken time reversal symmetry and show that this case has a larger window of stability to weak perturbations.

## 8.1 Gapless Majorana orbital liquid (MOL) on a two-leg ladder

We begin with a “spinless” (one species) MOL realized in a Kitaev-type model on a two-leg ladder shown in Fig. 8.1(a). The Hamiltonian is

$$\mathcal{H} = \mathcal{H}_0 + K_{\square_{xz}} \sum_{\square_{xz}} W_{\square_{xz}} + K_{\square_{yz}} \sum_{\square_{yz}} W_{\square_{yz}}, \quad (8.1)$$

where

$$\mathcal{H}_0 = \sum_{\lambda\text{-link}, \langle jk \rangle} J_{jk} \tau_j^\lambda \tau_k^\lambda, \quad (8.2)$$

$$W_{\square_{xz}} = \tau_1^y \tau_2^y \tau_3^y \tau_4^y, \quad (8.3)$$

$$W_{\square_{yz}} = \tau_2^x \tau_1^x \tau_4^x \tau_3^x. \quad (8.4)$$

The  $\vec{\tau}$  Pauli matrices can be thought of as acting on two-level orbital states. The  $W_p$  terms, with  $p = \square_{xz}$  or  $\square_{yz}$  formed by  $x$  and  $z$  or  $y$  and  $z$  links, respectively, are plaquette operators which commute among themselves and with all other terms in the Hamiltonian and are added to stabilize particular flux sector, see Fig. 8.1(a). Following Kitaev’s approach, we introduce Majorana representation as

$$\tau_j^\alpha = i b_j^\alpha c_j, \quad (8.5)$$

with the constraint  $D_j \equiv b_j^x b_j^y b_j^z c_j = 1$ . The Hamiltonian can be rephrased as

$$\mathcal{H}_0 = i \sum_{\langle jk \rangle} \hat{u}_{jk} J_{jk} c_j c_k, \quad (8.6)$$

$$W_{p=\{\square_{xz}, \square_{yz}\}} = - \prod_{\langle jk \rangle \in p} \hat{u}_{jk}, \quad (8.7)$$

where  $\hat{u}_{jk} \equiv -i b_j^\lambda b_k^\lambda$  for  $\lambda$ -link  $\langle jk \rangle$  and the product in the last line is circling the plaquette.

Following familiar analysis in Kitaev-type models, we observe that in the enlarged

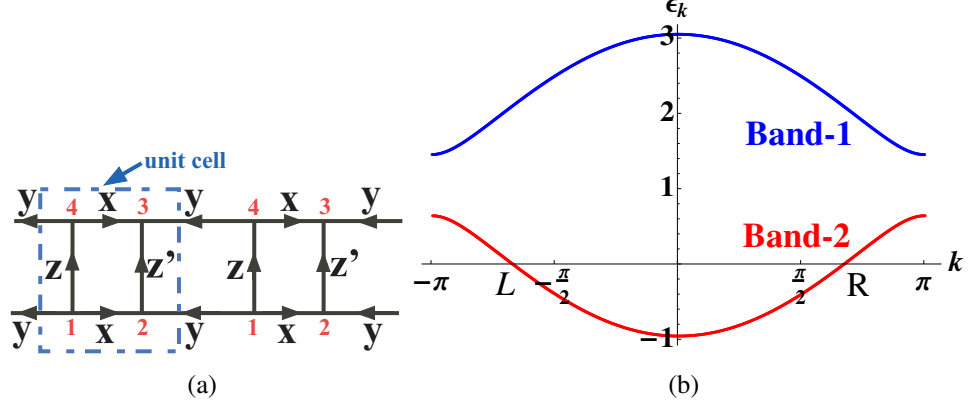


Figure 8.1: (a) Graphical representation of the exactly solvable Kitaev-type model on the two-leg ladder and its solution in the zero flux sector. The  $c$  Majoranas propagate with pure imaginary hopping amplitudes specified by the couplings  $J_x$ ,  $J_y$ ,  $J_z$ , and  $J'_z$ ; the signs in our chosen gauge are indicated by the arrows and the four-site unit cell is also indicated. (b) Dispersion of complex fermions that solve the Majorana problem for parameters  $\{J_x, J_y, J_z, J'_z\} = \{1.2, 0.8, 1.0, 1.1\}$

Hilbert space,  $\hat{u}_{jk}$  commute among themselves and with the Hamiltonian, and we can proceed by replacing them by their eigenvalues  $\pm 1$  and interpreting as static  $Z_2$  gauge fields. The  $W_p$  terms, with  $K_p > 0$  assumed to be sufficiently large, can be used to stabilize the sector with zero fluxes through all elementary plackets, and this can give a gapless phase. In our work, we fix the gauge by taking  $u_{jk} = 1$  for bonds  $j \rightarrow k$  as shown by the arrows in Fig. 8.1(a).

There are four physical sites per unit cell, so there are four Majoranas per unit cell. From now on, we replace the site labeling  $j$  with  $j = \{X, a\}$ , where  $X$  runs over the one-dimensional lattice of unit cells of the ladder and  $a$  runs over the four sites in the unit cell, see Fig. 8.1(a). The Hamiltonian can be written as,

$$\mathcal{H} = \sum_{\langle jk \rangle} c_j \mathcal{A}_{jk} c_k = \sum_{\langle (X,a), (X',a') \rangle} c_{X,a} \mathcal{A}_{X,a;X',a'} c_{X',a'}.$$

There is translational symmetry between different unit cells, and  $\mathcal{A}_{X,a;X',a'} = \mathcal{A}_{aa'}(X - X')$ .

In order to give a concise long-wavelength description, it will be convenient to use familiar complex fermion fields. To this end, we can proceed as follows. For a general

Majorana problem specified by an anti-symmetric pure imaginary matrix  $\mathcal{A}_{jk}$ , we diagonalize  $\mathcal{A}_{jk}$  for spectra, but only half of the bands are needed while the rest of the bands can be obtained by a specific relation and are redundant. Explicitly, for a system with  $2m$  bands, we can divide them into two groups. The first group contains bands from 1 to  $m$  with eigenvector-eigenenergy pairs  $\{\vec{v}_{b,k}, \epsilon_{b,k}\}$ , where  $b = 1, 2, \dots, m$  are band indices, and the second group contains bands from  $m + 1$  to  $2m$  related to the first group,  $\{\vec{v}_{b'=m+b,k}, \epsilon_{b'=m+b,k}\} = \{\vec{v}_{b,-k}^*, -\epsilon_{b,-k}\}$ . Using only the bands with  $b = 1$  to  $m$ , we can write the original Majoranas in terms of usual complex fermions as

$$c(X, a) = \sqrt{\frac{2}{N_{uc}}} \sum_{b=1}^m \sum_{k \in \text{B.Z.}} [e^{ikX} v_{b,k}(a) f_b(k) + \text{H.c.}],$$

where  $N_{uc}$  is the number of unit cells, B.Z. stands for the Brillouin zone, and the complex fermion field  $f$  satisfies the usual anticommutation relation,  $\{f_b^\dagger(k), f_{b'}(k')\} = \delta_{bb'} \delta_{kk'}$ . In terms of the complex fermion fields, the Hamiltonian becomes

$$\mathcal{H} = \sum_{b=1}^m \sum_{k \in \text{B.Z.}} 2\epsilon_b(k) \left[ f_b^\dagger(k) f_b(k) - \frac{1}{2} \right]. \quad (8.8)$$

In the present case,  $2m = 4$  and therefore two bands are sufficient to give us the full solution of the Majorana problem.

The above approach can be applied to any general Majorana problem and is needed when we consider a model lacking any symmetries in Appendix 8.D. In the present case, we require the model to respect time reversal symmetry [14] and leg interchange symmetry, which allows us to introduce convenient complex fermion fields already on the lattice scale as follows

$$f_{\text{I}}(X) = \frac{c(X, 1) + ic(X, 4)}{2}, \quad (8.9)$$

$$f_{\text{II}}(X) = \frac{-ic(X, 2) + c(X, 3)}{2}. \quad (8.10)$$

The Hamiltonian becomes

$$\mathcal{H} = 2 \sum_X \left\{ J_z f_I^\dagger(X) f_I(X) + J'_z f_{II}^\dagger(X) f_{II}(X) - \left[ J_x f_I^\dagger(X) f_{II}(X) + J_y f_{II}^\dagger(X) f_I(X+1) + \text{H.c.} \right] \right\},$$

where we ignored constant contribution. It is easy to calculate the band dispersions,

$$\epsilon(k) = J_z^+ \pm \sqrt{(J_z^-)^2 + J_x^2 + J_y^2 + 2J_x J_y \cos(k)}, \quad (8.11)$$

with  $J_z^\pm = (J_z \pm J'_z)/2$ . The spectrum is gapless for  $|J_x - J_y| \leq \sqrt{J_z J'_z} \leq J_x + J_y$ , where without loss of generality we assumed all couplings to be positive. For an illustration of the energy spectrum, we take  $\{J_x, J_y, J_z, J'_z\} = \{1.2, 0.8, 1.0, 1.1\}$  and show the two bands of the complex fermions in Fig. 8.1(b) labeled from top to bottom as band-1 and band-2. We note that the gapless phase occur in a large parameter regime and there is no fine tuning here. The specific parameters are chosen to emphasize that we do not require any symmetries other than time reversal and leg interchange.

The band-2 crosses zero at  $k_{FR}$  and  $k_{FL} = -k_{FR}$  from time reversal. For long wavelength physics, we can focus on this band and introduce continuum complex fermion fields  $f_{R/L}$ ; for the lattice Majoranas, we obtain the expansion,

$$c(X, a) \sim \sum_{P=R/L} [e^{ik_{FP}X} v_{2,P}(a) f_P(X) + \text{H.c.}] . \quad (8.12)$$

From the detailed band calculation, at the right Fermi point

$$\vec{v}_{2,R} = \sqrt{\frac{J'_z}{4J_z^+}} \begin{pmatrix} 1 \\ i\xi \\ \xi \\ -i \end{pmatrix}, \quad (8.13)$$

where  $\xi = (J_x + J_y e^{ik_{FR}})/J'_z$ . Using time reversal invariance, for the left Fermi point we

get  $v_{2,L}(a) = (-1)^{a+1}v_{2,R}^*(a)$ . The effective low-energy Hamiltonian density is

$$\mathcal{H} = v_F \left[ f_R^\dagger(-i\partial_x)f_R - f_L^\dagger(-i\partial_x)f_L \right], \quad (8.14)$$

describing a one-dimensional Dirac particle with Fermi velocity  $v_F = J_x J_y \sin(k_{FR})/J_z^+$ . We list the symmetry transformations of the continuum fields in Table 8.1 (ignoring the “spin” indices there). In particular, the leg interchange symmetry prohibits terms of the form  $f_R f_L$  from the continuum Hamiltonian that would gap out the spectrum.

### 8.1.1 Fixed-point theory of Majorana orbital liquid and observables

In this subsection, we first give the fixed-point theory of the MOL and then we will consider bond energy operators to characterize such gapless phase. We use bosonization, re-expressing the low-energy fermion operators with bosonic fields [156, 71, 106],

$$f_P = e^{i(\varphi+P\theta)}, \quad (8.15)$$

with canonical conjugate boson fields:

$$[\varphi(x), \varphi(x')] = [\theta(x), \theta(x')] = 0, \quad (8.16)$$

$$[\varphi(x), \theta(x')] = i\pi\Theta(x - x'), \quad (8.17)$$

where  $\Theta(x)$  is the heaviside step function.

The fixed-point bosonized Lagrangian of such gapless MOL is

$$\mathcal{L}_{MOL} = \frac{1}{2\pi g} \left[ \frac{1}{v} (\partial_\tau \theta)^2 + v (\partial_x \theta)^2 \right]. \quad (8.18)$$

For free fermions,  $g = 1$  and  $v = v_F$ , the bare Fermi velocity. Later when we discuss the stability of such a phase in Chapter 8.1.2, we will see that there is only one strictly marginal interaction which introduces one Luttinger parameter  $g$ . To detect the gaplessness of the phase using physical (gauge-invariant) observables, here we consider bond-energy operators [63],  $\mathcal{B}^{s/a}(X)$ , which we further categorize into symmetric or antisymmetric with

respect to the leg interchange symmetry. The specific microscopic operators are

$$\begin{aligned}\mathcal{B}^{s/a}(X) &= \tau^x(X, 1)\tau^x(X, 2) \pm \tau^x(X, 4)\tau^x(X, 3) \\ &= iu_{12}c(X, 1)c(X, 2) \pm iu_{43}c(X, 4)c(X, 3),\end{aligned}\quad (8.19)$$

where we used Majorana representation, Eq. (8.5). In our gauge, after expansion in terms of the continuum complex fermions using Eq. (8.12), the Fourier components are organized as follows

$$\mathcal{B}_{Q=0}^s \sim f_R^\dagger f_R + f_L^\dagger f_L = \frac{\partial_x \theta}{\pi}, \quad (8.20)$$

$$\mathcal{B}_{k_{FR}-k_{FL}}^s \sim f_L^\dagger f_R = ie^{i2\theta}, \quad (8.21)$$

$$\mathcal{B}_{k_{FR}+k_{FL}}^a \sim f_L f_R = -ie^{i2\varphi}. \quad (8.22)$$

( Note that with TRS, the wave vector  $k_{FR} + k_{FL}$  is the same as  $Q = 0$ ; to be more precise, we should write a Hermitian and time reversal symmetric combination,  $\mathcal{B}_{Q=0}^a = if_L f_R + \text{H.c.}$ ) Thus, the symmetric bond-energy correlations are expected to decay with oscillations at incommensurate wave vectors  $\pm 2k_{FR}$ , while the anti-symmetric bond-energy correlations decay without oscillations. Such a sharp difference can be confirmed in exact numerical calculations.

In the bosonized form, the scaling dimension of each term is apparent,

$$\Delta[\mathcal{B}_{Q=0}^s] = 1, \quad (8.23)$$

$$\Delta[\mathcal{B}_{2k_{FR}}^s] = g, \quad (8.24)$$

$$\Delta[\mathcal{B}_{Q=0}^a] = \frac{1}{g}. \quad (8.25)$$

In the non-interacting parton limit,  $g \rightarrow 1$ , we expect to see all components of bond-energy correlations decay as  $X^{-2}$ .

For illustration, we calculate correlations in the exactly solvable model, taking the same parameters as in Fig. 8.1. Figure 8.2(a) shows log-log plot of symmetric bond-energy correlations in a finite system with 500 unit cells, while Figure 8.2(b) shows antisymmetric

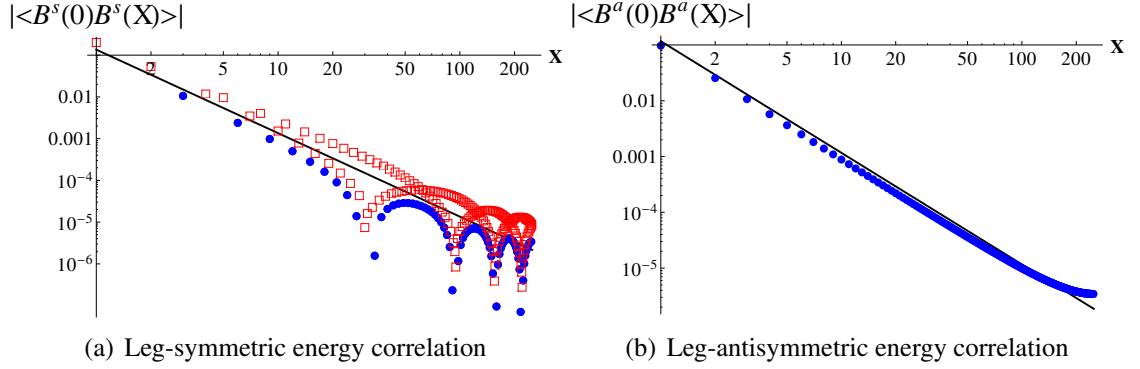


Figure 8.2: Figures (a) and (b) illustrate power law behaviors of the symmetric and anti-symmetric bond energy correlations, with  $B^{s/a}$  defined in Eq. (8.19), in the exactly solvable model with noninteracting partons. The system has 500 unit cells and we use the same parameters as in Fig. 8.1. We plot absolute values and indicate the sign with filled circles (blue) for positive correlations and open square boxes (red) for negative correlations. The log-log plots clearly show  $X^{-2}$  decay (straight lines) with incommensurate oscillations in the symmetric case and no oscillations in the antisymmetric case. The characteristic wavevectors can be determined from the structure factor study shown in Fig. 8.3.

bond-energy correlations [161]. We can see the overall  $X^{-2}$  envelope in both figures and also incommensurate oscillations in the symmetric bond-energy correlations, which confirm the theoretical analysis above.

Power-law correlations in real space correspond to singularities in momentum space, which we can study by considering the corresponding structure factors. Figure 8.3(a) shows the symmetric bond-energy structure factor and Fig. 8.3(b) shows the anti-symmetric bond-energy structure factor. It is clear that the singularities in the symmetric case occur exactly at  $Q = 0$  and  $Q = \pm(k_{FR} - k_{FL}) = \pm 2k_{FR} \equiv \pm 2k_F$  (which we also mark using values obtained by extracting the Fermi points of band 2), while there is only  $Q = 0$  singularity for the anti-symmetric case.

Let us now consider some other operators similar to generic XYZ energy terms but not present in the exactly solvable model; this will be also useful for the subsequent discussion of the MOL stability. First, operators like  $\tau^y(X, 1)\tau^y(X, 2)$  and  $\tau^z(X, 1)\tau^z(X, 2)$  have ultra-short-ranged correlations as they contain unpaired localized  $b$ -fermions. It is more interesting to consider operators like  $\tau^x(X, 1)\tau^x(X, 4)$  defined on the  $z$ -type (vertical) links in Fig. 8.1. In this case, even though the local operator contains unpaired  $b$ -Majoranas, in the physical Hilbert space these can actually be paired at the expense of introducing a string

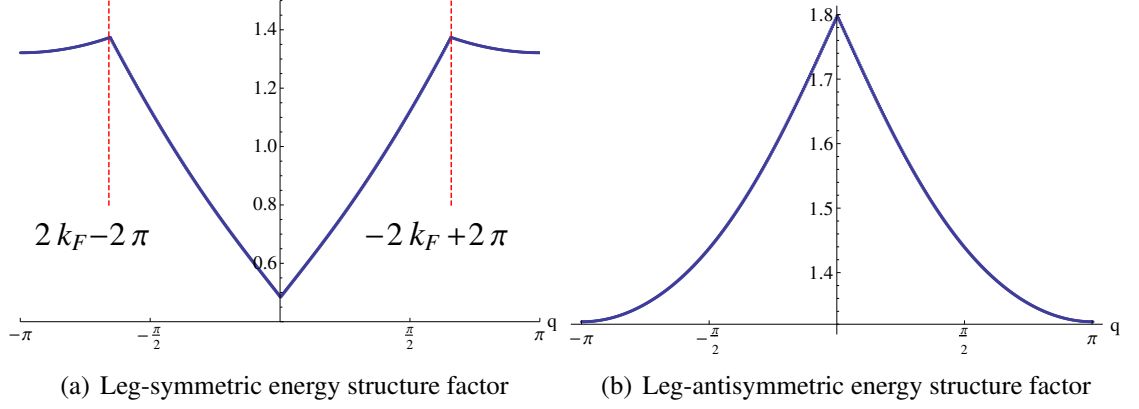


Figure 8.3: Figures (a) and (b) illustrate the symmetric bond-energy and antisymmetric bond-energy structure factors corresponding to Figs. 8.2(a) and 8.2(b), respectively. Both cases clearly show a singularity at  $Q = 0$ , while the symmetric case also shows singularities at  $\pm 2k_F$ .

product of the gapless  $c$ -Majoranas. For example, consider calculating correlation between rungs at  $X$  and  $X'$ :

$$\begin{aligned}
\hat{\mathcal{F}}(X, X') &\equiv \tau^x(X, 1)\tau^x(X, 4) \tau^x(X', 1)\tau^x(X', 4) = \\
&= \prod_{X \leq X'' < X'} (-1)c(X'', 1)c(X'', 4)c(X'', 2)c(X'', 3) \times \\
&\quad \times \prod_{\langle (X,1), (X,4) \rangle < \lambda\text{-link } \langle ij \rangle \leq \langle (X',1), (X',4) \rangle} \hat{u}_{ij}^\lambda
\end{aligned} \tag{8.26}$$

where the last product contains all links on the ladder located between the two vertical links excluding  $\langle (X, 1), (X, 4) \rangle$  and including  $\langle (X', 1), (X', 4) \rangle$  and oriented as shown in Fig. 8.1. The second line is 1 in our chosen gauge, and we then have a factor of

$$(-1)c(X'', 1)c(X'', 4)c(X'', 2)c(X'', 3) = e^{i\pi[f_{\text{I}}^\dagger(X'')f_{\text{I}}(X'') + f_{\text{II}}^\dagger(X'')f_{\text{II}}(X'')]} \tag{8.27}$$

for each unit cell, where we used Eqs. (8.9)–(8.10). In the present gauge, we can write schematically  $\tau^x(X, 1)\tau^x(X, 4) \sim \prod_{X'' < X} (-1)c(X'', 1)c(X'', 4)c(X'', 2)c(X'', 3)$ , and see that this contains non-local Jordan-Wigner-like string operator in terms of the gapless par-

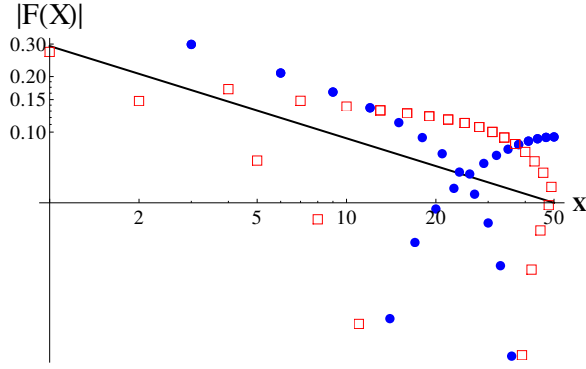


Figure 8.4: Figure illustrates power-law behavior of the correlation  $\mathcal{F}(X - X') = \langle \hat{\mathcal{F}}(X, X') \rangle$ , defined in Eq. (8.26). The system has 100 unit cells in chain length and the same parameters as in Fig. 8.1. We show the absolute values of  $|\mathcal{F}(X)|$  and indicate the sign with filled circles (blue) for positive correlations and open square boxes (red) for negative correlations. The log-log plot clearly shows  $X^{-1/2}$  envelope (straight line in the figure). The irregular behavior is due to incommensurate oscillations.

tons. In the bosonization language, the string operator becomes

$$\prod_{X'' < X} e^{i\pi[f_{\text{I}}^{\dagger}(X'')f_{\text{I}}(X'') + f_{\text{II}}^{\dagger}(X'')f_{\text{II}}(X'')]} \sim e^{\pm i[\theta(X) + \pi\bar{n}X]}. \quad (8.28)$$

This has scaling dimension  $1/4$  in the free-fermion case and hence the above correlation decays as  $X^{-1/2}$  power law and oscillates at wavevector  $\pi\bar{n} = k_F$  from Fig. 8.1(b). It may seem unusual that this appears to contain the specific gauge-dependent quantity  $k_F$ ; note, however, that in the full calculation we used the specific gauge to set the last line in Eq. (8.26) to unity, and the final result is independent of the gauge.

Evaluating expectation value of the string operator in the free fermion ground state leads to a Pfaffian of a matrix formed by the Majorana contractions and can be easily computed numerically for reasonable sizes [162]. The results are shown in Fig. 8.4 for a system with 100-unit cells [161]. The corresponding structure factor is shown in Fig. 8.5. We can clearly see the singularities at  $\pm k_F$  and confirm our theoretical analysis.

### 8.1.2 Stability of Majorana orbital liquid

Let us now consider going away from the exactly solvable point. First, we consider perturbations that are local in the continuum fermion fields. This ignores fluctuations in the  $Z_2$

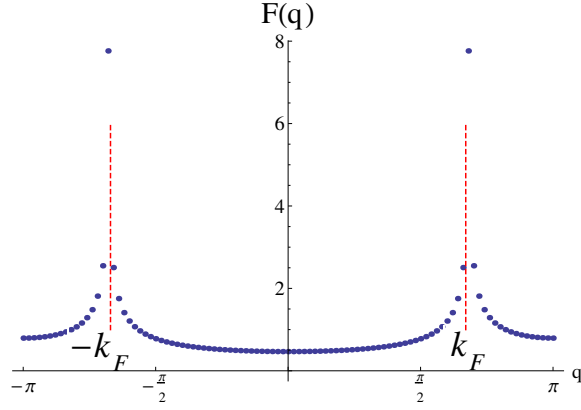


Figure 8.5: Structure factor corresponding to Fig. 8.4; we also mark the expected locations of the singularities,  $\pm k_F$ .

gauge fields, and we will address stability against confinement shortly. In the language of usual complex fermions, there is only one valid 4-fermion interaction,

$$\mathcal{H}_{\text{int}} = u f_R^\dagger f_R f_L^\dagger f_L . \quad (8.29)$$

This interaction is strictly marginal, and therefore the gapless MOL is stable also with  $\mathcal{H}_{\text{int}}$  and has one gapless mode. This interaction will renormalize the Luttinger parameter and the Fermi velocity to be

$$g = \sqrt{\frac{1 - \frac{u}{2\pi v_F}}{1 + \frac{u}{2\pi v_F}}} , \quad (8.30)$$

$$v = v_F \sqrt{1 - \left(\frac{u}{2\pi v_F}\right)^2} , \quad (8.31)$$

which completes our description of the fixed-point theory in Eq. (8.18) and will modify the power laws of various correlations as discussed above in Chapter 8.1.1.

We now want to address the issue of confinement, more precisely, the stability of the MOL theory when we allow fluctuations in the  $Z_2$  gauge fields. As we discuss in Appendix 8.A, allowing  $Z_2$  gauge field fluctuations in the (1+1)D space-time is like allowing half-vortices in the phase field in the bosonized harmonic liquid description and corresponds to allowing terms  $\lambda_{1/2} \cos(\theta + k_F X + \alpha_{1/2})$  in the dual harmonic liquid description,

Eq. (8.18). The key point is that this term is oscillating for generic  $k_F$  and hence averages out to zero (the underlying physics is destructive interference due to Berry phases). Thus, our gapless MOL with incommensurate momenta carried by the fermion fields persists also in the presence of  $Z_2$  gauge field dynamics even in (1+1)D, in the sense that we retain the gapless mode.

One may worry about the precise connection between the present system and the schematic  $Z_2$  gauge theory plus  $U(1)$  matter at incommensurate density considered in Appendix 8.A. Indeed, the connection is only crude, and we do not have one-to-one correspondences. Nevertheless, we can bolster our argument by considering explicitly some allowed perturbations to the exactly solvable model. Consider, e.g., adding small general XYZ interactions  $\sum_{\langle ij \rangle} \sum_{\mu=x,y,z} \delta J_{ij}^\mu \tau_i^\mu \tau_j^\mu$  on all bonds in a manner respecting the underlying lattice symmetries. As we have discussed earlier,  $\delta J^{y,z}$  terms on the  $x$ -type bonds and  $\delta J^{x,z}$  terms on the  $y$ -type bonds have short-range correlations and hence constitute irrelevant perturbations (of course, they can renormalize the Luttinger parameter). On the other hand,  $\delta J^{x,y}$  terms on the  $z$ -type bonds have power law correlations. However, these correlations oscillate at the incommensurate wavevector, see Fig. 8.4 and Fig. 8.5. Hence such terms, whose structure is similar to  $\lambda_{1/2} \cos(\theta + k_F X + \alpha_{1/2})$ , see Eq. (8.28), are washed out from the low-energy Hamiltonian. Thus, the fixed point description is the same as described earlier, but with the additional remark that now generic energy correlations that are symmetric under the leg interchange will also obtain a contribution oscillating at wavevector  $k_F$  with scaling dimension  $g/4$ .

Finally, we remark that the  $Z_2$  gauge fluctuations do lead to confinement in our two-leg model in gapped regimes, e.g., when the  $J_z$  terms dominate over the  $J_x, J_y$  terms in the original Hamiltonian Eq. (8.1). In this regime, we can start with effective (super)-spins on the rungs formed by the large  $J_z$  terms (e.g., after conveniently making the  $J_z$  coupling ferromagnetic). We perturbatively derive effective Hamiltonian governing these effective spins, which works out to be an Ising-like chain and has two degenerate ground states. Adding the  $\delta J^{x,y}$  perturbations on the  $z$ -type bonds gives local *longitudinal* fields in this Ising chain and immediately lifts the degeneracy. Hence, there is a unique ground state.

Furthermore, creating a single domain-wall-like excitation, which behaves as a free

particle in the exactly solvable model, requires infinite energy in the presence of the longitudinal field. On the other hand, a pair of domain walls, kink and anti-kink, are allowed, but to separate one from the other requires energy linearly proportional to the distance between them. Therefore, such  $\delta J^{x,y}$  perturbations on the  $z$ -type bonds give linear confinement of particles that were free at the exactly solvable point, and this applies to all particles that carry gauge charge with respect to the  $Z_2$  gauge field in the exactly solvable model.

## 8.2 Gapless SU(2)-invariant Majorana spin liquid (MSL) on the two-leg ladder

We now want to consider Majorana spin liquids with more degrees of freedom, in particular with physical spin degrees of freedom, and see what new issues and features arise in this case. In order to construct spin SU(2)-invariant Kitaev-type model, we follow [149, 147, 157] to take a system with both spin and orbital degrees of freedom on each site. The complete Hamiltonian is

$$\mathcal{H}_{SU(2)} = \mathcal{H}'_0 + K_{\square_{xz}} \sum_{\square_{xz}} W_{\square_{xz}} + K_{\square_{yz}} \sum_{\square_{yz}} W_{\square_{yz}}, \quad (8.32)$$

where

$$\mathcal{H}'_0 = \sum_{\lambda\text{-link}, \langle jk \rangle} J_{jk} (\tau_j^\lambda \tau_k^\lambda) (\vec{\sigma}_j \cdot \vec{\sigma}_k). \quad (8.33)$$

$\mathcal{H}'_0$  is a Kugel-Khomskii-like Hamiltonian with  $\vec{\sigma}$  being the spin-1/2 Pauli matrices and  $\vec{\tau}$  being the Pauli matrices acting on the orbital states, while the  $W_{\square_{xz}}$  and  $W_{\square_{yz}}$  terms are given in Eqs. (8.3)–(8.4).

Introducing Majorana representation of spin-1/2, we write the spin and orbital operators

as

$$\sigma_j^\alpha = -\frac{i}{2} \sum_{\beta,\gamma} \epsilon^{\alpha\beta\gamma} c_j^\beta c_j^\gamma, \quad (8.34)$$

$$\tau_j^\alpha = -\frac{i}{2} \sum_{\beta,\gamma} \epsilon^{\alpha\beta\gamma} d_j^\beta d_j^\gamma. \quad (8.35)$$

On each site  $j$  of the two-leg ladder, we realize the physical four-dimensional Hilbert space using six Majorana fermions  $c_j^x, c_j^y, c_j^z, d_j^x, d_j^y, d_j^z$ , with the constraint  $D_j \equiv -i c_j^x c_j^y c_j^z d_j^x d_j^y d_j^z = 1$  (namely, for any physical state  $|\Phi\rangle_{\text{phys}}$ , we require  $D_j |\Phi\rangle_{\text{phys}} = |\Phi\rangle_{\text{phys}}$ ). Therefore,  $\sigma_j^\alpha \tau_j^\beta |\Phi\rangle_{\text{phys}} = i c_j^\alpha d_j^\beta |\Phi\rangle_{\text{phys}}$ . In terms of the Majoranas, the Hamiltonian can be rephrased as

$$\mathcal{H}'_0 = i \sum_{\langle jk \rangle} \hat{u}_{jk} J_{jk} \sum_{\alpha=x,y,z} c_j^\alpha c_k^\alpha, \quad (8.36)$$

and the  $W_p$  terms are the same as in Eq. (8.7) with  $\hat{u}_{jk} \equiv -i d_j^\lambda d_k^\lambda$  for  $\lambda$ -link  $\langle jk \rangle$ .

For long-wavelength description, much of the development in Chapter 8.1 can be directly applied here with the replacement,  $c \rightarrow c^\alpha, f \rightarrow f^\alpha, \alpha = x, y, z$ . We now have three fermion species with identical dispersion taken to be similar to that in Fig. 8.1(b), and we introduce right and left moving complex fermion fields  $f_{R/L}^\alpha$  as in the spinless case. Under SU(2) spin rotations, the triple  $f^{x,y,z}$  transforms in the same way as the physical spin  $\sigma^{x,y,z}$ .

Just as in the MOL case in Chapter 8.1, we first establish the fixed point structure ignoring the gauge field fluctuations. In order to study the stability of such gapless SU(2)-invariant Majorana spin liquid under weak perturbations, we write down most general four-fermion interactions and perform renormalization group (RG) studies. The allowed four-fermion interactions are highly constrained by symmetry. In addition to the SU(2) spin rotation invariance, these terms must be preserved by projective symmetry group (PSG) [13] of spatial translational symmetry, time reversal symmetry, and leg interchange symmetry. We list the symmetry transformations in Table 8.1 and write the allowed nonchiral interac-

Table 8.1: PSG transformation properties of the continuum fields under  $T_x$  (spatial translation symmetry),  $\Theta$  (time reversal transformation plus gauge transformation), [14]  $M$  (leg interchange transformation plus gauge transformation). We also note that under spin rotation,  $\vec{f}_P = (f_P^x, f_P^y, f_P^z)$  and  $\vec{f}_P^\dagger = (f_P^{x\dagger}, f_P^{y\dagger}, f_P^{z\dagger})$  transform as 3-dimensional vectors. Note that, below,  $P = R/L$  and  $\bar{P} = -P = L/R$ .

	$T_x$	$\Theta$	$M$
$f_P^\alpha \rightarrow$	$e^{iPk_F} f_P^\alpha$	$f_{\bar{P}}^\alpha; i \rightarrow -i$	$-i f_P^\alpha$
$f_P^{\alpha\dagger} \rightarrow$	$e^{-iPk_F} f_P^{\alpha\dagger}$	$f_{\bar{P}}^{\alpha\dagger}; i \rightarrow -i$	$i f_P^{\alpha\dagger}$

tions (i.e., connecting right and left movers) as

$$\mathcal{H}_{\text{int}} = u_\rho \mathcal{J}_R \mathcal{J}_L - u_{\sigma 1} \vec{\mathcal{J}}_R \cdot \vec{\mathcal{J}}_L + u_{\sigma 2} I_{RL}^\dagger I_{RL} + w_4 (I_{RL} I_{RL} + \text{H.c.}), \quad (8.37)$$

where we defined

$$\mathcal{J}_P = \sum_{\alpha} f_P^{\alpha\dagger} f_P^\alpha, \quad (8.38)$$

$$\mathcal{J}_P^\alpha = -i \sum_{\beta, \gamma} \epsilon^{\alpha\beta\gamma} f_P^{\beta\dagger} f_P^\gamma, \quad (8.39)$$

$$I_{RL} = \sum_{\alpha} f_R^\alpha f_L^\alpha. \quad (8.40)$$

The general expression  $\mathcal{H}_{\text{int}}$  in Eq. (8.37) contains familiar-looking four-fermion terms  $f_R^{\alpha\dagger} f_L^{\beta\dagger} f_R^\gamma f_L^\delta$  that conserve fermion number, and also terms  $f_R^\alpha f_R^\beta f_L^\gamma f_L^\delta$  that do not conserve the fermion number but are nevertheless allowed by all symmetries of the problem. The less familiar terms need to be considered since the microscopic Majorana Hamiltonian does not have  $U(1)$  particle conservation, which is a new feature in such Majorana liquids.

We remark that the time reversal and translation symmetries alone would allow yet other terms expressed as  $f_R^{\alpha\dagger} f_R^\beta f_R^\gamma f_L^\delta$  and in fact would also allow a bilinear term ( $iI_{RL} + \text{H.c.}$ ) in the Hamiltonian that would immediately open a gap in the spectrum. However, these terms are prohibited if we also require the leg interchange symmetry, which is hence crucial for the time-reversal invariant  $SU(2)$  MSL.

The weak-coupling differential RG equations are

$$\dot{u}_\rho = \frac{1}{2\pi v} (u_{\sigma_2}^2 + 2u_{\sigma_1}u_{\sigma_2} - 4w_4^2), \quad (8.41)$$

$$\dot{u}_{\sigma_1} = \frac{1}{2\pi v} (-u_{\sigma_1}^2 + 2u_{\sigma_1}u_{\sigma_2}), \quad (8.42)$$

$$\dot{u}_{\sigma_2} = \frac{1}{2\pi v} (-3u_{\sigma_2}^2 - 6u_{\sigma_1}u_{\sigma_2} - 4w_4^2), \quad (8.43)$$

$$\dot{w}_4 = \frac{1}{2\pi v} (-2u_{\sigma_1} - 4u_{\sigma_2} - 4u_\rho) w_4, \quad (8.44)$$

where  $v$  is the Fermi velocity of right and left movers and  $\dot{O} \equiv dO/d\ell$  with  $\ell$  being logarithm of the length scale. The only fixed points have  $u_{\sigma_1}^* = u_{\sigma_2}^* = w_4^* = 0$ . Stability to small deviations in  $w_4$  requires  $u_\rho^* > 0$ . If we consider small deviations in  $u_{\sigma_1}$  and  $u_{\sigma_2}$  setting  $w_4^* = 0$ , the RG equations can be written as

$$\dot{g}_\rho \equiv 3\dot{u}_\rho + \dot{u}_{\sigma_2} = 0, \quad (8.45)$$

$$\dot{u}_{\sigma_1} = \frac{1}{2\pi v} (-u_{\sigma_1}^2 + 2u_{\sigma_1}u_{\sigma_2}), \quad (8.46)$$

$$\dot{u}_{\sigma_2} = \frac{1}{2\pi v} (-3u_{\sigma_2}^2 - 6u_{\sigma_1}u_{\sigma_2}), \quad (8.47)$$

and the last two equations are essentially identical to the RG equations in a level-one SU(3) Wess-Zumino-Witten (WZW) model discussed by Itoi and Kato. [163] Translated from their analysis, the stability to small deviation in  $u_{\sigma_1}$  and  $u_{\sigma_2}$  requires  $u_{\sigma_1} > 0$ ,  $u_{\sigma_1} + u_{\sigma_2} > 0$ . In a stable flow,  $u_\rho$  reaches some fixed value,  $u_\rho^* > 0$ , and is strictly marginal;  $u_{\sigma_1}$  and  $u_{\sigma_2}$  approach zero from the specific region described above and are marginally irrelevant; finally,  $w_4$  flows to zero as long as  $u_\rho^* > 0$  and is irrelevant. Thus, we have one Luttinger parameter in the ‘‘charge’’ sector. In Appendix 8.B, we give the fixed-point theory of the SU(2) MSL and list observables that can be obtained as fermion bilinears. We find that spin operator, Eq. (8.64), spin-nematic operator, Eq. (8.66), and bond-energy operator, Eq. (8.65), have correlations that decay in a power law with oscillations at incommensurate wave vectors, which is one of the hallmarks of such Majorana spin liquids as we discussed in [157] in a 2d example.

The inclusion of the  $Z_2$  gauge field fluctuations in this quasi-1d gapless MSL can be

discussed as in the spinless case (see also Appendix 8.A). The space-time gauge field fluctuations are suppressed by the destructive interference arising from the incommensurate momenta carried by the fermion fields. Thus, the system retains three gapless modes, but the local energy observable obtains new oscillating contributions.

We can also consider directly allowed perturbations going beyond the exactly solvable model. For example,  $\tau_i^x \tau_j^x$  terms on the vertical links  $\langle ij \rangle$  can be expressed as a product of three  $c$ -fermion strings, one for each flavor, and will oscillate at wavevector  $3k_F$  with power law  $X^{-3/2}$  in the free parton case. This is consistent with the schematic analysis in Appendix 8.A extended to multiple parton fields, where a vison can be seen as introducing a half-vortex for each flavor. The described low-energy theory is hence stable to generic perturbations in the sense of retaining the gapless fields, while the local energy observable that is symmetric under the leg-interchange obtains additional contributions oscillating at  $3k_F$  (which in turn induces new contributions to other observables as discussed in Appendix 8.B).

### 8.3 Discussion

Motivated by recent proposal of SU(2)-invariant Majorana spin liquids by Biswas et al. [128] and the realization of the SU(2) MSL in an exactly solvable model [149, 147, 157], we studied the MOL and SU(2) MSL on the two-leg ladder. Perturbing away from the exactly solvable points, in the MOL, there is only a strictly marginal four-fermion interaction and hence it is stable to residual interactions. In the SU(2) MSL, there are several allowed four-fermion terms, but it is stable against these in a large parameter regime. Furthermore, we also show that such gapless Majorana liquids persist against  $Z_2$  gauge field fluctuations. Some time ago, Shastry and Sen [153] studied an SU(2) MSL for a 1d Heisenberg chain at mean field level. Our description of the microscopically realized quasi-1d SU(2) MSL can be viewed as providing a theory beyond mean field for more general such states and distinguishes them from the Bethe phase of the 1d Heisenberg chain. The stable MOL and SU(2) MSL phases that we find are new quasi-1d phases, and we suggest numerical studies such as density matrix renormalization group (DMRG) [164] to test our theoretical ideas

of their stability. The DMRG studies can also determine the Luttinger parameters of the fixed-point MOL and SU(2) MSL theories.

The presence of gapless matter fields is the key against confining effects of  $Z_2$  gauge field fluctuations in (1+1)D, see Appendix 8.A. Without such gapless matter, the gapped phases realized in Kitaev-type models on two-leg ladders in our model are likely unstable to general generic perturbations, and this prediction can be checked by DMRG studies. This is reminiscent of a picture where gapless matter fields can suppress monopoles in a (2+1)D compact electrodynamics and thus make gapless U(1) spin liquids with sufficiently many Dirac points or with Fermi surfaces stable [3, 165, 166], while gapped U(1) spin liquids would be unstable to confinement in (2+1)D. An interesting finding is that allowing  $Z_2$  gauge fluctuations in our quasi-1d Majorana liquids leads to new contributions to various observables, with different characteristic wavevectors and potentially slower power laws compared to the mean field, see Appendix 8.B.

Let us discuss possible extensions of this work. Throughout, we focused on the MSL phase in which all couplings of the residual interactions, Eq. (8.37), converge to finite fixed point values in RG thinking. In principle, one can analyze situations where some of the residual interactions are relevant and explore possible nearby phases and characterize their properties using the observables listed in Appendix 8.B. Such theoretical analysis combined with DMRG studies [29] can give a complete phase diagram.

As discussed in Biswas et al. [128] and in our earlier work [157], the effects of Zeeman field on the SU(2) MSL are interesting. The Zeeman magnetic field only couples to  $f^x$  and  $f^y$  fermions, and we can define  $f_{\pm}^{\dagger} = (f^{x\dagger} \pm i f^{y\dagger})/\sqrt{2}$  which carry  $S^z = \pm 1$ , while  $f^{z\dagger}$  carries  $S^z = 0$  and remains unaltered. In the presence of the Zeeman field, the spin SU(2) rotation symmetry is broken and only  $S^z$  is conserved. In Appendix 8.C we write down general four-fermion interactions based on symmetry arguments and perform weak coupling RG analysis. Our RG Eqs. (8.125)–(8.129) interestingly show that instabilities only occur in the  $f^{\pm}$  channel but not in the  $f^z$  channel. Hence, the  $f^z$  partons are always gapless no matter how large the field is and can give metal-like contribution to specific heat and thermal conductivity, which is qualitatively similar to what we found previously in our 2D MSL model [157].

Last but not least, it is intriguing to understand how the ladder descendants of the MOL and SU(2) MSL relate to the mother 2d phases. A systematic way to access these could be via increasing the number of legs. It seems difficult to increase the number of legs in our toy two-leg square ladder model while maintaining the spin SU(2) symmetry of the MSL, but actually it can be achieved if we consider decorated square ladder [140, 157]. One more interesting direction is to consider new types of SU(2)-invariant spin liquid wave functions motivated by the Kitaev-like SU(2) MSL writing of the spin operators and search for more realistic models in 1d and 2d that may harbor such states.

## 8.A Stability of gapless U(1) matter against $Z_2$ gauge field fluctuations in (1+1)D

We need to address the issue whether the gapless parton field picture is stable against allowing  $Z_2$  gauge field fluctuations. It is well-known that the simplest so-called even  $Z_2$  gauge theory is confining in (1+1)D; this persists also in the presence of gapped matter fields, and quasi-1d Kitaev-type models with gapped partons would suffer from this instability. We will argue, however, that gapless parton fields can eliminate this instability, particularly when they carry incommensurate momenta.

We first give a heuristic argument. Let us consider the simplest model of a  $Z_2$  gauge field coupled to a U(1) matter field, with (1+1)D action

$$\mathcal{S} = -\beta \sum_{\langle jk \rangle} \sigma_{jk} \cos(\phi_j - \phi_k) - K \sum_{\square} \sigma_{12} \sigma_{23} \sigma_{34} \sigma_{41}. \quad (8.48)$$

For  $K \rightarrow \infty$ , we choose the gauge  $\sigma_{jk} = 1$  and obtain an XY model in the  $\phi$  variables. There is a Kosterlitz-Thouless transition at some critical  $\beta_c$  and gapless phase for  $\beta > \beta_c$ . Now, let us consider large  $K$  and large  $\beta$  limit. Starting with no  $Z_2$  fluxes and no vortices, since both  $\sigma$  and  $\phi$  are almost fixed, the insertion of a  $Z_2$  flux (“vison”) can be treated as creating a  $\pi$ -vortex in the  $\phi$ . Explicitly, we can rewrite  $\sigma_{jk} \cos(\phi_j - \phi_k) = \cos[\phi_j - \phi_k - \pi(1 - \sigma_{jk})/2]$ . The vison insertion can be carried out by changing  $\sigma_{jk}$  from

1 to  $-1$  on a cut from infinity to the vison location. This is a  $\pi$ -phase cut for the  $\phi$  variables and can be best accomodated by a gradual winding by  $\pi$  as we go around the vison from one side of the cut to the other; hence, we get a half-vortex in the  $\phi$ . We expect that for sufficiently large  $\beta$ , the half-vortex insertions are irrelevant because of their high energy cost, which means we have a phase without proliferation of half-vortices, and then we do not need to worry about the dynamics of the  $Z_2$  gauge field which could potentially produce confinement.

Thus, it is possible to avoid confinement of (1+1)D  $Z_2$  gauge fields if we have gapless matter field. For several gapless matter fields, there is a proportional increase in the energy cost of the vison insertion and hence its irrelevance. The above argument is valid for matter fields at integer filling. It is well known that vortices in (1+1)D  $U(1)$  systems can be further suppressed if the matter field is at noninteger filling due to Berry phase effects, and such a suppression is complete for incommensurate matter density. Heuristically, we expect the vison insertions to obtain similar Berry phases as half-vortices and hence to also experience complete suppression at incommensurate density. We present a more formal derivation [11] tailored to our needs below.

We consider a general  $Z_2$  gauge theory plus  $U(1)$  matter field (represented by quantum rotors) on a  $d$ -dimensional cubic lattice with a Hamiltonian [11]

$$\begin{aligned} \mathcal{H} = & -t \sum_{\langle rr' \rangle} \hat{\sigma}_{rr'}^z \cos(\hat{\phi}_r - \hat{\phi}_{r'}) + \frac{U}{2} \sum_r (\hat{n}_r - \bar{n})^2 \\ & - K \sum_{\square} \hat{\sigma}_{12}^z \hat{\sigma}_{23}^z \hat{\sigma}_{34}^z \hat{\sigma}_{41}^z - \Gamma \sum_{\langle rr' \rangle} \hat{\sigma}_{rr'}^x, \end{aligned} \quad (8.49)$$

where  $\hat{n}_r$  is the number operator conjugate to the phase  $\hat{\phi}_r$  at site  $r$  and  $\bar{n}$  is the average density. The Hilbert space constraint is

$$e^{i\pi\hat{n}_r} \prod_{r' \in r} \hat{\sigma}_{rr'}^x = 1. \quad (8.50)$$

We proceed to treat the system using standard Euclidean path integral formalism in the  $\sigma^z$ - $\phi$  basis. We implement the constraint at each site  $r$  and temporal coordinate  $\tau$  by using

the identity

$$\delta_{e^{i\pi n_r} \cdot \prod_{r' \in r} \sigma_{rr'}^x = 1} = \frac{1}{2} \sum_{\lambda(r, \tau) = \pm 1} e^{i\pi \frac{1-\lambda}{2} (n_r + \sum_{r' \in r} \frac{1-\sigma_{rr'}^x}{2})}.$$

After standard development of the path integral for the Ising gauge fields, we can write the partition function as

$$\begin{aligned} \mathcal{Z} = & \sum_{\{S_{rr'}^z(\tau); \lambda(r, \tau)\}} \int_0^{2\pi} \mathcal{D}\phi_r(\tau) \sum_{\{n_r(\tau)\}} e^{\sum_P K_P S_{12}^z S_{23}^z S_{34}^z S_{41}^z} e^{t\delta\tau \sum_{\tau, (rr')} S_{rr'}^z(\tau) \cos[\phi_r(\tau) - \phi_{r'}(\tau)]} \times \\ & \times e^{-\frac{U\delta\tau}{2} \sum_{\tau, r} [n_r(\tau) - \bar{n}]^2 + i \sum_{\tau, r} n_r(\tau) [\phi_r(\tau + \delta\tau) - \phi_r(\tau) + \pi \frac{1-\lambda(r, \tau)}{2}]} . \end{aligned} \quad (8.51)$$

Here we used  $S_{rr'}^z$  to denote eigenvalues of  $\hat{\sigma}_{rr'}^z$  on the spatial links and elevated the auxiliary fields  $\lambda(r, \tau)$  to become Ising gauge fields on the temporal links,  $S_{(r, \tau); (r, \tau + \delta\tau)}^z \equiv \lambda(r, \tau)$  (we use either field notation where more convenient);  $\sum_P$  is over all spatial and temporal plackets,  $K_P = \{K_{\text{spat}}, K_\tau\}$ , with  $K_{\text{spat}} = K\delta\tau$  and  $\tanh K_\tau = e^{-2\Gamma\delta\tau}$ .

Now we can use a variant of XY duality transformation [167, 168, 169] to go from the  $\phi$  and  $n$  variables to real-valued ‘‘currents’’  $\vec{j}_{\text{spat}} = \{j_{r, r+\hat{e}_1}, j_{r, r+\hat{e}_2}, \dots, j_{r, r+\hat{e}_d}\}$  (where  $\hat{e}_{k=1\dots d}$  represent unit lattice vectors) and  $j_\tau$  appearing as follows:

$$\begin{aligned} e^{t\delta\tau S_{rr'}^z(\tau) \cos[\phi_r(\tau) - \phi_{r'}(\tau)]} & \simeq \sum_{p_{rr'}(\tau) = -\infty}^{+\infty} e^{-\frac{t\delta\tau}{2} \left[ \phi_{r'}(\tau) - \phi_r(\tau) + \pi \frac{1-S_{rr'}^z(\tau)}{2} - 2\pi p_{rr'}(\tau) \right]^2} \\ & = \sum_{p_{rr'}(\tau) = -\infty}^{+\infty} \int_{-\infty}^{+\infty} dj_{rr'}(\tau) e^{-\frac{j_{rr'}^2(\tau)}{2t\delta\tau} + ij_{rr'}(\tau) \left[ \phi_{r'}(\tau) - \phi_r(\tau) + \pi \frac{1-S_{rr'}^z(\tau)}{2} - 2\pi p_{rr'}(\tau) \right]}, \quad (8.52) \\ \sum_{n_r(\tau) = -\infty}^{+\infty} F[n_r(\tau)] & = \int_{-\infty}^{+\infty} dj_\tau(r, \tau) \sum_{p_\tau(r, \tau) = -\infty}^{+\infty} e^{-ij_\tau(r, \tau) \cdot 2\pi p_\tau(r, \tau)} F[j_\tau(r, \tau)] \quad (8.53) \end{aligned}$$

In the first line, we approximated the left hand side by a standard Villain form; we also dropped constant numerical factors throughout. For short-hand, we write space-time points as  $i = (r, \tau)$  and define space-time vector  $p_{i, \mu=1\dots d+1} = \{\vec{p}_{\text{spat}}, p_\tau\}$ , with  $\vec{p}_{\text{spat}} = \{p_{r, r+\hat{e}_1}, p_{r, r+\hat{e}_2}, \dots, p_{r, r+\hat{e}_d}\}$ . Then we can divide configurations  $\{p_{i\mu}\}$  into classes  $C_p$  equivalent under integer-valued gauge transformations  $p_{i\mu} \rightarrow p_{i\mu} + \nabla_\mu N_i$  and perform

the configuration summation as

$$\sum_{\{p_{i\mu}\}=-\infty}^{+\infty} F[\{p_{i\mu}\}] = \sum_{C_P} \sum_{N_i=-\infty}^{\infty} F[\{p_{i\mu} = p_{i\mu}^{(0)} + \nabla_{\mu} N_i\}],$$

where  $p_{i\mu}^{(0)}$  is one representative of a class; the results do not depend on the specific choices of  $p^{(0)}$  but only on the ‘‘vorticities’’  $q_{\mu\nu} = \nabla_{\mu} p_{\nu} - \nabla_{\nu} p_{\mu}$  characterizing the classes. Using the  $N_i$  variables, we can extend the  $\phi_i$  integrations to  $(-\infty, +\infty)$  and obtain

$$\begin{aligned} \mathcal{Z} = & \sum_{\{S_{rr'}^z(\tau); \lambda(r, \tau)\}} \sum_{C_P} \int_{-\infty}^{\infty} \mathcal{D}\vec{j}_{\text{spat}} \mathcal{D}j_{\tau} \delta(\vec{\nabla} \cdot \vec{j}_{\text{spat}} + \nabla_{\tau} j_{\tau} = 0) \times e^{\sum_P K_P S_{12}^z S_{23}^z S_{34}^z S_{41}^z} \times \\ & \times e^{-\sum_{\tau, \langle rr' \rangle} \frac{j_{rr'}(\tau)^2}{2t\delta\tau} + i \sum_{\tau, \langle rr' \rangle} j_{rr'}(\tau) \left[ \pi \frac{1 - S_{rr'}^z(\tau)}{2} - 2\pi p_{rr'}^{(0)}(\tau) \right]} \times \\ & \times e^{-\sum_{\tau, r} \frac{U\delta\tau}{2} [j_{\tau}(r, \tau) - \bar{n}]^2 + i \sum_{\tau, r} j_{\tau}(r, \tau) \left[ \pi \frac{1 - \lambda(r, \tau)}{2} - 2\pi p_r^{(0)}(r, \tau) \right]}. \end{aligned} \quad (8.54)$$

The above result holds in general (d+1)D, [11] and from now on we specialize to (1+1)D system. We solve the current conservation condition by writing  $j_{\tau} = \bar{n} + \frac{\nabla_x \theta}{\pi} = \frac{\nabla_x(\theta + \bar{\theta})}{\pi}$ , with  $\bar{\theta}(x, \tau) \equiv \pi \bar{n} x$ ,  $x$  being the spatial coordinate on the dual lattice, and  $j_x = -\frac{\nabla_{\tau} \theta}{\pi} = -\frac{\nabla_{\tau}(\theta + \bar{\theta})}{\pi}$ . The dual field  $\theta$  encodes coarse-grained fluctuations in the particle number.

We have only temporal plackets, on which we define ‘‘vorticity’’  $q = \vec{\nabla} \times \vec{p} = \nabla_x p_{\tau} - \nabla_{\tau} p_x$  and ‘‘vison number’’  $n^{\text{vison}} = \vec{\nabla} \times (1 - \vec{S}^z)/2 \pmod{2} = 0$  or  $1$  corresponding to  $S_{12}^z S_{23}^z S_{34}^z S_{41}^z = 1$  or  $-1$ . We can absorb any modulo 2 shifts from  $n^{\text{vison}}$  by redefining  $q$  and write the partition function as

$$\mathcal{Z} = \sum_{\vec{S}^z, q} \int_{-\infty}^{\infty} \mathcal{D}\theta e^{\sum_P K_P (1 - 2n_P^{\text{vison}})} e^{-\sum \frac{U\delta\tau}{2} \frac{(\nabla_x \theta)^2}{\pi^2} - \sum \frac{1}{2t\delta\tau} \frac{(\nabla_{\tau} \theta)^2}{\pi^2} + i \sum 2(\theta + \pi \bar{n} x) \times (q - \frac{1}{2} n^{\text{vison}})}. \quad (8.55)$$

This is the main result, which we can now analyze in a number of standard ways. We can integrate out the field  $\theta$  and obtain a Coulomb gas representation. In the absence of the  $Z_2$  gauge field (e.g.,  $K \rightarrow \infty$  and  $n^{\text{vison}} = 0$ ), we get familiar integer-valued charges  $q$  representing vortices of the  $U(1)$  matter system. On the other hand, for any finite  $K$  we get effectively half-integer charges  $m = q - \frac{1}{2} n^{\text{vison}} \in \frac{1}{2} \times \mathbb{Z}$  with only short-scale energetics difference between integer and half-integer charges. We also see Berry phases

$e^{i2\pi\bar{n}x}$  for a vortex insertion in the presence of non-zero background density and halving of the Berry phase for a vison insertion. Alternatively, we can consider postulating some local energetics penalty for large values of  $m$  and perform the summation over  $m$  to obtain terms like

$$\lambda_{1/2} \cos(\theta + \pi\bar{n}x) + \lambda_1 \cos(2\theta + 2\pi\bar{n}x) + \dots, \quad (8.56)$$

where we omitted possible phase shifts in the cosines for brevity. The  $\lambda_1$  term is the familiar term in the dual sine-Gordon theory for a Luttinger liquid of bosons that represents allowing vortices, while the  $\lambda_{1/2}$  term can be now interpreted as effectively allowing half-vortices if the matter is coupled to  $Z_2$  gauge fields. Crucially, both vortices and visons experience destructive interference effects for incommensurate  $\bar{n}$ . On the other hand, for commensurate  $\bar{n}$  the vison insertions can still be rendered irrelevant by going deep enough into the Luttinger phase or increasing the number of gapless fields as discussed below.

We can generalize the above result to the case with several matter fields  $\phi_\alpha$  coupled to the same  $Z_2$  gauge field by replacing the Berry phase  $2(\theta + \pi\bar{n}x) \times (q - \frac{1}{2}n^{\text{vison}})$  with  $\sum_\alpha 2(\theta_\alpha + \pi\bar{n}_\alpha x) \times (q_\alpha - \frac{1}{2}n^{\text{vison}})$ . Here the summation over vison numbers leads effectively to terms like  $\lambda_{1/2} \cos(\sum_\alpha \theta_\alpha + \pi \sum_\alpha \bar{n}_\alpha x)$ . We can see that for three identical flavors with incommensurate  $\bar{n}$  as happens in the SU(2)-invariant MSL, the destructive interference effects will wash out any vison insertions (including any combinations with nonvison terms).

Looking back at the one-component case, we could rationalize the above structure more quickly by thinking about the theory Eq. (8.49) as coming from a formal splitting of some physical boson field  $e^{i\phi_{\text{phys}}}$  into two halves [11]: schematically,  $e^{i\phi_{\text{phys}}} = e^{i2\phi}$ . Then the described gapless phase can be thought of as a (1+1)D analogue of the ‘‘Higgs phase’’ that is expected [11] to reproduce the conventional ‘‘superfluid’’ (here, quasi-long-range ordered) phase of the physical bosons. Indeed, in the derived harmonic liquid description in terms of the dual field  $\theta$ , we can change to new variable  $\theta_{\text{phys}} = \theta/2$  canonically dual to  $\phi_{\text{phys}}$  and note that the identified vison insertion operator  $e^{i\theta} = e^{i2\theta_{\text{phys}}}$  is the same as the conventional vortex insertion in  $\phi_{\text{phys}}$ . We still like to show the above more formal derivation as it is not tied to the specific origin of the parton field  $\phi$ . For example, in Chapter 8.1.1 the conjugate

pair  $\{\phi, \theta\}$  arose from bosonizing the long-wavelength fermionic parton Hamiltonian, and we can continue using these fields in calculations but remember to include the  $Z_2$  gauge fluctuation effects by allowing local energy terms like  $\lambda_{1/2} \cos(\theta + \pi \bar{n} x)$ . The same formal treatment also holds transparently for the multi-flavor generalization where the parton fields provide a very convenient description of the unconventional gapless phase, which has the same number of gapless modes as in the parton mean-field, but with the identified new contributions to the local energy once we go beyond the mean field and include  $Z_2$  gauge field fluctuations.

## 8.B Fixed-point theory and observables in the SU(2) Majorana spin liquid

We use Bosonization to re-express the low energy fermion operators,

$$f_P^\alpha = \eta_\alpha e^{i(\varphi_\alpha + P\theta_\alpha)}, \quad (8.57)$$

with canonical conjugate boson fields:

$$[\varphi_\alpha(x), \varphi_\beta(x')] = [\theta_\alpha(x), \theta_\beta(x')] = 0, \quad (8.58)$$

$$[\varphi_\alpha(x), \theta_\beta(x')] = i\pi\delta_{\alpha\beta}\Theta(x - x'), \quad (8.59)$$

where  $\Theta(x)$  is the heaviside step function and we have introduced Klein factors, the Majorana fermions with  $\{\eta_\alpha, \eta_\beta\} = 2\delta_{\alpha\beta}$ , which assure that the fermion fields with different flavors anticommute with one another.

According to the RG analysis in Chapter 8.2, at the fixed point of the stable SU(2) MSL phase, only the coupling  $u_\rho$  is strictly marginal and will renormalize the Luttinger parameter  $g$  in the “charge” sector. The effective bosonized Lagrangian is

$$\mathcal{L}_{MSL}^{SU(2)} = \frac{1}{2\pi g} \left[ \frac{1}{v_\rho} (\partial_\tau \theta_\rho)^2 + v_\rho (\partial_x \theta_\rho)^2 \right] + \sum_{\mu=1,2} \frac{1}{2\pi} \left[ \frac{1}{v} (\partial_\tau \theta_\mu)^2 + v (\partial_x \theta_\mu)^2 \right], \quad (8.60)$$

where we defined

$$\theta_\rho = \frac{1}{\sqrt{3}} (\theta_x + \theta_y + \theta_z), \quad (8.61)$$

$$\theta_1 = \frac{1}{\sqrt{2}} (\theta_x - \theta_y), \quad (8.62)$$

$$\theta_2 = \frac{1}{\sqrt{6}} (\theta_x + \theta_y - 2\theta_z), \quad (8.63)$$

and similarly for the  $\varphi$ -s, which preserves the commutation relations, Eqs. (8.58)–(8.59).

Stability against the  $w_4$  term in Eq. (8.37) requires  $g \leq 1$ .

For the observables characterizing the SU(2) MSL phase, as discussed in [157], we can use spin operators,

$$\vec{S}_j = \frac{\vec{\sigma}_j}{2}, \quad (8.64)$$

bond energy operators,

$$\mathcal{B}_{jk} = iu_{jk} J_{jk} \sum_{\alpha} c_j^{\alpha} c_k^{\alpha}, \quad (8.65)$$

and spin-nematic operators

$$P_{jk}^+ = S_j^+ S_k^+. \quad (8.66)$$

The latter can be related to the usual traceless rank two quadrupolar tensor defined as

$$\mathcal{Q}_{jk}^{\alpha\beta} = \frac{1}{2} (S_j^{\alpha} S_k^{\beta} + S_j^{\beta} S_k^{\alpha}) - \frac{1}{3} \delta^{\alpha\beta} \langle \vec{S}_j \cdot \vec{S}_k \rangle, \quad (8.67)$$

through  $P_{jk}^+ = \mathcal{Q}_{jk}^{xx} - \mathcal{Q}_{jk}^{yy} + 2i\mathcal{Q}_{jk}^{xy}$ .

We expand the observables in terms of the continuum complex fermion fields and organize according to the momentum and the leg interchange symmetry, i.e., symmetric ( $s$ )

or antisymmetric ( $a$ ) under the leg interchange:

$$S_{Q=0}^{\alpha,s} = -i \sum_{\beta,\gamma} \epsilon^{\alpha\beta\gamma} (f_R^{\beta\dagger} f_R^\gamma + f_L^{\beta\dagger} f_L^\gamma), \quad (8.68)$$

$$\mathcal{B}_{Q=0}^s = \sum_{\beta} (f_R^{\beta\dagger} f_R^\beta + f_L^{\beta\dagger} f_L^\beta), \quad (8.69)$$

$$\mathcal{Q}_{Q=0}^{\alpha\alpha,s} = \sum_{\beta \neq \alpha} (f_R^{\beta\dagger} f_R^\beta + f_L^{\beta\dagger} f_L^\beta), \quad (8.70)$$

$$\mathcal{Q}_{Q=0}^{\alpha \neq \beta, s} = \sum_{P=R/L} (f_P^{\alpha\dagger} f_P^\beta + f_P^{\beta\dagger} f_P^\alpha), \quad (8.71)$$

$$S_{k_{FR}+k_{FL}}^{\alpha,a} = -i \sum_{\beta,\gamma} \epsilon^{\alpha\beta\gamma} f_R^\beta f_L^\gamma, \quad (8.72)$$

$$\mathcal{B}_{k_{FR}+k_{FL}}^a = -i \sum_{\beta} f_R^\beta f_L^\beta, \quad (8.73)$$

$$\mathcal{Q}_{k_{FR}+k_{FL}}^{\alpha\alpha,a} = -i \sum_{\beta \neq \alpha} f_R^\beta f_L^\beta, \quad (8.74)$$

$$\mathcal{Q}_{k_{FR}+k_{FL}}^{\alpha \neq \beta, a} = -i (f_R^\alpha f_L^\beta + f_R^\beta f_L^\alpha), \quad (8.75)$$

$$S_{k_{FR}-k_{FL}}^{\alpha,s} = -i \sum_{\beta,\gamma} \epsilon^{\alpha\beta\gamma} f_L^{\beta\dagger} f_R^\gamma, \quad (8.76)$$

$$\mathcal{B}_{k_{FR}-k_{FL}}^s = \sum_{\beta} f_L^{\beta\dagger} f_R^\beta, \quad (8.77)$$

$$\mathcal{Q}_{k_{FR}-k_{FL}}^{\alpha\alpha,s} = \sum_{\beta \neq \alpha} f_L^{\beta\dagger} f_R^\beta, \quad (8.78)$$

$$\mathcal{Q}_{k_{FR}-k_{FL}}^{\alpha \neq \beta, s} = f_L^{\alpha\dagger} f_R^\beta + f_L^{\beta\dagger} f_R^\alpha, \quad (8.79)$$

$$S_{2k_{FP}}^{\alpha,a} = -i \sum_{\beta,\gamma} \epsilon^{\alpha\beta\gamma} f_P^\beta f_P^\gamma, \quad (8.80)$$

with  $S_{-Q}^\alpha = S_Q^{\alpha\dagger}$ , etc., and  $O^{s/a}$  observables mean symmetric or antisymmetric under the leg interchange. If the TRS is broken explicitly as in Appendix 8.D, all the above momenta are distinct. With TRS,  $k_{FL} = -k_{FR}$ , we have coincident momenta  $k_{FR} + k_{FL} = 0$  and  $k_{FR} - k_{FL} = 2k_{FR} = -2k_{FL}$ . Strictly speaking, with TRS, we should define  $O_{Q=0}^a = O_{k_{FR}+k_{FL}}^a + \text{H.c.}$ , instead of Eqs. (8.72)–(8.75); similarly, instead of Eq. (8.80), we should define  $S_{2k_F}^{\alpha,a} = S_{2k_{FR}}^{\alpha,a} + S_{-2k_{FL}}^{\alpha,a}$ . In the present case, the listed terms with such equal momenta transform differently under leg interchange, which is encoded in the above definitions.

The bosonized forms at  $Q = 0$  are:

$$S_{Q=0}^{x,s} = 4i\eta_z\eta_y \cos\left(\frac{\sqrt{3}\varphi_2 - \varphi_1}{\sqrt{2}}\right) \cos\left(\frac{\sqrt{3}\theta_2 - \theta_1}{\sqrt{2}}\right), \quad (8.81)$$

$$S_{Q=0}^{y,s} = 4i\eta_x\eta_z \cos\left(\frac{\sqrt{3}\varphi_2 + \varphi_1}{\sqrt{2}}\right) \cos\left(\frac{\sqrt{3}\theta_2 + \theta_1}{\sqrt{2}}\right), \quad (8.82)$$

$$S_{Q=0}^{z,s} = 4i\eta_y\eta_x \cos(\sqrt{2}\varphi_1) \cos(\sqrt{2}\theta_1), \quad (8.83)$$

$$\mathcal{B}_{Q=0}^s = \frac{\sqrt{3}}{\pi} \partial_x \theta_\rho, \quad (8.84)$$

$$\mathcal{Q}_{Q=0}^{xx,s} = -\frac{\partial_x \theta_1}{\sqrt{2}\pi} - \frac{\partial_x \theta_2}{\sqrt{6}\pi}, \quad (8.85)$$

$$\mathcal{Q}_{Q=0}^{yy,s} = \frac{\partial_x \theta_1}{\sqrt{2}\pi} - \frac{\partial_x \theta_2}{\sqrt{6}\pi}, \quad (8.86)$$

$$\mathcal{Q}_{Q=0}^{zz,s} = \frac{1}{\pi} \sqrt{\frac{2}{3}} \partial_x \theta_2, \quad (8.87)$$

$$\mathcal{Q}_{Q=0}^{xy,s} = 4i\eta_y\eta_x \cos(\sqrt{2}\theta_1) \sin(\sqrt{2}\varphi_1), \quad (8.88)$$

$$\mathcal{Q}_{Q=0}^{yz,s} = 4i\eta_z\eta_y \cos\left(\frac{\sqrt{3}\theta_2 - \theta_1}{\sqrt{2}}\right) \sin\left(\frac{\sqrt{3}\varphi_2 - \varphi_1}{\sqrt{2}}\right), \quad (8.89)$$

$$\mathcal{Q}_{Q=0}^{xz,s} = 4i\eta_z\eta_x \cos\left(\frac{\sqrt{3}\theta_2 + \theta_1}{\sqrt{2}}\right) \sin\left(\frac{\sqrt{3}\varphi_2 + \varphi_1}{\sqrt{2}}\right). \quad (8.90)$$

The corresponding scaling dimension in the fixed-point theory Eq. (8.60) is

$$\Delta[\vec{S}_{Q=0}^s] = \Delta[\mathcal{B}_{Q=0}^s] = \Delta[\mathcal{Q}_{Q=0}^{\alpha\beta,s}] = 1, \quad (8.91)$$

which is not modified by the strictly marginal interactions.

The bosonized forms at  $Q_+ \equiv k_{FR} + k_{FL}$  are:

$$S_{Q_+}^{x,a} = 2i\eta_z\eta_y e^{i(\frac{2}{\sqrt{3}}\varphi_\rho - \frac{\varphi_2}{\sqrt{6}} - \frac{\varphi_1}{\sqrt{2}})} \cos\left(\frac{\sqrt{3}\theta_2 - \theta_1}{\sqrt{2}}\right), \quad (8.92)$$

$$S_{Q_+}^{y,a} = 2i\eta_x\eta_z e^{i(\frac{2}{\sqrt{3}}\varphi_\rho - \frac{\varphi_2}{\sqrt{6}} + \frac{\varphi_1}{\sqrt{2}})} \cos\left(\frac{\sqrt{3}\theta_2 + \theta_1}{\sqrt{2}}\right), \quad (8.93)$$

$$S_{Q_+}^{z,a} = 2i\eta_y\eta_x e^{i(\frac{2}{\sqrt{3}}\varphi_\rho + \sqrt{\frac{2}{3}}\varphi_2)} \cos(\sqrt{2}\theta_1), \quad (8.94)$$

$$\mathcal{B}_{Q_+}^a = e^{i\frac{2}{\sqrt{3}}\varphi_\rho} \left[ 2e^{i\sqrt{\frac{2}{3}}\varphi_2} \cos(\sqrt{2}\varphi_1) + e^{-i2\sqrt{\frac{2}{3}}\varphi_2} \right], \quad (8.95)$$

$$\mathcal{Q}_{Q_+}^{xx,a} = e^{i\frac{2}{\sqrt{3}}\varphi_\rho} \left[ e^{i(\sqrt{\frac{2}{3}}\varphi_2 - \sqrt{2}\varphi_1)} + e^{-i2\sqrt{\frac{2}{3}}\varphi_2} \right], \quad (8.96)$$

$$\mathcal{Q}_{Q_+}^{yy,a} = e^{i\frac{2}{\sqrt{3}}\varphi_\rho} \left[ e^{i(\sqrt{\frac{2}{3}}\varphi_2 - \sqrt{2}\varphi_1)} + e^{-i2\sqrt{\frac{2}{3}}\varphi_2} \right], \quad (8.97)$$

$$\mathcal{Q}_{Q_+}^{zz,a} = 2e^{i(\frac{2}{\sqrt{3}}\varphi_\rho + \sqrt{\frac{2}{3}}\varphi_2)} \cos(\sqrt{2}\varphi_1), \quad (8.98)$$

$$\mathcal{Q}_{Q_+}^{xy,a} = 2\eta_x\eta_y e^{i(\frac{2}{\sqrt{3}}\varphi_\rho + \sqrt{\frac{2}{3}}\varphi_2)} \sin(\sqrt{2}\theta_1), \quad (8.99)$$

$$\mathcal{Q}_{Q_+}^{yz,a} = 2\eta_y\eta_z e^{i(\frac{2}{\sqrt{3}}\varphi_\rho - \frac{\varphi_2}{\sqrt{6}} - \frac{\varphi_1}{\sqrt{2}})} \sin\left(\frac{\sqrt{3}\theta_2 - \theta_1}{\sqrt{2}}\right), \quad (8.100)$$

$$\mathcal{Q}_{Q_+}^{xz,a} = 2\eta_x\eta_z e^{i(\frac{2}{\sqrt{3}}\varphi_\rho - \frac{\varphi_2}{\sqrt{6}} + \frac{\varphi_1}{\sqrt{2}})} \sin\left(\frac{\sqrt{3}\theta_2 + \theta_1}{\sqrt{2}}\right). \quad (8.101)$$

The corresponding scaling dimension is:

$$\Delta[\vec{S}_{Q_+}^a] = \Delta[\mathcal{B}_{Q_+}^a] = \Delta[\mathcal{Q}_{Q_+}^{\alpha\beta,a}] = \frac{2}{3} + \frac{1}{3g}. \quad (8.102)$$

The bosonized forms at  $Q_- \equiv k_{FR} - k_{FL}$  are:

$$S_{Q_-}^{x,s} = 2i\eta_z\eta_y e^{i(\frac{2}{\sqrt{3}}\theta_\rho - \frac{\theta_2}{\sqrt{6}} - \frac{\theta_1}{\sqrt{2}})} \cos\left(\frac{\sqrt{3}\varphi_2 - \varphi_1}{\sqrt{2}}\right), \quad (8.103)$$

$$S_{Q_-}^{y,s} = 2i\eta_x\eta_z e^{i(\frac{2}{\sqrt{3}}\theta_\rho - \frac{\theta_2}{\sqrt{6}} + \frac{\theta_1}{\sqrt{2}})} \cos\left(\frac{\sqrt{3}\varphi_2 + \varphi_1}{\sqrt{2}}\right), \quad (8.104)$$

$$S_{Q_-}^{z,s} = 2i\eta_y\eta_x e^{i(\frac{2}{\sqrt{3}}\theta_\rho + \sqrt{\frac{2}{3}}\theta_2)} \cos(\sqrt{2}\varphi_1), \quad (8.105)$$

$$\mathcal{B}_{Q_-}^s = ie^{i\frac{2}{\sqrt{3}}\theta_\rho} \left[ 2e^{i\sqrt{\frac{2}{3}}\theta_2} \cos(\sqrt{2}\theta_1) + e^{-i2\sqrt{\frac{2}{3}}\theta_2} \right], \quad (8.106)$$

$$\mathcal{Q}_{Q_-}^{xx,s} = ie^{i\frac{2}{\sqrt{3}}\theta_\rho} \left[ e^{i(\sqrt{\frac{2}{3}}\theta_2 - \sqrt{2}\theta_1)} + e^{-i2\sqrt{\frac{2}{3}}\theta_2} \right], \quad (8.107)$$

$$\mathcal{Q}_{Q_-}^{yy,s} = ie^{i\frac{2}{\sqrt{3}}\theta_\rho} \left[ e^{i(\sqrt{\frac{2}{3}}\theta_2 + \sqrt{2}\theta_1)} + e^{-i2\sqrt{\frac{2}{3}}\theta_2} \right], \quad (8.108)$$

$$\mathcal{Q}_{Q_-}^{zz,s} = 2ie^{i(\frac{2}{\sqrt{3}}\theta_\rho + \sqrt{\frac{2}{3}}\theta_2)} \cos(\sqrt{2}\theta_1), \quad (8.109)$$

$$\mathcal{Q}_{Q_-}^{xy,s} = 2i\eta_y\eta_x e^{i(\frac{2}{\sqrt{3}}\theta_\rho + \sqrt{\frac{2}{3}}\theta_2)} \sin(\sqrt{2}\varphi_1), \quad (8.110)$$

$$\mathcal{Q}_{Q_-}^{yz,s} = 2i\eta_z\eta_y e^{i(\frac{2}{\sqrt{3}}\theta_\rho - \frac{\theta_2}{\sqrt{6}} - \frac{\theta_1}{\sqrt{2}})} \sin\left(\frac{\sqrt{3}\varphi_2 - \varphi_1}{\sqrt{2}}\right), \quad (8.111)$$

$$\mathcal{Q}_{Q_-}^{xz,s} = 2i\eta_z\eta_x e^{i(\frac{2}{\sqrt{3}}\theta_\rho - \frac{\theta_2}{\sqrt{6}} + \frac{\theta_1}{\sqrt{2}})} \sin\left(\frac{\sqrt{3}\varphi_2 + \varphi_1}{\sqrt{2}}\right). \quad (8.112)$$

The corresponding scaling dimension is:

$$\Delta[\vec{S}_{Q_-}^s] = \Delta[\mathcal{B}_{Q_-}^s] = \Delta[\mathcal{Q}_{Q_-}^{\alpha\beta,s}] = \frac{2}{3} + \frac{g}{3}. \quad (8.113)$$

The bosonized forms at the  $2k_{FP}$  are:

$$S_{2k_{FP}}^{x,a} = 2i\eta_z\eta_y e^{i(\frac{2}{\sqrt{3}}\varphi_\rho - \frac{\varphi_2}{\sqrt{6}} - \frac{\varphi_1}{\sqrt{2}})} e^{iP(\frac{2}{\sqrt{3}}\theta_\rho - \frac{\theta_2}{\sqrt{6}} - \frac{\theta_1}{\sqrt{2}})}, \quad (8.114)$$

$$S_{2k_{FP}}^{y,a} = 2i\eta_x\eta_z e^{i(\frac{2}{\sqrt{3}}\varphi_\rho - \frac{\varphi_2}{\sqrt{6}} + \frac{\varphi_1}{\sqrt{2}})} e^{iP(\frac{2}{\sqrt{3}}\theta_\rho - \frac{\theta_2}{\sqrt{6}} + \frac{\theta_1}{\sqrt{2}})}, \quad (8.115)$$

$$S_{2k_{FP}}^{z,a} = 2i\eta_y\eta_x e^{i(\frac{2}{\sqrt{3}}\varphi_\rho + \sqrt{\frac{2}{3}}\varphi_2)} e^{iP(\frac{2}{\sqrt{3}}\theta_\rho + \sqrt{\frac{2}{3}}\theta_2)}, \quad (8.116)$$

where  $P = R/L = \pm$ ,

$$\Delta[\vec{S}_{2k_{FP}}^a] = \frac{1}{3} + \frac{g}{3} + \frac{1}{3g}. \quad (8.117)$$

We can see that when  $g = 1$ , each scaling dimension is 1, the value in the exactly solvable models with non-interacting partons. In the stable SU(2) MSL, we require  $g \leq 1$  and hence

$$\Delta[O_{Q_-}] \leq \Delta[O_{Q=0}] \leq \Delta[O_{2k_{FP}}] \leq \Delta[O_{Q_+}]. \quad (8.118)$$

Besides the observables constructed out of local fermion fields discussed above, there are local physical observables that require non-local expressions in terms of fermion fields similar to the string operator defined in Eq. (8.28). In this SU(2) case, we can consider the “rung energy” operator which is symmetric under leg interchange,

$$\epsilon(X) \equiv \tau^x(X, 1)\tau^x(X, 4). \quad (8.119)$$

Considering correlation function of such an operator similar to Eq. (8.26) in the spinless case, we can write schematically in our gauge

$$\tau^x(X, 1)\tau^x(X, 4) \sim \prod_{X' < X} \prod_{\alpha} (-1)^{\sum_{\alpha} c^{\alpha}(X', 1)c^{\alpha}(X', 4)c^{\alpha}(X', 2)c^{\alpha}(X', 3)}. \quad (8.120)$$

Such nonlocal operator in fermionic language seems very intractable but the expression can be greatly simplified under bosonization,

$$\begin{aligned} & \prod_{X' < X} \prod_{\alpha} c^{\alpha}(X', 1)c^{\alpha}(X', 4)c^{\alpha}(X', 2)c^{\alpha}(X', 3) \\ & \sim e^{\pm i \sum_{\alpha} [\theta(X) + \pi \bar{n}_{\alpha} X]} = e^{\pm i [\sqrt{3}\theta_{\rho} + 3k_F X]}, \end{aligned} \quad (8.121)$$

where we used the definition of  $\theta_{\rho}$  in Eq. (8.61),  $k_{FR} \equiv k_F$  and  $\bar{n}_{\alpha} = k_F/\pi$  is the average density of  $\alpha$ -species fermion. Thus, we can write a contribution to the leg-symmetric energy observable as

$$\epsilon_{3k_{FR}} \sim e^{i\sqrt{3}\theta_{\rho}}, \quad (8.122)$$

with scaling dimension  $\Delta[\epsilon_{3k_{FR}}] = \frac{3g}{4}$  and  $\epsilon_{3k_{FL}} = \epsilon_{3k_{FR}}^{\dagger}$ . We can also consider other rung energy operator such as  $\tau^y(X, 1)\tau^y(X, 4)$ , but the long-wavelength description of such an

operator is qualitatively the same as the above  $\tau^x(X, 1)\tau^x(X, 4)$ . Finally, these local energy observables can be combined with any observables listed earlier to produce further critical operators with potentially enhanced scaling dimension, e.g.,  $O_{k_{FR}+2k_{FL}}^s \sim \epsilon_{3k_{FL}} O_{Q-}^s$  with  $\Delta[O_{k_{FR}+2k_{FL}}^s] = \frac{2}{3} + \frac{g}{12}$  and  $\vec{S}_{2k_{FR}+3k_{FL}}^a \sim \epsilon_{3k_{FL}} \vec{S}_{2k_{FR}}^a$  with  $\Delta[\vec{S}_{2k_{FR}+3k_{FL}}^a] = \frac{1}{3} + \frac{g}{12} + \frac{1}{3g}$ .

## 8.C Zeeman magnetic field effects on the SU(2) Majorana spin liquid

In the SU(2) MSL phase, Zeeman magnetic field only couples to  $f^x$  and  $f^y$  fermions, and we can define  $f_{\pm}^{\dagger} = (f^{x\dagger} \pm if^{y\dagger})/\sqrt{2}$  which carry  $S^z = \pm 1$  and get Zeeman-shifted, while  $f^{z\dagger}$  carries  $S^z = 0$  that remains unaltered. The spin SU(2) rotation symmetry is broken and only  $S^z$  is conserved. Using symmetry arguments, we can write general four-fermion perturbations in terms of long-wavelength right-moving and left-moving complex fermions as

$$\mathcal{H}_{int} = \frac{1}{2} \sum_{\mu, \nu} \lambda^{\mu\nu} (\rho_{\mu, R} \rho_{\nu, L} + \rho_{\mu, L} \rho_{\nu, R}) \quad (8.123)$$

$$+ w^{+-} (f_{+, R} f_{+, L} f_{-, R} f_{-, L} + \text{H.c.}), \quad (8.124)$$

with  $\rho_{\mu, P} \equiv f_P^{\mu\dagger} f_P^{\mu}$ ,  $\mu = +, -, z$ , and  $P = R/L$ . The differential RG equations are

$$\dot{\lambda}^{++} = -\frac{(w^{+-})^2}{2\pi v_-}, \quad (8.125)$$

$$\dot{\lambda}^{--} = -\frac{(w^{+-})^2}{2\pi v_+}, \quad (8.126)$$

$$\dot{\lambda}^{+-} = -\frac{(w^{+-})^2}{\pi(v_+ + v_-)}, \quad (8.127)$$

$$\dot{w}^{+-} = -\frac{w^{+-}}{2\pi} \left[ \frac{\lambda^{++}}{v_+} + \frac{\lambda^{--}}{v_-} + \frac{4\lambda^{+-}}{v_+ + v_-} \right], \quad (8.128)$$

$$\dot{\lambda}^{zz} = \dot{\lambda}^{+z} = \dot{\lambda}^{-z} = 0. \quad (8.129)$$

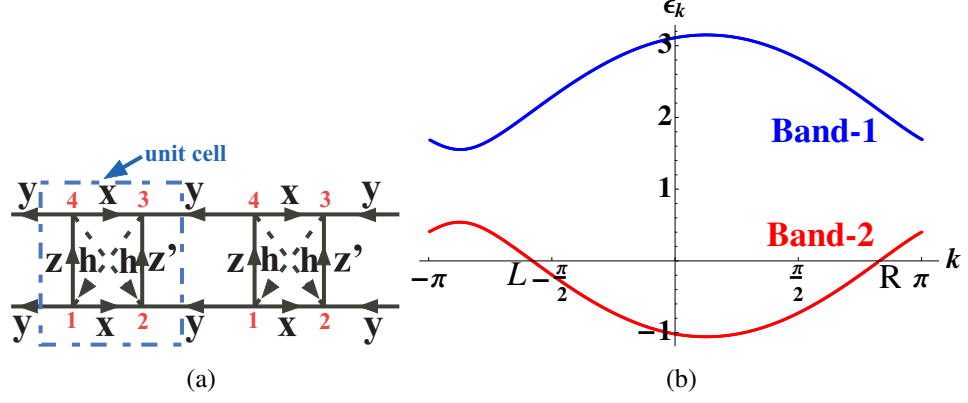


Figure 8.6: (a) Graphical representation of the exactly solvable Kitaev-type model, with time reversal breaking (TRB) introduced by hand, and its solution in the zero flux sector. (b) Complex fermion spectrum, Eq. (8.8), for the Majorana spin liquid with TRB with  $\{J_x, J_y, J_z, J'_z, h\} = \{1.2, 0.8, 1.0, 1.1, 0.5\}$ .

Here  $\dot{O} \equiv dO/d\ell$ , where  $\ell$  is logarithm of the length scale and  $v_{\pm}$  represent Fermi velocities of the  $f^{\pm}$  bands. We see that the MSL is stable if

$$\frac{\lambda^{++}}{v_+} + \frac{\lambda^{--}}{v_-} + \frac{4\lambda^{+-}}{v_+ + v_-} > 0. \quad (8.130)$$

Comparing the RG equations (8.125)–(8.129) in the presence of the Zeeman magnetic field with those Eqs. (8.41)–(8.44) without the Zeeman field, we see that the instabilities in the “spin” sector,  $u_{\sigma 1}$  and  $u_{\sigma 2}$ , are removed by the magnetic field, and the couplings that contain both  $f^{\pm}$  and  $f^z$  do not flow (the reason is that interactions that could cause these to flow do not conserve  $S^z$  and thus are not allowed). An interesting fact about these RG equations is that the instabilities only occur in the  $f^{\pm}$  fermion but not in the  $f^z$  channel. Hence, the gapless  $f^z$  partons are always gapless no matter how large the Zeeman magnetic field is and always give metal-like contribution to specific heat and thermal conductivity.

## 8.D SU(2) Majorana spin liquid with time reversal breaking (TRB)

In this appendix, we will break the time reversal symmetry explicitly by including a term,

$$\mathcal{H}_{TRB} = \frac{\hbar}{2} \sum_{\square_{xz}} \left[ (\tau_1^x \tau_2^y \tau_3^z - \tau_3^x \tau_4^y \tau_1^z) (\vec{\sigma}_3 \cdot \vec{\sigma}_1) \right. \quad (8.131)$$

$$\left. + (\tau_2^z \tau_3^y \tau_4^x - \tau_4^z \tau_1^y \tau_2^x) (\vec{\sigma}_4 \cdot \vec{\sigma}_2) \right]. \quad (8.132)$$

Later we will see that such terms reduce the number of four-fermion interactions due to momentum conservation. Using the Majorana representation, this term can be rephrased as

$$\mathcal{H}_{TRB} = i \frac{\hbar}{2} \sum_{\square_{xz}} \left[ (\hat{u}_{34} \hat{u}_{41} + \hat{u}_{12} \hat{u}_{23}) \sum_{\alpha=x,y,z} c_3^\alpha c_1^\alpha \right. \quad (8.133)$$

$$\left. - (\hat{u}_{41} \hat{u}_{12} + \hat{u}_{23} \hat{u}_{34}) \sum_{\alpha=x,y,z} c_4^\alpha c_2^\alpha \right]. \quad (8.134)$$

The graphical representation is shown in Fig. 8.6(a). Before we proceed, we remark that in this case with TRB, we do not need any symmetry to protect the gaplessness, unlike the time reversal invariant case. The bilinear term  $I_{RL}$  that could open a gap is not allowed in the Hamiltonian due to momentum conservation, see below. For illustration and simplicity, we proceed to take the same parameters as in Chapter 8.2 and include  $\hbar, \{J_x, J_y, J_z, J'_z, \hbar\} = \{1.2, 0.8, 1.0, 1.1, 0.5\}$ . The complex fermion spectrum is shown in Fig. 8.6(b), and we can clearly see that due to the presence of the time-reversal breaking term, there is no right-left symmetry anymore (i.e.,  $k_{FL} \neq -k_{FR}$ ). In the weak-coupling regime, the general four-fermion interactions can be written as

$$\mathcal{H}_{int}^{TRB} = \tilde{u}_\rho \mathcal{J}_R \mathcal{J}_L - \tilde{u}_{\sigma 1} \vec{\mathcal{J}}_R \cdot \vec{\mathcal{J}}_L + \tilde{u}_{\sigma 2} I_{RL}^\dagger I_{RL}, \quad (8.135)$$

where  $\mathcal{J}_P, \vec{\mathcal{J}}_P$ , and  $I_{RL}$  are defined in Eqs. (8.38)–(8.40). We can see that the number of allowed interactions is reduced because there is no special relation between  $k_{FR}$  and  $k_{FL}$  and additional terms are forbidden by momentum conservation.

The weak-coupling differential RG equations in this case are

$$\dot{\tilde{u}}_\rho = \frac{1}{\pi(v_R + v_L)} [\tilde{u}_{\sigma_2}^2 + 2\tilde{u}_{\sigma_1}\tilde{u}_{\sigma_2}], \quad (8.136)$$

$$\dot{\tilde{u}}_{\sigma_1} = \frac{1}{\pi(v_R + v_L)} [-\tilde{u}_{\sigma_1}^2 + 2\tilde{u}_{\sigma_1}\tilde{u}_{\sigma_2}], \quad (8.137)$$

$$\dot{\tilde{u}}_{\sigma_2} = \frac{1}{\pi(v_R + v_L)} [-3\tilde{u}_{\sigma_2}^2 - 6\tilde{u}_{\sigma_1}\tilde{u}_{\sigma_2}]. \quad (8.138)$$

We can give a qualitative description of the stable flows [163]. If  $\tilde{u}_{\sigma_1} > 0$  and  $\tilde{u}_{\sigma_1} + \tilde{u}_{\sigma_2} > 0$ , the couplings  $\tilde{u}_{\sigma_{1,2}}$  are marginally irrelevant and flow to zero,  $u_{\sigma_1}^* = u_{\sigma_2}^* = 0$ . The coupling  $\tilde{u}_\rho$  approaches a fixed value,  $\tilde{u}_\rho^*$ , and is strictly marginal; unlike the time reversal symmetric case in Chapter 8.2, there is no condition on the sign of  $\tilde{u}_\rho^*$ . We conclude that the SU(2) MSL with explicit time reversal breaking is stable in a wide regime of parameters. We also note that, even though initially there is no conservation of the  $f$ -fermions in this model, breaking TRS leads to  $k_{FL} \neq -k_{FR}$  and prohibits four-fermion interactions such as  $f^\alpha f^\beta f^\gamma f^\delta$  and  $f^{\alpha\dagger} f^\beta f^\gamma f^\delta$ , so the fermion conservation emerges at low energy. We note that if we rewrite the couplings as

$$\tilde{u}_{\sigma_1} = -\frac{\pi(v_R + v_L)}{2\sqrt{2}}g_1, \quad (8.139)$$

$$\tilde{u}_{\sigma_2} = \frac{\pi(v_R + v_L)}{2\sqrt{2}}(g_1 + g_2), \quad (8.140)$$

the RG equations can be rephrased as

$$\dot{\tilde{g}}_\rho = 3\dot{\tilde{u}}_\rho + \dot{\tilde{u}}_{\sigma_2} = 0, \quad (8.141)$$

$$\dot{g}_1 = \frac{1}{2\sqrt{2}}(3g_1^2 + 2g_1g_2), \quad (8.142)$$

$$\dot{g}_2 = \frac{1}{2\sqrt{2}}(-3g_2^2 - 2g_1g_2). \quad (8.143)$$

The last two equations are exactly the same as one-loop RG equations in an SU(3) WZW model in [163]. Note that in the SU(2) MSL the ‘‘charge’’ ( $\rho$ ) sector also remains gapless, see Appendix 8.B.

# Bibliography

- [1] J. des Cloizeaux and J. J. Pearson, Phys. Rev. **128**, 2131 (1962).
- [2] F. D. M. Haldane, Phys. Rev. Lett. **50**, 1153 (1983).
- [3] P. A. Lee, N. Nagaosa, and X.-G. Wen, Rev. Mod. Phys. **78**, 17 (2006).
- [4] P. A. Lee, Science **321**, 1306 (2008).
- [5] L. Balents, Nature **464**, 199 (2010).
- [6] V. Kalmeyer and R. B. Laughlin, Phys. Rev. Lett. **59**, 2095 (1987).
- [7] S. A. Kivelson, D. S. Rokhsar, and J. P. Sethna, Phys. Rev. B **35**, 8865 (1987).
- [8] N. Read and B. Chakraborty, Phys. Rev. B **40**, 7133 (1989).
- [9] N. Read and S. Sachdev, Phys. Rev. Lett. **66**, 1773 (1991).
- [10] X. G. Wen, Phys. Rev. B **44**, 2664 (1991).
- [11] T. Senthil and M. P. A. Fisher, Phys. Rev. B **62**, 7850 (2000).
- [12] R. Moessner and S. L. Sondhi, Phys. Rev. Lett. **86**, 1881 (2001).
- [13] X.-G. Wen, Phys. Rev. B **65**, 165113 (2002).
- [14] A. Kitaev, Ann. Phys. **321**, 2 (2006).
- [15] Y. Shimizu, K. Miyagawa, K. Kanoda, M. Maesato, and G. Saito, Phys. Rev. Lett. **91**, 107001 (2003).

- [16] Y. Kurosaki, Y. Shimizu, K. Miyagawa, K. Kanoda, and G. Saito, *Phys. Rev. Lett.* **95**, 177001 (2005).
- [17] S. Yamashita et al., *Nature Physics* **4**, 459 (2008).
- [18] M. Yamashita et al., *Nature Physics* **5**, 44 (2009).
- [19] R. H. McKenzie, *Comments Condens. Matter Phys.* **18**, 309 (1998), cond-mat/9802198.
- [20] T. Itou, A. Oyamada, S. Maegawa, M. Tamura, and R. Kato, *J. Phys. Cond. Mat.* **19**, 145247 (2007).
- [21] T. Itou, A. Oyamada, S. Maegawa, M. Tamura, and R. Kato, *Phys. Rev. B* **77**, 104413 (2008).
- [22] T. Itou, A. Oyamada, S. Maegawa, and R. Kato, *Nature Physics* **6**, 673 (2010).
- [23] M. Yamashita et al., *Science* **328**, 1246 (2010).
- [24] B. J. Powell and R. H. McKenzie, *Reports on Progress in Physics* **74**, 056501 (2011).
- [25] S. Yamashita, T. Yamamoto, Y. Nakazawa, M. Tamura, and R. Kato, *Nature Communications* **2**, 275 (2011).
- [26] K. Kanoda and R. Kato, *Annual Review of Condensed Matter Physics* **2**, 167 (2011).
- [27] O. I. Motrunich, *Phys. Rev. B* **72**, 045105 (2005).
- [28] S.-S. Lee and P. A. Lee, *Phys. Rev. Lett.* **95**, 036403 (2005).
- [29] D. N. Sheng, O. I. Motrunich, and M. P. A. Fisher, *Phys. Rev. B* **79**, 205112 (2009).
- [30] H.-H. Lai and O. I. Motrunich, *Phys. Rev. B* **79**, 235120 (2009).
- [31] H.-H. Lai and O. I. Motrunich, *Phys. Rev. B* **81**, 045105 (2010).
- [32] H.-H. Lai and O. I. Motrunich, *Phys. Rev. B* **82**, 125116 (2010).

- [33] H.-H. Lai and O. I. Motrunich, Phys. Rev. B **82**, 195119 (2010).
- [34] M. S. Block, D. N. Sheng, O. I. Motrunich, and M. P. A. Fisher, Phys. Rev. Lett. **106**, 157202 (2011).
- [35] H. Katsura, N. Nagaosa, and P. A. Lee, Phys. Rev. Lett. **104**, 066403 (2010).
- [36] S.-S. Lee, P. A. Lee, and T. Senthil, Phys. Rev. Lett. **98**, 067006 (2007).
- [37] V. Galitski and Y. B. Kim, Phys. Rev. Lett. **99**, 266403 (2007).
- [38] H. C. Kandpal, I. Opahle, Y.-Z. Zhang, H. O. Jeschke, and R. Valenti, Phys. Rev. Lett. **103**, 067004 (2009).
- [39] K. Nakamura, Y. Yoshimoto, T. Kosugi, R. Arita, and M. Imada, J. Phys. Soc. Jpn. **78**, 083710 (2009).
- [40] I. Kezsmarki et al., Phys. Rev. B **74**, 201101 (2006).
- [41] K. Miyagawa, A. Kawamoto, Y. Nakazawa, and K. Kanoda, Phys. Rev. Lett. **75**, 1174 (1995).
- [42] K. Miyagawa, A. Kawamoto, K. Uchida, and K. Kanoda, Physica B: Condensed Matter **284-288**, Part 2, 1589 (2000).
- [43] D. F. Smith et al., Phys. Rev. B **68**, 024512 (2003).
- [44] Y. Shimizu, K. Miyagawa, K. Kanoda, M. Maesato, and G. Saito, Phys. Rev. B **73**, 140407 (2006).
- [45] R. S. Manna, M. de Souza, A. Brühl, J. A. Schlueter, and M. Lang, Phys. Rev. Lett. **104**, 016403 (2010).
- [46] G. Koutroulakis, T. Zhou, S. E. Brown, J. D. Thompson, and R. Kato, APS March meeting (2012), <http://meetings.aps.org/link/BAPS.2012.MAR.Q8.5> .

- [47] M. P. A. Fisher, Course 7: Mott Insulators, Spin Liquids and Quantum Disordered Superconductivity, in *Topological Aspects of Low Dimensional Systems*, edited by A. Comtet, T. Jolicoeur, S. Ouvry, and F. David, page 575, (1999).
- [48] C. L. Kane, Univeristy of Colorado, Boulder, summer school (2005).
- [49] L. Balents and M. P. A. Fisher, *Phys. Rev. B* **53**, 12133 (1996).
- [50] R. Shankar, *Rev. Mod. Phys.* **66**, 129 (1994).
- [51] J. Cardy, *Scaling and Renormalization in Statistical Physics*, Cambridge University Press (1996).
- [52] J. von Delft and H. Schoeller, *Annalen der Physik* **7**, 225 (1998).
- [53] A. Luther and V. J. Emery, *Phys. Rev. Lett.* **33**, 589 (1974).
- [54] L. B. Ioffe and A. I. Larkin, *Phys. Rev. B* **39**, 8988 (1989).
- [55] T. Holstein, R. E. Norton, and P. Pincus, *Phys. Rev. B* **8**, 2649 (1973).
- [56] M. Reizer, *Phys. Rev. B* **40**, 11571 (1989).
- [57] P. A. Lee, *Phys. Rev. Lett.* **63**, 680 (1989).
- [58] P. A. Lee and N. Nagaosa, *Phys. Rev. B* **46**, 5621 (1992).
- [59] J. Polchinski, *Nucl. Phys. B* **422**, 617 (1994).
- [60] B. L. Altshuler, L. B. Ioffe, and A. J. Millis, *Phys. Rev. B* **50**, 14048 (1994).
- [61] Y. B. Kim, A. Furusaki, X. G. Wen, and P. A. Lee, *Phys. Rev. B* **50**, 17917 (1994).
- [62] E. H. Lieb, *Phys. Rev. Lett.* **73**, 2158 (1994).
- [63] H.-H. Lai and O. I. Motrunich, *Phys. Rev. B* **83**, 155104 (2011).
- [64] M. Fabrizio, *Phys. Rev. B* **54**, 10054 (1996).
- [65] K. Louis, J. V. Alvarez, and C. Gros, *Phys. Rev. B* **64**, 113106 (2001).

- [66] C. Gros, K. Hamacher, and W. Wenzel, *Europhysics Letters (EPL)* **69**, 616 (2005).
- [67] S. Daul and R. M. Noack, *Phys. Rev. B* **61**, 1646 (2000).
- [68] R. Arita, K. Kuroki, H. Aoki, and M. Fabrizio, *Phys. Rev. B* **57**, 10324 (1998).
- [69] G. I. Japaridze, R. M. Noack, D. Baeriswyl, and L. Tincani, *Phys. Rev. B* **76**, 115118 (2007).
- [70] C. Kane, L. Balents, and M. P. A. Fisher, *Phys. Rev. Lett.* **79**, 5086 (1997).
- [71] H.-H. Lin, L. Balents, and M. P. A. Fisher, *Phys. Rev. B* **56**, 6569 (1997).
- [72] M. Capello, F. Becca, M. Fabrizio, S. Sorella, and E. Tosatti, *Phys. Rev. Lett.* **94**, 026406 (2005).
- [73] L. F. Tocchio, A. Parola, C. Gros, and F. Becca, *Phys. Rev. B* **80**, 064419 (2009).
- [74] A. H. MacDonald, S. M. Girvin, and D. Yoshioka, *Phys. Rev. B* **37**, 9753 (1988).
- [75] A. D. Klironomos, J. S. Meyer, T. Hikihara, and K. A. Matveev, *Phys. Rev. B* **76**, 075302 (2007).
- [76] J. S. Meyer and K. A. Matveev, *J. Phys. Cond. Matt.* **21**, 023203 (2009).
- [77] A. Kawamoto, Y. Honma, and K. Kumagai, *Phys. Rev. B* **70**, 060510(R) (2004).
- [78] A. Kawamoto, Y. Honma, K. Kumagai, N. Matsunaga, and K. Nomura, *Phys. Rev. B* **74**, 212508 (2006).
- [79] K. Okunishi, Y. Hieida, and Y. Akutsu, *Phys. Rev. B* **60**, R6953 (1999).
- [80] K. Okunishi and T. Tonegawa, *J. Phys. Soc. Jpn.* **72**, 479 (2003).
- [81] I. P. McCulloch et al., *Phys. Rev. B* **77**, 094404 (2008).
- [82] K. Okunishi, *J. Phys. Soc. Jpn.* **77**, 114004 (2008).
- [83] T. Hikihara, T. Momoi, A. Furusaki, and H. Kawamura, *Phys. Rev. B* **81**, 224433 (2010).

- [84] R. Shindou and T. Momoi, Phys. Rev. B **80**, 064410 (2009).
- [85] A. A. Nersesyan, A. O. Gogolin, and F. H. L. Essler, Phys. Rev. Lett. **81**, 910 (1998).
- [86] A. V. Chubukov, Phys. Rev. B **44**, 4693 (1991).
- [87] T. Vekua, A. Honecker, H.-J. Mikeska, and F. Heidrich-Meisner, Phys. Rev. B **76**, 174420 (2007).
- [88] T. Hikihara, L. Kecke, T. Momoi, and A. Furusaki, Phys. Rev. B **78**, 144404 (2008).
- [89] M. Sato, T. Momoi, and A. Furusaki, Phys. Rev. B **79**, 060406 (2009).
- [90] N. Shannon, T. Momoi, and P. Sindzingre, Phys. Rev. Lett. **96**, 027213 (2006).
- [91] T. Momoi, P. Sindzingre, and N. Shannon, Phys. Rev. Lett. **97**, 257204 (2006).
- [92] K. A. Muttalib and V. J. Emery, Phys. Rev. Lett. **57**, 1370 (1986).
- [93] M. Fabrizio, Phys. Rev. B **48**, 15838 (1993).
- [94] U. Ledermann and K. Le Hur, Phys. Rev. B **61**, 2497 (2000).
- [95] T. Grover, N. Trivedi, T. Senthil, and P. A. Lee, Phys. Rev. B **81**, 245121 (2010).
- [96] G. Roux, E. Orignac, S. R. White, and D. Poilblanc, Phys. Rev. B **76**, 195105 (2007).
- [97] B. N. Narozhny, S. T. Carr, and A. A. Nersesyan, Phys. Rev. B **71**, 161101 (2005).
- [98] S. T. Carr, B. N. Narozhny, and A. A. Nersesyan, Phys. Rev. B **73**, 195114 (2006).
- [99] E. Orignac and T. Giamarchi, Phys. Rev. B **64**, 144515 (2001).
- [100] D. S. Rokhsar, Phys. Rev. Lett. **65**, 1506 (1990).
- [101] D. Sen and R. Chitra, Phys. Rev. B **51**, 1922 (1995).
- [102] O. I. Motrunich, Phys. Rev. B **73**, 155115 (2006).
- [103] L. N. Bulaevskii, C. D. Batista, M. V. Mostovoy, and D. I. Khomskii, Phys. Rev. B **78**, 024402 (2008).

- [104] K. A. Al-Hassanieh, C. D. Batista, G. Ortiz, and L. N. Bulaevskii, *Phys. Rev. Lett.* **103**, 216402 (2009).
- [105] D. I. Khomskii, *Journal of Physics: Condensed Matter* **22**, 164209 (2010).
- [106] J. O. Fjaerestad and J. B. Marston, *Phys. Rev. B* **65**, 125106 (2002).
- [107] Y.-F. Wand and C.-D. Gong, arXiv:0909.1622v1 (unpublished).
- [108] K. Gregor and O. I. Motrunich, *Phys. Rev. B* **79**, 024421 (2009).
- [109] Y. B. Kim and A. J. Millis, *Phys. Rev. B* **67**, 085102 (2003).
- [110] A. Kolezhuk, S. Sachdev, R. R. Biswas, and P. Chen, *Phys. Rev. B* **74**, 165114 (2006).
- [111] D. H. Kim and P. A. Lee, *Annals of Physics* **272**, 130 (1999).
- [112] S. Eggert and I. Affleck, *Phys. Rev. B* **46**, 10866 (1992).
- [113] S. Eggert and I. Affleck, *Phys. Rev. Lett.* **75**, 934 (1995).
- [114] M. Takigawa, N. Motoyama, H. Eisaki, and S. Uchida, *Phys. Rev. B* **55**, 14129 (1997).
- [115] N. Fujiwara, H. Yasuoka, Y. Fujishiro, M. Azuma, and M. Takano, *Phys. Rev. Lett.* **80**, 604 (1998).
- [116] C. L. Kane and M. P. A. Fisher, *Phys. Rev. Lett.* **68**, 1220 (1992).
- [117] S. Eggert and S. Rommer, *Phys. Rev. Lett.* **81**, 1690 (1998).
- [118] S. Rommer and S. Eggert, *Phys. Rev. B* **62**, 4370 (2000).
- [119] S. Eggert, D. P. Gustafsson, and S. Rommer, *Phys. Rev. Lett.* **86**, 516 (2001).
- [120] I. Affleck, arXiv:0809.3474 (unpublished).
- [121] R. J. Bursill, T. Xiang, and G. A. Gehring, *Journal of Physics: Condensed Matter* **8**, L583 (1996).

- [122] X. Wang and T. Xiang, Phys. Rev. B **56**, 5061 (1997).
- [123] N. Shibata, Journal of the Physical Society of Japan **66**, 2221 (1997).
- [124] M. Bortz and J. Sirker, J. Phys. A **38**, 5957 (2005).
- [125] S.-S. Lee and P. A. Lee, Phys. Rev. Lett. **95**, 036403 (2005).
- [126] Y. Qi, C. Xu, and S. Sachdev, Phys. Rev. Lett. **102**, 176401 (2009).
- [127] C. Xu and S. Sachdev, Phys. Rev. B **79**, 064405 (2009).
- [128] R. R. Biswas, L. Fu, C. R. Laumann, and S. Sachdev, Phys. Rev. B **83**, 245131 (2011).
- [129] X.-G. Wen, Phys. Rev. D **68**, 065003 (2003).
- [130] X.-Y. Feng, G.-M. Zhang, and T. Xiang, Phys. Rev. Lett. **98**, 087204 (2007).
- [131] G. Baskaran, S. Mandal, and R. Shankar, Phys. Rev. Lett. **98**, 247201 (2007).
- [132] D.-H. Lee, G.-M. Zhang, and T. Xiang, Phys. Rev. Lett. **99**, 196805 (2007).
- [133] H. Yao and S. A. Kivelson, Phys. Rev. Lett. **99**, 247203 (2007).
- [134] H.-D. Chen and J. Hu, Phys. Rev. B **76**, 193101 (2007).
- [135] J. Vidal, K. P. Schmidt, and S. Dusuel, Phys. Rev. B **78**, 245121 (2008).
- [136] H. Yao, S.-C. Zhang, and S. A. Kivelson, Phys. Rev. Lett. **102**, 217202 (2009).
- [137] S. Mandal and N. Surendran, Phys. Rev. B **79**, 024426 (2009).
- [138] C. Wu, D. Arovas, and H.-H. Hung, Phys. Rev. B **79**, 134427 (2009).
- [139] Z. Nussinov and G. Ortiz, Phys. Rev. B **79**, 214440 (2009).
- [140] G. Baskaran, G. Santhosh, and R. Shankar, arXiv:0908.1614v3 (unpublished).
- [141] A. J. Willans, J. T. Chalker, and R. Moessner, Phys. Rev. Lett. **104**, 237203 (2010).

- [142] K. S. Tikhonov and M. V. Feigel'man, Phys. Rev. Lett. **105**, 067207 (2010).
- [143] K. S. Tikhonov, M. V. Feigel'man, and A. Y. Kitaev, Phys. Rev. Lett. **106**, 067203 (2011).
- [144] G.-W. Chern, Phys. Rev. B **81**, 125134 (2010).
- [145] F. Wang, Phys. Rev. B **81**, 184416 (2010).
- [146] V. Chua, H. Yao, and G. A. Fiete, Phys. Rev. B **83**, 180412 (2011).
- [147] H. Yao and D.-H. Lee, Phys. Rev. Lett. **107**, 087205 (2011).
- [148] K. Dhochak, R. Shankar, and V. Tripathi, Phys. Rev. Lett. **105**, 117201 (2010).
- [149] F. Wang and A. Vishwanath, Phys. Rev. B **80**, 064413 (2009).
- [150] O. I. Motrunich and M. P. A. Fisher, Phys. Rev. B **75**, 235116 (2007).
- [151] A. M. Tsvelik, Phys. Rev. Lett. **69**, 2142 (1992).
- [152] P. Coleman, E. Miranda, and A. Tsvelik, Phys. Rev. B **49**, 8955 (1994).
- [153] B. S. Shastry and D. Sen, Phys. Rev. B **55**, 2988 (1997).
- [154] Furthermore, we also calculated the energy spectrum in a cylindrical geometry with one open boundary and confirmed that there are no gapless edge modes in this system.
- [155] M. P. A. Fisher, O. I. Motrunich, and D. N. Sheng, arXiv:0812.2955 (unpublished).
- [156] R. Shankar, Acta Phys. Pol. B **26**, 1835 (1995).
- [157] H.-H. Lai and O. I. Motrunich, Phys. Rev. B **84**, 085141 (2011).
- [158] R. Moessner, S. L. Sondhi, and E. Fradkin, Phys. Rev. B **65**, 024504 (2001).
- [159] E. Fradkin and S. H. Shenker, Phys. Rev. D **19**, 3682 (1979).
- [160] T. Senthil and M. P. A. Fisher, Phys. Rev. B **62**, 7850 (2000).

- [161] In the calculations, we used antiperiodic boundary conditions in the horizontal direction, which gives exact solution in the sector with  $\prod_{j \in \text{leg}-1} \tau_j^z = \prod_{j \in \text{leg}-2} \tau_j^z = 1$ .
- [162] M. Wimmer, arXiv:1102.3440 (unpublished).
- [163] C. Itoi and M.-H. Kato, Phys. Rev. B **55**, 8295 (1997).
- [164] H.-C. Jiang, Z.-C. Gu, X.-L. Qi, and S. Trebst, Phys. Rev. B **83**, 245104 (2011).
- [165] W. Rantner and X.-G. Wen, Phys. Rev. B **66**, 144501 (2002).
- [166] M. Hermele et al., Phys. Rev. B **70**, 214437 (2004).
- [167] A. M. Polyakov, Gauge Fields and Strings, Harwood Academic, London (1987).
- [168] M. E. Peskin, Annals of Physics **113**, 122 (1978).
- [169] R. Savit, Rev. Mod. Phys. **52**, 453 (1980).